PHYSICAL INVESTIGATION OF CAVITATION VORTEX COLLAPSE

THÈSE N^{O} 2463 (2001)

PRÉSENTÉE AU DÉPARTEMENT DE GÉNIE MÉCANIQUE

ÉCOLE POLYTECHNIQUE FÉDÉRALE DE LAUSANNE

POUR L'OBTENTION DU GRADE DE DOCTEUR ÈS SCIENCES TECHNIQUES

PAR

Philippe COUTY

D.E.A en dynamique des fluides, Ecole Centrale de nantes, France
et de nationalité française

acceptée sur proposition du jury:

Prof. F. Avellan, directeur de thèse
prof. H. Bleuler, rapporteur
Dr M. Farhat, rapporteur
Prof. J. Field, rapporteur
Dr F. Pereira, rapporteur

Lausanne, EPFL
2002

Je vous vois dans cette entreprise comme un homme qui a un but, et qui se met en route. Pour faire ce voyage il choisit le véhicule le plus incertain, l'itinéraire le plus dangereux, ce qui implique un grand nombre de péripéties. Lorsqu'il arrive, il s'apperçoit qu'il n'y a plus de but, ou pire, qu'il n'y en a jamais eu. Il peut avoir alors deux réactions. Ou il est désespéré et il maudit son voyage inutilement périlleux. Ou il se dit que le but était le voyage lui-même, ce qui justifie après coup son absurbe choix, car la plus grande imprudence devient alors le plus grand plaisir.

Michel Rio, "Mélancolie Nord"

Remerciements

Je tiens à exprimer ma reconnaissance envers le personnel du laboratoire de machines hydrauliques pour son aide quotidienne et sans faille. Je tiens à remercier tous ceux qui ont contribué à une ambiance chaleureuse.

J'adresse mes vifs remerciements au professeur François Avellan, qui a assuré la direction de ma thèse. Je le remercie de la confiance et de l'aide scientifique qu'il m'a accordé au cours de ces 5 ans. Je remercie le docteur Mohamed Farhat et le Docteur Philippe Dupont pour l'encadrement scientifique et technique de haute qualité dont ils m'ont fait bénéficier.

Je tiens également à remercier Electricité de France et le Fonds National Suisse pour leur apport scientifique et financier.

Résumé

Parmi les effets néfastes de la cavitation (chute de performance, bruit, vibrations, etc.), l'érosion de cavitation reste l'un des facteurs les plus limitatifs dans une perspective de conception de machines de taille réduite. La cavitation est particulièrement indésirable, car elle agit en synergie avec d'autres procédés d'endommagement tels que la corrosion et l'abrasion par le sable. L'ensemble de ces phénomènes conduit à une destruction progressive des aubages d'une machine hydraulique. Bien que de nombreuses études qui visent à prédire le taux d'érosion de cavitation aient été réalisées, les modèles existants ont encore besoin d'être améliorés.
Dans une perspective d'élaboration de nouveaux modèles de l'agressivité de la cavitation, ce travail a pour but d'étudier les mécanismes hydrodynamiques qui sont à l'origine de l'érosion de cavitation. La démarche proposée s'appuie à la fois sur l'étude des impacts de cavitation, et sur l'exploration des phénomènes hydrodynamiques liés à l'implosion d'un vortex cavitant. Ainsi, l'étude dans son ensemble comprend deux parties.

Premièrement, l'étude de l'agressivité de la cavitation de bord d'attaque, qui est l'une des situations les plus érosives, est réalisée à l'aide d'une technique de marquage. Celle-ci est appliquée à deux aubages 2D d'échelle différente en tunnel de cavitation, les aubages pouvant être placés soit dans une veine d'essai rectangulaire, soit dans une veine d'essai divergente qui simule la présence d'un gradient de pression. Les matériaux exposés à une cavitation de bord d'attaque sont analysés à l'aide d'un profilomètre 3D. Cette étude a permis de valider le modèle énergétique en considérant le rendement d'implosion qui représente le transfert global d'énergie des cavités de vapeur vers le matériau. Les résultats démontrent que la vitesse de l'écoulement et la présence d'un gradient de pression sont les paramètres prépondérants, indifféremment du mode de la cavitation de bord d'attaque, stable ou instable. De plus, deux types d'agressivité de la cavitation de bord d'attaque ont été identifiés : les structures de vapeur qui sont crées par les instabilités de cisaillement à proximité de l'interface eau-vapeur et qui génèrent des impacts isolés, et les lâchers de grosses structures de vapeur de tailles plus importantes qui sont à l'origine d'impacts groupés.

Deuxièmement, l'exploration des phénomènes physiques liés au collapse d'un vor-

tex cavitant est entreprise. La conception d'une cellule de visualisation ainsi que le développement d'un système de visualisation par ombroscopie ont été nécessaires. Les résultats de cette étude mettent en évidence la phénoménologie très riche et très complexe du collapse d'un vortex cavitant. La phase finale de l'implosion conduit à une forme de cavité imprédictible et irrégulière. Le collapse ainsi que l'émission d'ondes de choc sont des phénomènes très locaux qui surgissent depuis différentes origines pour une même cavité principale. Les vitesses de l'interface ont été estimées. Elles sont supérieures à 350 $m\ s^{-1}$ au rebond. Etant donné que le collapse n'est pas régulier, les vitesses locales à l'interface sont probablement bien plus importantes. Par ailleurs, le phénomène de luminescence du vortex cavitant a été exploité pour localiser les collapses. La luminescence est détectée à l'aide d'un tube photomultiplicateur de photons et d'une caméra à intensification de lumière. La luminescence d'un vortex cavitant isolé a été mise en évidence pour la première fois. De plus, des visualisations simultanées de la luminescence et des ondes de choc ont été accomplies. La luminescence a été caractérisée en termes d'intensité, de taux de succès de la détection et de localisation pour différentes conditions hydrodynamiques. La luminescence du vortex cavitant se traduit par des impulsions lumineuses de durées variables de 10 ns à 100 ns. L'intensité du vortex est l'un des paramètres déterminants de l'émission. Les visualisations simultanées démontrent que les sources luminescentes se confondent avec l'épicentre des ondes de choc. De plus, l'émission de la lumière et la génération des ondes peuvent être considérées comme synchrones avec une incertitude inférieure à 500 ns. Il résulte également que le stade final de l'implosion est d'autant plus proche de la paroi que l'intensité du tourbillon est accrue. Ce résultat peut être extrapolé pour le cas des tourbillons cavitants transitoires qui sont générés par une cavitation de bord d'attaque. Il explique comment l'agressivité de la cavitation est accrue lorsque la vitesse de l'écoulement augmente : le collapse des tourbillons cavitants a lieu plus proche de la paroi lorsque la vitesse de l'écoulement augmente.

Abstract

Among the different negative cavitation effects that are associated with the cavitation presence (efficiency drop, noise and vibrations etc.), cavitation erosion is still one of the main limiting features in the modern trend towards designing hydraulic machines with smaller size. Cavitation erosion is particularly undesirable, because it can act in synergy with other erosion processes like corrosion and sand abrasion, which all lead to the progressive destruction of blades of runners. Although many studies attempt to predict the erosion intensity for a given set of hydrodynamic conditions, existing prediction models still need to be largely improved. Towards the development of new cavitation aggressiveness models, the context of this present work is to study the hydrodynamic mechanisms involved in cavitation erosion.

The proposed approach is based on both the study of cavitation impacts and on the physical investigation of a cavitation vortex collapse. Thus, the whole study can be divided into two main parts.

Firstly, a study of the cavitation aggressiveness of leading edge cavitation, which one of the most aggressive cavitation types, is achieved by performing pitting experiments in cavitation tunnel with two 2D blades of different scale. They are either placed in a rectangular test section, or in a diverging test section in order to simulate the presence of a pressure gradient. Material specimens which are exposed to a leading edge cavitation are analysed with the help of a 3D profilometry. This study has validated the energetic model by considering the collapse efficiency which represent the global energy transfer from the vapour structures to the material. It has been shown that the flow velocity and the pressure gradient are the principal influencing macroscopic parameters for both stable and unstable leading edge cavitation. Moreover, two different kinds of cavitation attack can be suggested : the vapour structures that are created at the water-vapour interface lead to isolated impacts, the large shed transient cavities yield larger and grouped impacts.

Secondly, the physical study of a cavitation vortex collapse has been carried out. This involved the cavitation vortex generator of IMHEF for the generation of an isolated vortex. The development of a visualization test section and a high-speed video shadowgraphy technique has been be required. This study has shown the complex

hydrodynamic characteristics involved in the collapse of a cavitation vortex. The cavitation vortex collapse leads to an irregular and unpredictable vapour cavity shape at the final stage of the collapse. The collapse and the associated emission of shock waves are very local phenomena which can arise from different locations of the same main cavitation vortex. Estimations of the boundary velocity result in maximum values greater than 350 $m\,s^{-1}$ at the rebound. As the collapse is not regular, local velocity at the boundary might be much higher. Furthermore, the reliability of determining the centre of collapses by using the luminescence phenomenon of the cavitation vortex is evaluated. Luminescence has been detected with the help of a photomultiplier tube and an intensified light camera. The luminescence of an isolated cavitation vortex collapse has been experimentally shown for the first time. Moreover, a simultaneous captures of luminescence and shock waves have been achieved. The luminescence of the cavitation vortex has been characterized in the terms of time occurrence, location, success rate and intensity for variable hydrodynamic conditions.

The luminescence of the cavitation vortex appears as short light bursts with duration down to 10 ns and up to 100 ns. The vortex intensity is a driving parameter of the luminescence emission. Simultaneous visualizations demonstrate that luminescence sources mingle with the shock waves epicentres. Moreover, luminescence and shock wave ignition occur within a time interval which is less than 500 ns. As a remarkable result, the higher the vortex intensity is, the closer to the wall the cavitation vortex collapse takes place. Furthermore, this main result can be extrapolated to the case of transient cavitation vortices generated by a leading edge cavitation. It also explains the increase of the cavitation aggressiveness when the flow velocity increases : the cavitation vortices collapse closer to the wall when the flow velocity increases.

Table of Contents

List of Figures

List of Tables

Nomenclature

Principal notations

a_0	speed of sound in water		$m\,s^{-1}$
C_{ref}	flow velocity in the cavitation tunnel		$m\,s^{-1}$
C'_{ref}	flow velocity (diverging test section)		$m\,s^{-1}$
C_p	pressure coefficient	$\frac{p-p_{ref}}{\frac{1}{2}\rho C^2_{ref}}$	–
C_{pmax}	pressure coefficient in the main cavity closure region		–
C_s	velocity of the shock wave		$m\,s^{-1}$
D	collapse distance	$\sqrt{X^2+Y^2}$	mm
DO	dissolved oxygen contents in water		$mg\,l^{-1}$
ds	step sampling of the 3-D profilometry		μm
E_c	potential energy of vapour cavity		J
E_s	minimal damaging energy of material		J
E_d	deformation energy of material impacts		J
E_{dmoy}	mean deformation energy of impacts		J
E_a	acoustic energy		J
f_c	shed frequency of macroscopic vapour structures		Hz
f_s	frequency of the main cavity pulsation		Hz
H	impact depth		μm
H_{moy}	mean impact depth at location k		μm
i	flow angle of incidence		$^\circ$
l_c	main cavity length		m
n_r	index of refraction		–
N	rotation speed of the rotating valve in CVG		rpm
N_d	number of pits per second		s^{-1}
N_k	number of cavitation impacts at the specimen location k		–
N_{max}	maximum number of cavitation impacts		–
$\hat{n}(E_d)$	number of generated impacts during one time unit and having the energy E_d		$J^{-1}s^{-1}$
$n(E_d)$	probability density distribution of the indentation deformation energy having the deformation energy E_d		J^{-1}

$n(V_d)$	probability density distribution of the indentation volume		μm^{-3}
$\hat{n}(E_c)$	number of generated cavities during one time unit and having the potential energy E_c		$J^{-1}s^{-1}$
$\hat{n}(\lambda)$	statistical density		$m^{-1}s^{-1}$
p	pressure		Pa
P_{dyn}	dynamic pressure		Pa
p_{max}	maximum pressure		Pa
$p_v(T)$	vapour pressure		Pa
p_{ref}	reference pressure		Pa
p_∞	far field pressure		Pa
p_1	pressure at the convergence inlet of the cavitation tunnel		Pa
p_2	pressure at the test section inlet of cavitation tunnel		Pa
P_{er}	cavitation erosive power		W
P_d	deformation power		W
Q	flow rate in CVG		$l\,s^{-1}$
R_{moy}	mean impact radius		μm
$R_{10\%}$	cavitation impact radius		μm
R_c	equivalent radius of vapour structure		mm
R_s	radius of shock wave		mm
T	time duration of a pitting test		s
T	temperature		$^\circ C$
t_c, t'_c	collapse time of the cavitation vortex		μs
t_{max}	time of the maximum pressure peak		μs
t_r	collapse time of Rayleigh		s
t_{win}	start of the integration period of the IC		μs
V_d	volume of impact		μm^3
V_{dmoy}	mean impact volume		μm^3
V_{dlim}	minimum measured volume		μm^3
V_c	volume of a vapour cavity		mm^3
V_c, V'_c	boundary velocity of cavitation vortex		$m\,s^{-1}$
X	coordinate of the CVG test section		mm
X_{median}	median distance, X test section axis (wall distance)		mm
X_{mean}	mean distance, X test section axis (wall distance)		mm
Y	coordinate of the CVG test section		mm
Y_{median}	median distance, Y test section axis		mm
Y_{mean}	mean distance, Y test section axis		mm
ΔP	overpressure induced by a shock wave		Pa
σ,σ'	cavitation coefficient	$\sigma = \frac{p_2 - p_v(T)}{\frac{1}{2}\rho C_{ref}^2}$	$-$
τ	collapse time of Rayleigh		μs

$\tau_N(k)$	mean pitting rate at location k	$mm^{-2}\,s^{-1}$
$\tau_V(k)$	mean deformation volume rate at location k	$\mu m^3\,mm^{-2}\,s^{-1}$
$\tau_E(k)$	mean energy deformation rate at location k	$J\,mm^{-2}\,s^{-1}$
$\tau_n^{(1)}$	averaged pitting rate by interpolation	$mm^{-2}\,s^{-1}$
$\tau_e^{(1)}$	averaged energy deformation rate by interpolation	$J\,mm^{-2}\,s^{-1}$
$\tau_v^{(1)}$	averaged volume deformation rate by interpolation	$\mu m^3\,mm^{-2}\,s^{-1}$
η_{co}	collapse efficiency $\frac{\hat{n}(E_d)}{\hat{n}(E_c)}$	–
$\lambda = \lambda_x$	main dimension of the vapour cavity in flow direction	m
$\lambda_{x,y,z}$	main dimensions of a vapour cavity	m
Γ	vortex intensity in CVG	m

Constants

G	electric voltage of the *QUICK 05A* ® camera [0–1000]	V
h_{lim}	depth cut-off parameter of the 3D profilometry	$2\ \mu m$
k	index of profilometric measurement zone along the 2D blade chord 10%–90%	–
D_{in}	diameter of the flow inlet in CVG	$8\ mm$
D_v	diameter of the cylindrical chamber in CVG	$80\ mm$
L	hydrofoil chord length	$60mm\&100mm$
Lx, Ly	dimensions of profilometric measurement locations	$3mm\&5mm$
N_{lim}	diameter cut-off parameter of the 3D profilometry	3

Abbreviations

CCD	Charged Coupled Device
CS	Cranz-Schardin camera
CVG	Cavitation Vortex Generator
IC	Intensified light camera *QUICK 05A* ®
PMT	Photomultiplier tube

INTRODUCTION

Introduction

Context

Cavitation definition

The cavitation is the thermodynamic phenomenon that defines the transition from the liquid state to the gas state with no external heat source (Batchelor, 1967). Cavitation corresponds to a discontinuity of the fluid continuum, which takes the form of vapour cavities. Initialised by the presence of nuclei in the fluid (micro-bubbles, solid particles etc.), vapour cavities appear in liquids when the pressure p is lower than a critical value $p_c(T)$, which approximately corresponds to the vapour pressure of the fluid $p_v(T)$. The cavitation is therefore conditioned by an absolute pressure condition given by :

$$p < p_c(T) \text{ with } p_c(T) \simeq p_v(T) \text{ [Pa]}$$

These vapour cavities disappear violently under a surrounding recompression. As a more global definition, cavitation is defined as the history of appearance and disappearance of these vapour cavities. Cavitation is observed in water or in other liquids as long as the cavitation condition is fulfilled. This can occur in flow regions where low pressure is reached because of local high velocities, and by local vortices or pressure fluctuations due to flow shears, acceleration etc.

Types of cavitation

Bubbles and vortices

Cavitation can appear in the form of isolated bubbles, clouds of micro-cavities or vortices. Cavitation bubble is for example met close to underwater ultrasound transmitters or in hydraulic turbines working at best efficiency point under low Thomas numbers. The occurrence of such a cavitation is very sensitive to nuclei contents in water. Moreover, the presence of complex vapour structures and vortices is typical

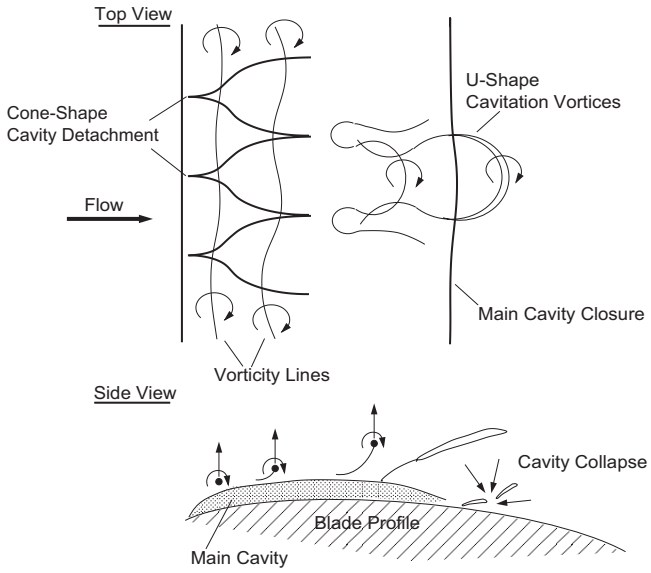

Figure 1: Generation mechanism of transient vortices from Avellan *et al.* (1988)

of many high velocity turbulent flows. Important examples of flow-cavitation interaction include cavitation in shear layers, boundary layers, the wake behind leading edge cavitation, the shear layer of submerged jets etc. These vapour structures can be generated from the interface of an attached cavitation and interact with the flow itself. A schematic of the generation mechanism of cavitation vortices in the closure region of leading edge cavitation on a 2-D blade is proposed in figure 1 (Avellan *et al.*, 1988; Dupont, 1993). In this illustration, the important role of the flow vorticity in the attack process of cavitation is also introduced. According Kelvin's theorem, the vapour structures which extend along the vortex tubes, can end on the blade surface and thus cause erosion. Accordingly, the intensity of theses vortices govern the location of the collapses and therefore has an influence on the aggressiveness of the vapour structures.

Attached cavitation

Cavitation can be attached to a solid boundary like tip vortex or leading edge cavitation on blades. This is for example the case for the blades of ship propeller, pump impeller or turbine runners. For this type of cavitation, in addition to the pressure condition and nuclei population, the cavitation appearance is strongly influenced by the surface roughness from which the cavitation detachment is observed. Moreover, physical and chemical properties of material of the solid surface can strongly influence the detachment as well.

Cavitation erosion in hydraulic machines

Among the different negative effects that are associated with the cavitation presence (efficiency drop, noise, vibrations etc.), cavitation erosion is still one of the main limiting features in the modern trend towards designing hydraulic machines with smaller size. The diminution of the size of hydraulic machines, which is motivated by the reduction of the cost of construction while keeping high performance machines, results in an enlargement of cavitation by increasing the relative flow velocity.
Cavitation erosion is particularly undesirable, because it can act in synergy with other erosion processes like corrosion and sand abrasion, which all lead to the progressive destruction of blades of runners. It is easy to understand the interest, on the one hand, for learning about erosion process, and on the other hand, for improving cavitation flow calculation in hydraulic machines. This will help to design hydraulic machines with an acceptable erosion rate. In addition, the prediction of location of erosion will assist turbine suppliers for an optimisation of the protective coatings on blades. Thus, one can expect to reduce the cost of maintenance and the associated cost of a premature shut down.

State of the art

Erosive situations

Experimental studies have allowed the erosive cavitation flow situations to be identified. This has been done by comparing observation of damages on blades of prototypes with cavitation patterns as found on the corresponding model in the laboratory. It is now accepted that leading edge cavitation is one of the most erosive cavitation types. However, the complexity of cavitation flows and their associated physical phenomena push to develop experimental investigating tools that simulate simpler hydrodynamic conditions of cavitation flows. Avellan & Karimi (1986) have compared erosion patterns obtained with different cavitation devices with erosion observed in Francis turbine model. It appears that such devices, as for example the cavitation water tunnel and the cavitation vortex generator, are suitable for erosion tests on material owing the strong similarities of physical characteristics of cavitation impacts in the turbine model as compared to those in the cavitation devices. Many authors have proposed to simulate cavitation erosion of hydraulic turbine runners or propellers on 2-D blades in a cavitation tunnel. Through visualisations of leading edge cavitation and erosion measurements on blades, many authors agreed with the fact that erosion is due to the repeated collapses of transient cavities in the closure region of back pressure collapse (Farhat, 1994; Avellan *et al.*, 1988). According to these studies, leading edge cavity can

be segregated into two classes : it is defined as stable when the length of the sheet cavity does not vary significantly with time, and as unstable when only an average length can be given. This latter mode is characteristic of large vapour structures shedding that are transported by the flow. This mode also corresponds to the highest erosion rates that have been measured by using an electro-chemical technique (Chincholle, 1988; Simoneau *et al.*, 1989), or by using a pitting technique (Pereira *et al.*, 1995).

Prediction of cavitation aggressiveness

Cavitation erosive power

Although many studies attempt to predict the erosion intensity for a given set of hydrodynamic conditions, existing prediction models still need to be largely improved.

Thiruvengadam (1971) proposed erosion prediction laws by considering the influence of the principal hydrodynamic parameters of the flow on erosion ; but the properties of material are not taken into account in this model. This gap was filled by Kato *et al.* (1978), who established a relation between impact erosion through the "Mean Depth of Penetration Rate", flow velocity, a characteristic length scale of sheet cavity, and material resistance. On the whole, the modern trend in erosion modeling is principally based on an energetic approach, which has been introduced by Hammitt (1963), and more recently improved by Avellan *et al.* (1991); Farhat *et al.* (1991); Pereira *et al.* (1998).

The energetic approach is based on the hypothesis of the potential energy of macroscopic vapour structures. The aggressiveness of a vapour cavity is supposed to be proportional to the potential energy E_c , which can be defined as the product of the maximum volume V_c of the vapour structure by the pressure driving the collapse (p_{max} - $p_v(T)$) :

$$E_c \simeq (p_{max} - p_v(T))V_c \text{ [J]}$$

Considering the shed frequency f_c of the macroscopic vapour structures, the dissipated power of cavitation is given by :

$$E_c f_c = (p_{max} - p_v(T))V_c f_c \text{ [W]}$$

Considering the particular case of a strong unstable leading edge sheet cavitation on 2D blades, the main pulsation of sheet cavity as well as the shed frequency of large vapour structures, are governed by a Strouhal law (Farhat *et al.*, 1992). Assuming that the volume of shed vapour structures is proportional to the volume of the sheet cavity length, the application of the energetic model is straight forward.
In a more general case, one can postulate that the aggressiveness of a cavitation flow

is correlated with the sum of energetic contribution of cavities of different volumes, which can be generated at different rates. Thus, the cavitation erosive power term P_{er} is thought as an integral form and defined by :

$$P_{er} = \int_{E_s}^{E_m} E_c \, \hat{n}(E_c) dE_c \text{ [W]}$$

where E_s be the minimum energy of the cavity yielding the plastic deformation of material, E_m the maximum cavity energy, and $\hat{n}(\epsilon)$ the number of generated cavities during one time unit and having the potential energy E_c. Material properties are here taken into account by assuming that the minimum cavity energy is equal to the plastic deformation threshold of the material. This energetic model has been used by Pereira (1997) who has proposed a formulation for the energy spectrum $\hat{n}(\epsilon)$ in the case of a symmetric 2-D blade.
In fact, the energetic approach model has two main advantages :

1. Firstly, although the cavitation erosive power depends explicitly on the back pressure at the collapse point and on the production rate of cavities, it is expressed as a function of macroscopic parameters of the flow, which are in the case of a 2-D blade the upstream velocity C_{ref} , the cavity length l_c , the cavitation number σ and the blade incidence i. Consequently, the cavitation power model can be scaled up for variable hydrodynamic conditions of leading edge cavitation.
2. Secondly, the cavitation erosive power can be compared with the deformation power P_d . This can be estimated by considering all deformation energies E_d of measured cavitation impact on material per unit time. Moreover, this model can be improved by considering the collapse location of vapour structures.

Collapse efficiency

Cavitation erosion process involves complex micro-hydrodynamic mechanisms which may be strongly governed by the flow itself. Consequently, the prediction of material damage due to the repeated collapses of cavities (or clusters of cavities) is a rather difficult task from a deterministic point of view. Nevertheless, the global transfer of energy from all cavities to the material can be thought as being a stochastic process, which can be characterized by the collapse efficiency.

Considering the number of generated cavities $\hat{n}(E_c)$ having the potential energy E_c during a unit time, and the number of impacts $\hat{n}(E_d)$ having the deformation energy E_d per unit time, the collapse efficiency η_{co} is defined as the ratio $\hat{n}(E_d)$ /$\hat{n}(E_c)$. By definition, the collapse efficiency represents thus the global transfer of energy between the vapour structures and the material. This transfer includes the loss of cavity energy during the collapse, the wall distance of the collapse and the cavity energy (bubble,

cavitation vortex, cloud cavitation). The few results show that this collapse efficiency strongly depends on material and flow conditions (Pereira, 1997; Pereira *et al.*, 1998). The main advantage of the collapse efficiency approach is that the vapour structures and the cavitation impacts are explicitly linked from a statistical point of view.

Physical mechanisms involved in cavitation collapse

Hydrodynamics of cavitation attack

Even though it is assumed that cavitation erosion is due to the collapse of vapour cavities near the solid surface, the mechanisms by which it is caused are not fully understood. In order to understand the physics involved in cavitation erosion, the collapse of isolated cavities have been studied using different techniques. Bubbles can be positioned using thin wires (Brunton, 1967; Coley & Field, 1973; Shima *et al.* , 1983) or bubbles of chosen gas content can also be attached to surfaces (Chaudhri & Field, 1974; Tomita, Shima & Takahashi , 1983; Tomita, Shima & Ohno , 1984). The bubbles can be produced by electric discharges (Naudé & Ellis, 1961; Tomita & Shima, 1986), or by focusing laser pulses (Vogel *et al.*, 1989; Brujan *et al.*, 2001). Moreover, controlled planar shocks have been passed over cavities using flyer-plate methods (Dear & Field, 1988; Bourne & Field , 1992) where cavities are positioned in a gel.

High-speed visualisations have allowed physical mechanisms involved in cavitation erosion to be recorded. These are shock wave emission due to compressibility effects of water or high velocity micro-jet generation due to the asymmetrical collapse of an initial spherical bubble located near a solid boundary. Both phenomena come with the last stage of cavity collapse and act as intense microscopic singularity loads on the material and they are therefore directly involved in cavitation erosion process. The intensity of such pressure impacts due to supersonic rebounds of bubble collapse has also been numerically estimated by Hickling & Plesset (1964) and Fujikawa & Akamatsu (1980), leading to overpressures as high as 1 GPa. More recently, thanks to numerical fluid-solid simulations of the impact response of an elastoplastic medium, Fortes-Patella & Reboud (1998) pointed out that the calculated pit deformations fit well with the observed indentations if a spherical shock wave pressure impact is assumed. These simulations have also shown that the global energy transfer associated with one cavity depends on many microscopic parameters such as the distance of the collapse, the overpressure amplitude and the transit time of wave on solid boundary. In addition, it is well known that collapse of cloud of vapour cavities, in which many collapses interact, can be the source of more intense overpressure impact (Bark & Berlekom, 1978; Wang & Brennen, 1996).

Bubble collapse

A rapid overview of history on solution and calculation progresses in the final stage of a collapsing bubble can be presented, see also Brennen (1995).

Rayleigh (1917) studied the collapse of a vapour bubble filled with a void, and the created field in an incompressible fluid, at rest, and where the driving pressure does not vary with time. The main step towards bubble dynamic was the introduction of a variable external driving pressure, and of the influence of the surface tension and viscosity (Plesset, 1949). This has led to the so-called Rayleigh-Plesset equation (RP), which allows to calculate the time evolution of a spherical bubble radius R(t). In addition to the RP equation, considerations of a gas in the bubble (polytropic gas when neglecting thermal effects) can be made in order to improve the model.

However, the final stage of the collapse involves such high velocities (and pressures), so that the assumption of liquid incompressibility may be no longer appropriate. Herring (1941) introduced the first-order correction for the liquid compressibility, assuming the bubble wall Mach number was much lower than unity and neglecting any condensable gas and thermal effect so that the pressure in the bubble remains constant. In an attempt to give higher order approximation, the so-called Kirwood-Bethe hypothesis (Kirkwood & Bethe, 1942; Cole, 1948), has been used by Gilmore (1952). He studied the collapse and rebound of a bubble that contains ideal gas, by considering isentropic compression. Later, Hickling & Plesset (1964) were the first to give numerical solutions which describe the flow in the vicinity of a collapsing bubble. They explored the formation of pressure waves or shocks during the rebound phase. They also showed that the primary importance of liquid compressibility is not the effect it has on the bubble dynamics, but the role it plays in the formation of the shock. Other numerical calculations have since been carried out by Fujikawa & Akamatsu (1980), whose results are in accordance with the results of Hickling and Plesset : the $1/r$ decay of the amplitude of a spherical shock wave pressure is also valid for the non linear domain in the vicinity of the collapse centre. In this area the effects due to the dissipation of sound energy is balanced for by the development of a shock wave front.

Sonoluminescence

It is nowadays assumed that light can be emitted when an initial air bubble is excited by a superimposed sound field. This phenomenon is known as sonoluminescence. Discovered in early 30-40's, this phenomenon presents an increasing interest in science. This is still studied and used in many fields of application : sonochemistry, auto-ignition phenomena in commercial explosive (Field *et al.*, 1992) etc. For a review of sonoluminescence, see Walton & Reynolds (1984). The light emission may also be induced by cavitation of the liquid. Some workers dealt with a cavition luminescence

which is caused by the rapid collapse of a bubble or a group of cavitation bubbles, see Dear *et al.* (1988), Bourne & Field (1992) and Field (1994). More recently, research on single-bubble sonoluminescence (SBSL) pushes again the interest for bubble collapse. In these experiments, the sensitivity to experimental parameters (temperature, driving acoustic pressure, dissolved gas, etc.) has been studied. Moreover, the characteristics can be explained by a hydrodynamic approach of bubble collapse. In these theoretical studies, the bubble wall dynamics is described by RP equation (Hilgenfeldt *et al.*, 1998), which can be for example supplemented by a van der Walls gas with a constant specific heat (Wu & Roberts, 1994). Then, the strongly supersonic collapse suggests that an imploding shock wave is launched into the interior of the bubble as the outer bubble radius decreases. Thus, the gas within the bubble is intensely heated and luminescence is generated (Hilgenfeldt *et al.*, 1998; Wu & Roberts, 1994). A recent review of sonoluminescent bubbles is given in Putterman & Weninger (2000).

Proposed approach

Problematic

The context of this present work is the study of hydrodynamic mechanisms involved in cavitation erosion towards the improvement of the cavitation aggressiveness models. The energetic models appear to be well adapted to the cavitation aggressiveness prediction because of their ability to conciliate both fluid mechanics and metallurgical aspects of the erosion problem.

Moreover, in order to improve these energetic models, one must determine how the macroscopic parameters of the flow can influence the energy transfers from the fluid to the material. In the case of leading edge cavitation, the macroscopic parameters of the flow are the flow velocity, the pressure gradient, the cavitation coefficient and the main cavity length. Starting from the potential energy of the vapour structures, energy transfers include the acoustic energy dissipated during the collapse, the energy furnished to the material and the fluid-solid response to the overpressure impact. Thus, the corresponding microscopic parameters respectively are the shock wave characteristics, the distance to the wall of the shock wave epicentre and the material properties. This leads to the postulate :

Postulate

In order to improve the energetic models, the potential energy of a vapour cavity has to be weighted by the distance from the centre of the collapse to the wall.

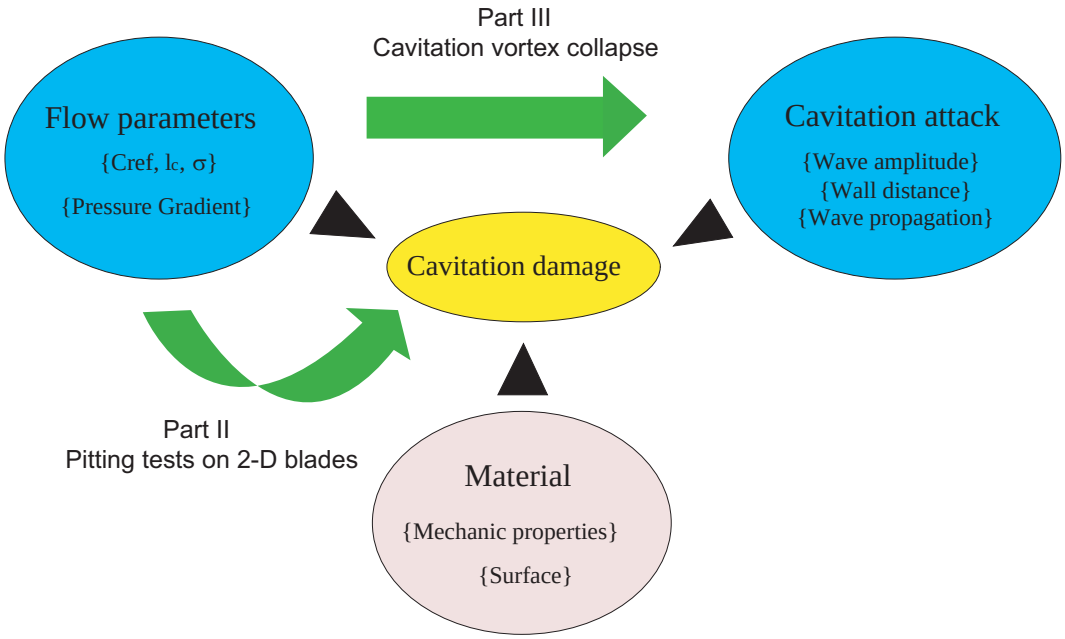

Figure 2: Problematic and approach

Approach

The proposed approach will be based on both the study of cavitation impacts on 2-D blades and on the physical investigation of a cavitation vortex collapse. Joint results will be proposed in the end of this work, thus the characteristics of the isolated cavitation vortex created in the cavitation vortex generator will be assumed comparable to those of transient vortices generated in the closure region of the leading edge cavitation on 2-D blades.

The study can be represented by the diagram in figure 2. It is divided into two main parts.

1. Firstly, a study of the cavitation aggressiveness on 2-D blades is achieved by pitting experiments in the cavitation tunnel of the IMHEF. Pits will be analysed by using a 3-D profilometry technique. The results will provide important insights in how the macroscopic parameters of the flow influence the pitting rates and the collapse efficiency, and what are the main impact characteristics (morphology, volume and energy).
2. Secondly, unlike most of former studies which deal with spherical cavities disregarding the flow interaction, the investigation of the physical characteristics of the final stage of the collapse of a cavitation vortex will be carried out. This will involve the cavitation vortex generator of the IMHEF for the generation of

an isolated cavitation vortex. In addition, the development of a 4-windows test section and a high-speed video shadowgraphy technique will be required. On the basis of high-speed visualisations, the cavitation vortex characteristics at collapse time as well as the emission of shock waves can be determined. Furthermore, the luminescence phenomenon associated with the collapse will be used to determine the averaged collapse location. Finally, simultaneous captures of the shock waves and the luminescence will be achieved in order to determine the collapse time, and verify whether the centre of collapses corresponds to the location of luminescence sparks.

The present work will be presented as follows. Experimental facilities are described in part I. These are the cavitation tunnel and the cavitation vortex generator. The associated instrumentations, the pitting technique and the visualisation systems are also presented. The results of the pitting experiments are available in part II. The physical investigation of the cavitation vortex collapse is developed in part III. This study is split into three chapters : the luminescence of the cavitation vortex, the physical characteristics of shock waves and cavitation vortex cavities, and the simultaneous captures of shock waves and luminescence. Part IV gives the conclusions and the work perspectives.

Part I

Experimental techniques and facilities

Chapitre 1

The cavitation vortex generator

1.1 Principle of operation

The cavitation vortex generator (CVG) is a laboratory facility which has been designed to test the resistance of different materials to cavitation erosion. Moreover, it has been optimised to study the mechanisms of formation and collapse of a cavitation vortex. Created vortices are actually similar to those observed in cavitation flow. In addition, erosion patterns obtained with the CVG are in good agreement with those obtained with a cavitation water tunnel and a Francis turbine model (Avellan & Karimi, 1986).

The principle of operation of the CVG is to produce a cycle of low-pressure and high-pressure waves in a vortex flow using a rotating valve. The vortex flow is generated in a cylindrical chamber $D_v = 80\ mm$ fed by a tangential flow inlet which enters through a pipe $D_{in} = 8\ mm$ in diameter (see figure 1.1). This chamber is prolonged on one side with a prismatic test section in which the created vortex ends and where visualisations are performed. On the other side of the chamber, the flow goes in a downstream pipe $24\ mm$ in diameter.

While the valve is open, a rotation is promoted in the test section and the downstream pipe. As the valve closes, a "water hammer" pressure is created, and a low-pressure wave then propagates in the test section and its downstream pipe. Due to this, a vapour core is created on the vortex axis, tending to extend to the entire radius of the pipe. The closure duration of the valve which depends on the rotational velocity, limits the expansion of the vapour core. When the valve opens again, the pressure wave coming from the upstream vessel causes the vapour cavity to collapse violently (Avellan & Farhat, 1989; Farhat, 1994).

The whole CVG, illustrated in figure 1.2, is a closed loop consisting of the test section, the rotating valve, a low and high-pressure vessels and a circulating pump. The circulating pump draws water from the low-pressure vessel through the heat exchanger.

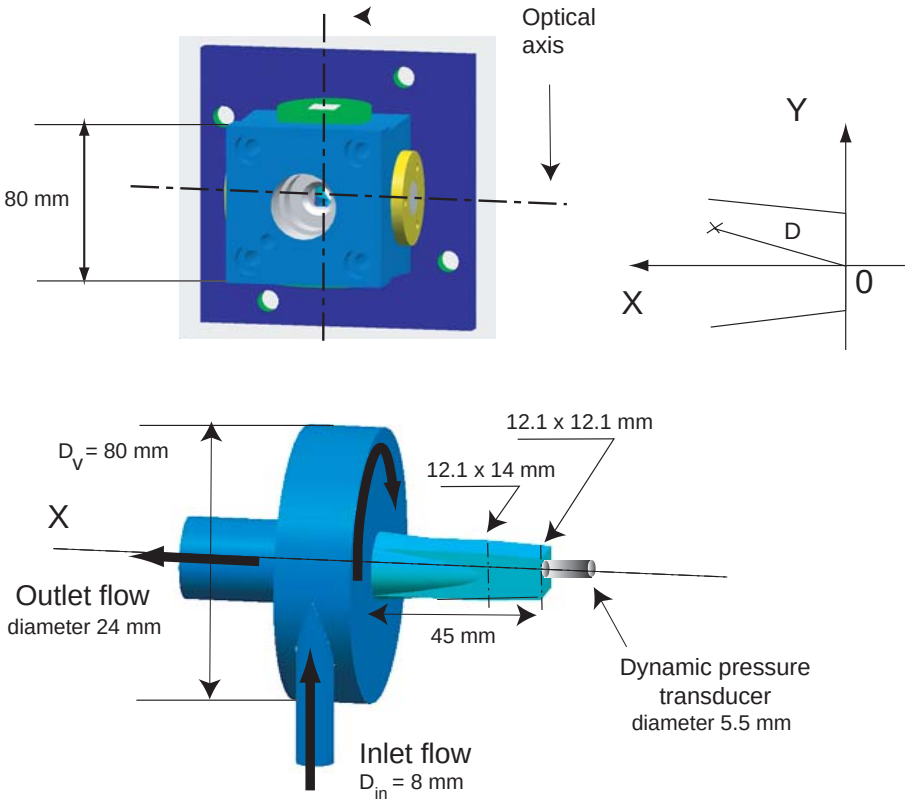

Figure 1.1: 4-windows test section

Both the low and high pressure vessel play the role of decoupling chambers to reduce the pressure pulsations in the circuit.

1.2 Test section

1.2.1 4-windows test section

The visualisation part of the test section has been optimised. Substantial efforts have been made to allow simultaneous visualisations from two perpendicular axis to be performed. A global view of the bulk flow of the entire test section with is given in figure 1.1. The end of the test section is a prismatic chamber resulting from the intersection of 4 windows : 2 rectangular prism glasses and 2 cylinder glasses. These are mounted in metal sleeves, which are fixed to a mono-block structure. An accurate design of the structure allows the volume to be closed, with 2 parallel faces formed by cylinders, and 2 faces with an angle of 3.72° formed by rectangular prisms. The glasses are BK7 type with an anti-reflecting coating on the glass-air interface in order to limit

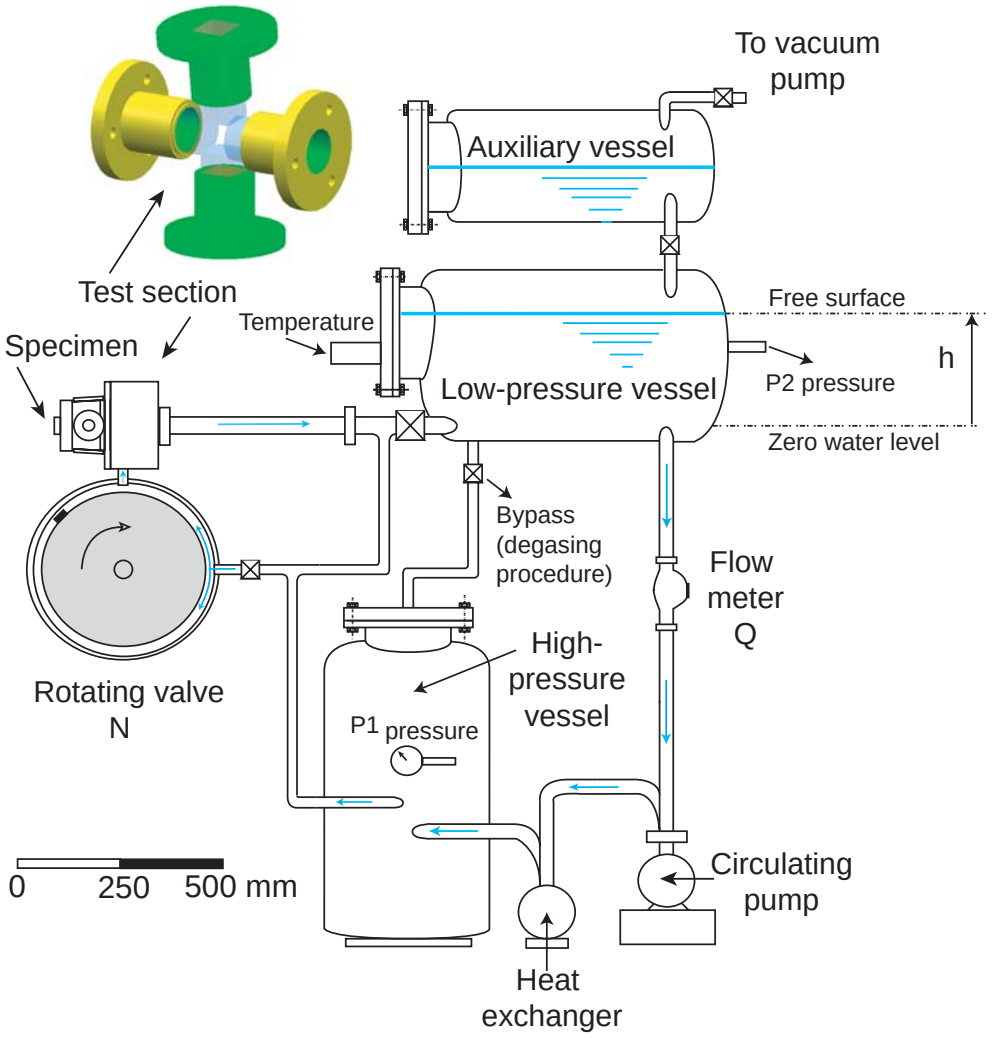

Figure 1.2: The Cavitation Vortex Generator (CVG)

Fresnel losses. Thus, high quality visualisations through 2 perpendicular axes can be achieved.

Finally, test specimen is presented as a cylinder in 12 mm diameter, and is mounted in a socket which is screwed at the extremity of the structure. In order to measure pressure transients during the collapse, material sample can be replaced by a pressure transducer. This is a *Kistler*® 601A type, with a 0-20 MPa range, a natural frequency of 130 kHz, and a rise time of 1 μs.

1.2.2 2-windows test section

The 2-windows test section components are depicted in figure 1.3. Visualisations along an horizontal axis can be achieved owing to a set of shaped glasses which is placed between metal parts of the test section. The resulting bulk flow is the same than which is described in the previous paragraph.

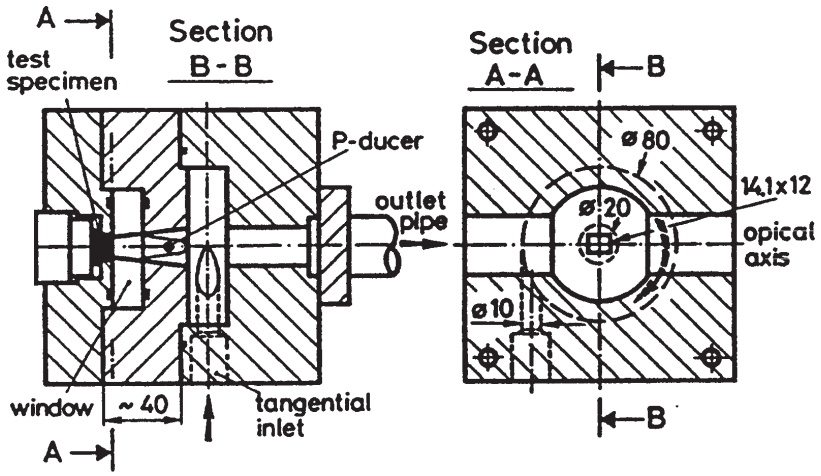

Figure 1.3: 2-windows test section

1.3 Hydrodynamic parameters

The hydrodynamic parameters of CVG are the flow rate Q, the cavitation number σ and the rotation speed of the valve N. Pressures are measured with 2 piezo-resistive pressure transducers in both the high-pressure vessel, and the low-pressure vessel. The hydrodynamic parameters Q and σ can be expressed as a function of pressures p_1 and p_2 by introducing the head loss coefficient of the circuit K :

$$Q = \mathrm{KA}\sqrt{\frac{p_1 - p_2}{\rho}} \text{ with K } = 163.5\ 10^3 \text{ , A}=\pi(\tfrac{\mathrm{D}_{in}}{2})^2 \ . \tag{1.1}$$

$$\sigma = \frac{p_2 - p_v(T)}{\frac{1}{2}\rho(\frac{Q}{\mathrm{A}})^2} \tag{1.2}$$

The maximum flow rate is 0.76 $l\ \mathrm{s}^{-1}$ for an upstream pressure of 0.84 MPa. The vortex intensity is defined by the circulation Γ :

$$\Gamma = 2\pi\frac{\mathrm{D}_v}{2}\frac{Q}{\mathrm{A}} \tag{1.3}$$

1.4 Low level light detection

1.4.1 Photons detection

Photons are detected using a photomultiplier tube (EMI-Gencom Inc. B-289 F), which is coupled with an electronic peak detection system EG&G 5C14 via a preamplifier with rise time of 1.5 ns. Photons are detected by pulses of 5 ns duration. The signal is then stored with an oscilloscope *LeCroy*® 9304 100 MHz with 8 bits resolution.

1.4.2 Intensified light camera

An intensified light video camera is used to visualise the luminescence sources. This camera is a *QUICK 05A* ® model. It consists of a Phosphor Micro Channel Plate (MCP) for the light amplification stage, which is coupled with a video CCD (Charged Coupled Device) image sensor via a high quality optic. This camera is able to detect light of wave lengths within a 300–820 nm bandwidth and the maximum quantum efficiency is 20% at 400 nm. The electric shutter can be driven by a TTL signal, and the time delay for effective triggering is 30 ns.

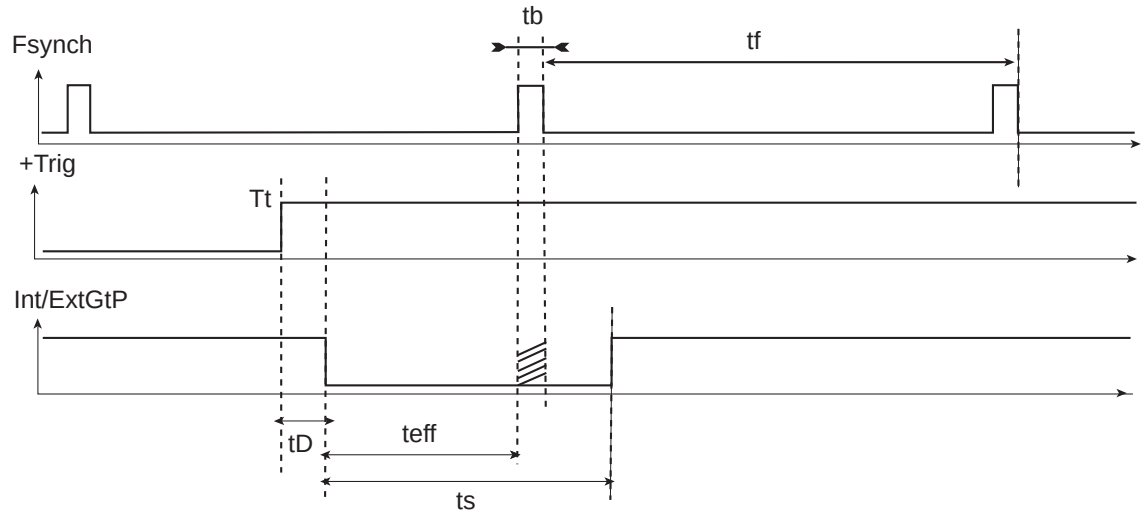

tD : time delay (0 - 8s, with minimum 50 ns step and minimum 30 ns propagation delay)
tb : blanking period approx. 1.5 ms
ts : shutter time (50 ns resolution)
teff : effective time exposure
tf : field time 20 ms
Tt : trigger time

Fsynch : TTL output, synchronous to internal video camera synchro
+ Trig : Input for pos. edge trigger (1V - 25 V)
Int/ExtGtP : control of shutter, internal mode, negative logic TTL

Figure 1.4: Time diagram from the intensified camera : electric shutter & video cycle

The video signal has 290 TV lines of 752 pixels (frame scan mode). It can be noted that 1.5 ms over 20 ms are devoted to the blanking period of video cycle of the CCD. Thus the light is not integrated during this period, and a test on TTL level of the video synchronization signal F_{synch} is therefore performed to validate image acquisition. A time diagram of electric shutter and video cycle is given in figure 1.4. The frames are grabbed on a PC using a *Matrox*© Genesis frame grabber.

1.5 High-speed visualisations

1.5.1 The Cranz-Schardin camera

Specifications

In order to visualise the high-pressure gradient produced during the very last moments of cavitation vortex collapse, a shadowgraphy technique is used.
The principle of this system is still very close to the original Cranz-Schardin camera. Substantial efforts have been made to replace the photosensitive film by a set of CCD image sensors. This camera takes advantages both of the versatility of digital images for processing and the simplicity of the Cranz-Schardin camera (Couty *et al.*, 1998). This system, as well as a visualisation example are presented in figure 1.5.

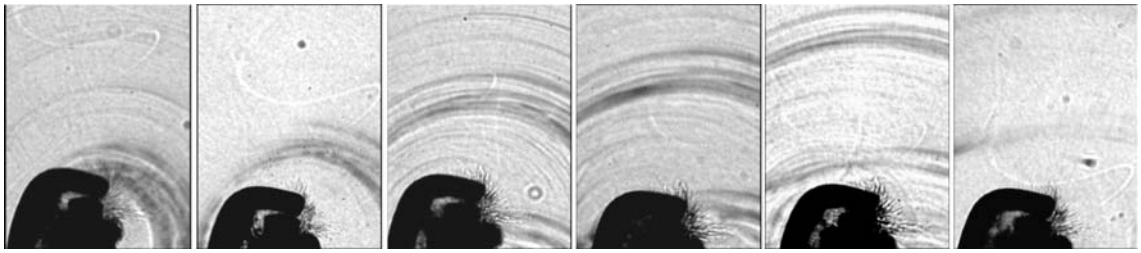

Figure 1.5: Collapse of a bubble created by a spark in water, 5 10^5 frames per second

Short duration light sources are provided by a set of spark generators which have a mean time exposure of 300 ns. Discharges are controlled by an electronic time unit, which provides an adjustable spark rate of 1 kHz to 10 MHz. As the maximum jitter is 200 ns, a fast photodiode EG&G FND 100 is used to detect exact occurrences of flashes. Sparks are considered as punctual light sources and are placed at the focal plane of a long focal lens f = 1600 mm (object plane). The optical bench allows the 8 shadowgraphs to be formed on 8 achromatic objectives $fi = 380$ mm, which are placed at the conjugated plane. This arrangement allows images to be focused on a set of 8 image planes of individual CCD video cameras with an optical magnification of 0.29. Mechanical mount allows fine adjustment of each camera for focal plane positioning.

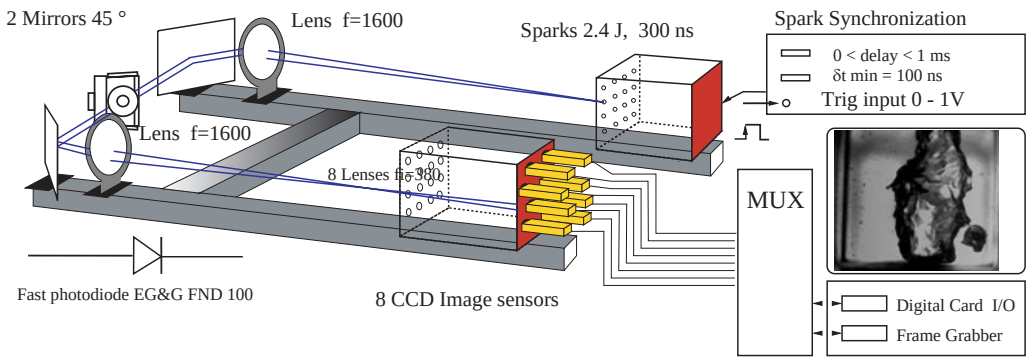

Figure 1.6: The Cranz-Schardin video shadowgraphy system

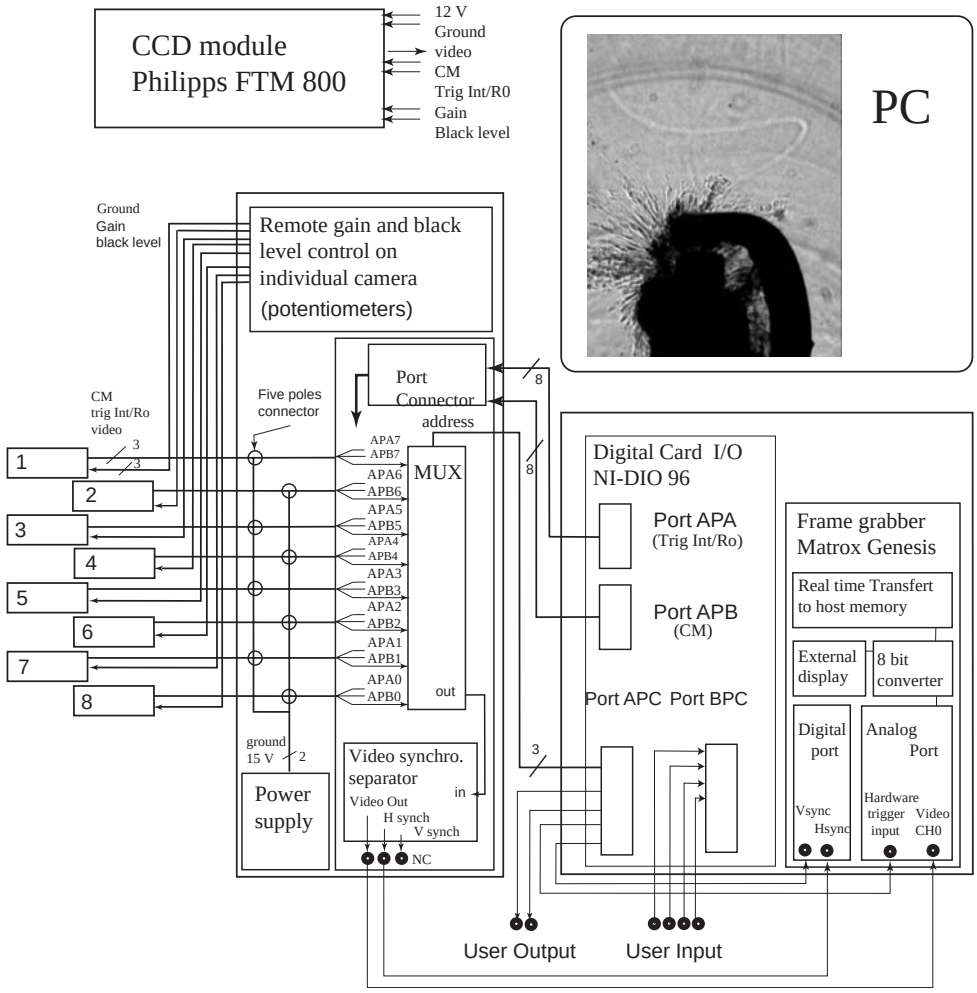

Figure 1.7: Electronic design of the Cranz-Schardin video system

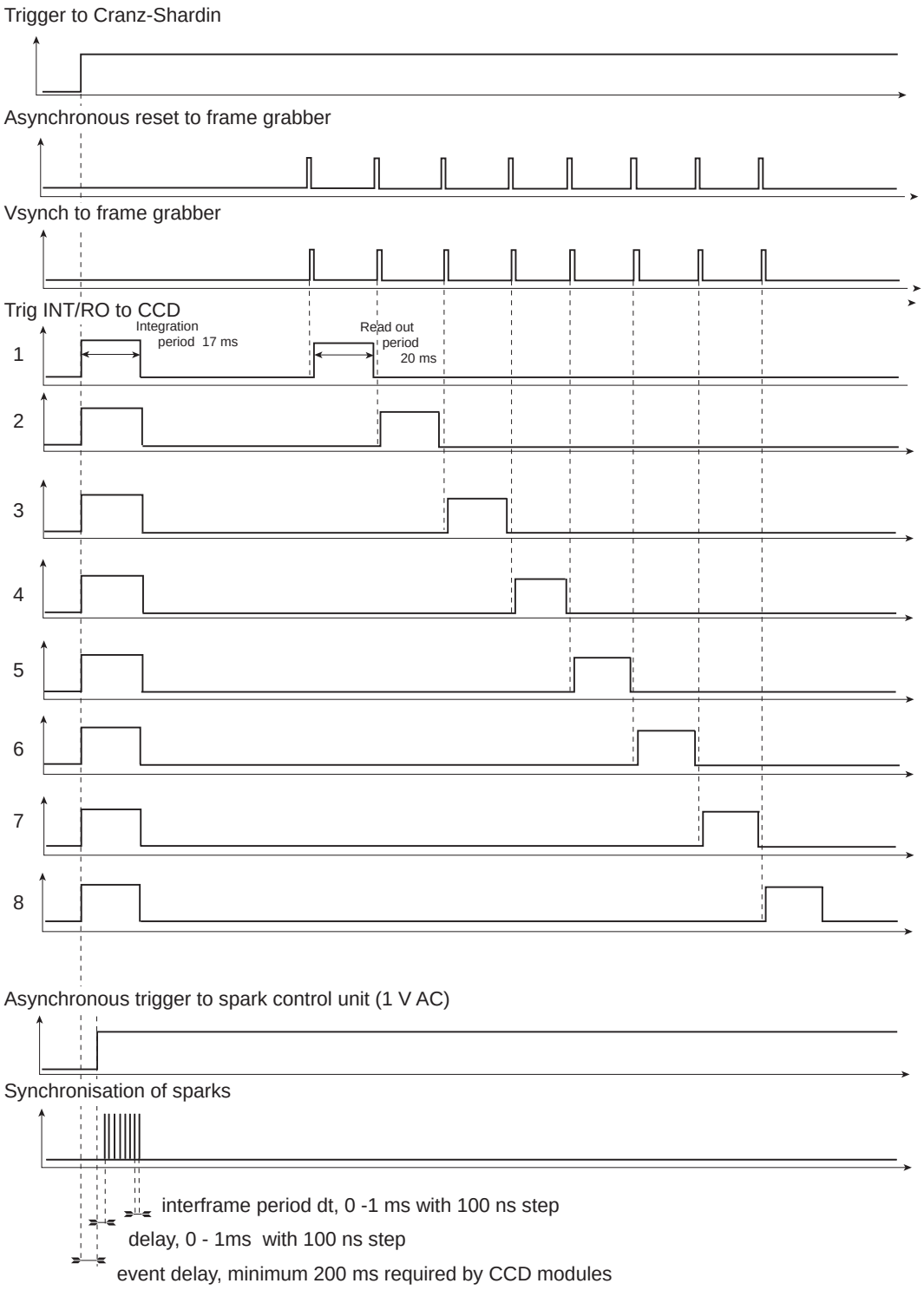

Figure 1.8: Time diagram from the Cranz-Schardin video system

Video acquisition

The video system is composed by a PC computer equipped with a Matrox Genesis frame grabber, a digital I/O data card for synchronization purposes, 8 CCD images sensors and a video control unit. A global synoptic diagram of the video system is given in figure 1.7, as well as time diagram figure 1.8.
The CCD cameras are Philips FTM 800 model. The image sensor is a progressive frame type with 754 x 575 pixels. A remote control of the gain and black level allows image sensors to be well adapted to the intensity delivered by spark flashes. Each camera, normally running in a continuous non-interleaved mode, can be asynchronously triggered in order to start its integration period of 17 ms duration. This is achieved through a TTL pulse applied to INT/RO input of the CCD camera. The delay for effective integration is 200 μs. After the integration period is completed, the frame is transferred in the storage section of the image sensor and can be retrieved for grabbing by applying a second TTL pulse on the INT/RO input.
Acquisition can be armed on an asynchronous event, which is given by a TTL signal to the PC. After flashes emission, and when integration period of image sensors is achieved, frames are sequentially retrieved by the frame grabber. The frame grabber digitiser is adapted to video specifications of CCD modules and dimensions of grabbed images are 754 x 288 lines with 8 bits resolution. It has to be noted that the frame grabber functions as "slave" under an asynchronous reset mode. Therefore, video synchronization signals H_{synch} (from the CCD modules) as well as V_{synch} and an asynchronous reset signal (generated by I/O card) must be supplied to the frame grabber.

1.5.2 Calibration procedure

The calibration of the sequences of the Cranz-Schardin camera is achieved. The image of the *QUICK 05A* ® camera has to be calibrated as well. By that way, simultaneous visualisations from the two perpendicular views of the test section allow the physical coordinates of an object to be retrieved. The calibration procedure is performed in 3 steps.

1. The image scale factors for each frame have to be solved. This is achieved by placing a calibration target with 100 reference points in the test section (see figure 1.9). The distortion is negligible, with less than 1 pixel difference over the entire test section. The mean values of image scaling factors for the two axes are equal to 34 $pixels/mm$ and 17.2 $pixels/mm$.
2. Alignment of the frames of a reference sequence is obtained by an intercorrelation method. The vertical and horizontal displacements as well as the rotation of

target frames are calculated by comparing the location of a unique model, taken from the first frame, with its actual location in target images. The unique model is chosen from any location in the source image as long as the model is known to appear in shifted target image. The model is in our case given by the shadow of a screw of 2 mm in diameter. The screw is centred at the epicentre of cavitation impacts on a test specimen, which actually does not correspond to the centre of the test specimen.
This step of the alignment procedure is necessary because the test section borders, which are deformed due to parallax effects, cannot be taken as the screw as a target for calibration. As examples of a non aligned reference sequence and the corresponding calibration result, see figures 1.10 and 1.11 . In these sequences, the first 7 frames come from the Cranz-Schardin camera, and the eighth frame comes from the *QUICK 05A* ® camera.

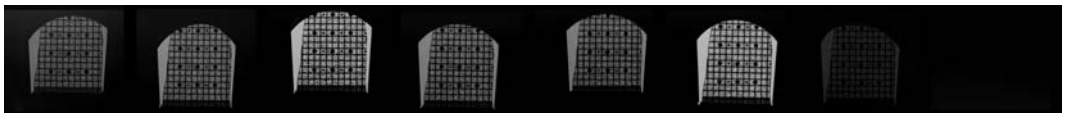

Figure 1.9: Target used to solve the image scaling factors

Figure 1.10: Reference sequence before the alignment procedure

Figure 1.11: Reference sequence after the alignment procedure

3. Because of line synchronization jitter which is due to a peculiar characteristic of the FTM 800 video signal, all sequences must be aligned individually for each acquisition. As the screw model cannot remain in test section during experiments, the intercorrelation method is therefore applied between the reference sequence, and the current sequence. Alignment is performed by comparing models (for example the border of test section) in frames of the reference sequence, with their actual locations in the current sequence.

Chapitre 2

The cavitation tunnel

2.1 Description

The high-speed cavitation tunnel of the Laboratory for Hydraulic Machines (Avellan *et al.*, 1988), is a closed circuit (figure 2.1) which allows cavitation flows on a blade to be generated. The maximum velocity in the test section is 50 $m\,s^{-1}$. It is obtained using a pump which is driven by a 500 kW electric DC motor. The velocity, as well as the static pressure with a maximum of 1.6 MPa are controlled.

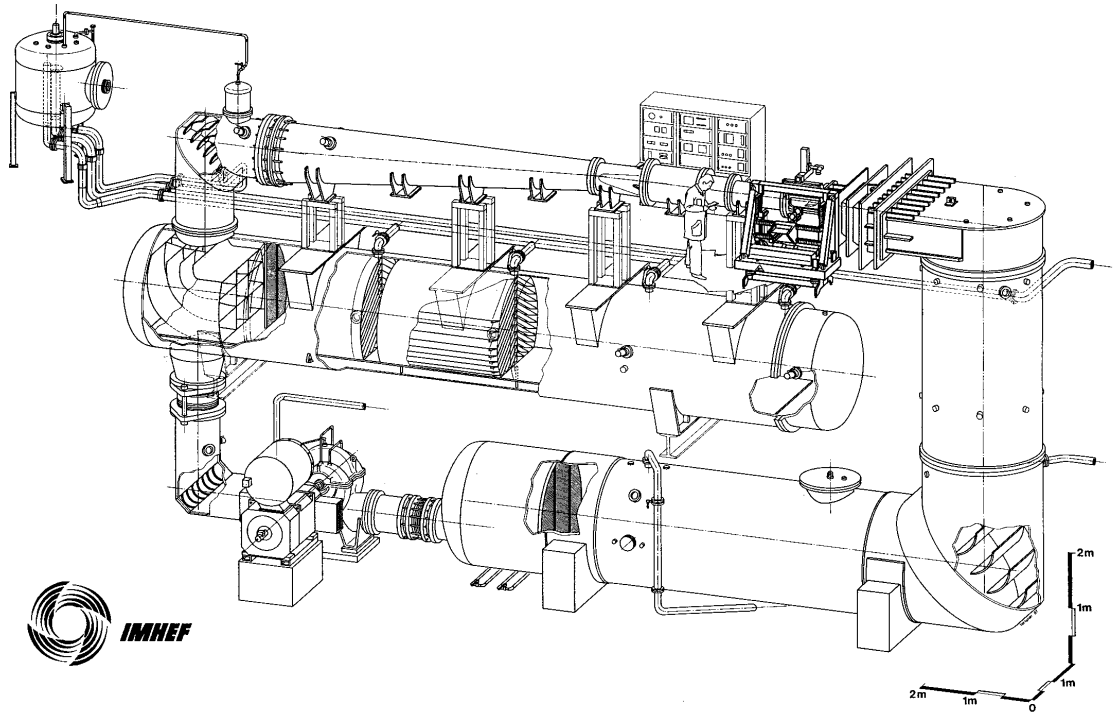

Figure 2.1: The high-speed cavitation tunnel

The hydrodynamic parameters are accessible from ETHERNET (TCP) network with a refresh rate of 4 Hz. The operation parameters are the following :

- p_1 : measured pressure at the nozzle inlet ;
- p_2 : measured pressure at the test section inlet ;
- C_{ref} : upstream velocity at test section inlet :

$$C_{ref} = \xi \sqrt{\frac{p_1 - p_2}{\rho}} \tag{2.1}$$

  where ξ is the contraction ratio
- σ : cavitation number defined by :

$$\sigma = \frac{p_2 - p_v(T)}{\frac{1}{2}\rho C_{ref}^2} \ , \ p_{ref} = p_2 \tag{2.2}$$

  where $p_v(T)$ is the vapour pressure of water at temperature T ;

- i : blade incidence ;
- T : water temperature during tests.

2.2 Parallel test section

The parallel test section geometry is represented figure 2.2. It has a square section of 150 mm × 150 mm of 750 mm length. Three over the four faces of the test section are equipped with Perspex windows for easy visualisations. The incidence system, which is constituted of an indented wheel and a endless screw, is hold by a brass scuttle. x

2.3 Diverging test section

A diverging test section has been realized in order to simulate an additional pressure gradient in the test section. It is an adaptation of the parallel test section, on which Perspex pads have been added. Moreover, the metal scuttle which holds the 2-D blade has been flipped (compare figure 2.2 and figure 2.3). The leading edges of pads are elliptic 2-D blades. The diverging angles are 7° for the top pad (suction side of blade), and 9° for the bottom one. By this way, a restricted section of 0.10 m × 0.15 m can be obtained. This allows a 2-D blade to be placed in a diverging section. By simply considering the ratio between the restricted section height at the leading edge of the 2-D blade and the parallel inlet section, the upstream velocity is equal to C'_{ref}=(0.15/0.11) C_{ref}.

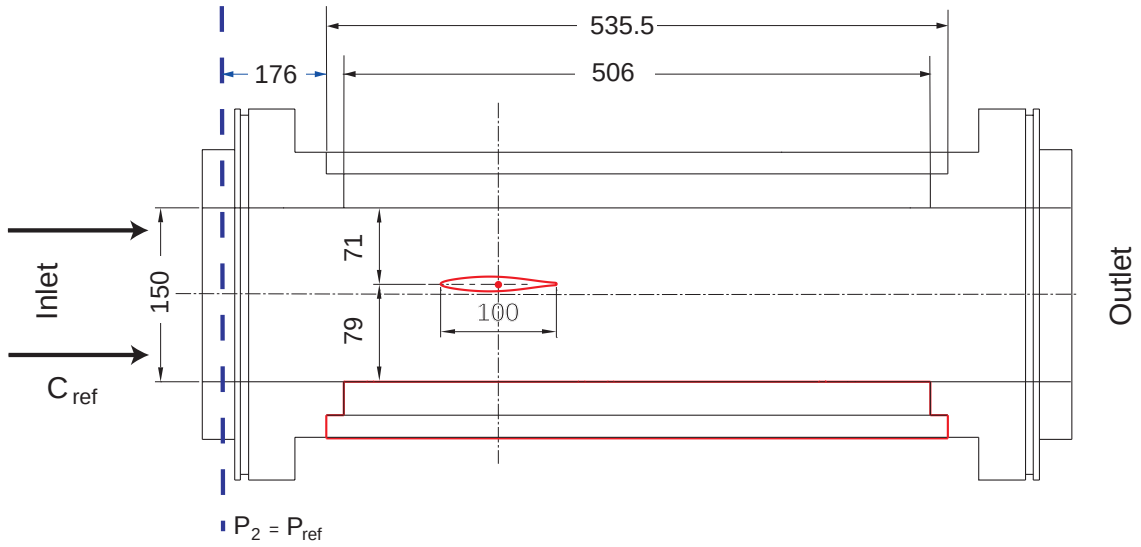

Figure 2.2: Parallel test section of the cavitation tunnel

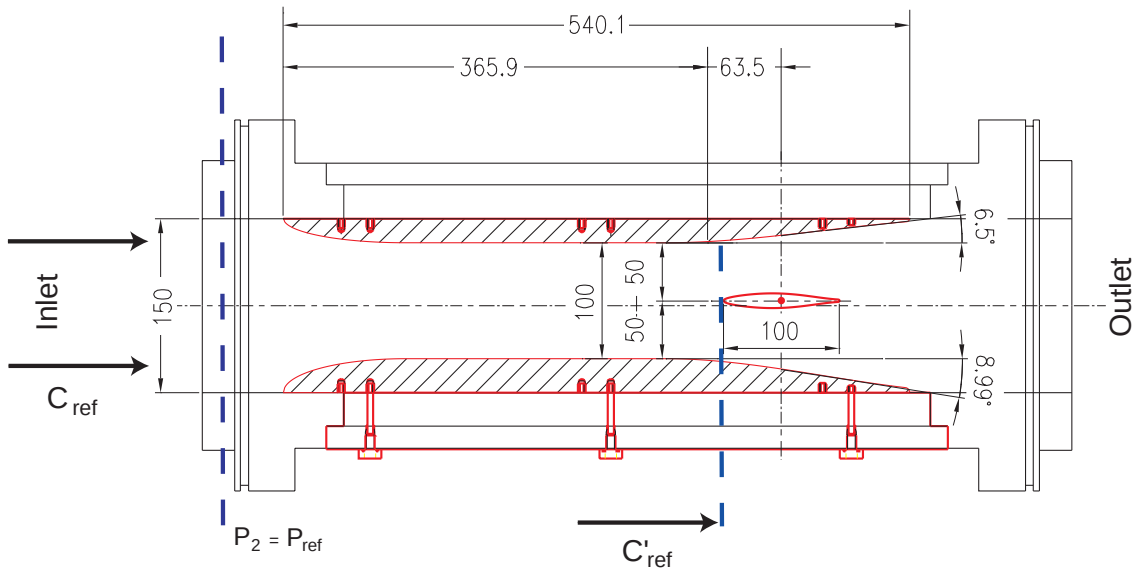

Figure 2.3: Diverging test section of the cavitation tunnel

2.4 Pitting experiments

2.4.1 Experimental 2-D blades

Two 2-D blades of 100 mm and 60 mm chord are used for pitting experiments. These are NACA 65012 type (see figure 2.5) and they will be referred in the document as the full scale and the small scale 2-D blade. The 2-D blades are made of stainless steel and includes inserted specimen of material polished down to mirror (Copper, Aluminium, stainless Steel). The width of test specimens are 10 mm for the small scale 2-D blade and 30 mm for the full scale 2-D blade (see figure 2.4). As the leading edge cavitation pattern is sensitive to surface defect, the sample geometry is obtained by an accurate electro-erosion machining. Test specimen are glued with cyano-acrylate and removed by 400 $°C$ heating. Although the geometric discontinuity of the leading edge is limited, the leading edge cavitation still presents a non-uniform detachment of leading edge cavity that leads to the generation of shed vortices. In order to overcome this problem, it has been decided that an adhesive tape will be placed from the trailing edge of the pressure side to the beginning of leading edge of the suction side (see figure 2.5). The adhesive guarantees a continuity of pressure side, which has holes initially used for sample fixing.

2.4.2 3-D profilometry

Cavitation aggressiveness can be estimated by using impact densities (or pit number rates) observed on material surfaces marked by cavitation during the incubating period. Progress in the field of complex surface analysis provides us extended data about the geometric characteristics of the cavitation marks.

Test specimen are analysed with a 3-D laser profilometer (type UBC14 from UBM®) at defined locations which are represented in figure 2.6. The surface is scanned with a step $ds = 5\ \mu m$ for the full scale 2-D blade and $ds = 3\ \mu m$ for the small scale 2-D blade. A 50 μm depth range and a depth accuracy of 0.02 μm are set. In order to eliminate the geometric curvature, a four-degree polynomial is fitted and is subtracted to the original surface data.

The surfaces are treated with the software UBsoft. Surfaces are smoothed in order to eliminate eventual outlier points. Then, each mark is identified if it is deeper than the threshold level parameter h_{lim}, and larger than the threshold diameter $N_{lim} \times ds$.

The geometric characteristics of the impacts are measured. The acoustic energy associated to each pit is also calculated by using an inverse fluid-solid modelling, provided by the software ADRESSE (Fortes-Patella, 1994). The acoustic energy is as-

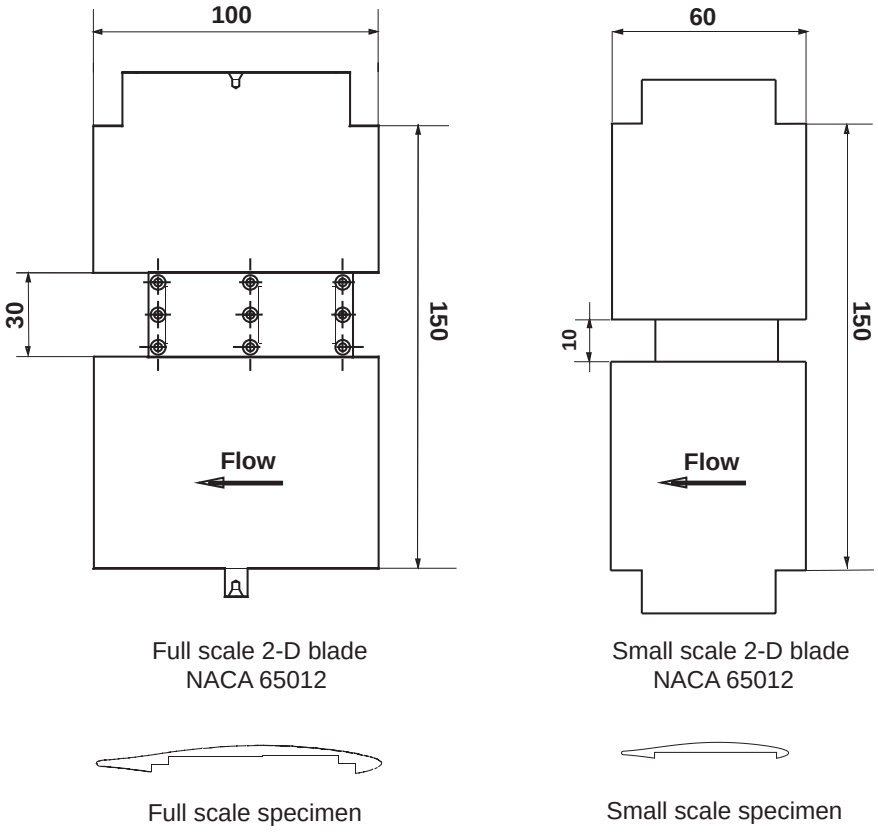

Figure 2.4: Experimental 2-D blades NACA 65012

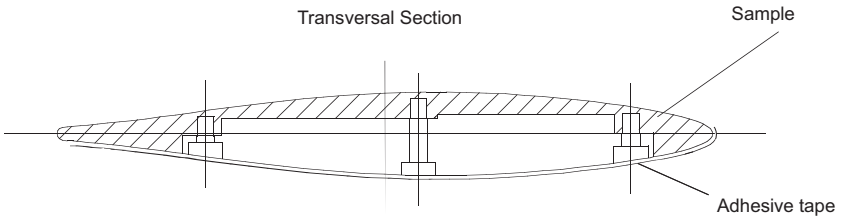

Figure 2.5: 2-D blade NACA 65012

sumed proportional to the deformation energy E_d , the calculated acoustic energy E_a will be noticed to E_d in the results. The calculated variables are the followings :

- relative coordinates (Xi,Yi) of impacts at measurement location k ;
- geometric characteristics of impact : radius $R_{10\%}$, depth H ;
- impact volume V_d ;
- acoustic energy E_a, which will be assimilated to deformation energy E_d .

Assuming an axisymmetric shape of the impacts, their volume can be approximated

by a cone. Thus the theoretical volume V_{dlim} can be calculated :

$$\mathrm{V}_{dlim} \simeq \frac{\pi}{3}.\mathrm{h}_{lim}.(\mathrm{N}_{lim} * ds)^2 \tag{2.3}$$

The values of the cut-off parameters h_{lim} and N_{lim} as well corresponding cut-off volumes are given in table 2.1.

Full scale 2-D blade	$\mathrm{h}_{lim} = 0.2\mu m$	$\mathrm{N}_{lim} = 3$	ds=$5\mu m$	$\mathrm{V}_{dlim} = 47\mu m^3$
Small scale 2-D blade	$\mathrm{h}_{lim} = 0.2\mu m$	$\mathrm{N}_{lim} = 3$	ds=$3\mu m$	$\mathrm{V}_{dlim} = 17\mu m^3$

Table 2.1: Cut-off parameters of the 3-D profilometry measurements

A database is associated with each zone of measurement. It includes the list of identified pits with their position and geometric characteristics. A procedure has been developed to analyse the results of the 3-D profilometry. This procedure includes local (each measurement location) and global (all measurement locations) pitting and deformation volume rates as well as the area damaged by the cavitation for each measurement location.

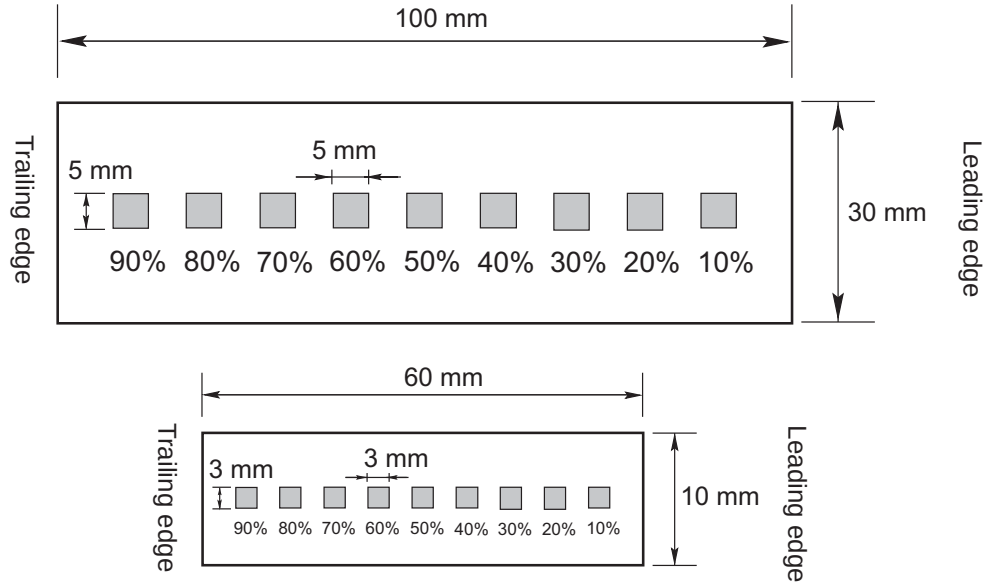

Figure 2.6: Location of analysed zones on an experimental specimen

Part II

Cavitation aggressiveness on 2-D blades

Chapitre 3

Purpose

The objective of these experiments was originally to obtain experimental correlations, which link hydrodynamic parameters of cavitation flow (flow velocity, pressure gradient, blade incidence, ...), as well as the size of an attached leading edge cavity, with the main characteristics and the number of impacts on material specimens.

Moreover, in order to study the scale effect and the effect of an additional pressure gradient on the cavitation aggressiveness, pitting tests have been achieved as follows :

1. 2-D blades of the same type NACA65012 but with 2 different chord lengths are tested. They are referred to the small scale and the full scale 2-D blades.
2. The full scale 2-D blade is either placed in the parallel test section of the cavitation tunnel, or in the diverging test section to create the additional pressure gradient.

On the basis of studies of the indentation deformation energies and the production rate of vapour cavities, the cavitation erosion power model was proposed to link material deformation with macroscopic parameters of the flow. For a complete review of this work, which has been realized with the collaboration of Electricité de France, see the technical report Couty (2000).

Furthermore, these experiments have provided extended pitting data for a broad range of hydrodynamic conditions. Analysis of such data, associated with results of previous research dealing with the production rate of vapour cavities, will help us to determine the influence of macroscopic parameters of the flow on the cavitation aggressiveness through the collapse efficiency.

The purpose of the present work is principally the determination of the collapse efficiency, which represents the energy transfer from the cavitation cavities to the material. In addition, morphology of cavitation impacts is briefly depicted, and the reliability of pitting tests is also discussed.

Chapitre 4

Measurement

4.1 Experimental protocol

4.1.1 Cavitation tunnel

As the water tunnel is filled before each test, a degassing procedure is performed before the exposure of the material specimens in order to obtain a constant air content in water.

For short time exposure of the specimens, cavitation coefficient σ and flow velocity C_{ref} in the cavitation tunnel are set for cavitation free condition with a flow angle of incidence i = 0°. Then, the test starts by a rapid change of the incidence of the 2-D blade. In that case, the cavity length reaches the desired value in 3 s ± 1 s. This has incited to limit the duration of the tests to a minimum of 30 s.

4.1.2 Test specimen

The leading edge and the 2-D blade pressure side are recovered by an adhesive tape (see paragraph 2.4.1). In the case of experiments in the diverging test section, despite the presence of the adhesive tape, it has been noted that the leading edge cavity detachment is not continuous along the span at the leading edge. A continuous detachment is obtained by a smooth sand blasting of the leading edge. After the test, exposed specimen is removed.

4.1.3 Practical test conditions

On the basis of impact observations and of the nature of cavitation flow itself, one has to state the practical test conditions in order to obtain the best relevant statistics of cavitation indentations.

1. It is rather desirable that the detachment of the leading edge cavity be uniform over the whole span of the 2-D blade. The solution of placing an adhesive tape from the leading edge to the trailing edge at the 2-D blade pressure side partly fulfills this requirement.

2. In order to reduce the uncertainty of the statistically estimated parameters, the amount of pit data must be high enough. However, the pitting result for one condition is based on a single sample with one exposure time. Moreover, only parts of this sample are scanned. Consequently, the count of the largest cavitation marks, which are much more rare, can be biased. This is particularly critical since the total deformation volume is highly weighted by the biggest pits. In order to increase the number of impacts, the time exposure can be longer. However, this can yield impact overlapping and thus can lead to an under-estimation of the averaged rates (Reboud *et al.*, 1999).

3. Another difficulty arises in the measurements because of the important differences of impact concentration along the chord. Indeed, as the difference in dispersion of concentration is sharp, an extra distortion in the impact size distribution may be also induced by the lack of data between location measurements.

The pitting test for a given hydrodynamic condition would require at least two runs : a first test with a long exposure time in order to have sufficient mark population at the low concentration zone. In order to limit the impact overlapping at the high concentration area, another test with a shorter duration would be required. Moreover, because of the sharp differences of pitting rates along the chord, the analysis of the whole specimen would be desirable.

4.1.4 Exposure time and damage area

Durations are initially chosen on the basis of the results of the previous experiments. Then, durations are adjusted in a way to maximize the number of pits with a limited impact overlapping risk. This is roughly estimated due to direct observations of cavitation impacts on specimen with an optical microscope. Moreover, assuming that the risk of impact overlapping is proportional to the damaged area fraction, this can be considered as a posterior validation criterion for the pitting test. The damaged surface is equal to the sum of the equivalent $R_{10\%}$ radius disc areas that are associated with each impact. The damage area percentage S_k is defined as the ratio between the damaged area and the total area.

4.2 Hydrodynamic conditions

4.2.1 Parallel test section

The 2-D blades are placed in the parallel test section with an upstream velocity C_{ref}. The average length l_c of the attached leading edge cavity is determined with the help of visualisations (video camera and stroboscope). Examples of photos of hydrodynamic conditions are given in figure 4.1.

(a) 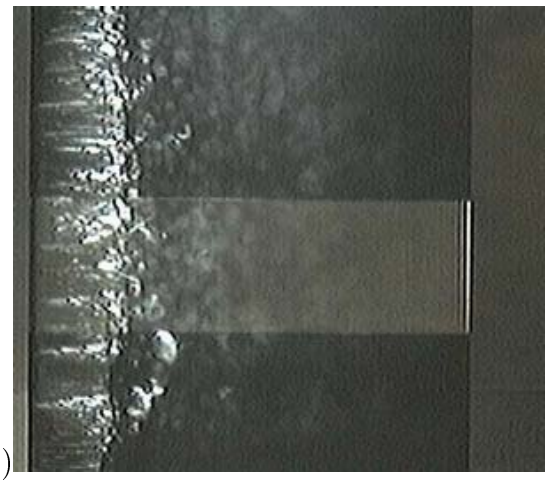 (b) 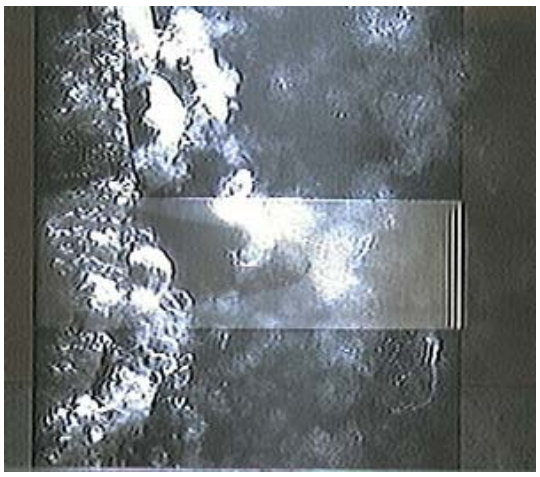

Figure 4.1: Leading edge cavitation of the full scale 2-D blade with an Aluminium specimen, (a) i=4°, C_{ref} =30 $m\ s^{-1}$, l_c=20%, (b) i=6°, C_{ref} =15 $m\ s^{-1}$, l_c=20%

The visualisations show that for a 4° incidence, the leading edge cavity dynamics nearly corresponds to a so-called stable leading edge cavity, with small shed transient cavities in the wake (compared with leading edge cavity length). Nevertheless, larger cavities can be observed, which indicates that the leading edge cavity is not fully stable for 4° incidence.
For the 6° incidence, the leading edge cavity is clearly defined as unstable.
The breakdown of pitting tests represents a large set of hydrodynamic conditions :
- material : Aluminium 1050, pure Copper, Stainless Steel 316 L ;
- 2-D blade incidences : i = 4° and 6° ;
- upstream velocities : C_{ref} = 15, 20, 25 and 30 $m\ s^{-1}$;
- leading edge cavity length : l_c = 20% and 40%.

The operating conditions and specimen materials for which cavitation pitting tests are performed are listed in table 4.1 for the full scale blade. It has to be noted that all combinations of hydrodynamic conditions and material cannot be tested. For example, this is the case of Copper material, with an upstream velocity higher than 25 $m\ s^{-1}$

and an incidence of 6°. Indeed, exposure time would have to be lower than 30 s in order to avoid a probable overlapping of cavitation impacts. This duration would yield a non stabilized flow condition because of the time response of the cavitation tunnel control. It is therefore desirable to use Steel specimen instead of Copper specimen for these conditions.

i [°]	C_{ref} $[m/s]$	σ [−]	l_c [%]	Aluminum	Copper	Stainless Steel
4°	15	1.20	20%	60 min	no pits	no pits
-	15	1.10	40%	40 min	no pits	no pits
-	20	1.25	20%	40 min	120 min	no pits
-	20	1.10	40%	15 min	90 min	no pits
-	25	1.25	20%	7 min 30 s	90 min	3 h
-	25	1.11	40%	5 min	40 min	6 h
-	30	1.26	20%	1 min 30 s	15 min	125 min
-	30	1.12	40%	1 min	10 min	90 min
-	32	1.26	20%	overlapping pits	overlapping pits	120 min
-	32	1.13	40%	overlapping pits	overlapping pits	100 min
6°	15	1.83	20%	2 min 30 s	14 min	120 min
-	15	1.55	40%	3 min 30 s	20 min	135 min
-	20	1.85	20%	overlapping pits	5 min	40 min
-	20	1.58	40%	overlapping pits	5 min	60 min
-	25	1.86	20%	overlapping pits	45 s	8 min
-	25	1.58	40%	overlapping pits	1 min	12 min
-	30	1.87	20%	overlapping pits	overlapping pits	1 min 40 s
-	30	1.60	40%	overlapping pits	overlapping pits	2 min 30 s

Table 4.1: Hydrodynamic conditions, full scale 2-D blade, parallel test section

Concerning the small scale blade, as Copper and Steel material revealed no pits (see report Brite-Euram $n°$ 4158 at l'IMHEF-LMH), only Aluminium material is used. Nevertheless, conditions with a velocity lower than 20 $m\,s^{-1}$ and for 4° incidence lead to no pits, and conditions with velocity higher than 25 $m\,s^{-1}$ for 6° incidence would lead to unacceptable overlapping pits. Hydrodynamic conditions are listed in table 4.5. The durations are identical to those in the case of the full scale 2-D blade in order to estimate the scale effect avoiding a bias effect due to the duration.

As listed in tables 4.2, 4.3 and 4.4, the corresponding pitting measurements for the full scale specimens are indexed as follows : [material][i][C_{ref}][l_c]. For example, a4152

corresponds to the test of the Aluminium material, with $C_{ref} = 15\ ms^{-1}$ and $l_c = 20\%$. It has to be noted that only locations with pits have been analysed.

Nomenclature	Locations [%]	τ_N $[1/mm^2/s]$	τ_{Vd} $[\mu m^3/mm^2/s]$	τ_{Ed} $[J/mm^2/s]$
a.4.15.2	10, 20, 30, 40	1.9e-5	1.3e-2	5.9e-11
a.4.15.4	30, 40, 50, 60	4.0e-5	1.3e-2	8.0e-11
a.4.20.2	10, 20, 30, 40	8.7e-4	4.6e-1	2.7e-9
a.4.20.4	30, 40, 50, 60	1.3e-3	3.3	1.4e-8
a.4.25.2	20, 30, 40, 50	4.2e-3	4.5	3.4e-8
a.4.30.2	10, 20, 30, 50	1.8e-2	11.2	7.3e-8
a.4.30.4	30, 40, 50	2.3e-2	18.7	1.5e-7
a.6.15.2	10, 20, 30, 40, 50	7.0e-3	11.4	9.5e-8
a.6.15.4	20, 30, 40, 50, 60, 70	2.6e-3	7.5	6.5e-8

Table 4.2: 3-D Profilometry measurements, full scale specimen, Aluminium

Nomenclature	Locations [%]	τ_N $[1/mm^2/s]$	τ_{Vd} $[\mu m^3/mm^2/s]$	τ_{Ed} $[J/mm^2/s]$
c.4.20.2	10, 20, 30, 40, 50, 60	1.3e-4	4.6e-2	3.9e-9
c.4.20.4	30, 40, 50, 60	2.0e-4	9.3e-2	8.9e-9
c.4.25.2	20, 30, 40, 50, 60	6.6e-4	5.1e-1	5.7e-8
c.4.25.4	20, 30, 40, 50, 60	1.2e-3	6.5e-1	6.4e-8
c.4.30.2	30, 40, 50, 60	4.1e-4	5e-1	9.0e-8
c.4.30.4	30, 40, 50	2.3e-3	2.4	3.6e-7
c.4.32.2	20, 30, 40, 50, 60	6.2e-3	45.3	5.3e-6
c.4.32.4	20, 30, 40, 50, 60	7.9e-3	19.8	2.3e-6
c.6.15.2	10, 20, 30, 40, 50, 60	1.6e-3	1.9	2.5e-7
c.6.15.4	20, 30, 40, 50, 60, 70	1.7e-3	3.2	5.0e-7
c.6.20.2	20, 30, 40, 50, 60	3.4e-3	12.7	2.5e-6
c.6.20.4	20, 30, 40, 50, 60, 70	8.1e-3	32.9	6.0e-6
c.6.25.2	20, 30, 40, 50, 60	1.9e-2	47.1	8.0e-6
c.6.25.4	10, 20, 30, 40, 50, 60, 70	3.7e-2	283	4.4e-5

Table 4.3: 3-D Profilometry measurements, full scale specimen, Copper

Nomenclature	Locations [%]	τ_N $[1/mm^2/s]$	τ_{Vd} $[\mu m^3/mm^2/s]$	τ_{Ed} $[J/mm^2/s]$
i.4.30.2	10, 20, 30	4.5e-6	2.5e-3	1.0e-9
i.4.30.4	30, 40, 50	5.1e-5	2.1e-2	8.1e-9
i.4.32.2	20, 30, 40, 50, 60	1.6e-4	1.7e-1	7.4e-8
i.4.32.4	20, 30, 40, 50, 60	1.7e-4	1.3e-1	5.2e-8
i.6.15.2	10, 20, 30, 40	5.8e-6	1.3e-3	3.6e-10
i.6.15.4	30, 40, 50, 60	6.9e-6	3.4e-3	1.3e-9
i.6.20.2	10, 20, 30, 40	5.2e-5	2.4e-2	6.9e-9
i.6.20.4	30, 40, 50, 60, 70	1.2e-4	2.7e-1	1.5e-7
i.6.25.2	20, 30, 40, 50	1.5e-4	1.4e-1	5.9e-8
i.6.25.4	40, 50, 60, 70	3.7e-4	4.9e-1	3.0e-7
i.6.30.2	20, 30, 50	4.2e-4	3.5e-1	1.3e-7
i.6.30.4	30, 40, 50, 60, 70	3.5e-3	10.3	4.4e-6

Table 4.4: 3-D Profilometry measurements, full scale specimen, Stainless Steel

i [°]	C_{ref} $[m/s]$	σ $[-]$	l_c [%]	Aluminum
4°	20	1.02	40%	40 min
-	25	1.19	20%	7 min 30 s
-	25	1.02	40%	5 min
-	30	1.17	20%	1 min 30 s
-	30	1.03	40%	1 min
6°	15	1.76	20%	2 min 45 s
-	15	1.45	40%	3 min 30 s
-	20	1.77	20%	1 min
-	20	1.43	40%	3 min
-	25	1.77	20%	30 s
-	25	1.44	40%	45 s et 2 min 30 s

Table 4.5: Hydrodynamic conditions, small scale 2-D blade, parallel test section

Nomenclature	Locations [%]	τ_N $[1/mm^2/s]$	τ_{Vd} $[\mu m^3/mm^2/s]$	τ_{Ed} $[J/mm^2/s]$
pa.4.20.4	40, 50	9.0e-4	7.6e-2	3.1e-10
pa.4.25.2	20, 30	1.8e-3	1.4e-1	8.0e-10
pa.4.25.4	40, 50	2.8e-2	3.3	1.8e-8
pa.4.30.2	20, 30	1.8e-2	2.2	1.2e-8
pa.4.30.4	40, 50	1.1e-1	71.2	5.4e-7
pa.6.15.2	20, 30	1.0e-2	2.3	1.5e-8
pa.6.15.4	40, 50	6.4e-3	2.3	1.7e-8
pa.6.20.2	20, 30	5.1e-2	34.6	2.4e-7
pa.6.20.4	40, 50	6.0e-3	1.7	9.1e-9
pa.6.25.2	20, 30	1.8e-1	197	1.4e-6
pa.6.25.4	40, 50, 60	2.2e-1	287	2.1e-6
pabis.6.25.4	40, 50, 60	7.9e-2	238	1.5e-6

Table 4.6: 3-D Profilometry measurements, small scale specimen, Aluminium

4.2.2 Diverging test section

Pitting tests have been realized with the full scale 2-D blade placed in the diverging test section with Copper, and Steel specimen for the most aggressive conditions (C_{ref} = 25 $m\ s^{-1}$ and i = 6°). It is desirable to choose similar durations to those in the case of parallel test section (for the same hydrodynamic conditions and material). By this way, the effect of the pressure gradient could be evaluated without the bias effect due to the duration. However, the exposure time has been reduced during the experiments because of the obtained high pitting rates. The test conditions, as well as the corresponding pitting measurements, are listed in tables 4.7 and 4.8. C'_{ref} is the upstream velocity and σ' the corresponding cavitation coefficient. C_{ref} and σ are the parameters that are set to the cavitation tunnel. Time, as well as σ and C_{ref} of the corresponding tests for the parallel test section, are noted with parenthesis as "reminder".

i [°]	C_{ref} $[m/s]$	C'_{ref} $[m/s]$	σ $[-]$	σ' $[-]$	l_c [%]	Copper	Steel
4°	15 (20)	20	3.10 (1.25)	1.74	20%	120 min (120 min)	-
-	15 (20)	20	2.84 (1.10)	1.59	40%	90 min (90 min)	-
-	22.5 (30)	30	3.12 (1.25)	1.75	20%	10 min (15 min)	-
-	22.5 (30)	30	2.85 (1.12)	1.60	40%	5 min (10 min)	-
6°	15 (20)	20	4.15 (1.85)	2.32	20%	1 min 15 (5 min)	-
-	15 (20)	20	3.45 (1.57)	1.93	40%	1 min (5 min)	-
-	17.5 (25)	25	4.15 (1.86)	2.32	20%	-	5 min (8 min)
-	17.5 (25)	25	3.45 (1.58)	1.93	40%	-	9 min (12 min)

Table 4.7: Hydrodynamic conditions, full scale 2-D blade, diverging test section

Nomenclature	Locations [%]	τ_N $[1/mm^2/s]$	τ_{Vd} $[\mu m^3/mm^2/s]$	τ_{Ed} $[J/mm^2/s]$
dc.4.20.2	20, 30, 40	1.3e-3	0.45	4.2e-8
dc.4.20.4	30, 40, 50	4.2e-3	1.1	8.3e-8
dc.4.30.2	30, 40, 50	3.0e-2	10.3	9.0e-7
dc.4.30.4	40, 50, 60, 70, 80	2.7e-2	116	1.5e-5
dc.6.20.2	20, 30, 40, 50	1.1e-2	4.7	4.6e-7
dc.6.20.4	30, 40, 50, 60, 70, 80	4.2e-2	108	1.8e-5
di.6.25.2	20, 30, 50, 60	5.7e-4	1.6	1.4e-6
di.6.25.4	30, 40, 50, 60, 70, 80	1.6e-3	6.5	3.8e-6

Table 4.8: 3-D Profilometry measurements, full scale specimen, diverging test section

Chapitre 5

Results

5.1 Characteristics of the pits

5.1.1 Overlapping risk

The damage area fraction S_k has been maintained below 15% even for the most aggressive conditions (Aluminium and Copper at high upstream velocity). Consequently, the pitting tests show a low overlapping risk.

5.1.2 Influence of flow velocity on impacts size

The maximum volumes Vd_{max} with their associated location are listed in tables 5.1, 5.2 and 5.3 for the full scale specimens, and in table 5.4 for the small scale specimens. All geometrical characteristics of the impacts are listed in the statistics presented in annexe B.

Let us consider the evolution of the volume of impacts versus the flow velocity for Copper material (figure 5.1). The examination of impact volumes for the different flow velocities indicated that higher maximum volumes are obtained when the velocity increased. However, this hypothesis cannot be validated for all measurements. As an explanation, the maximum volumes Vd_{max} are probably not fully representative because of the lack of pit data, which can be amplified if a short duration is chosen.

5.1.3 Impacts location

The maximum number of impact N_{max}, associated location and damaged area S_k are listed in tables 5.1, 5.2 and 5.3 for the full scale specimens, and in table 5.4 for the small scale specimens. In the stable mode ($i = 4°$), the impacts are mainly concentrated at about cavity closure.

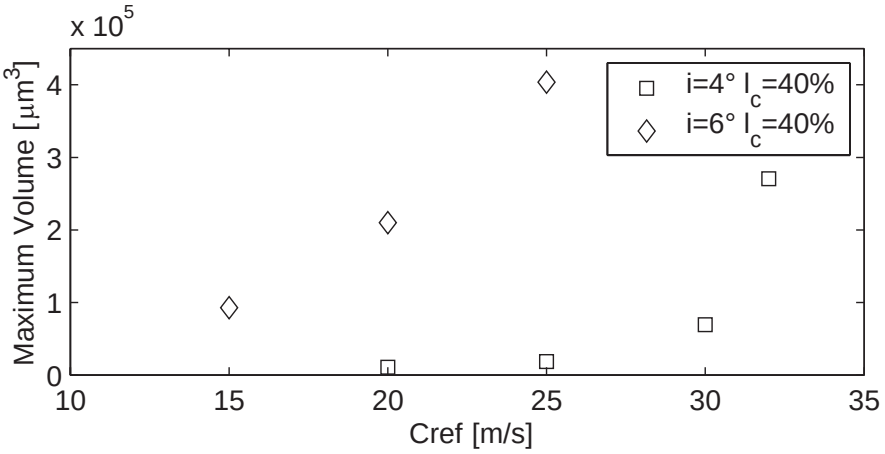

Figure 5.1: Influence of flow velocity on maximum volumes, Aluminium specimens

In the case of unstable leading edge cavity (i = 6°), because of the uncertainty of the leading edge cavity length and the large shed transient vapour cavities, indentations are much more scattered. This result is in good harmony with findings of many authors dealing with erosion prediction (Kato *et al.*, 1978; Simoneau *et al.*, 1989). Moreover, in comparison to the stable mode, the presence of very large impacts has to be noted.

Concerning the impacts in the diverging test section (see table 5.5), they are much more scattered for both incidences.

Nomenclature	N_{max} [−]	Location [%]	S_k [%]	Vd_{max} [μm^3]	Location [%]
a.4.15.2	10	10%	0.03	1815	30%
a.4.15.4	10	40%	0.06	1058	50%
a.4.20.2	493	20%	3.44	6782	20%
a.4.20.4	269	40%	2.73	580458	40%
a.4.25.2	274	20%	2.42	35958	30%
a.4.30.2	395	20%	3.10	11544	20%
a.4.30.4	289	40%	3.51	18305	40%
a.6.15.2	118	20%	2.04	89150	20%
a.6.15.4	55	40%	1.49	82929	50%

Table 5.1: 3-D Profilometry statistics, full scale specimen, Aluminium

Nomenclature	N_{max} [−]	Location [%]	S_k [%]	Vd_{max} [μm^3]	Location [%]
c.4.20.2	104	30%	0.66	5864	50%
c.4.20.4	196	40%	1.52	10932	40%
c.4.25.2	1012	20%	7.74	68320	30%
c.4.25.4	642	40%	5.35	18671	20%
c.4.30.2	61	50%	0.45	40992	40%
c.4.30.4	312	40%	3.44	69390	50%
c.4.32.2	777	20%	11.9	253489	50%
c.4.32.4	874	40%	16.6	270411	40%
c.6.15.2	153	30%	2.81	24108	20%
c.6.15.4	331	30%	2.36	92860	70%
c.6.20.2	136	20%	3.49	107428	40%
c.6.20.4	227	40%	8.26	210149	50%
c.6.25.2	143	20%	1.97	57268	30%
c.6.25.4	234	40%	10.8	403781	50%

Table 5.2: 3-D Profilometry statistics, full scale specimen, Copper

Nomenclature	N_{max} [−]	Location [%]	S_k [%]	Vd_{max} [μm^3]	Location [%]
i.4.30.2	4	20%	0.02	3152	30%
i.4.30.4	59	40%	0.37	2991	50%
i.4.32.2	130	30%	2.48	27969	20%
i.4.32.4	149	40%	1.55	14741	50%
i.6.15.2	5	30%	0.02	424	40%
i.6.15.4	7	50%	0.10	2178	50%
i.6.20.2	16	20%	0.09	2660	40%
i.6.20.4	36	50%	1.81	62086	50%
i.6.25.2	9	20%	0.10	10667	50%
i.6.25.4	29	50%	0.86	11379	50%
i.6.30.2	9	20%	0.08	6286	30%
i.6.30.4	53	40%	1.60	51110	50%

Table 5.3: 3-D Profilometry statistics, full scale specimen, Stainless Steel

Nomenclature	N_{max} [−]	Location [%]	S_k [%]	Vd_{max} [μm^3]	Location [%]
pa.4.20.4	57	40%	0.23	346	40%
pa.4.25.2	71	20%	0.39	224	20%
pa.4.25.4	632	40%	4.11	2824	50%
pa.4.30.2	149	20%	1.00	1861	20%
pa.4.30.4	483	40%	6.93	43136	50%
pa.6.15.2	150	20%	1.23	4920	20%
pa.6.15.4	96	40%	1.45	4557	40%
pa.6.20.2	249	20%	5.24	15210	20%
pa.6.20.4	73	50%	0.68	11001	50%
pa.6.25.2	438	20%	9.94	67035	20%
pa.6.25.4	446	50%	10.80	75999	50%
pabis.6.25.4	601	40%	20.70	330604	50%

Table 5.4: 3-D Profilometry statistics, small scale specimen, Aluminium

Nomenclature	N_{max} [−]	Location [%]	S_k [%]	Vd_{max} [μm^3]	Location [%]
dc.4.20.2	1050	40%	6.5	3516	40%
dc.4.20.4	2540	30%	11.3	5957	30%
dc.4.30.2	2016	50%	13.1	20169	30%
dc.4.30.4	643	70%	20.6	486097	60%
dc.6.20.2	169	20%	1.06	12141	40%
dc.6.20.4	218	30%	1.73	186070	50%
di.6.25.2	22	30%	0.33	50058	60%
di.6.25.4	89	50%	4.9	94514	50%

Table 5.5: 3-D Profilometry statistics, full scale specimen, diverging test section

5.1.4 Visualisations

The characteristics of the pits can be described by 3-D profilometry visualisations. The surfaces of the specimens are represented by using colour images. The colour-map indicates the depth in μm.
As an example of the impacts obtained for the 4° incidence, see the locations 40% and 50% of the Copper specimen c4304 in figures 5.2. As a matter of fact, the impacts are well distributed with little overlapping. Concerning the unstable mode, let us consider the Copper specimen c6254 in figure 5.3. This mode leads to 2 families of impacts :

1. isolated impacts which are similar to those observed with the stable mode ;
2. grouped impacts.

The presence of grouped impacts could let us conclude that large shed transient cavities are at the origin of multiple impacts. It has to be noted that these grouped impacts also appear if the exposure time is reduced.
Moreover, observations let us suppose that large "smooth" impacts are present on which smaller but deeper impacts are superposed. Due to the damage threshold of the material, this fact is all the more true if the material is ductile.

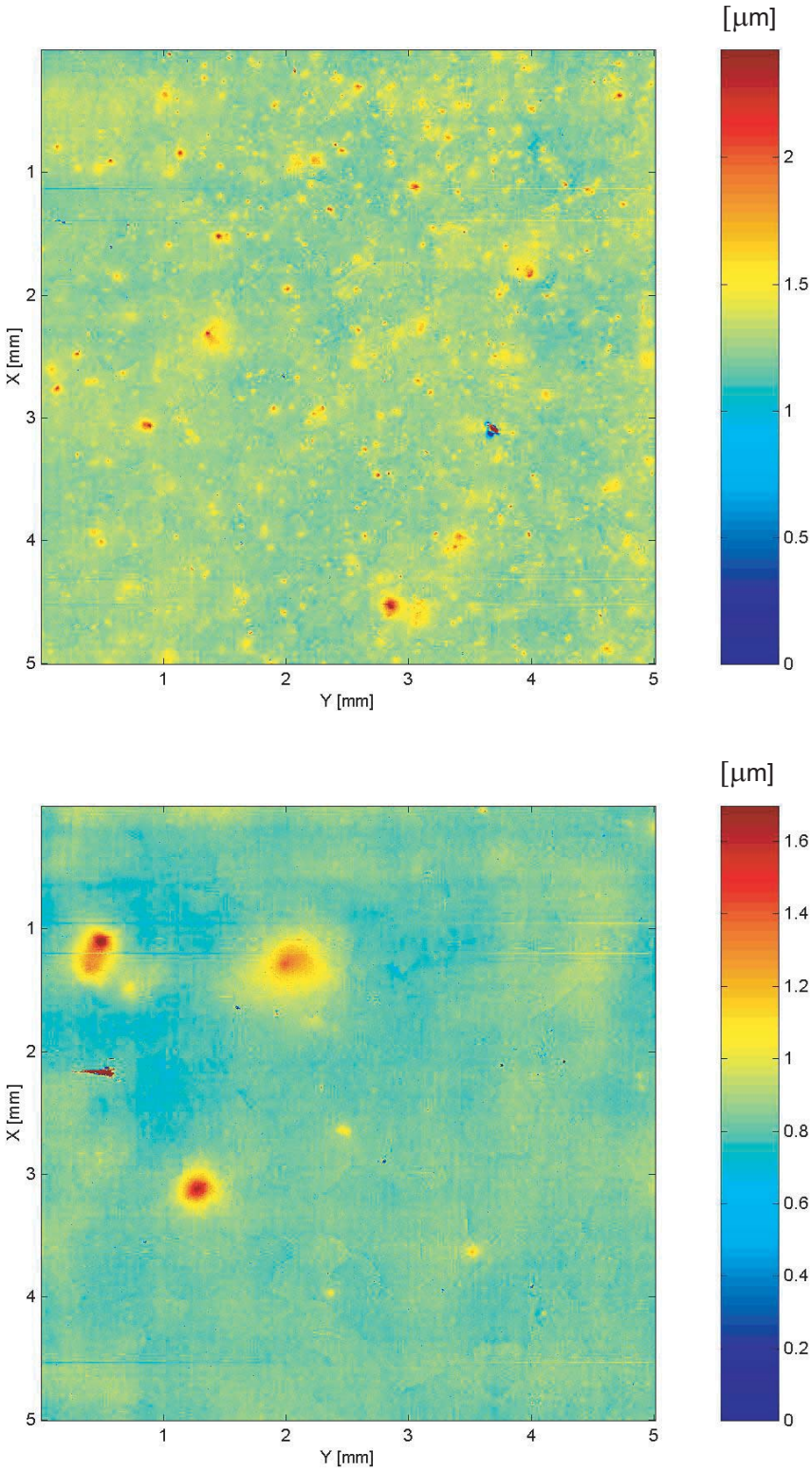

Figure 5.2: Surface visualisation at location 40% and 50% for condition c4304

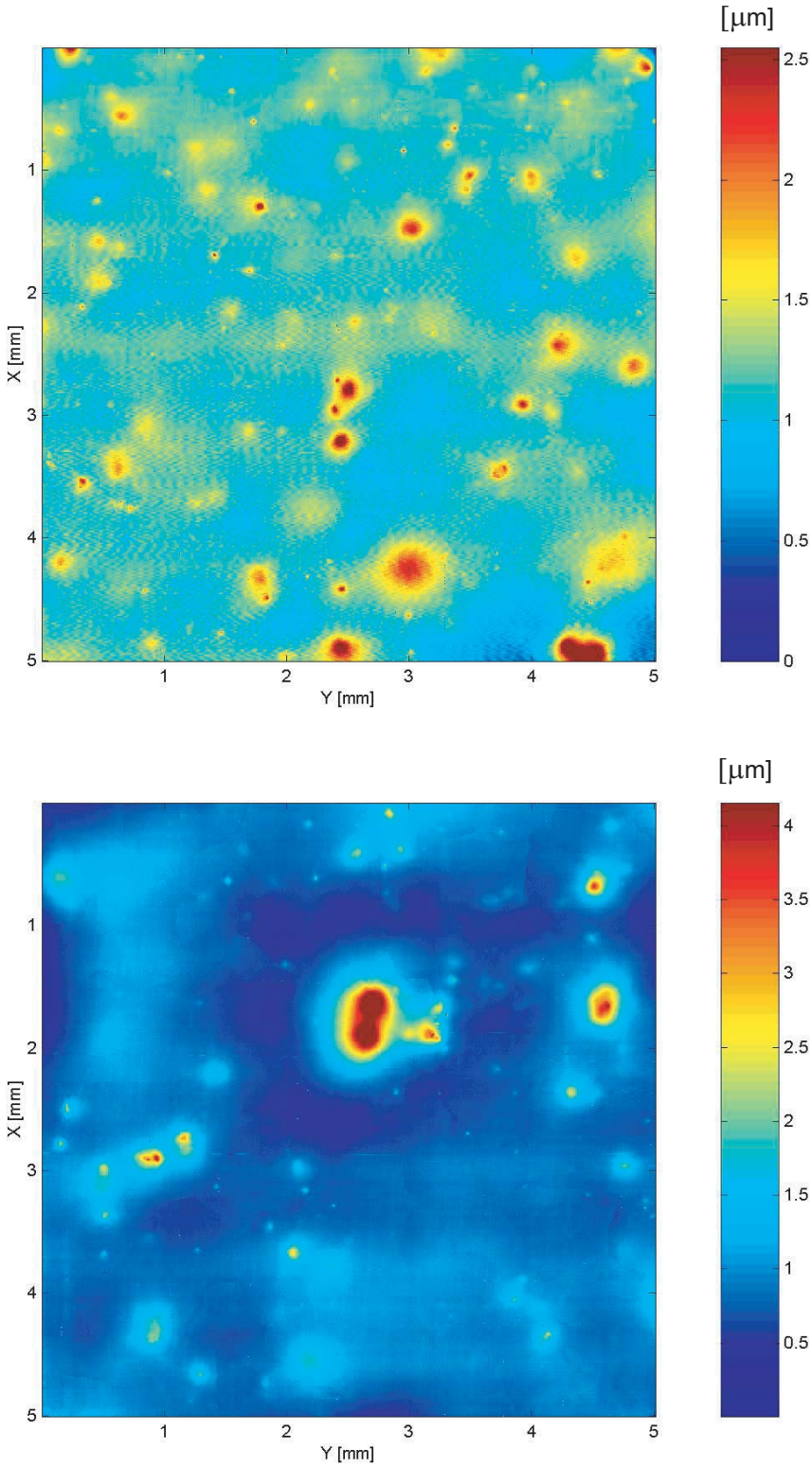

Figure 5.3: Surface visualisation at location 40% and 50% for condition c6254

5.2 Pitting rates

5.2.1 Calculation method

Averaged rates

As it has been early suggested by Knapp *et al.* (1970), pitting rate alone would not be able to measure precisely the damage caused by cavitation.
Despite the lack of data for the largest pits, the total deformation provides a more accurate measurement of the overall energy transfer from the vapour structures to the material. Therefore, both the averaged pitting rates and the averaged deformation volume rates have been calculated. Deformation energy rates have been also calculated They are obtained by numerical integration along the chord of the pitting rates or deformation volume rates. The whole considered surface is equal to the sum of all measurement zones, which is equivalent to 9 areas (from 10% up to 90%) of $Lx \times Ly$ mm^2. They are expressed per unit time and per unit surface.

The numerical integration is obtained by considering a linear interpolation $\tau^{(1)}(x)$ of the volumes and the number of indentations between the locations "k". The averaged pitting rate τ_N, the averaged deformation volume rate τ_{Vd} and the averaged deformation energy rate τ_{Ed} are given by the following integration formula :

$$\tau_N = \frac{1}{9 \times Lx \times Ly \times T} \frac{1}{L} \int_{x_{min}}^{x_{max}} \tau_N(x)^{(1)} \delta x_i \qquad [mm^{-2}\, s^{-1}] \qquad (5.1)$$

$$\tau_{Vd} = \frac{1}{9 \times Lx \times Ly \times T} \frac{1}{L} \int_{x_{min}}^{x_{max}} \tau_{Vd}(x)^{(1)} \delta x_i \qquad [\mu m^3\, mm^{-2}\, s^{-1}] \qquad (5.2)$$

$$\tau_{Ed} = \frac{1}{9 \times Lx \times Ly \times T} \frac{1}{L} \int_{x_{min}}^{x_{max}} \tau_{Ed}(x)^{(1)} \delta x_i \qquad [J\, mm^{-2}\, s^{-1}] \qquad (5.3)$$

whereas the interval $[x_{min}, x_{max}]$ is the integration domain along the chord L of the 2-D blade, T the duration of the test.
The overall numerical results are summarized in the previous section in tables 4.2, 4.3 and 4.4 for the full scale specimens, and in table 4.6 for the small scale specimens. Results can be presented with charts. See the figures 5.4, 5.6 and 5.7 for the full scale 2-D blade. Comparison between the results obtained for the parallel test section and the diverging one is presented in figure 5.5. Results for the small scale 2-D blade are given in figure 5.8.

Local rates

As complementary results, the rates which correspond to each location "k" are listed in annexe A.
Local rates have been expressed as :

$$\tau_N(k) = \frac{N_k}{T \times Lx \times Ly} \qquad [mm^{-2}\, s^{-1}] \tag{5.4}$$

$$\tau_V(k) = \frac{\sum_{(x_i,y_i)\in k} Vd_{(x_i,y_i)}}{T \times Lx \times Ly} \qquad [\mu m^3\, mm^{-2}\, s^{-1}] \tag{5.5}$$

$$\tau_E(k) = \frac{\sum_{(x_i,y_i)\in k} Ed_{(x_i,y_i)}}{T \times Lx \times Ly} \qquad [J\, mm^{-2}\, s^{-1}] \tag{5.6}$$

whereas N_k is the number of indentations at the location "k".

5.2.2 Global characteristics of averaged rates

1. The high dependence of the averaged rates upon the flow velocity is confirmed.
2. The leading edge cavity length $l_c = 40\%$ leads to higher rates than the leading edge cavity length $l_c = 20\%$.
3. Much higher rates are obtained in the case of the unstable leading edge cavitation.
4. In comparison to the full scale 2-D blade results, lower volume deformation rates are obtained for the small scale experiments. Nevertheless, this is not the case for the pitting rates which are mostly higher. This can be explained by the cut-off parameter ds of the 3-D profilometry. The latter is smaller for the small scale 2-D blade than for the full scale 2-D blade (see table 2.1). Consequently, the minimum measured volume is smaller for the small scale 2-D blade. Thus, the total number of pits can be biased.
5. Strong effect of the additional pressure gradient is remarkable for all the tested flow velocities. Both the averaged pitting rate and the averaged deformation volume rate are much higher in this configuration (typical factor 10).

5.2.3 Comparison between the materials

The total dissipated deformation power between the different materials can be compared for a same hydrodynamic condition. Indeed, by considering the averaged energy deformation rates, it is shown that equivalent deformation energies are obtained by using either Copper or Aluminium. This also demonstrates that the calculation of the deformation energy is consistent for the 2 materials.

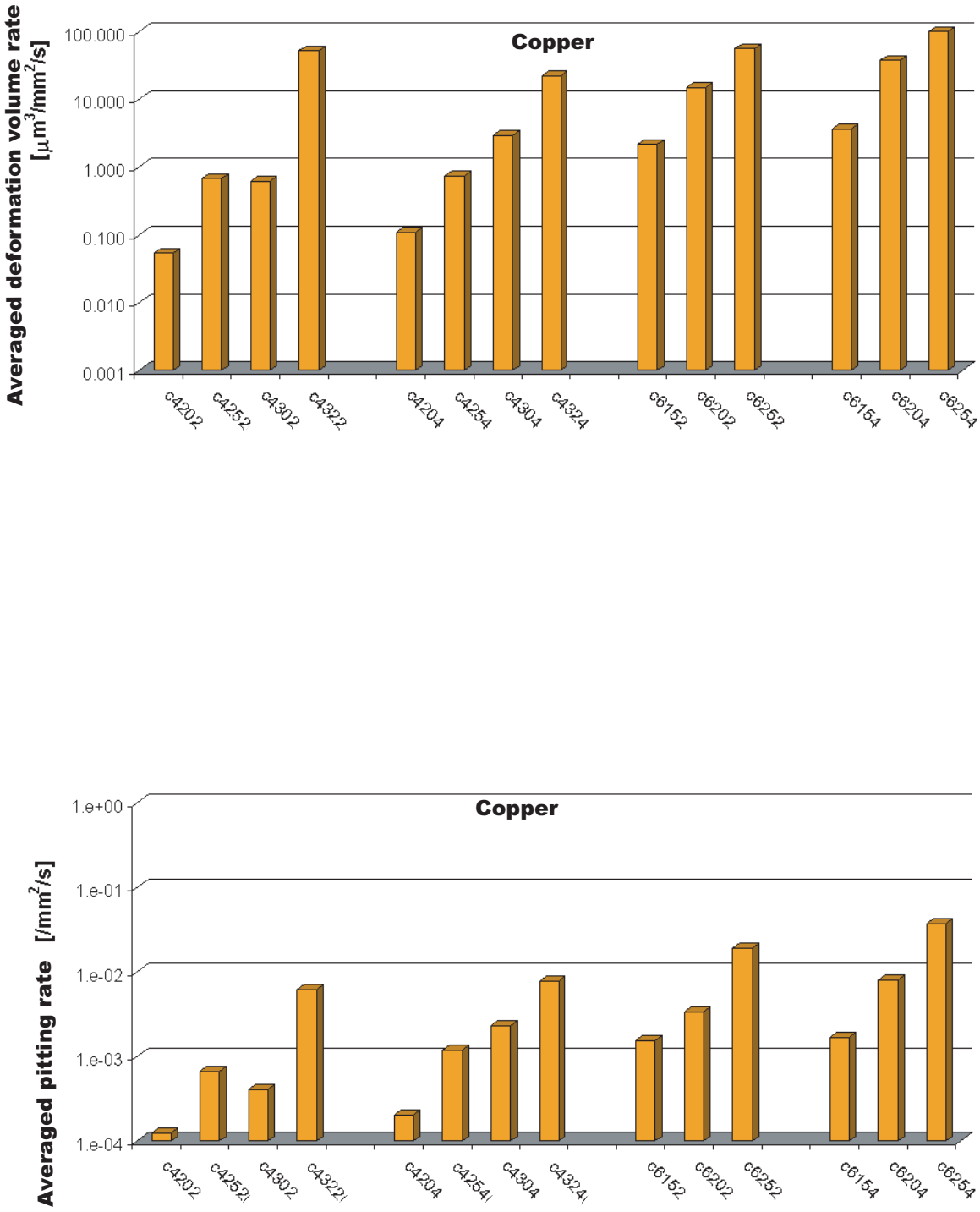

Figure 5.4: Averaged pitting and deformation volume rates for Copper specimens with the full scale 2-D blade

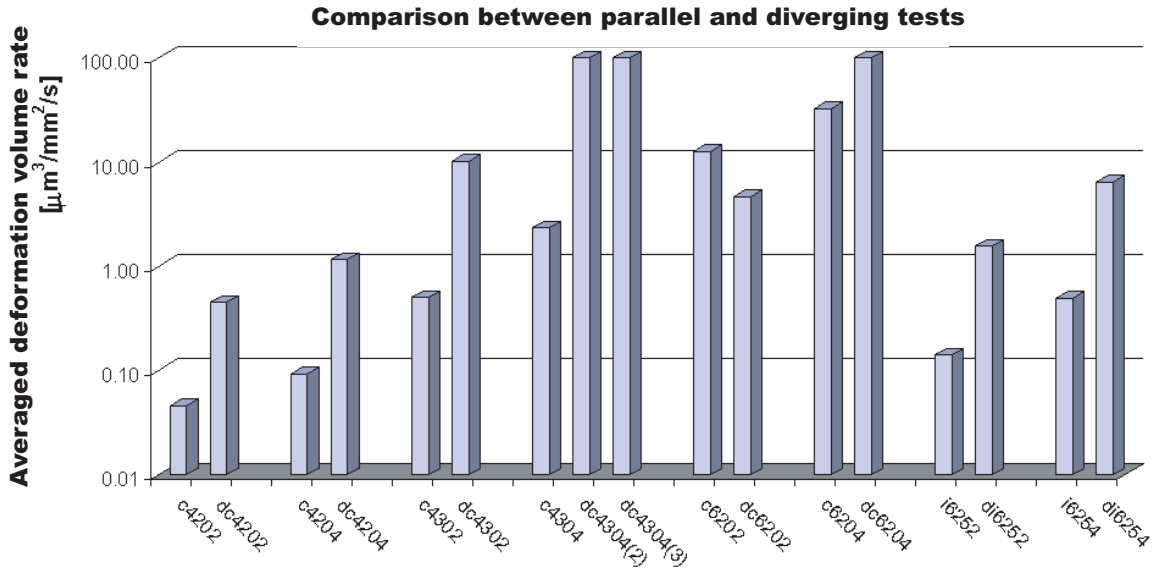

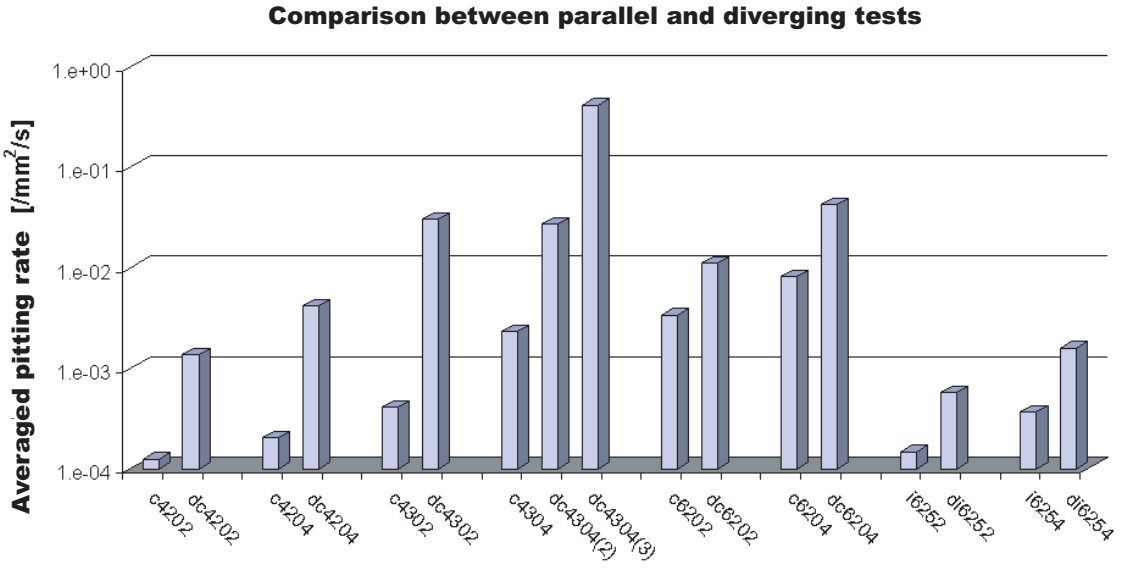

Figure 5.5: Averaged pitting and deformation volume rates, comparison between the parallel and the diverging test section

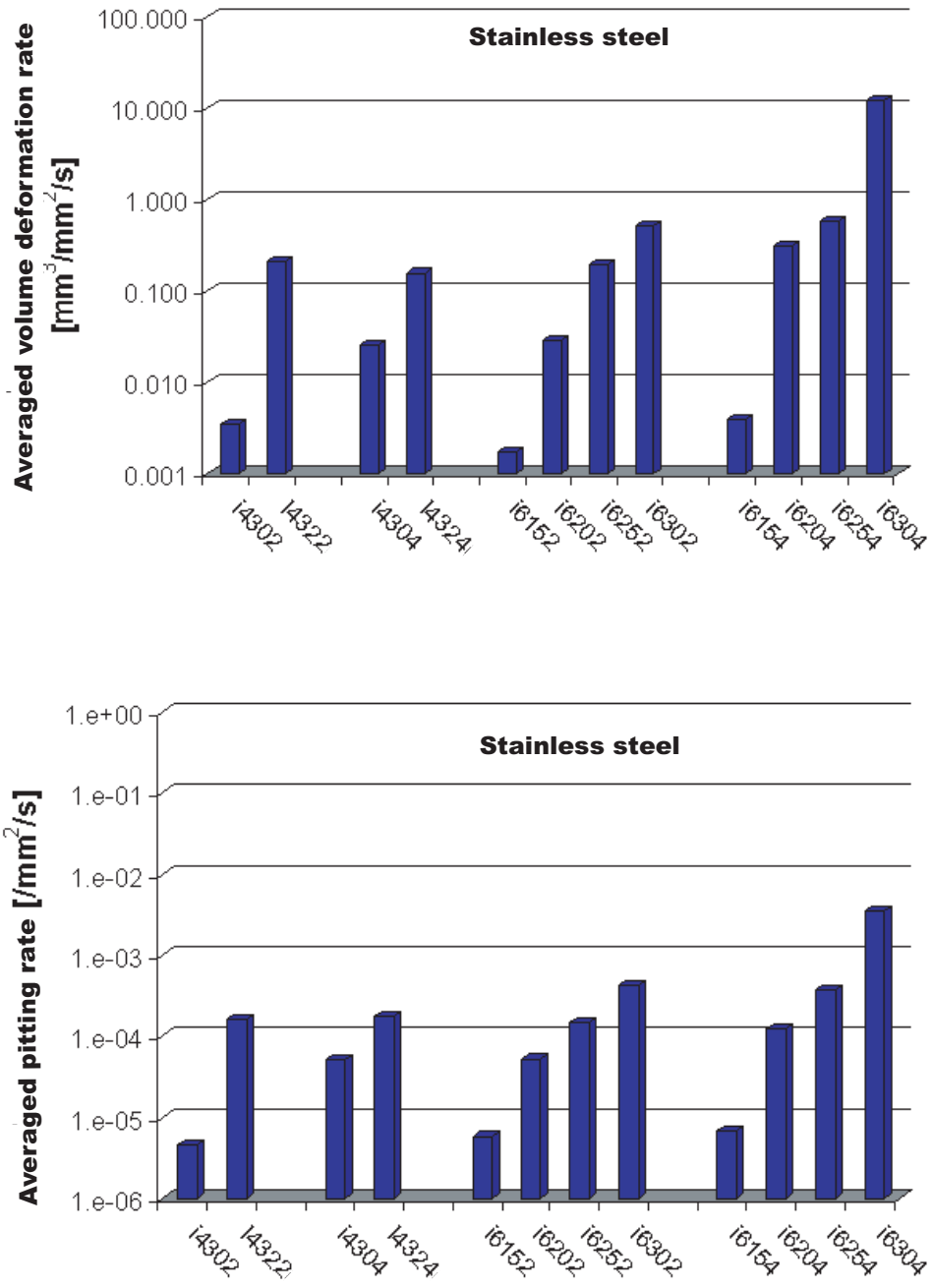

Figure 5.6: Averaged pitting and deformation volume rates for Stainless Steel specimens with the full scale 2-D blade

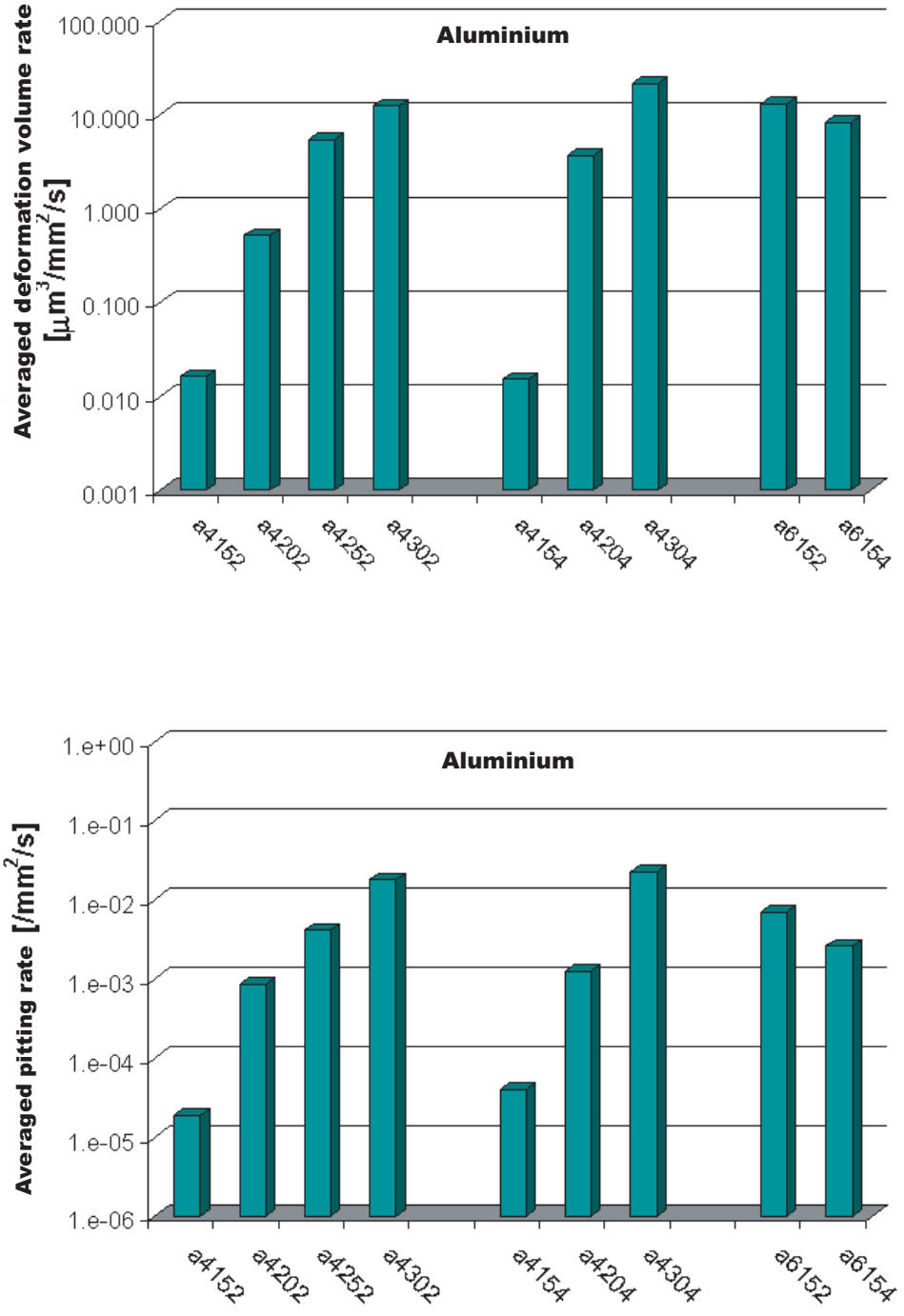

Figure 5.7: Averaged pitting and deformation volume rates for Aluminium specimens with the full scale 2-D blade

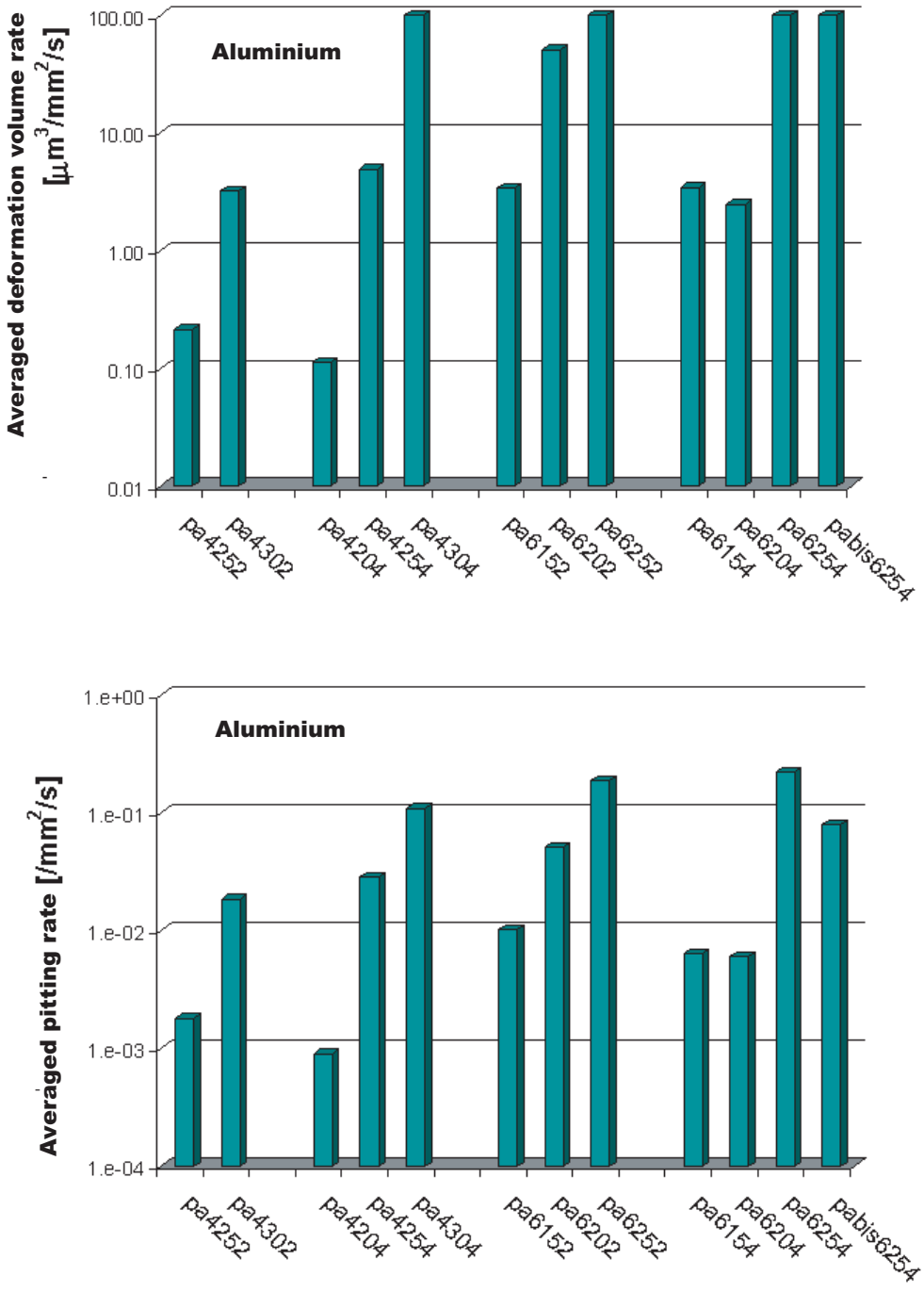

Figure 5.8: Averaged pitting and deformation volume rates for Aluminium specimens with the small scale 2-D blade

5.3 Probability density distributions

5.3.1 Basis of the analysis

Although results globally show that both the maximum volumes and the maximum averaged rates are situated at about the cavity closure or downstream of it, it has to be noted that measurements could be affected by the uncertainty of the leading edge cavity length, as well as by the lack of data between location zones. Therefore, statistical results have to be considered with care and only the global statistics to the whole 2-D blade are relevant.

The probability densities of deformation volume for the small scale 2-D blade are presented in figure 5.9. Distributions for the parallel test section situation and the full scale 2-D blade are shown in figures 5.10 and 5.11. Similarly, the probability density of the deformation energy is presented in figures 5.13, 5.14 and 5.15. The conditions are noted [material][i][C_{ref}][l_c], where material is "a" for Aluminium, "c" for Copper and "i" for Steel. Conditions for the small scale 2-D blade are noted "pa", and conditions for the diverging situation are respectively noted "dc" and "di" for Copper and Stainless Steel. To simplify the comparison between conditions, the different velocities and leading edge cavity lengths are noted with symbols as catalogued in table 5.6.

Symbols	C_{ref} $[m/s]$	l_c [%]
○	15	20%
×	15	40%
+	20	20%
∗	20	40%
□	25	20%
◊	25	40%
▽	30	20%
△	30	40%
◁	32	20%
▷	32	40%

Table 5.6: List of symbols with the corresponding hydrodynamic conditions

Probability distributions of the different materials are grouped in a same page for each incidence i = 4° and i = 6°.

5.3.2 Main characteristics

Minimum volume and energy

As shown in all graphics, probability density distributions are cut for the volumes lower than the cut-off volumes V_{dlim} defined in equation 2.3 in chapter 2. These are $V_{dlim} \simeq 47\ \mu m^3$ for the full scale 2-D blade and $V_{dlim} \simeq 17\ \mu m^3$ for the small scale 2-D blade. Therefore, minimum volumes and energies in probability density distributions are not relevant.

Maximum probability peak

All the densities present a common shape : they increase from the minimum volumes or energies up to a unique probability peak which corresponds to the most probable volume or energy of the measured impacts. However, the maximum volume of the distributions is fixed and has to be related to the chosen resolution of the profilometer measurement. As an argument, the step sampling of the profilometer scanning have been set to $ds = 3\ \mu m$ and $ds = 5\ \mu m$ respectively for the small and the full scale 2-D blade (keeping the same depth resolution), which is equivalent to a factor 2. Obtained maximum probability volumes in distributions are 50 μm^3 and 200 μm^3, respectively for the small and the full scale 2-blade, thus leading to a factor 4. Nevertheless, this peak clearly shows that the small impacts are the most probable. To this characteristic volume corresponds a characteristic energy which strongly depends on the material, respectively $10^{-6}\ J$, $210^{-5}\ J$ and $510^{-5}\ J$ for aluminium, copper and stainless steel.

Probability decay with volume and energy

A density decay has to be noted from the maximum probability peak up to the maximum volumes and energies. This is an important characteristic of distributions. Very similar decay and probability values are obtained for all conditions especially at the first part of the curves, from the probability peak (smallest pits) towards the middle volumes (up to 10^3–$10^4\ \mu m^3$). In this part, the amount of pits have been sufficient to obtain correct statistics. In the second part of the curves, some discrepancies can be noted between the densities. This can be partly explained by the lack of pit data for the large pits.

Maximum volumes and energies

Maximum volumes and energies are very dependent upon the conditions. However, as these can be strongly biased by the lack of data for the corresponding pits, they must be considered with care.

5.3.3 Influencing flow parameters

Influence of the flow velocity

Obviously, maximum values of pit volume and energy are noticed for high upstream velocity conditions. Moreover, although the shape the densities remain similar for all conditions, some influence of the flow velocity onto the decay can be noted for conditions with copper material for the 4° incidence. In these conditions, the decay is lowered when the flow velocity increases.

Scale effect

Lower maximum volumes are obtained in the case of the small scale experiments.

Flow angle of incidence

For the 4° incidence, the maxima obtained for both cavity lengths 20% and 40% are similar. Compared to this, higher maximum volumes are obtained for the 6° incidence. Higher volumes are noted for the cavity length 40% . It has to be noted that some conditions (a4252, a4204, c4252, c6204 and i6204) present unpredictable high maxima. This might explained by a peculiar placement of the adhesive tape, yielding the shedding of much larger and erosive transient cavities.

Pressure gradient effect

Distributions are graphically shown in figures 5.12 and 5.16 with green symbols. In comparison to the experiments with the parallel test section which are plotted on the same graphic in black, the presence of larger impacts (and energetic) is seen for the conditions (i = 6°, C_{ref} = 25 $m\,s^{-1}$, l_c = 20% and l_c = 40%) and (i = 4°, C_{ref} = 30 $m\,s^{-1}$, l_c = 40%). Moreover, discrepancy of the shapes of the density curves are noted for the test with copper material in the diverging situation.

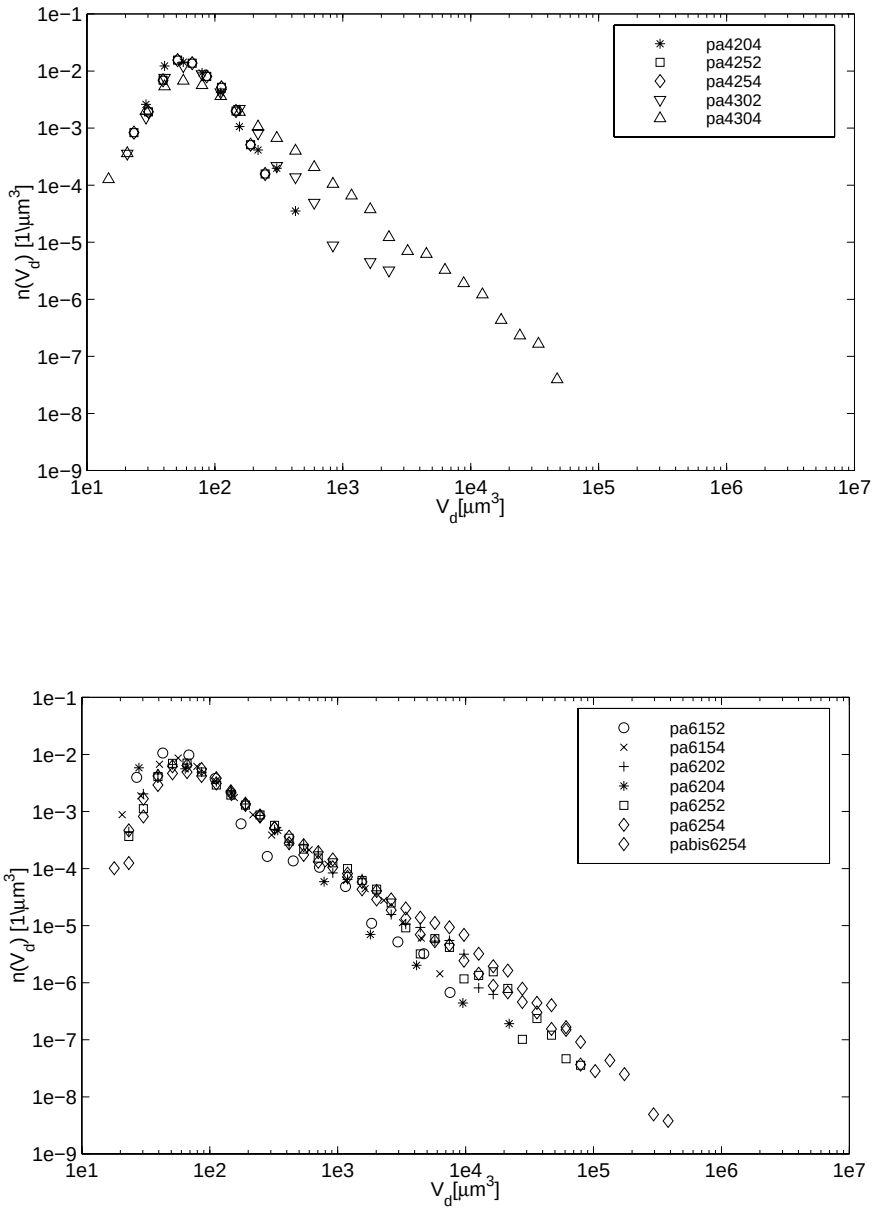

Figure 5.9: Probability density distribution of deformation volume, small scale 2-D blade, i=4° & 6 °

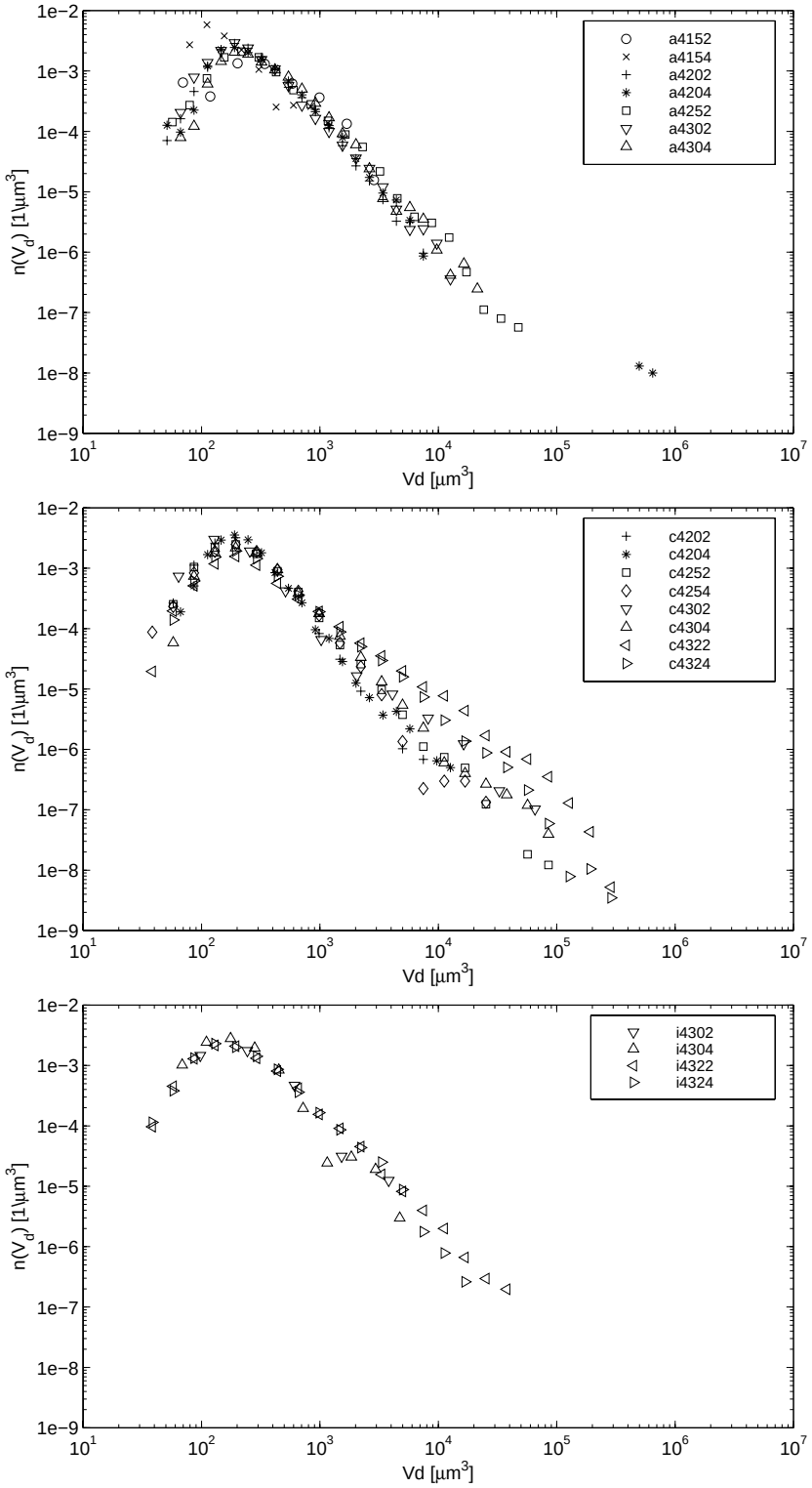

Figure 5.10: Probability density distribution of deformation volume, full scale 2-D blade, i=4°

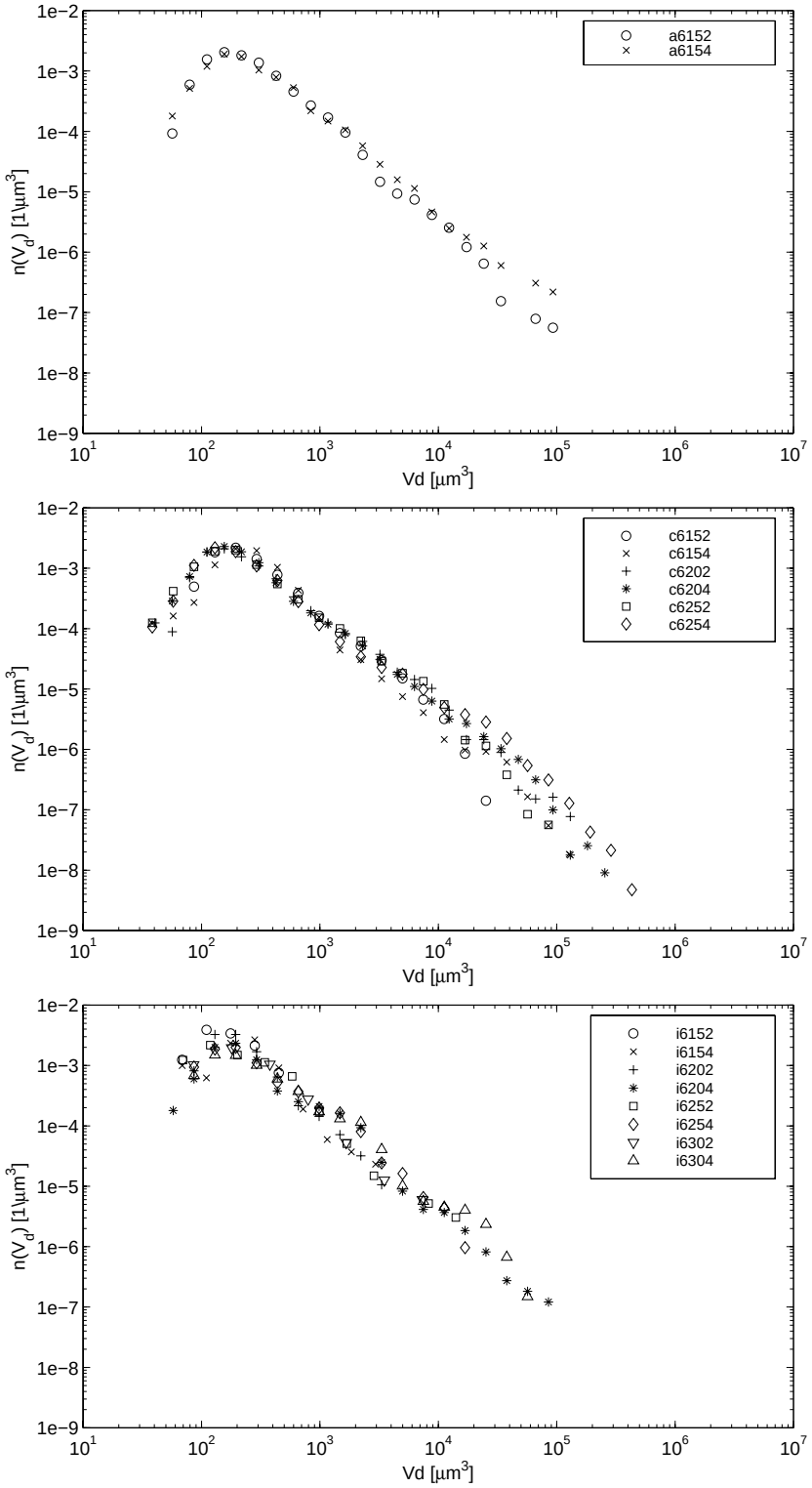

Figure 5.11: Probability density distribution of deformation volume, full scale 2-D blade, i=6°

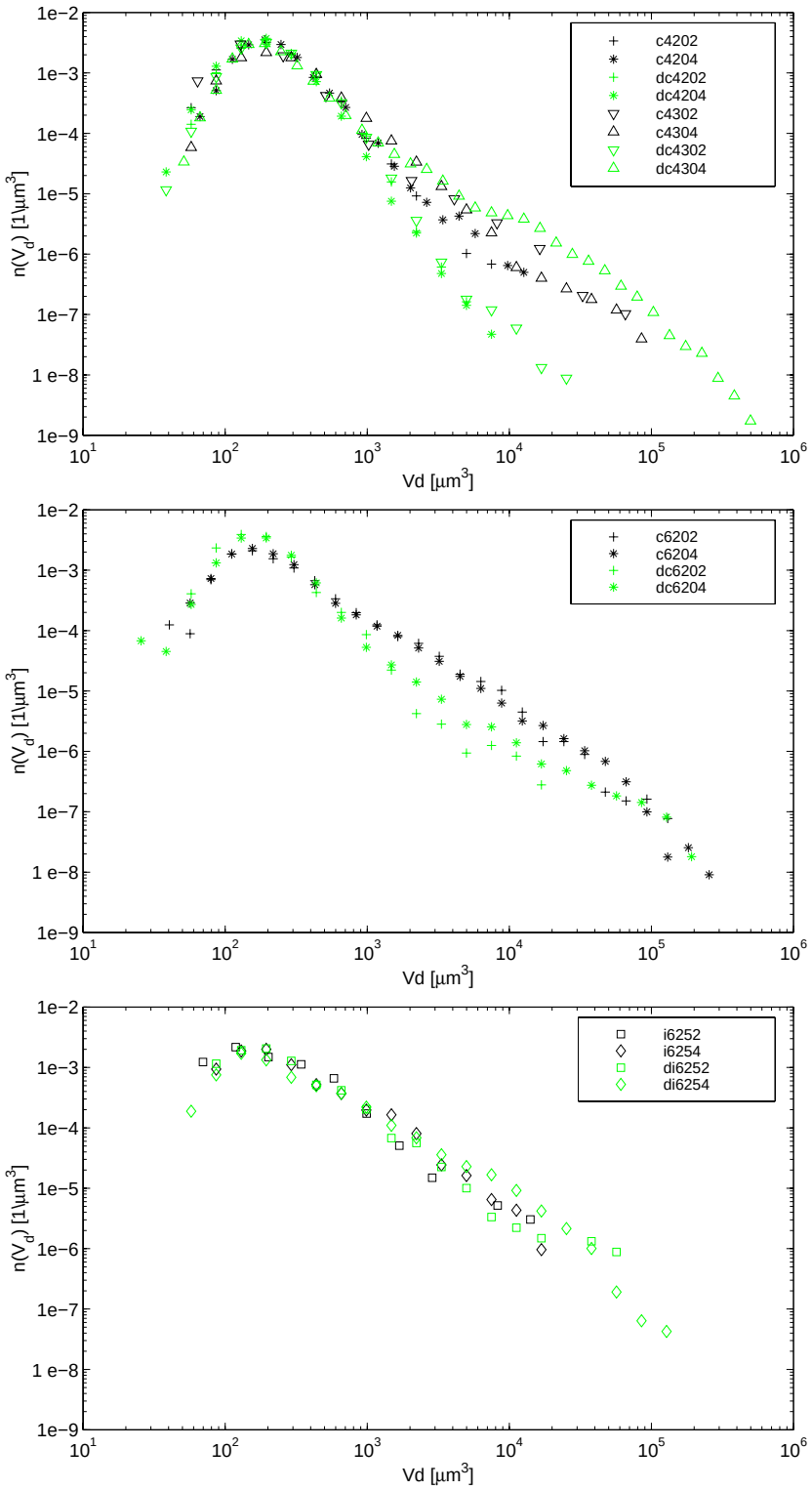

Figure 5.12: Probability density distribution of deformation volume, diverging test section, i=4° & 6°

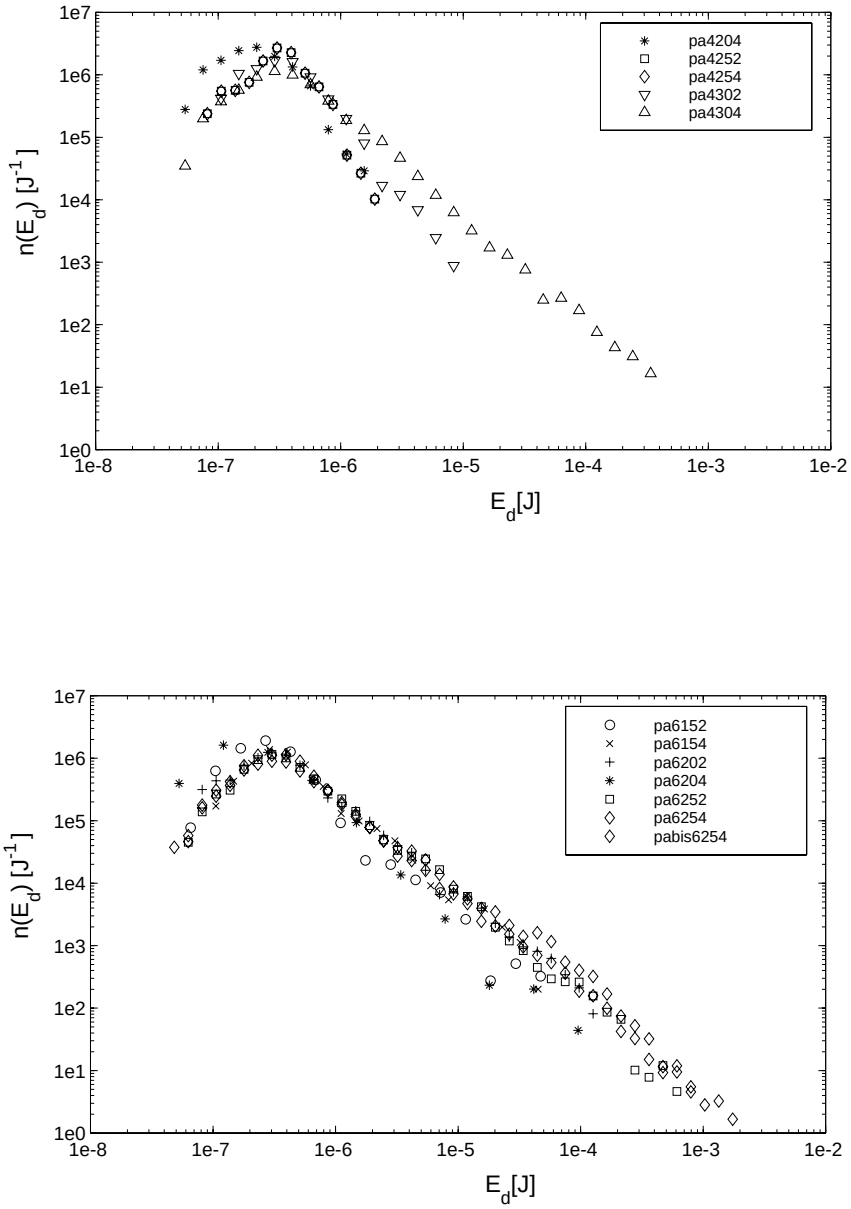

Figure 5.13: Probability density distribution of deformation energy, small scale 2-D blade, i=4° & 6°

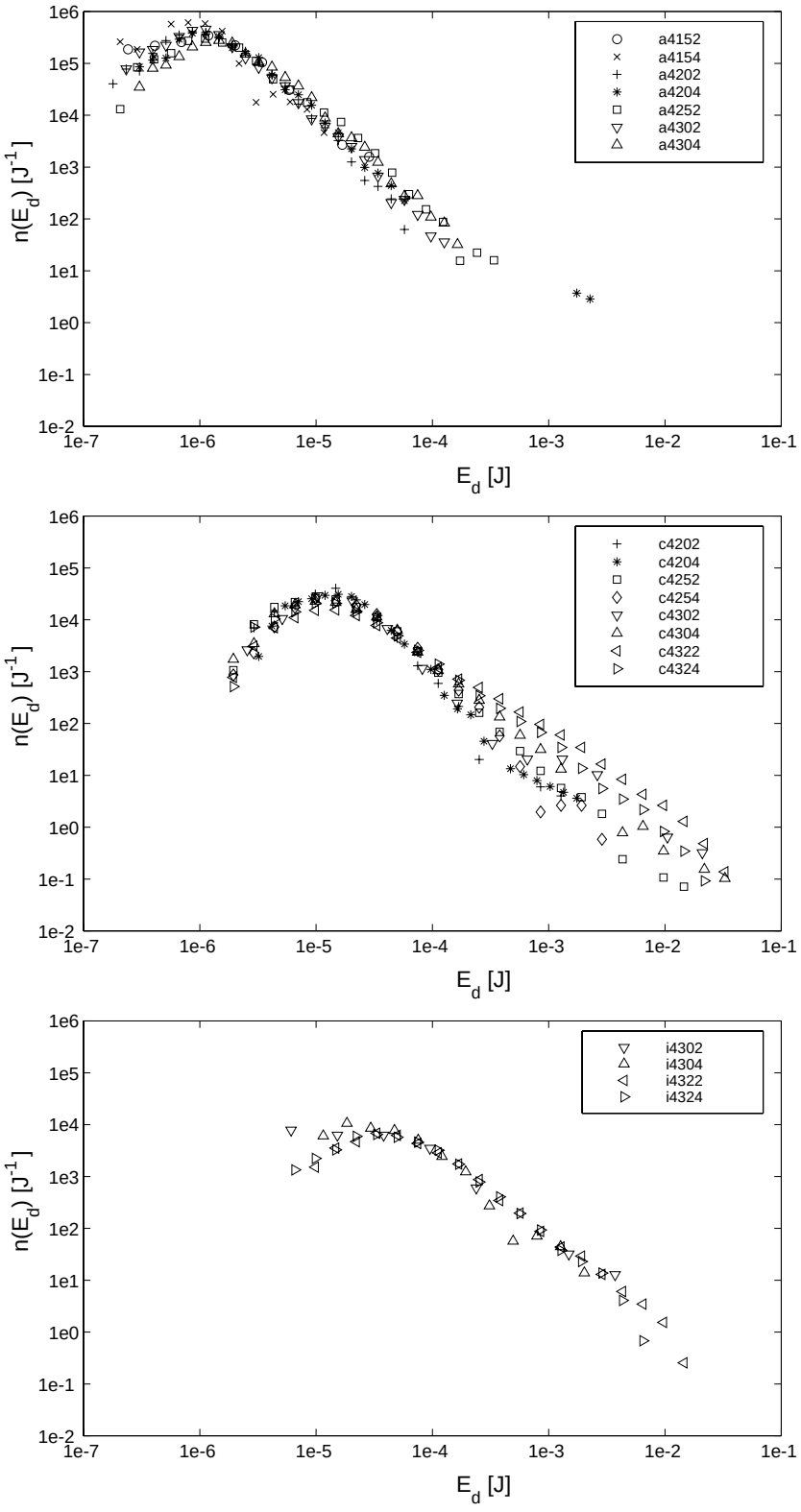

Figure 5.14: Probability density distribution of deformation energy, full scale 2-D blade, i=4°

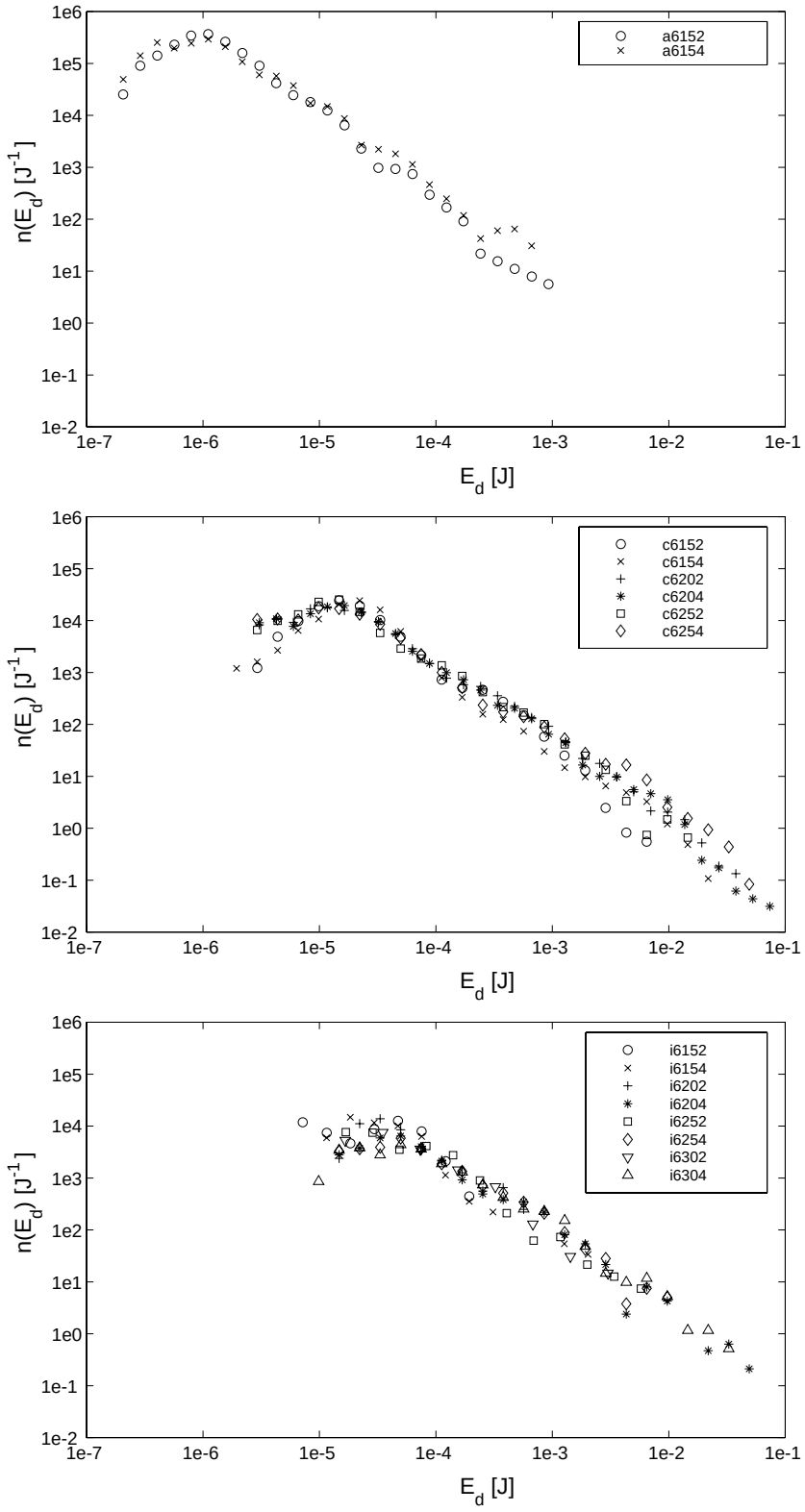

Figure 5.15: Probability density distribution of deformation energy, full scale 2-D blade, i=6°

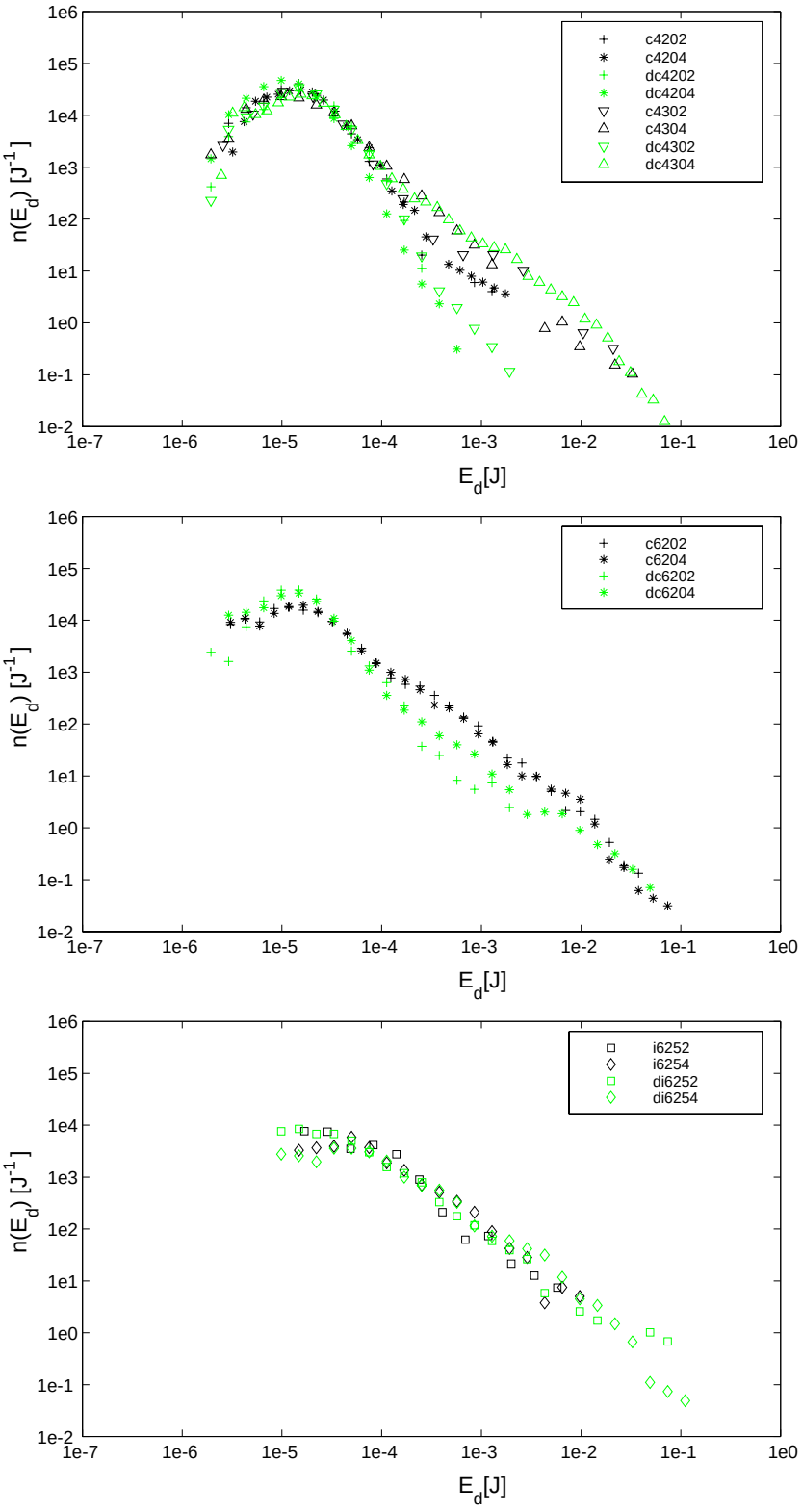

Figure 5.16: Probability density distribution of deformation energy, diverging test section, i=4° & 6°

5.4 Validation of the energetic model

5.4.1 Acoustic energy versus deformation energy

The method by which the deformation energy is calculated is briefly described. The dynamic response of various materials exposed to liquid jet and pressure wave impacts has been simulated by using an elasto-plastic solid model (Fortes-Patella & Reboud, 1998). It has been found that a high pressure wave emission is the main mechanism contributing to the observed cavitation damage. A parametric study of the pressure waves and corresponding impacts allows to obtain similarity laws. These laws allow the impact hydrodynamic parameters to be deduced from the pit geometric characteristics and the material properties. The energy of a spherical acoustic transient as derived by Cole (1948) is :

$$E_a = \frac{4\pi r^2}{\rho a_0} \int p dt \tag{5.7}$$

where p is the amplitude pressure of the wave and r is the distance of the wave epicentre. As it has already been mentioned in paragraph 2.4.2, the acoustic energy E_a associated to each impact is provided by the inverse fluid-solid model implemented in the software ADRESSE.
Furthermore, acoustic energies have been assumed proportional to the deformation energy of the impact denoted E_d.

5.4.2 Production rate of cavity energies

In an attempt to determine the collapse efficiency, it is required to estimate the production rate of vapour structures. A technique to measure the production rate of cavities has been developed in the field of work of Pereira (1997). The measurements are obtained by using a one-point beam laser technique. The principle of this method is based on the intensity measurement of a laser beam reflected on a polished sample, the beam being perpendicular to the surface sample at the closure wake region of the leading edge cavity. The light signal is measured with a fast photodiode, and the normalized extreme signal values obtained are one, if there is no cavity, and zero, if a cavity goes through the laser beam. Assuming a constant velocity of cavities, which has been taken to 0.6 C_{ref} , a time scale analysis of the signal by continuous wavelet transform (CWT) has been performed. This treatment allows us to calculate the production rate n_λ of cavity with longitudinal size λ_x. In addition, the cavity dimensions λ_y and λ_z, as well as the associated longitudinal dimension λ_x, are provided by stereometry measurements. The results demonstrate that an equivalent sphere diameter λ can be taken as λ_x.

For both the 4° and the 6° incidences, the statistical density has been expressed as:

$$\hat{n}(\lambda) = S_c \frac{C_{ref}}{\lambda^2} \ [m^{-1}s^{-1}] \text{ with } S_c \simeq 86.\ 10^{-3} \tag{5.8}$$

Afterwards, the energy production rate $\hat{n}(E_c)$ is derived as follows :

$$\hat{n}(E_c)dE_c = \hat{n}(\lambda)d\lambda \tag{5.9}$$

By considering the potential energy of cavity E_c defined in equation (1) :

$$\begin{aligned} E_c &= (p_{max} - p_v)V_c \\ &= \Delta p V_c \qquad (5.10) \\ \text{with } \Delta p &= \frac{1}{2}\rho(\sigma + C_{p_{max}})C_{ref}^2 \qquad (5.11) \end{aligned}$$

the relation (5.9) becomes :

$$\begin{aligned} \hat{n}(E_c) \ \alpha \ & \frac{\hat{n}(\lambda)}{\Delta p \lambda^2} \qquad (5.12) \\ \alpha \ & \frac{C_{ref}}{E_c \lambda} \qquad (5.13) \end{aligned}$$

and as,

$$\begin{aligned} V_c &= \frac{4}{3}\pi\lambda^3 \qquad (5.14) \\ \lambda \ \alpha \ & E_c^{\frac{1}{3}} \Delta p^{-\frac{1}{3}} \qquad (5.15) \end{aligned}$$

energy density can be finally expressed as follows :

$$\hat{n}(E_c) = K_o S_c C_{ref} \Delta p^{\frac{1}{3}} E_c^{-\frac{4}{3}} \ [J^{-1}s^{-1}] \text{ with } K_o = \sqrt[3]{\frac{\pi}{162}} \tag{5.16}$$

This distribution is different from the ones obtained by other researchers. Generally, they are described by classical probability laws, such as exponential laws (Hammitt, 1963; Kato *et al.*, 1978) or Weibull laws (Selim, 1985).

5.4.3 Collapse efficiency

The collapse efficiency is defined as being the ratio of $\hat{n}(E_d)$ and $\hat{n}(E_c)$ distributions. The number of cavities with the deformation energy E_d per time unit is obtained by multiplying the probability density distribution by the number of pits per second rate N_d :

$$\hat{n}(E_d) = N_d.n(E_d) \tag{5.17}$$

Experimental collapse efficiency is represented in figure 5.17 for the full scale 2-D blade with the 4° incidence, and in figure 5.18 for the 6° incidence. The characteristics of the collapse efficiency are the following :

1. The threshold volume of the profilometer measurement, which led to the underestimation of probability density distribution of deformation (V_d et E_d) for low energies, yield also low values of collapse efficiency for the low energies.
2. η_{co} is highly dependent on the flow conditions as well as on the material. The curves point out that η_{co} globally increases with C_{ref} , whatever the material be for a given angle of incidence.
3. The collapse efficiency decreases with the energy for moderate flow velocities (15–25 $m\ s^{-1}$) with aluminium and copper materials, especially for the 4° incidence conditions. It can also be noted that this tendency diminishes when the upstream velocity increases. This tendency is slightly noted for the 6° incidence conditions. This decay of the collapse efficiency can be explained by the lack of pit data for the largest pits, which results in a bias in the statistics for the corresponding pits. However, the low efficiency of the large cavities could also be explained by an hydrodynamic approach : the distance of the collapses from the leading edge cavity closure is increased for the largest cavities (and so the more energetic ones, considering the potential energy). Then, according to the collapse time given by Rayleigh (1917) (equation 5.18) and assuming a constant velocity for all cavities, which is a crude assumption, this distance is proportional to the maximum size λ_{max} reached by the cavity. Finally, it can be suggested that the more the distance from the cavity closure increases, the more the distance to the wall of the collapses increases as well, leading to a low collapse efficiency.

$$t_r = 0.91\lambda_{max}\sqrt{\frac{\rho}{p_{max} - p_v(T)}} \tag{5.18}$$

4. Lower collapse efficiency are generally obtained for the cavity length l_c =20% than for the one l_c =40%. This can be explained by the potential energy of the cavities. Assuming the larger the main cavity length is, the larger the shedding cavities are generated. Consequently, dissipated energy by cavitation is higher when the main cavity length is increased, and thus the cavitation aggressiveness is also increased.
5. Skipping the low energies (cut-off parameters) and high energies (lack of data), typical values of the collapse efficiency are the following :
   - η_{co} $\tilde{[}10^{-6}$–$5\ 10^{-4}]$ for aluminium specimens, i = 4° and C_{ref} =15–30 $m\ s^{-1}$;
   - η_{co} $\tilde{[}210^{-4}]$ for aluminium specimens, i = 6° and C_{ref} =15 $m\ s^{-1}$;
   - η_{co} $\tilde{[}10^{-5}$–$3\ 10^{-4}]$ for copper specimens, i = 4° and C_{ref} =20–32 $m\ s^{-1}$;
   - η_{co} $\tilde{[}210^{-4}$–$210^{-3}]$ for copper specimens, i = 6° and C_{ref} =15–25 $m\ s^{-1}$;

- η_{co} $\tilde{[}210^{-7}$–$10^{-5}]$ for stainless steel specimens, i = 4° and C_{ref} =30–32 $m\ s^{-1}$;
- η_{co} $\tilde{[}10^{-6}$–$210^{-4}]$ for stainless steel specimens, i = 6° and C_{ref} =15–30 $m\ s^{-1}$.

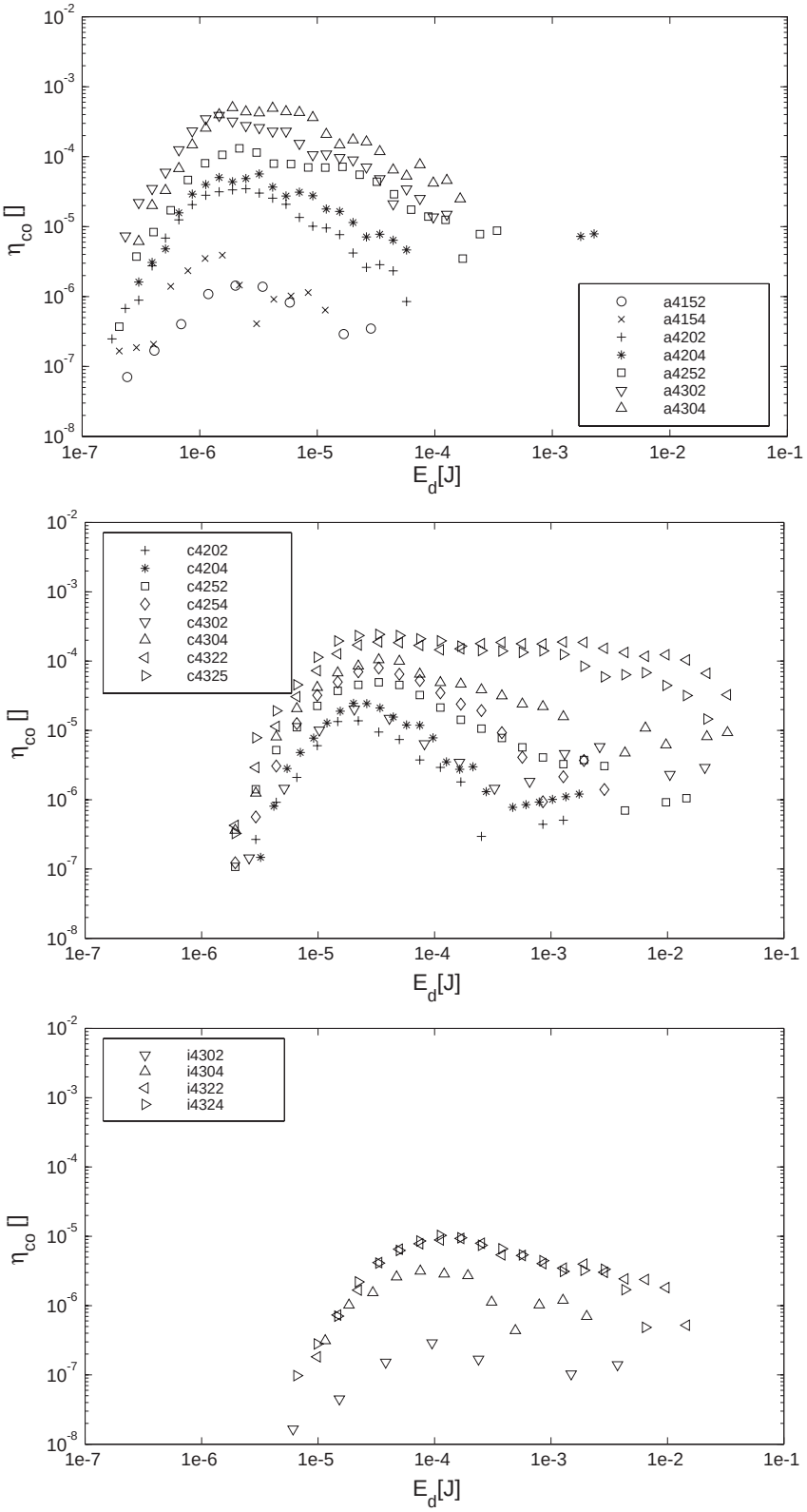

Figure 5.17: Collapse efficiency, full scale 2-D blade, i=4°

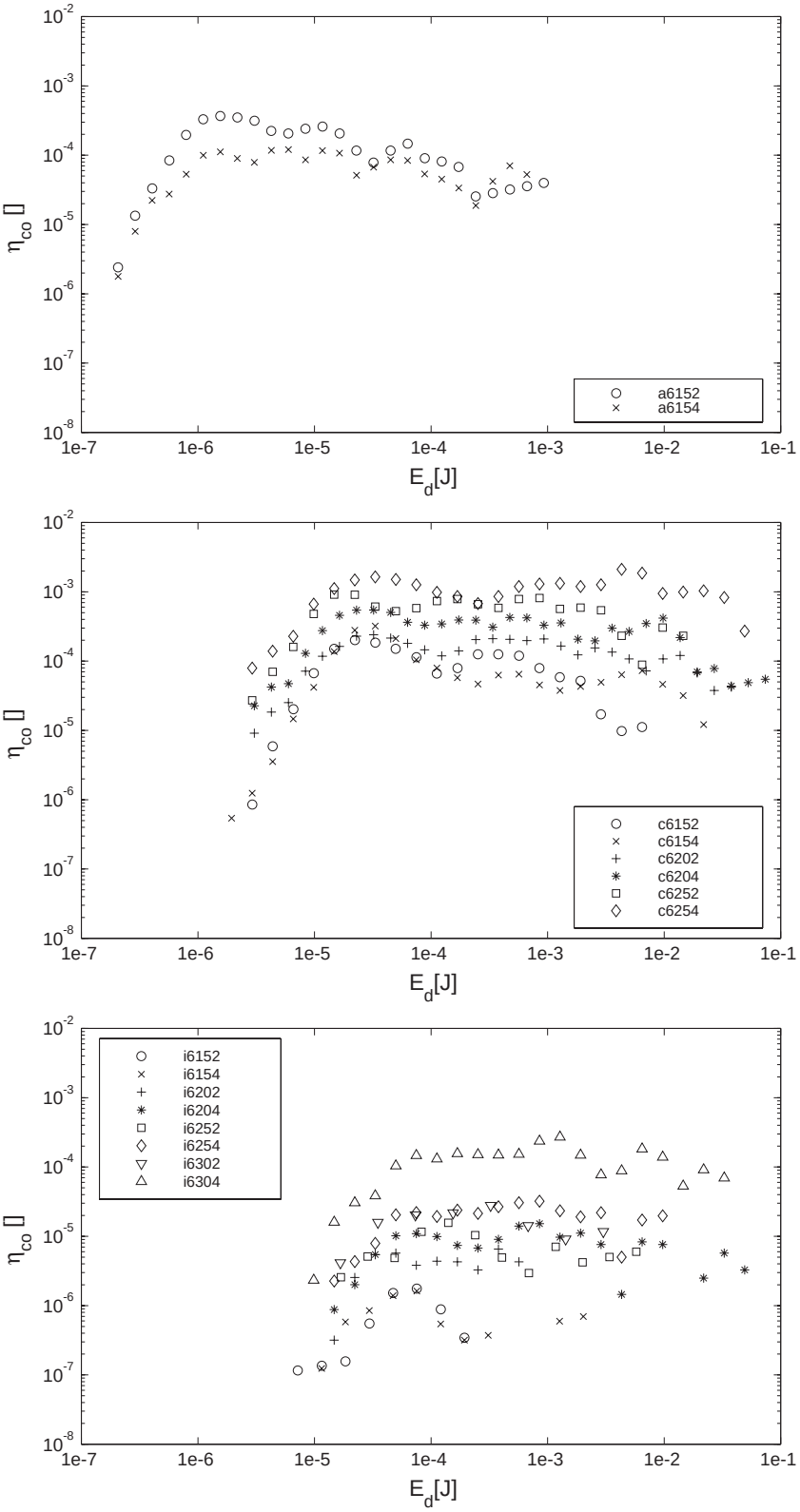

Figure 5.18: Collapse efficiency, full scale 2-D blade, i=6°

Chapitre 6

Synthesis

- The following general comments about pitting experiments can be made :
  1. Pitting results can strongly be biased by the lack of pit data for the largest indentations and by the lack of data caused by analysing a patched surface along the 2-D blade chord. This also confirms the requirement to perform several pitting tests for a same hydrodynamic condition with variable durations.
  2. Cut-off parameters of profilometry analysis yield a cut-off minimum volume. This leads to a bias in the statistics for the small volumes (and the low energies).
  3. It is highly desirable to obtain a repetitive leading edge cavitation detachment, from which instabilities can arise which can partly govern the generation process of vapour structures.
- On the basis of the 3-D profilometry results, which are completed by direct observations with the help of a microscope, it can be stated that :
  1. The stable mode of the leading edge cavity leads to impacts that are concentrated at the cavity closure and which are mostly non overlapping impacts.
  2. Concerning the unstable mode, impacts are more spread around the main cavity closure. Two families of impacts are observed in this mode : non overlapping impacts which are similar to those observed in the stable case, and much larger impacts which often are grouped.

  Therefore, 2 different kinds of cavitation attack can be suggested. On the one hand, if one considers the stable case, the vapour structures are created at the water-vapour interface (Avellan & Dupont, 1988), yielding vorticity lines due to Kelvin-Helmotz instabilities (Saffman, 1992). In that case, impacts are mostly non overlapping.
  On the other hand, if one considers the unstable case, the presence of large shed transient cavities yields larger multiple impacts.

- As to the tests in the diverging test section, it is striking that the cavitation aggressiveness is increased (up to a factor 10). As an explanation, the gradient pressure effect could be the cause of such a result. However, it is also evident that the global change of hydrodynamic flow and vorticity can induce the generation of more erosive vapour structures.
- The global energy transfer from the vapour structures to the material has been estimated with the collapse efficiency in the case of full scale experiments in the parallel test section. The collapse efficiency presents two main characteristics :
  1. The upstream velocity is the principal influencing macroscopic parameter for both the stable and unstable partial leading edge cavities. As an explanation, it can be argued that this result is due to the synergism of the pressure gradient driving the collapse and of the increasing of the circulation of the transient vortices. The potential energy of the cavity depends on the driving pressure, and the increasing of the circulation of vortices can lead the cavitation vortices to collapse closer to the wall.
  2. The collapse efficiency is quasi constant for the high flow velocities (30–32 $m\,s^{-1}$). This result is in good agreement with the previous works of Pereira (1997). However, when flow velocities are moderate (15–20 $m\,s^{-1}$), the collapse efficiency is lower for the high energies. Despite this characteristic could be explained by the lack of data for the largest pits, an hydrodynamic approach can be suggested. Assuming that the higher energies are related to the larger indentations and the larger vapour volumes, the corresponding collapse efficiency is lower. This could be due to the increase of the distance to the wall of the large cavity collapses, which take place more often in the far downstream region of the leading edge cavity closure due to the inertia of these large vapour structures.

Part III

Physical investigation of a single cavity collapse

Chapitre 7

Purpose

The aim of these experiments is to investigate the micro-hydrodynamic mechanisms involved in the final stage of a cavitation vortex collapse, as well as to determine the influence of macroscopic parameters of the flow. This study is divided into three parts :

- The reliability of determining the centre of collapses by using the luminescence phenomenon is evaluated. The idea of enhancing of luminescence emission by adding Argon gas is tested as well. On this purpose, luminescence is detected using an intensified video camera and a photomultiplier tube. By that means, luminescence is characterized in terms of occurrence, location, success rate and intensity for variable hydrodynamic conditions. Moreover, the sensitivity of the luminescence of the cavitation vortex to experimental parameters is also discussed.
- The complex physical characteristics of vapour structures and associated emitted shock waves are demonstrated using a high-speed shadowgraphy. The shock waves and vapour vortex boundary velocities are calculated using a suitable image processing.
- In order to determine the collapse time and observe whether the luminescence occurs with the production of the shock waves, simultaneous capture of the shock waves and the luminescence is achieved. Overpressures induced by the shock waves are estimated as well.

Chapitre 8

Luminescence of a cavitation vortex collapse

8.1 Measurement

8.1.1 Experimental protocol

Experiments are achieved in both the 2-windows test section and the 4-windows test section. The luminescence phenomenon is very sensitive to experimental parameters (Barber *et al.*, 1994). The latter might be not only the hydrodynamic parameter (driving pressure, vortex intensity,...), but also the dissolved gas and temperature. Therefore, in order to maintain the amount of dissolved gas in the water below an acceptable value, a degassing procedure is performed before each experiment. The measured dissolved oxygen (DO), which is measured with WTW OXI 340 at constant temperature, is then less than 2 $mg.l^{-1}$ for the duration of the experiments less than 2 hours. Typical increase of DO versus time for the nominal flow rate is graphically shown in figure 8.1. The temperature is kept constant at $14.5°C \pm 0.5°C$. The CVG is then run during a period of 15 minutes before the beginning of experiments, which gives the time zero of the experiment.

8.1.2 Vortex collapse detection

Since the collapse time cannot be predicted satisfactorily if the reference time is based on the valve closure, signal acquisitions as well as luminescence visualisations can be triggered on a threshold of the dynamic pressure signal. This is achieved owing to the slow pressure rise preceding the first sharp pressure peak. Considering the dynamic response of the pressure transducer, this provides a time scale resolution of 1 μs.

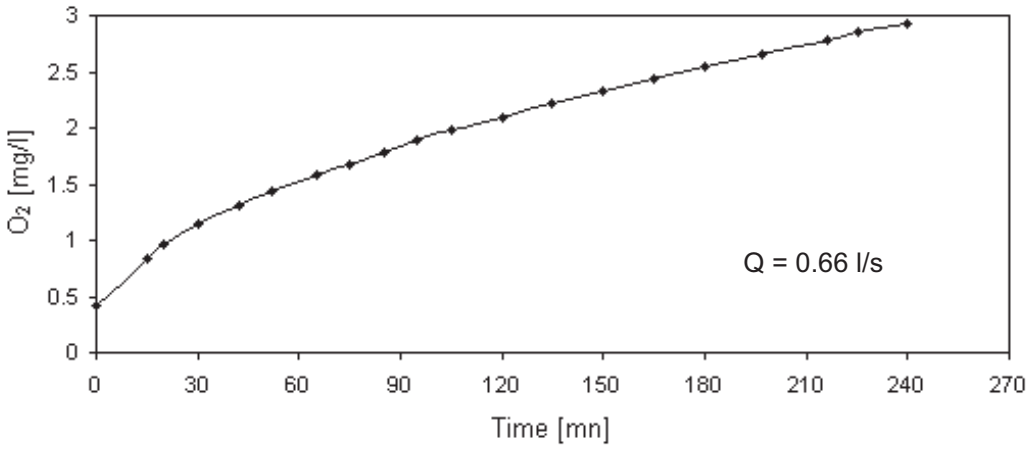

Figure 8.1: Dissolved oxygen versus time in CVG experiments
N=200 rpm, Q=0.66 l/s, σ=1.2

8.1.3 Image acquisition

Luminescence sources are visualised with the help of the intensified light camera (IC), either along the vertical axis for the 4-windows test section, like it is depicted in figure 8.2, or aligned with the horizontal optical axis of the 2-windows test section, like it is depicted in figure 8.8.
The image acquisition, whose synoptic diagram is presented in figure 8.2, can be described as follows :

1. The TTL signal delivered by the rotating valve position detector is connected onto the I/O data card of the PC, which is waiting for the valve closure.
2. The oscilloscope is asynchronously armed prior to the cavity collapse owing to a fast GPIB communication. At the same time, the frame grabber is asynchronously reset, in order to grab the next video field that will contain the luminescence information. At this step, the whole system is ready and waits for the collapse which is detected by the pressure transient.
3. When collapse occurs and thus the threshold of dynamic pressure is reached, the oscilloscope delivers an external trigger signal, which triggers the IC shutter at time t_{win} with the exposure time δt_{win}.
4. Time signals are retrieved by a GPIB data transfer from the oscilloscope to the PC, and the video frame containing luminescence is grabbed. The experiment is terminated when the number of desired successful visualisations is obtained.

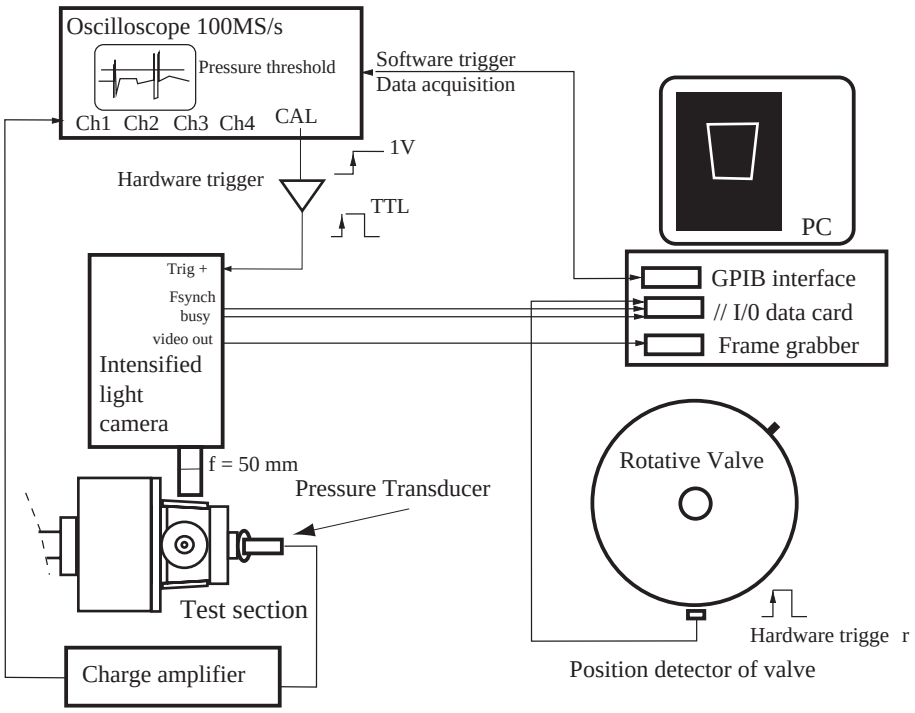

Figure 8.2: Schematic of the luminescence visualisations

8.2 Image processing

8.2.1 Luminescence characterization

Image processing is on-line performed during the experiments in order to record the global luminescence intensity. One must point out the interest of such a method. On the one hand, this allows time and memory mass (1.8 Mbyte/frames and 200 Kbyte/signal) to be saved in case of low luminescence detection due to false setting. On the other hand, this helps us for a rough appreciation of the number of acquisitions to be set. Real-time image processing of the acquired frame is performed during revolutions of the valve. As a first result of the procedure, visualisation is either validated or rejected. This is achieved by processing the image histogram, so that luminescence spots are detected if there is at least an intensity value of pixel which is greater than the upper limit of background noise. As an additional result of the procedure, validated images are superposed in order to record the global luminescence. The number of rejected images is also taken in consideration in order to calculate the success rate of the luminescence detection, and the global representation of luminescence pattern is immediately available through the superposed image.

8.2.2 Superposition of visualisations

The global representation of the statistical location of luminescence emission is obtained by superposing the images through a suitable threshold operation, which allows the luminescence spots to be segregated from background noise.

Firstly, one applies the threshold operation to each acquired image with a threshold value higher than the upper limit of background noise pixel intensities. A typical intensity histogram of the image with luminescence is given in figure 8.3. One must note that the background noise is increased with long time exposure and high electric voltage of the IC. Nevertheless, most background noise can be cut off by setting a suitable video black level threshold of the frame grabber digitiser. Moreover, a second threshold cut-off is adjusted in the image processing program in order to eliminate the residual noise in a more adapted manner.

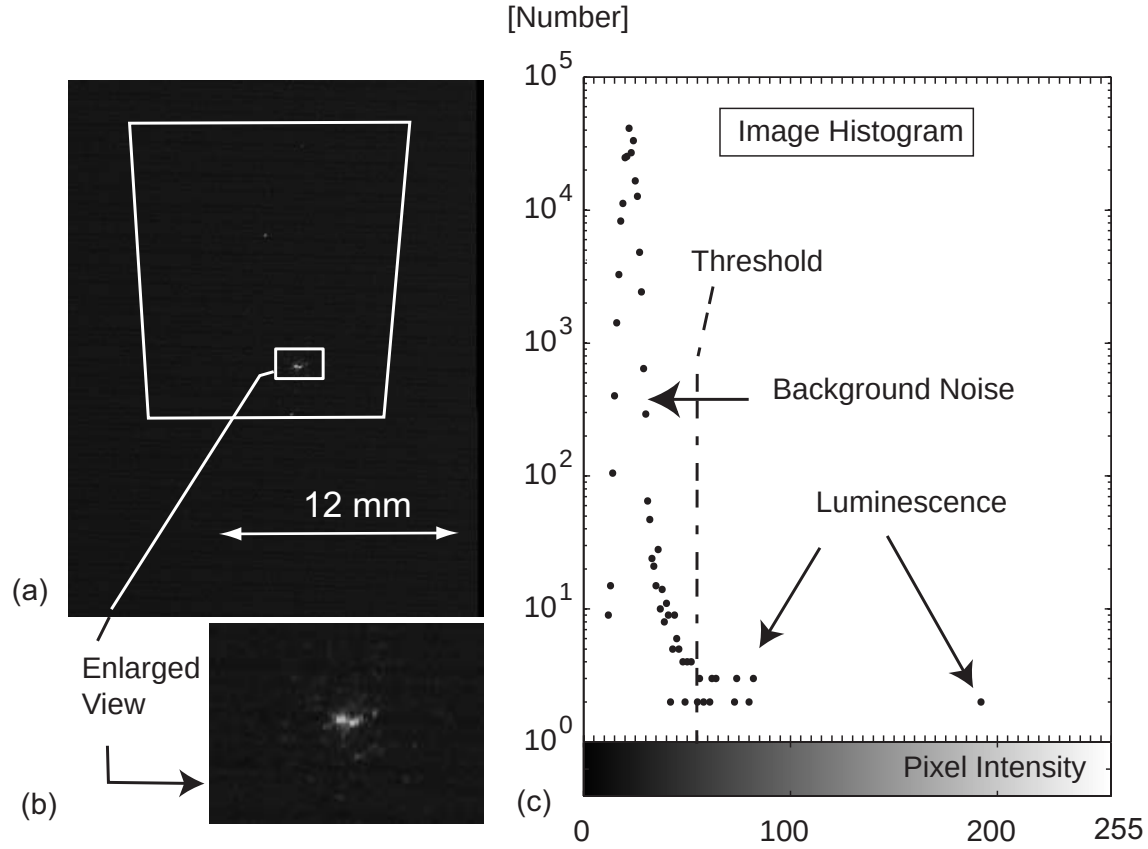

Figure 8.3: (a) Image of the luminescence in the test section drawn in white.
(b) Enlarged view of the luminescence. (c) Image histogram.
N=120 rpm, Q=0.66 l/s, σ=1.2

Secondly, the resulting threshold operation defines a binary mask, where the non-zero values of the mask correspond to the image pixel values that are greater than the defined threshold. This mask is then applied to the original image : pixel values outside the mask are set to 0, and values of validated pixels are down-shifted from the threshold value.

Finally, images are superposed by performing a simple addition. The resulting image is scaled to 255 values.

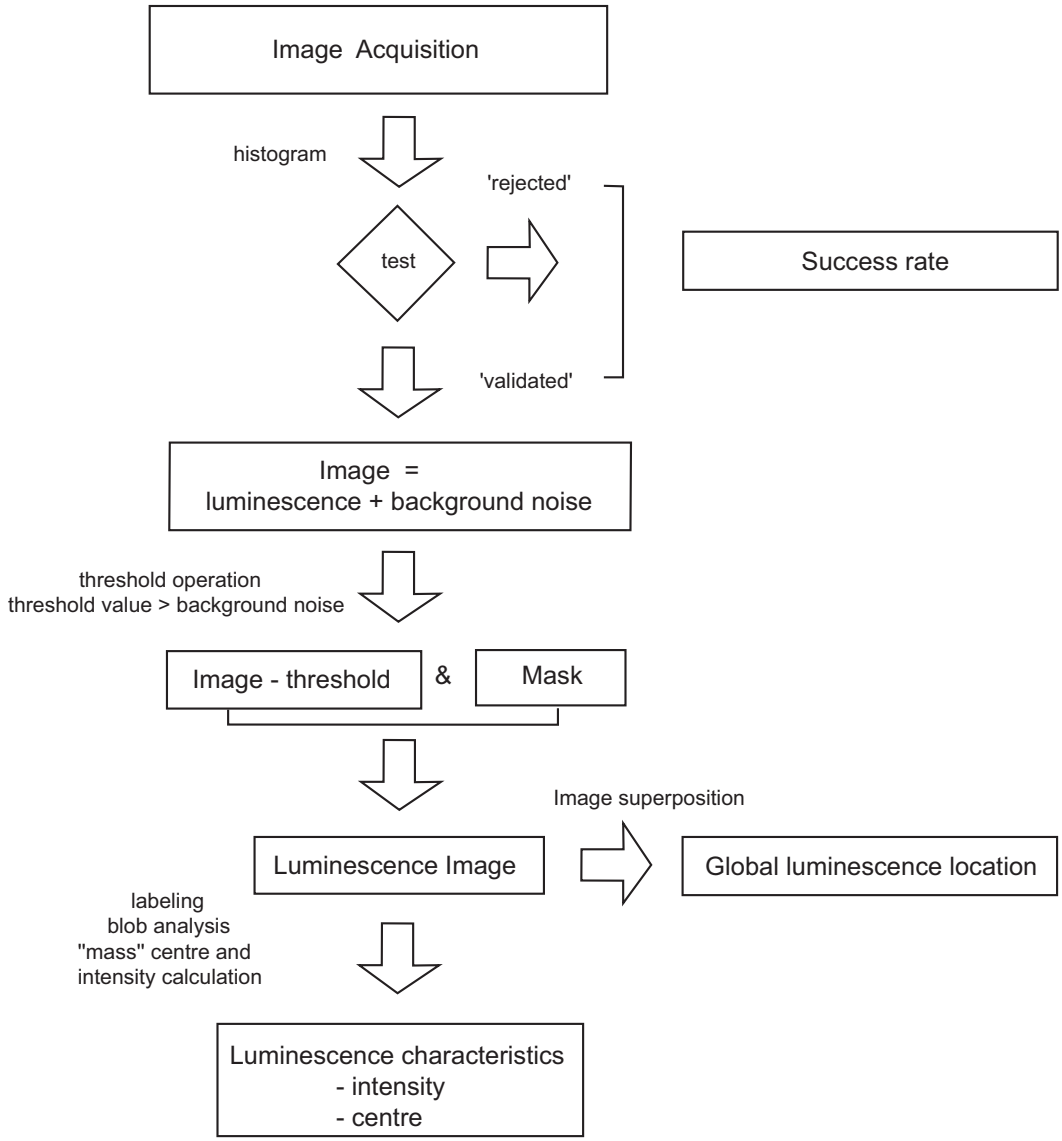

Figure 8.4: Luminescence detection and image processing

8.2.3 Blob analysis of luminescence pattern

In order to study each luminescence images in detail, a labelling of luminescence spots is performed.
Labelling is achieved on binary masks, which are obtained by a zero threshold operation on images. Spatial "mass" centre of each binary entity (luminescence spots) is then calculated by taking the corresponding original pixel values as virtual weight masses. The sum of pixel values for each luminescence entity is attributed to each centre and is defined as the luminescence intensity of the luminescence entity. A summary of the whole image processing procedure can be depicted by the diagram in figure 8.4.

8.3 Preliminary study

8.3.1 Driving pressure

In order to characterize the actual driving pressures in CVG test section, cavitation free condition is obtained by setting the whole circuit at 16.6 bar static pressure.

An example of the obtained response of pressure transducer is illustrated in figure 8.5. The zero time corresponds to the recovering pressure peak on which the signal acquisition is triggered. The generated low-pressure wave which causes the vapour appearance is followed by the recovering pressure peak driving the collapse. Moreover, the presence of pressure oscillations which are due to generated acoustic waves in the circuit are also presents.

In the second example presented in figure 8.6, the flow rate and valve rotation speed are kept constant, but the low-pressure vessel is set at atmospheric pressure. Cavitation collapses are identified by sharp peaks in time signal, and the amplitude of the first sharp peak is generally the highest one. The presence of oscillating acoustic waves in the circuit, whose velocity is increasing as the amount of vapour phase in the circuit decreases, can be identified by smooth pressure transient.

Time signals corresponding to other hydrodynamic conditions have been studied as well. It appears that the pressure signal signature is very complex and is highly influenced by the set of hydrodynamic conditions Q, N and σ (example of the condition Q = 0.66 l/s and N = 120 rpm is given in figure 8.9). Nevertheless, the principal characteristics of pressure signal remain the same.

8.3.2 Vortex collapse time jitter

As an important characteristic of the cavitation vortex time history, times of appearance and collapse of the cavitation vortex cannot be predicted with an accuracy

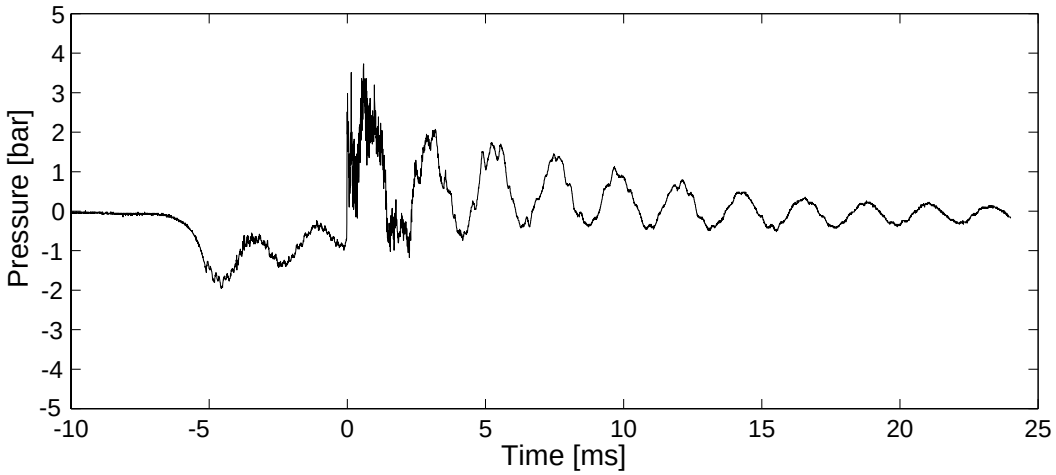

Figure 8.5: Dynamic pressure signal, cavitation free condition
N=200 rpm, Q=0.66 l/s , σ=11.4

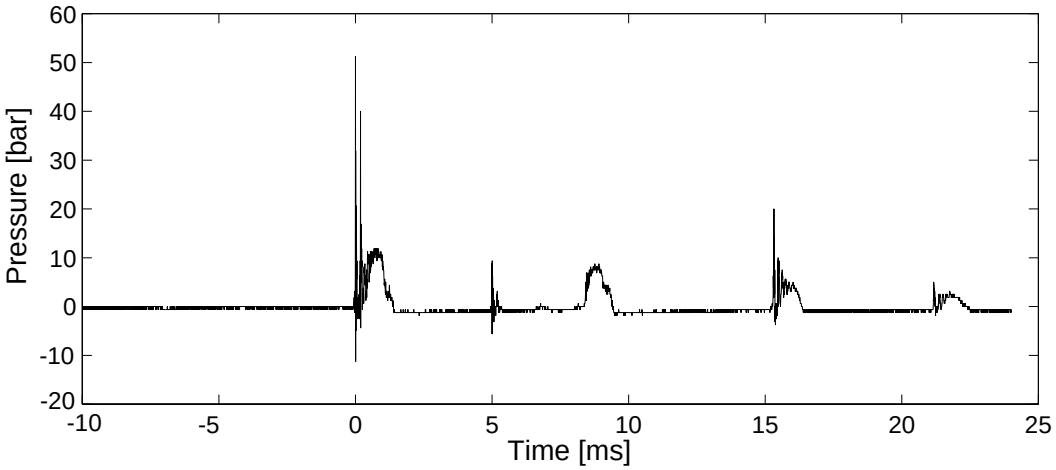

Figure 8.6: Dynamic pressure signal, cavitation condition
N=200 rpm, Q=0.66 l/s, σ=1.2

better than few milliseconds. This characteristic is demonstrated by considering the time intervals between the valve closure (positive edge of TTL signal) and the first pressure peak. Measured time intervals as well as the associated amplitudes, are given on graphic in figure 8.7. The corresponding independent visualisations of the cavitation vortex are given in figures 8.11 and 8.12. These visualisations have been obtained with the IC with a fixed exposure time of 10 μs and by setting different delays from the valve closure.

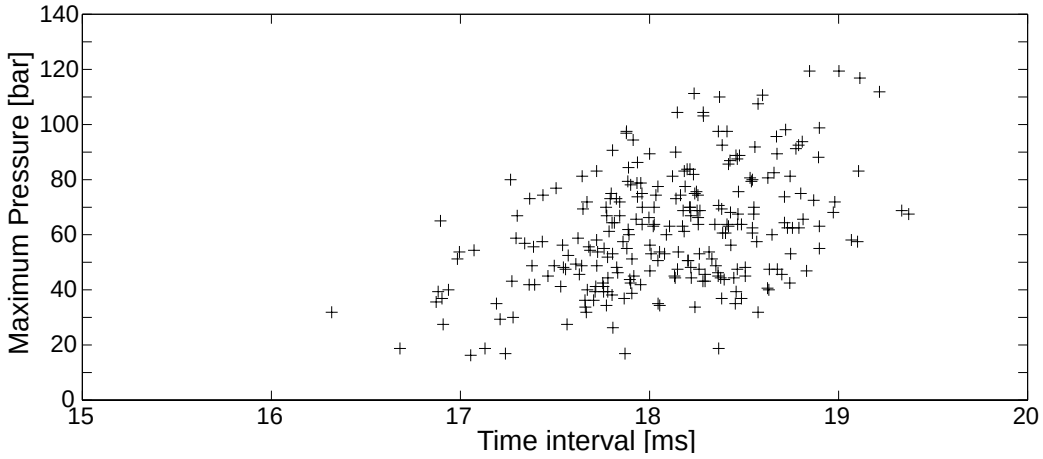

Figure 8.7: Jitter of the collapse time, N=200 rpm, Q=0.66 l/s, σ=1.2

8.3.3 Detection of luminescence bursts

Simultaneous detection of photons and visualisation of luminescence sparks have been performed for a single hydrodynamic condition in the 2-windows test section : N = 120 rpm, Q = 0.66 l/s, and $\sigma = 1.2$.
It has to be noted that the measured luminescence with the photomultiplier tube (PMT) and the IC depends on the path length through the liquid, the window material and the response of the detector. The PMT and the IC are aligned with the optical axis of the 2-windows test section as depicted in figure 8.8. It must be noted that no focusing lens is coupled with the PMT. Shielding from light has been made in order to avoid environmental light background noise. Photon signal units are given in volts. However, as the system is not calibrated, the signal amplitude has only a qualitative significance.

A single of 80 mm focal length, 20 mm in diameter lens is used to focus the image on the IC. The obtained image resolution is 40 microns $\times$ 77 microns. Although a limited exposure time of the IC has to be set in order to limit the electronic background, the exposure time is fixed to a maximum of 20 ms, and the electric voltage is fixed to its maximum value (G = 1000 V) in order to maximize the detection. The beginning of the light integration corresponds to the valve closure.

The detection of photons is focused on the first peak of the pressure signal, to which the time t_{max} is associated. Taking the reference time as $t_{max} = 0$, photons pulses are clearly observed within the time interval [-4.5 μs, -2 μs] (18 samples), and thus prior to the maximum pressure peak. The luminescence is emitted as short time duration sparks, which are not unique. The luminescence peaks are either individuals (time width lower or equal to sampling resolution 10 ns) or grouped with a variable

width from 10 ns to 100 ns. These observed short pulses are consistent with the tens of picoseconds pulses observed in a sonoluminescent bubble excited by acoustic waves (Barber & Putterman, 1991/92). Other photons are emitted after the first pressure peak, but their occurrence is more randomly distributed with time. Examples of typical signals are given in figures 8.9 and 8.10.

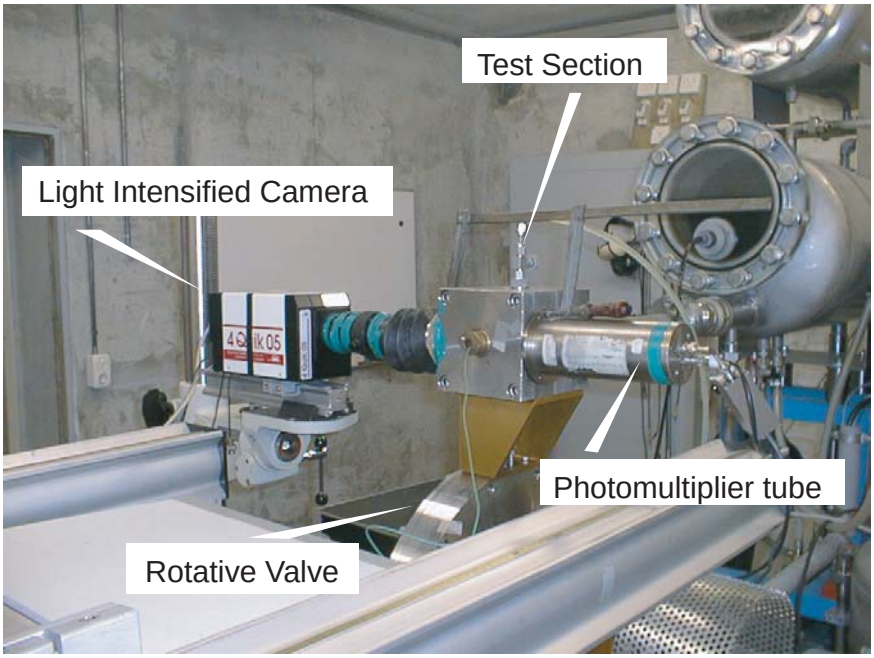

Figure 8.8: PMT and IC with the 2-windows test section

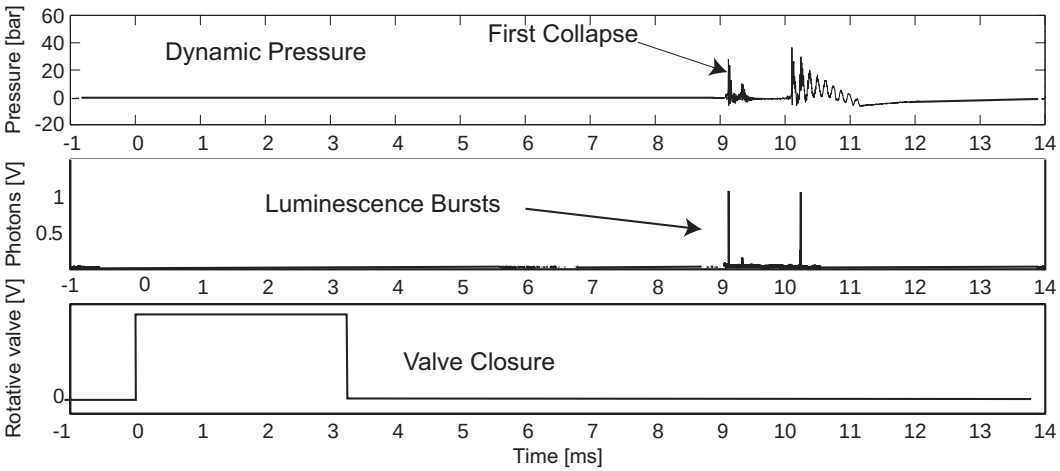

Figure 8.9: Valve, pressure and photons signals, N=120 rpm, Q=0.66 l/s, σ=1.2

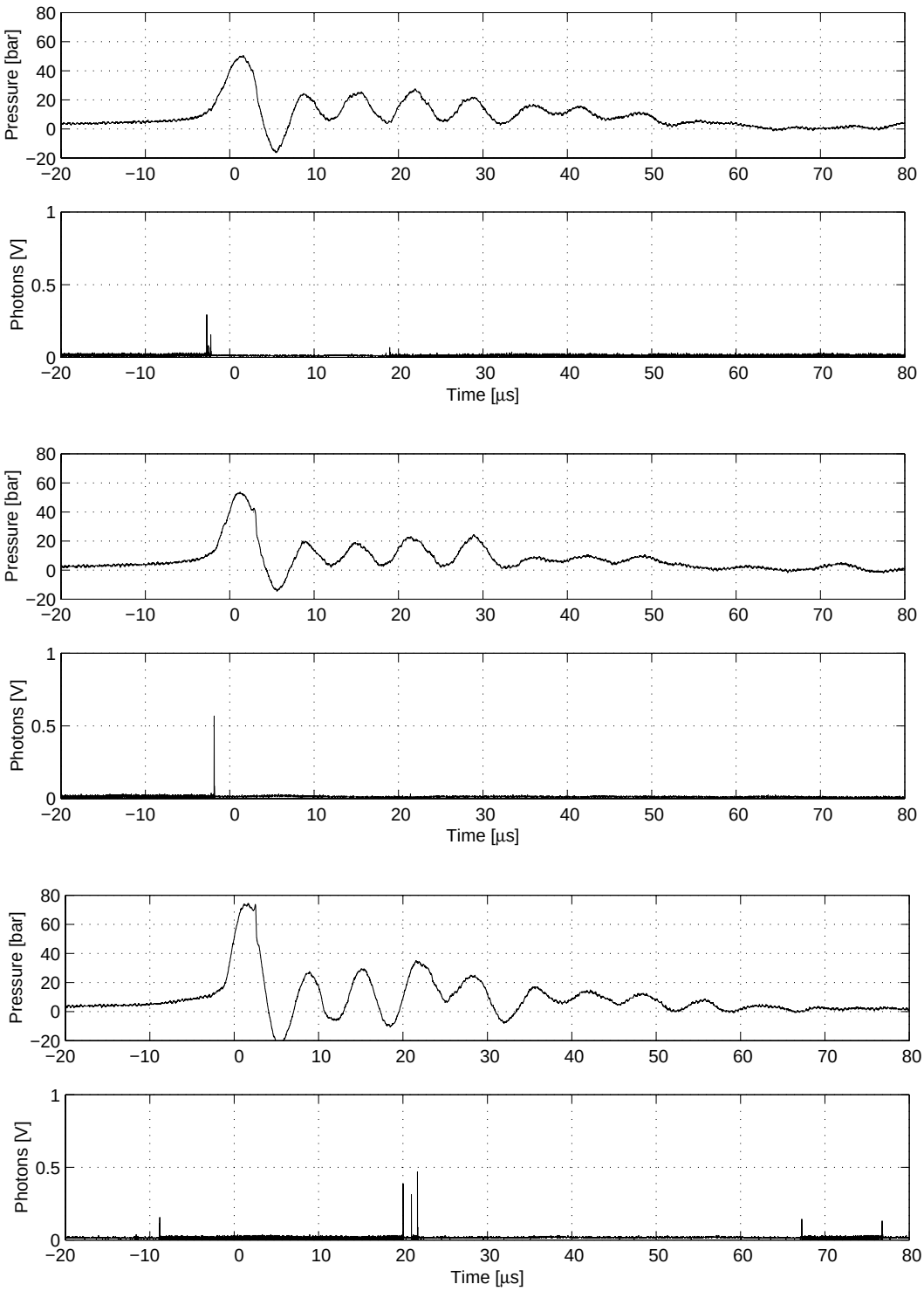

Figure 8.10: Photons emission at the main collapse
N=120 rpm, Q=0.66 l/s, σ=1.2

Figure 8.11: Images of cavitation vortex from different time intervals after the valve closure, N=200 rpm, Q=0.66 l/s, σ=1.2

Figure 8.12: Images of cavitation vortex from different time intervals after the valve closure, N=200 rpm, Q=0.66 l/s, σ=1.2

8.3.4 Effect of Argon gas injection

Assuming that doping the circuit with Argon gas could enhance luminescence phenomenon (Lohse & Hilgenfeldt, 1997), a continuous Argon flow rate is provided for the circuit after being initially degassed.

As a main result, it appears that the number of luminescence peaks has substantially increased, especially during the first 20 μs following the maximum pressure value. An example of a luminescence spark with the corresponding time signals is presented in figure 8.13. Nevertheless, due to the rotation speed of the valve N = 120 rpm, the tested hydrodynamic condition presents a peculiar pressure signature, compared to the one obtained with N = 200 rpm.

In short, luminescence is enhanced by additional Argon gas. However, the luminescence emission with natural dissolved air is sufficient to detect cavitation vortex collapses (Couty *et al.*, 1999).

To illustrate the global representation of luminescence sources with Argon gas injection, the superposition of 50 collapses is represented in figure 8.14, where the test section contour is drawn in white. From the obtained luminescence pattern, it can be noted that light spots are present outside the test section zone. This can be caused by parasitic reflection of glass test section, a bad focus of photons due to optical defect of the lens, or the noise generated by a long exposure time. This also point out the need for high quality optics with limited light losses and parasite reflections.

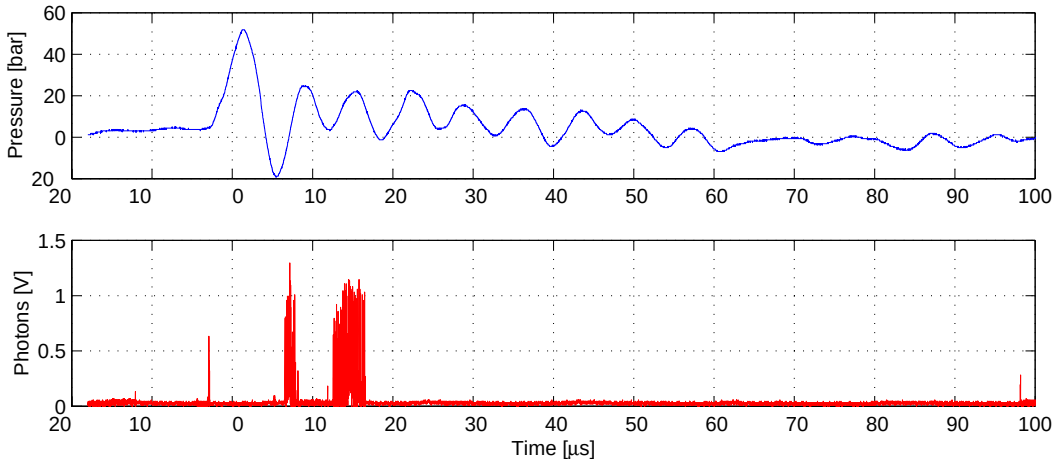

Figure 8.13: Photons emission with Argon gas injection
N=120 rpm, Q=0.66 l/s, σ=1.2

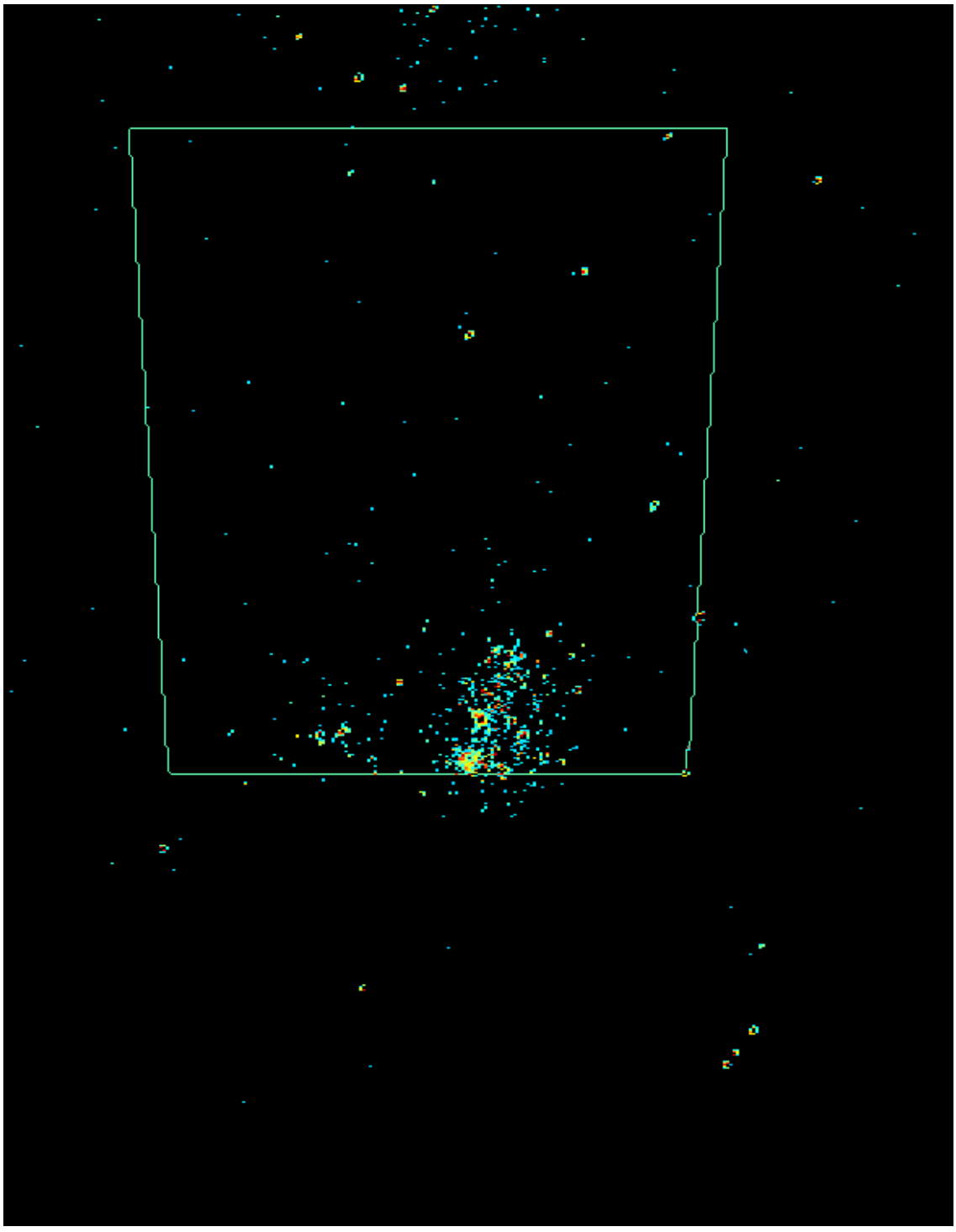

Figure 8.14: Superposition of 50 collapses with Argon gas injection
N=120 rpm, Q=0.66 l/s, σ=1.2

8.4 Luminescence of the cavitation vortex

8.4.1 Hydrodynamic conditions

The parametric study of luminescence phenomenon is performed in the 4-windows test section. Corresponding results are established on data obtained with five selected different runs. Purposes and conditions can be summarized as follows :

- Determination of the collapse time by varying the shutter delay and the exposure time :
  run# 1 ;
  N = 200 rpm, Q = 0.66 l/s, and $\sigma = 1.2$.
- Luminescence intensity and success rate obtained by varying the electric voltage of the IC :
  run# 2 ;
  N = 200 rpm, Q = 0.66 l/s, and $\sigma = 1.2$.
- Luminescence drift caused by an increase of dissolved air in water :
  run# 3 ;
  N = 200 rpm, Q = 0.66 l/s, and $\sigma = 1.2$.
- Influence of the flow rate on luminescence characteristics and on collapse centres :
  run# 4-5 ;
  N = 200 rpm, Q = 0.58 l/s, and $\sigma = 1.6$;
  N = 200 rpm, Q = 0.66 l/s, and $\sigma = 1.2$;
  N = 200 rpm, Q = 0.76 l/s, and $\sigma = 0.9$.

Special care has been paid to the stability and repeatability of experimental conditions. Indeed, the low pressure vessel $p_2 = 1.04$ bar is maintained at atmospheric pressure in order to avoid any fluctuations due to sigma regulation.

8.4.2 Occurrence of luminescence in cavitation vortex dynamics

Around the main collapse

In order to detect luminescence at the principal collapse (first peak in pressure signal), and at the following few 100 μs, synchronization of visualisations is achieved at different delays t_{win} from zero time reference given by the pressure threshold. Time delays as well as time exposures are adjusted so that they correspond to different peak events in pressure signal (see signal in figure 8.6). The electric voltage of the IC has been set to the maximum G = 1000 V in order to maximize the amount of detected photons. Example of obtained luminescence patterns, as well as the view of the test section with ambient light, are illustrated by superposed collapses in figure 8.15. Associated

success rates, luminescence intensity and source emission coordinates, obtained by image processing, are given in table 8.1. The median operator is used as an estimator of the central value of the statistical distribution of the luminescence location. Median distance along the X test section axis is denoted X_{median} (median wall distance) and median distance along the Y test section axis is denoted Y_{median}. Moreover, the distance from the test section origin is denoted $D = \sqrt{X^2 + Y^2}$.

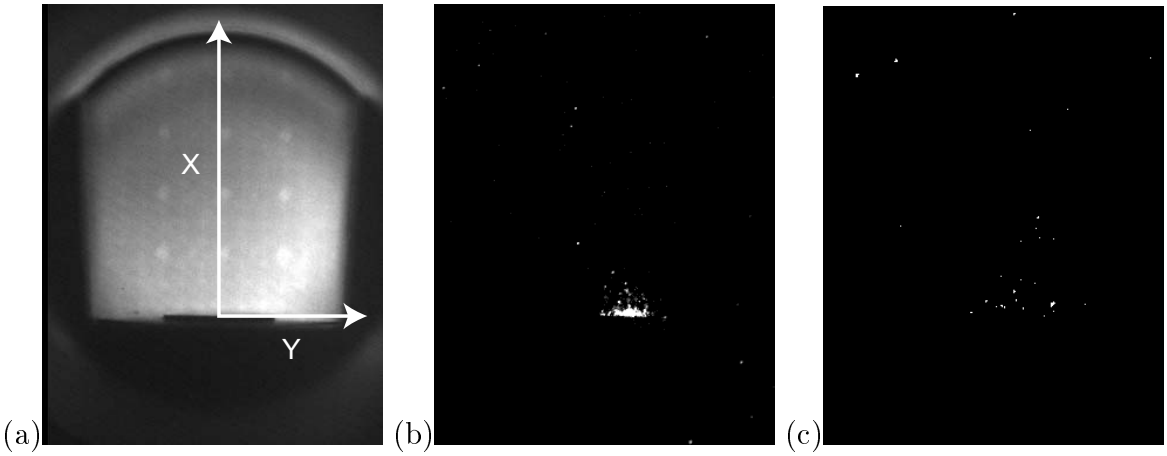

Figure 8.15: Visualisations of luminescence for variable time windows, (a) view of the test section with axis, (b) time window $[0\ \mu s, 10\ \mu s]$, (c) time window $[100\ \mu s, 300\ \mu s]$
Run# 1 : N=200 rpm, Q=0.66 l/s, σ=1.2

t_{win}	δt_{win}	Success rate	Mean Intensity	X_{median}	Y_{median}
0 μs	10 μs	193/263	763	0.28 mm	0.81 mm
10 μs	10 μs	8/178	372	10.2 mm	0.25 mm
20 μs	10 μs	4/152	24.5	0.55 mm	-6 mm
30 μs	100 μs	-	-	-	-
100 μs	300 μs	25/110	210	1.51 mm	0.86 mm

Table 8.1: Luminescence characteristics for variable time windows of interest
Run# 1 : N=200 rpm, Q=0.66 l/s, σ=1.2, G=1000 V

Visualisations and image processing results show that luminescence is principally emitted during the first 10 μs, with a source emission situated very close to the end wall of the test section. A weak luminescence is detected at time window [100 μs, 300 μs], but no clearly preferred emission source location is noted. As it will be demonstrated in the chapter 9 dealing with high-speed visualisations, this second luminescence occurrence peak can be related to observed weak and unpredictable secondary vapour cavity collapses.

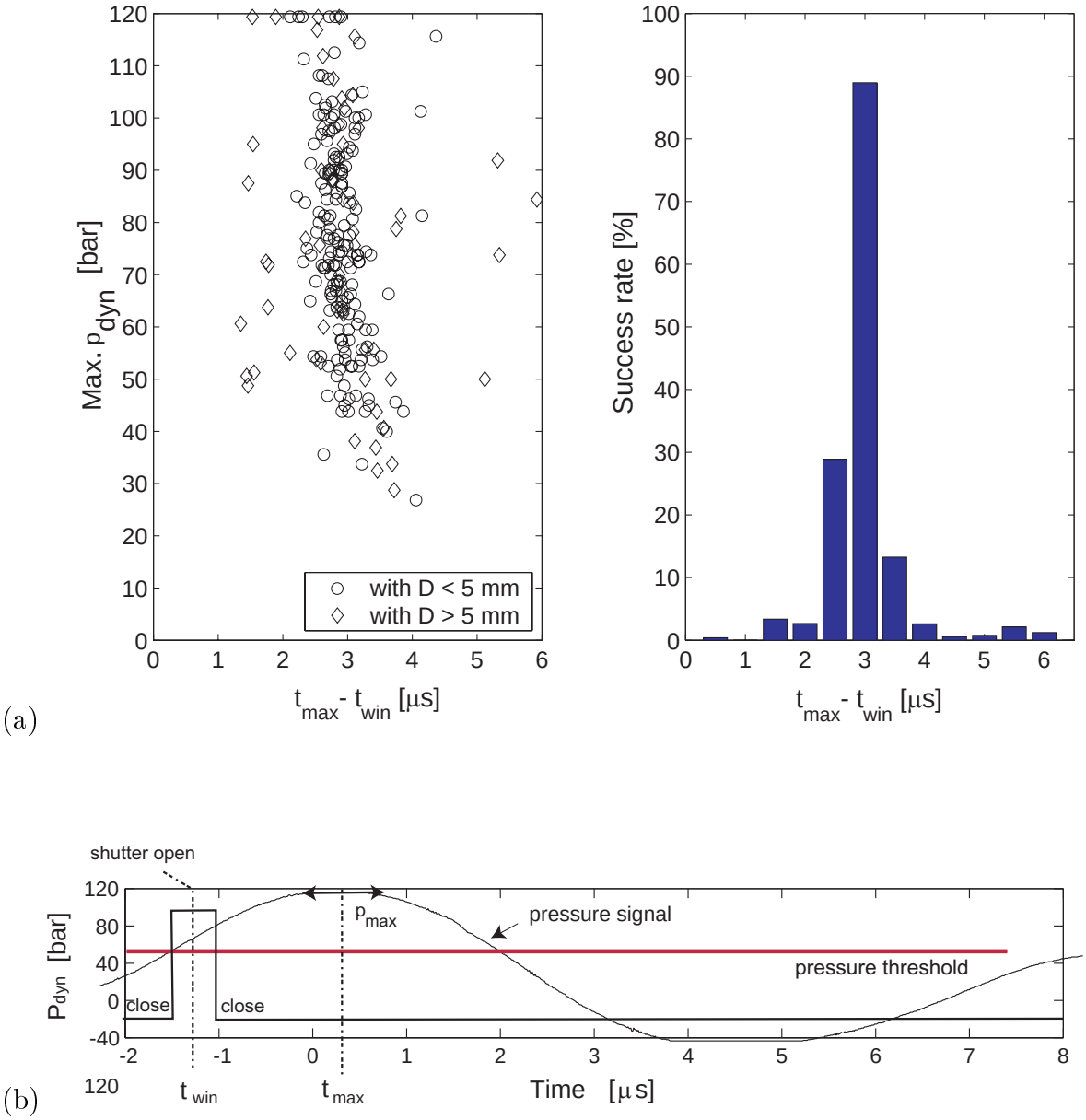

Figure 8.16: (a) Luminescence intensity and success rate versus $t_{max} - t_{win}$. (b) Shutter and dynamic pressure signals. Run# 1 : N=200 rpm, Q=0.66 l/s, σ= 1.2

Main collapse

Time occurrence of luminescence sparks is determined by varying the shutter delay t_{win} with a fixed exposure time $\delta t_{win} = 500\ ns$: time occurrence is deduced from the maximum success rate of luminescence events for the specific time interval $t_{max} - t_{win}$. A total of 268 luminescence spots are obtained on the basis of 3'052 visualisations

during the same run# 1. The maximum electric voltage of the IC is G = 1000 V. Results are shown in figure 8.16. Max.P_{dyn} is the maximum value of the pressure peak. This experiment reveals that the maximum success rate of detected luminescence is obtained at about $t_{max} - t_{win} = 3\ \mu s$.

As a conclusion, assuming that the pressure signal gives a reference of the cavitation vortex history with a time accuracy of 1 μs (due to the time constant of the pressure transducer), this result shows obviously that the luminescence event is well correlated with the principal cavity collapse.

8.4.3 Collapse location

As an example, the statistics of calculated centres of preceding experiments are given in figure 8.17. Centres of luminescence emission are marked by dots in the real coordinates of the test section. Median distances X_{median} and Y_{median}, as well as standard deviations δX and δY, are also given in the left graphic. Assuming that luminescence spots correspond to collapse centres, most of collapses take place near the wall. A deviation of the collapses from the test section axis can also be noted, which has to be related to the non centred erosion pattern observed on exposed test specimen (see figures 8.18).

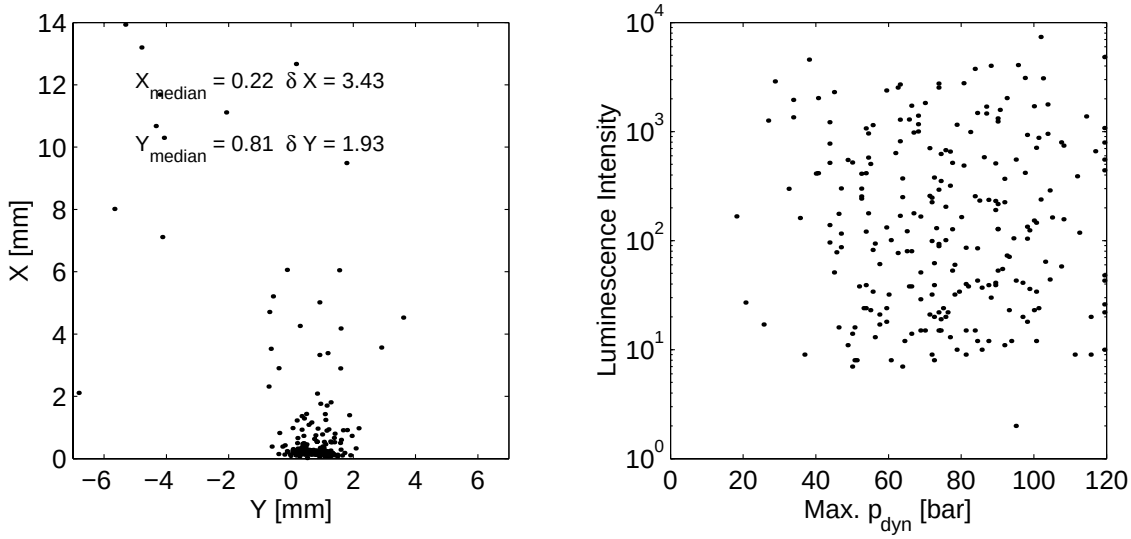

Figure 8.17: Location of luminescence sparks in the test section coordinates
Run# 1 : N=200 rpm, Q=0.66 l/s, σ=1.2

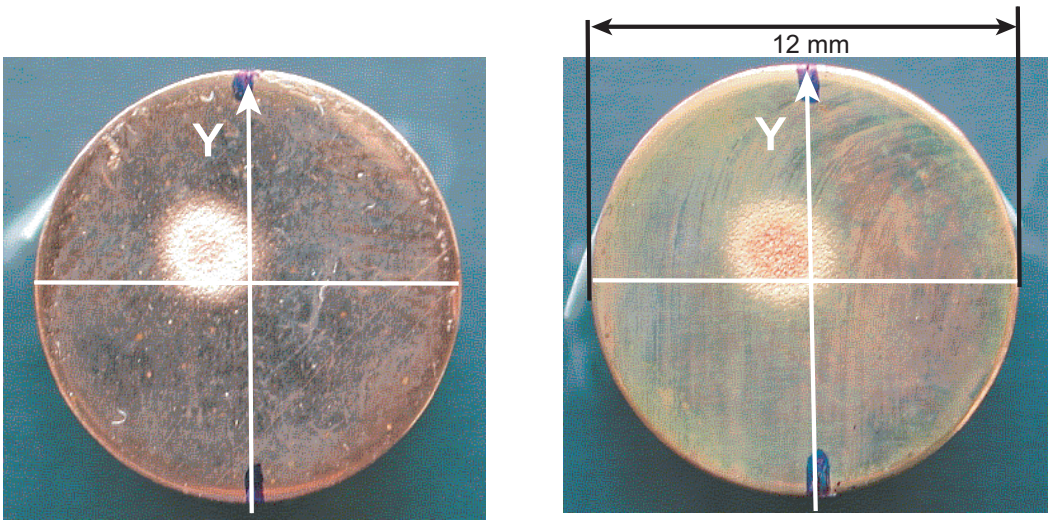

Figure 8.18: Erosion on Copper specimens

8.4.4 Unpredictibility of the scattered light

Since it is demonstrated that luminescence is principally emitted during the main collapse, the time window of interest is set to [0,10 μs] with $\delta t_{win} = 10\ \mu s$. In order to estimate the dynamic range of emission of photons, experiments have been conducted by varying the electric voltage of the IC (G = 1000 V, 950 V, 900 V, 850 V). The current intensity of the IC is exponentially depending upon the electric voltage : a difference of 150 V is approximately equivalent to a reduction of the gain of 10. Considering image histograms, the luminescence intensity can be studied.

Electric Voltage	1000V	950V	900V	850V
Time slot	120 mn	130 mn	40 mn	110 mn
Population	333	329	461	367
Success rates	73%	48%	38%	18%
Saturation occurrence	20%	7%	3%	<1%
Average Intensity	737	413	250	190

Table 8.2: Luminescence success rates for variable electric voltage of the IC
Run# 2 : N=200 rpm, Q=0.66 l/s, σ=1.2

As a first comment, results show that pixel intensities can extend from the threshold value to the maximum pixel saturation value 255, regardless of the gain of IC. This implies that the calculated luminescence intensity can be underestimated for most

intense emissions. Furthermore, the obtained success rates are highly dependent on the gain. Numerical results are presented in table 8.2.

As a main result, the luminescence intensity is unpredictable. Assuming the maximum pressure peak is weighted by the collapse distance D, e.g in figure 8.19 where a 1/D curve has been fitted on the data, the luminescence intensity is compared with the corrected pressure $\mathrm{Max.P}_{dyn} \times \mathrm{D/D_0}$ with $\mathrm{D_0} = 1$ mm. As shown in figure 8.20 for the condition $\mathrm{Q} = 0.66\ l/s$, where 4'120 visualisations have been processed, it is notable that the luminescence intensity is not correlated to the corrected pressure. In fact, the unpredictibility of scattered light is not surprising if one considers that the number of captured photons depends on an unpredictable scattered light which might be partly due to the unstable form of the vapour cavity (Lentz *et al.*, 1995).

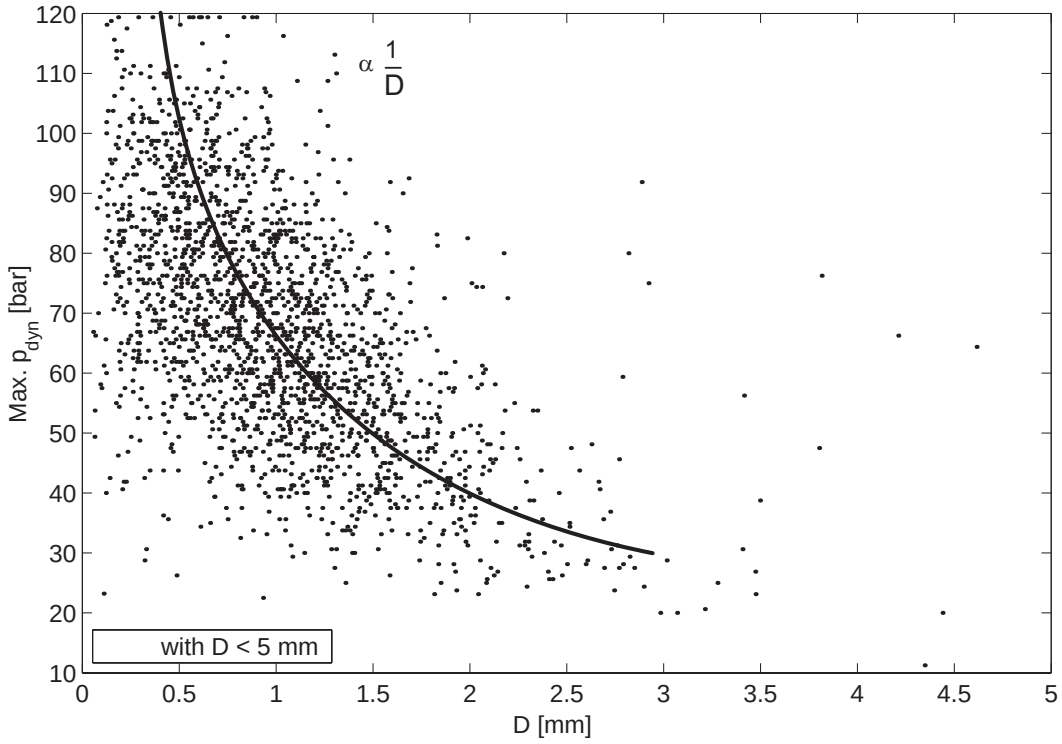

Figure 8.19: Maximum peak pressure $\mathrm{Max.p}_{dyn}$ versus collapse distances $D = \sqrt{X^2 + Y^2}$. Run# 3 : $\mathrm{Q} = 0.66\ l/s$, $\sigma = 1.2$, $\mathrm{N} = 200\ rpm$

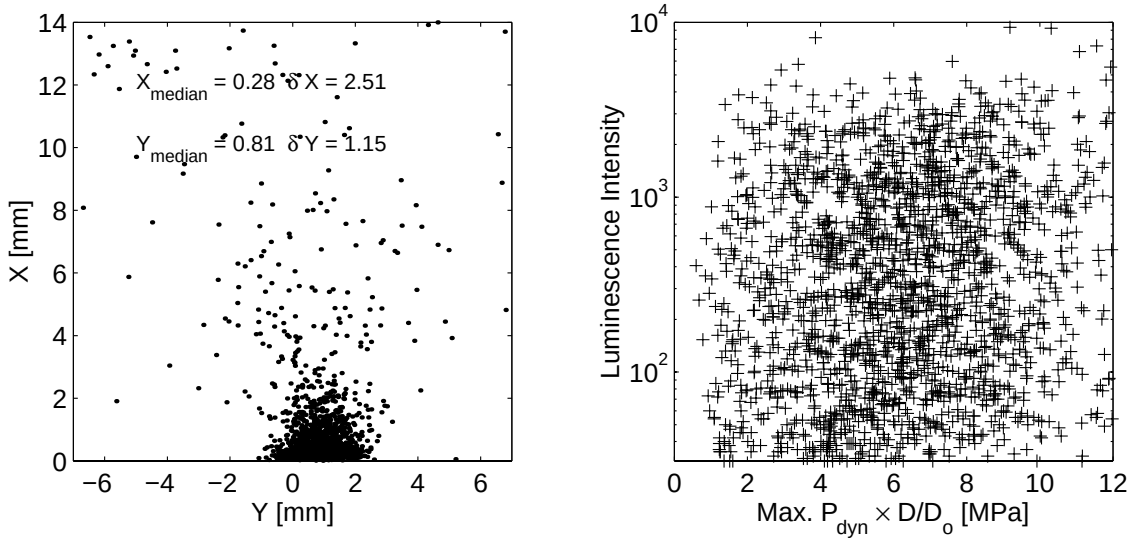

Figure 8.20: Luminescence locations in the real coordinates of the test section & luminescence intensity versus corrected pressure Max.$P_{dyn} \times D/D_0$.
Run# 3 : Q = 0.66 l/s, σ = 1.2, N = 200 rpm

8.4.5 Influence of dissolved gas in water

In order to evaluate the influence of the natural increase of dissolved gas in the circuit on luminescence drift in terms of success rate and intensity, visualisations have been achieved over a long duration of 2h 30. The shutter has still been triggered on pressure threshold and exposure time has been set to $\delta t_{win} = 10\ \mu s$. The maximum gain of IC has been set. Acquisitions are organized with 15 time slots of 200 successful measurements each. The number of acquisitions is 4'120, which corresponds to an average success rate of 73%. The mean wall distance X_{mean} and the mean axis distance Y_{mean} are calculated for each time slot in order to evaluate drifts. As illustrated in figure 8.21, the collapse location is stationary. However, the luminescence increases with time and thus with the gas contents, which is monitored by DO measurements (see graph in figure 8.1).

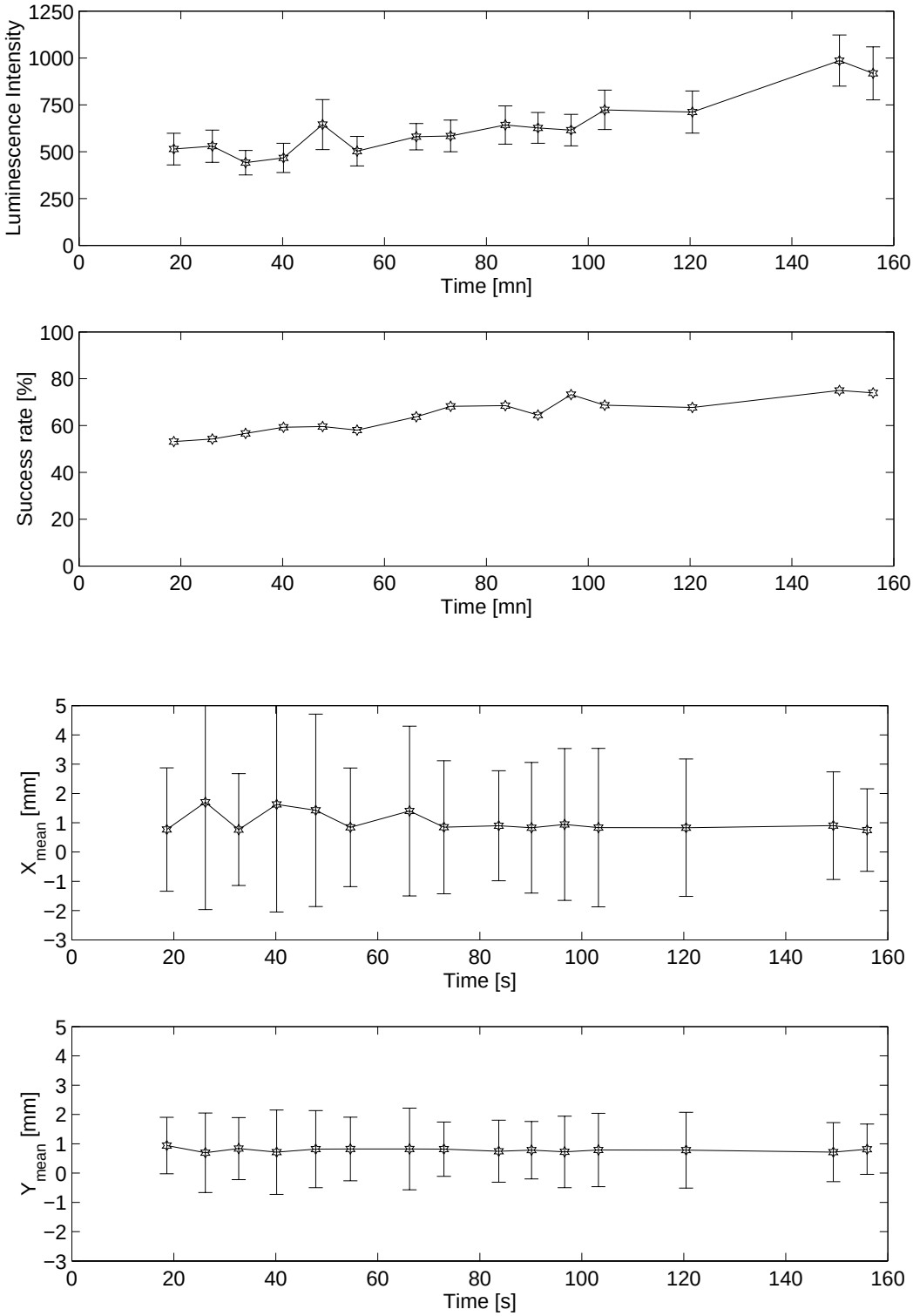

Figure 8.21: Luminescence and collapse location versus time
Run# 3 : Q=0.66 l/s, σ=1.2, N=200 rpm

8.4.6 Influence of hydrodynamic parameters

Test conditions

In these experiments, the influence of the flow rate Q has been studied. Moreover, the flow rate can be related to the vortex intensity Γ defined in equation 1.3. However, as it has been shown in chapter 1, the change of the flow rate yields a change of the cavitation coefficient σ defined in equation 1.2. Three flow rates have been tested :
N = 200 rpm, Q = 0.58 l/s, and $\sigma = 1.6$;
N = 200 rpm, Q = 0.66 l/s, and $\sigma = 1.2$;
N = 200 rpm, Q = 0.76 l/s, and $\sigma = 0.9$.
As it has been demonstrated in the preceding paragraph, the luminescence is sensitive to the dissolved gas in water (DO). In order to take into account the DO increase during the experiment, the hydrodynamic conditions can be varied during the same "run". In run# 4, flow rate have been set to 0.58 and 0.76 l/s (2×4 series of 100 acquisitions). Experiments have been conducted for the flow rates 0.58, 0.66 and 0.76 l/s during run# 5 (3×2 series of 100 acquisitions). A summary of the hydrodynamic conditions and obtained results is presented in tables 8.3 and 8.4.

Run# 4						
Q	σ	Succ. rate	Mean Int.	Mean Sat. Occ.	X_{median}	Y_{median}
0.58 l/s	1.6	400/913	605	13%	0.45 mm	0.89 mm
0.76 l/s	0.9	400/591	615	16%	0.27 mm	0.26 mm

Table 8.3: Luminescence characteristics in average (run# 4)

Run# 5						
Q	σ	Succ. rate	Mean Int.	Mean Sat. Occ.	X_{median}	Y_{median}
0.58 l/s	1.6	200/368	543	15%	0.31 mm	0.83 mm
0.66 l/s	1.2	200/298	662	12%	0.25 mm	0.70 mm
0.76 l/s	0.9	200/257	700	19%	0.26 mm	0.38 mm

Table 8.4: Luminescence characteristics in average (run# 5)

Luminescence characteristics

Time evolution of success rate, mean intensity and saturation occurrence for each flow rate during run# 4 are presented in figure 8.22. The error bars for the luminescence intensity have to be multiplied by 10, which shows the high dynamics of luminescence. The corresponding superposed images are presented in figure 8.23, where test section border is drawn in white.
The luminescence characteristics for each hydrodynamic condition are listed in tables 8.3 and 8.4 respectively for run# 4 and run# 5.

The luminescence success rate increases drastically with the flow rate. In addition, a slight increase of luminescence intensity is observed. However, by considering time evolution of luminescence characteristics, one must outline that the increase of DO is still an important parameter to take into account. As an explanation on these changes of the luminescence characteristics, one can refer again to experiments of Barber *et al.* (1994), who established that the intensity of a sonoluminescent bubble principally depends on the driving pressure, with a constant temperature and a constant DO. On the basis of a hydrodynamic approach, it is also shown how luminescence phenomenon could be related to an inward converging shock wave in the non condensable gas within the bubble : the shock is created by the supersonic vapour wall velocity, and the luminescence intensity might increase with the vapour wall velocity. Therefore, as an extrapolation to the cavitation vortex case, one could postulate that the increasing of vortex intensity leads to a stronger shock and thus a more violent collapse. Moreover, as it will be shown in high-speed visualisations, cavitation vortex cavities are very much different from a spherical symmetry. This would contradict the theory of the requirement of an initial spherical symmetry for sonoluminescence, which is one of the main parameters considered for the converging shock (Evans, 1996).

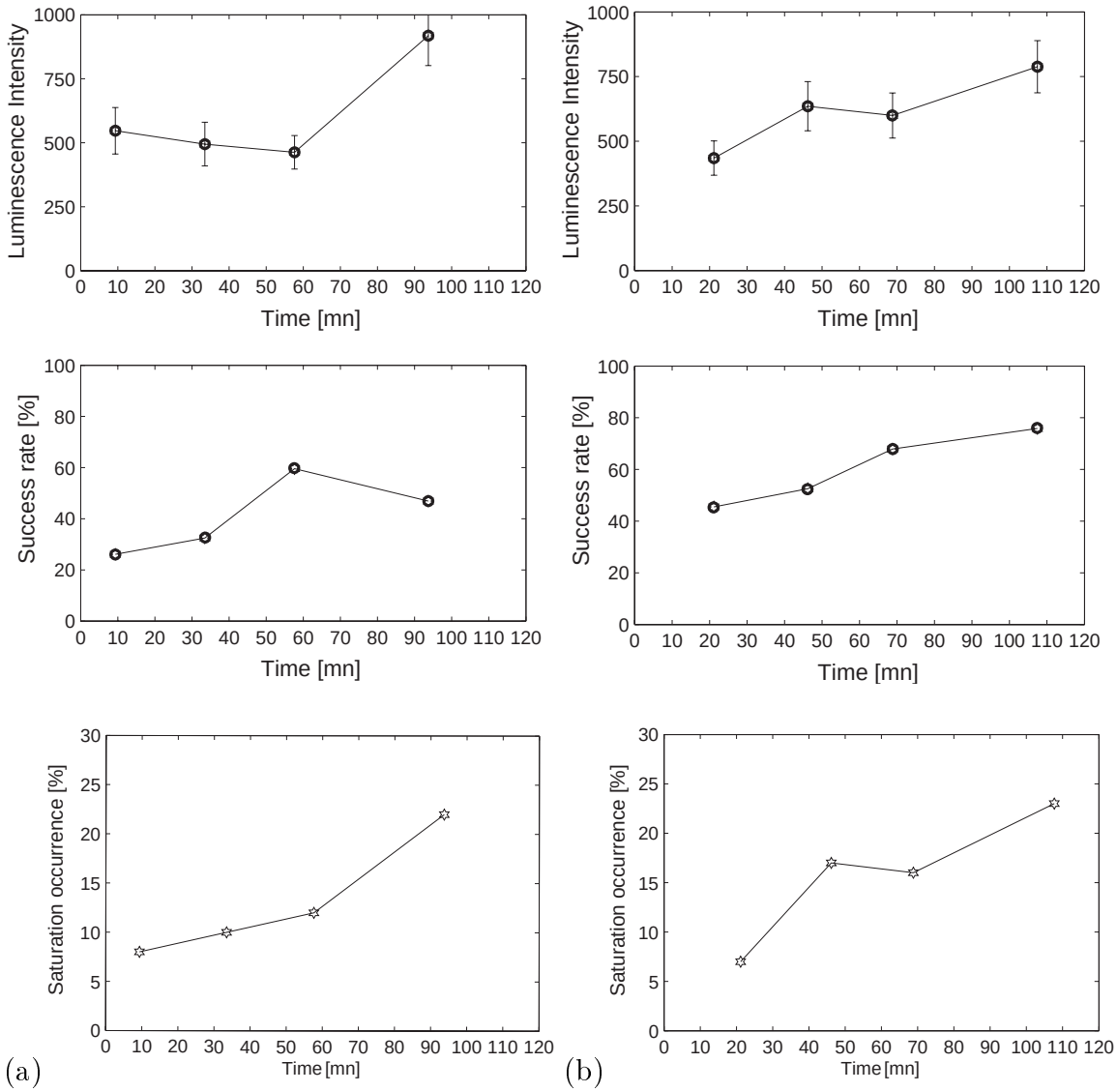

Figure 8.22: Time evolution of luminescence characteristics (run# 4)
(a) Q=0.58 l/s, σ=1.6, N=200 rpm, (b) Q=0.76 l/s, σ=0.9, N=200 rpm

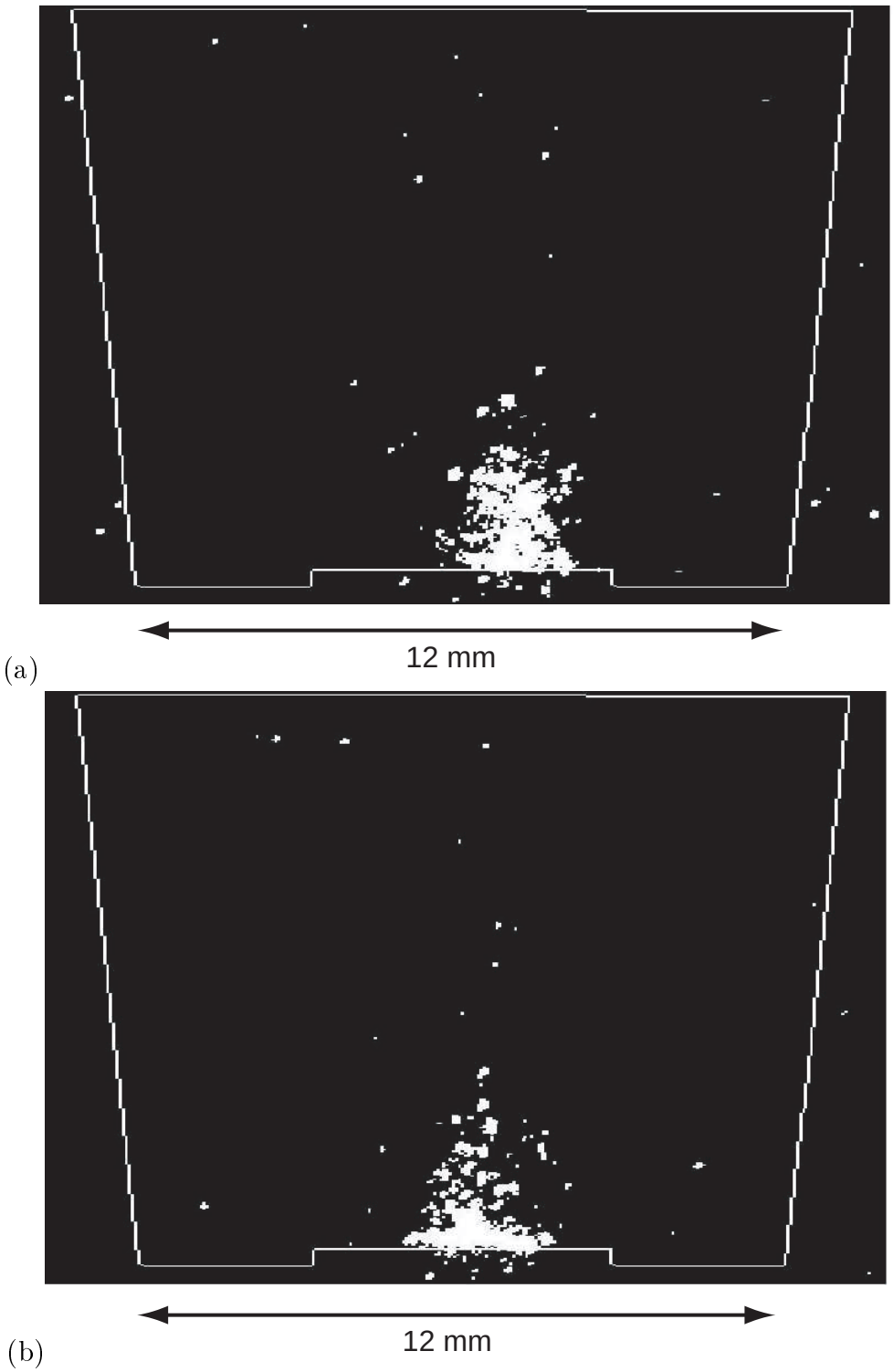

Figure 8.23: Superposition of 400 luminescence emission sources (run# 4). Note the distribution of sites ; though there is a cluster close to the bottom surface
(a) Q=0.58 l/s, σ=1.6, N=200 rpm, (b) Q=0.76 l/s, σ=0.9, N=200 rpm

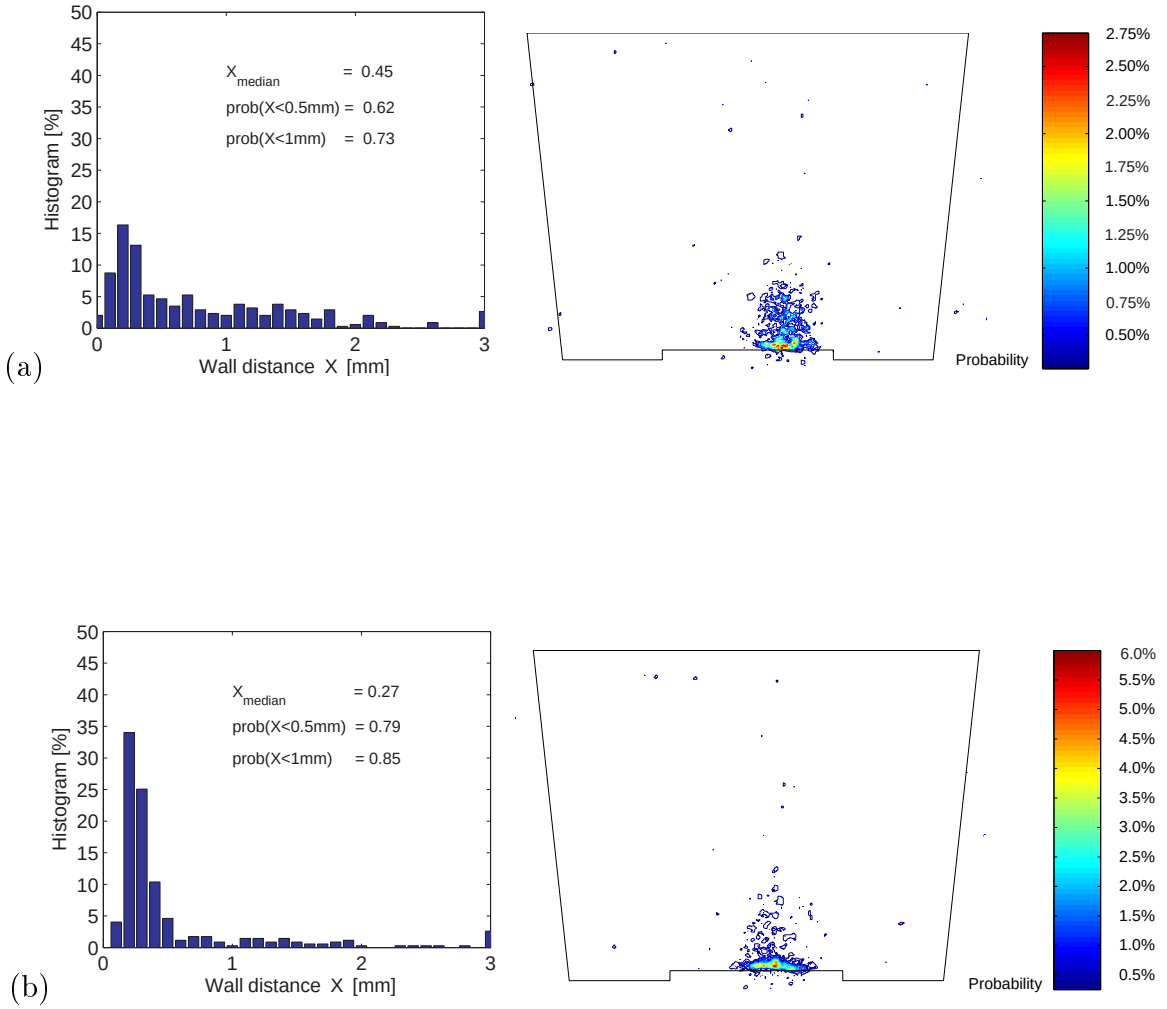

Figure 8.24: Probability map of the collapse location and wall distance (run# 4). The collapses locate closer to the wall when the flow rate increases
(a) Q=0.58 l/s, σ=1.6, N=200 rpm. (b) Q=0.76 l/s, σ=0.9, N=200 rpm

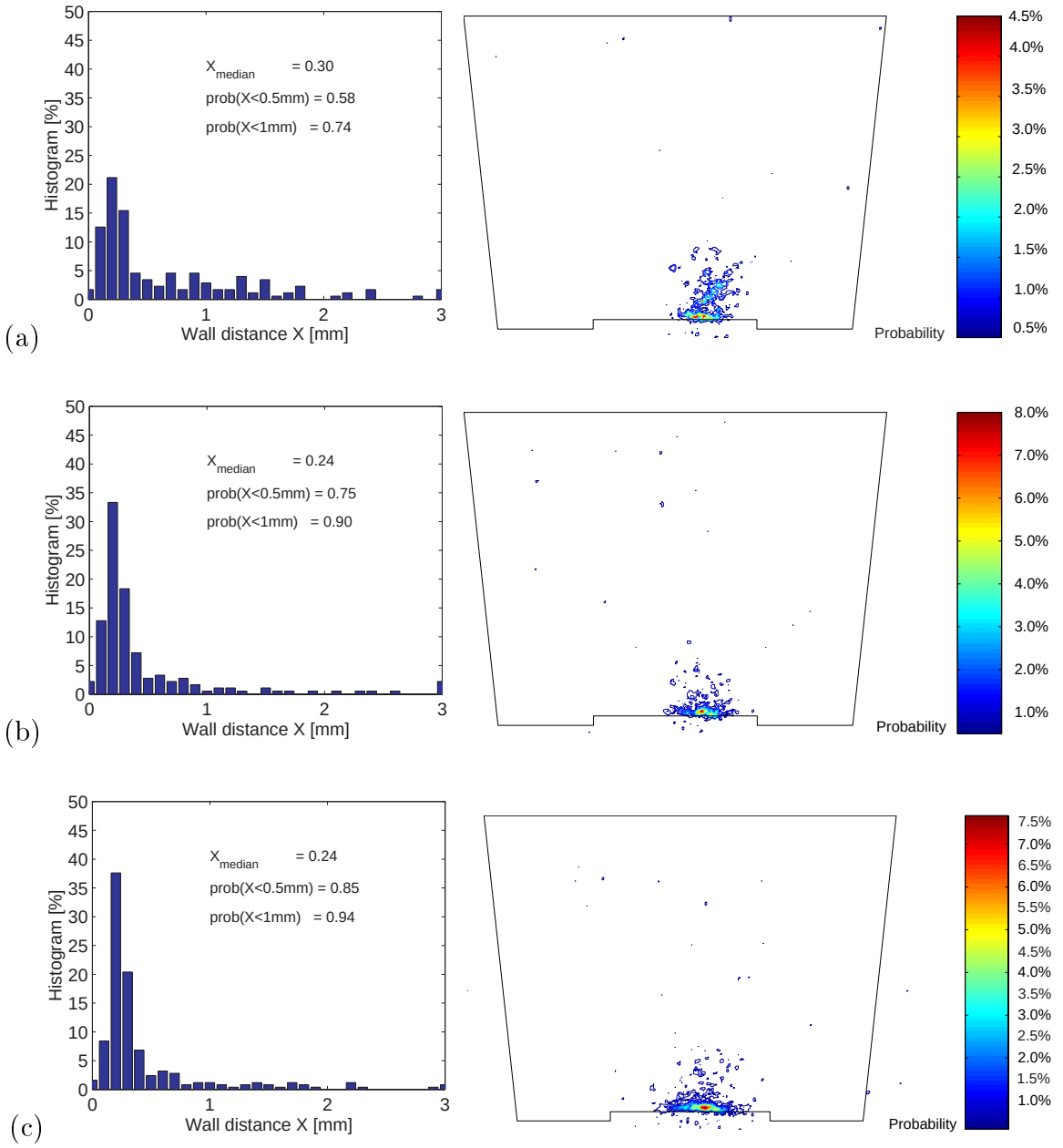

Figure 8.25: Probability map of the collapse location and wall distance (run# 5). The collapses locate closer to the wall when the flow rate increases. (a) Q=0.58 l/s, σ=1.6, N=200 rpm. (b) Q=0.66 l/s, σ=1.2, N=200 rpm. (c) Q=0.76 l/s, σ=0.9, N=200 rpm

Influence of the vortex intensity on the collapse location

The probability to have luminescence for each pixel in superposed images is calculated. The probabilities are normalized by the total number of pixels of the superposed images. They are represented through colour-maps in figure 8.24 for run# 4 and in figure 8.25 for run #5. Moreover, the histograms of wall collapse distance X obtained for the variable flow rate conditions have been calculated. They are represented by the right charts in the figures. Furthermore, the probability to have the collapse at a wall distance lower than a given value can be calculated. Probabilities are normalized by the total number of luminescence centres. These probabilities are also given in charts.

It is notable that collapse centres depend upon the flow rate. The median wall distance X_{median} diminishes with the flow rate while the probabilities prob(X<1mm) and prob(X<0.5mm) increase, which demonstrates that the collapses locate closer to the wall when the flow rate increases.

The vortex intensity Γ calculated according to the equation 1.3 is related to flow rate. The evolution of the collapse location through the estimators prob(X<1mm) and prob(X<0.5mm) with the vortex intensity is given in figure 8.26. As graphically shown, as the flow rate and thus the vortex intensity increases, the collapses are statistically located closer to the wall.

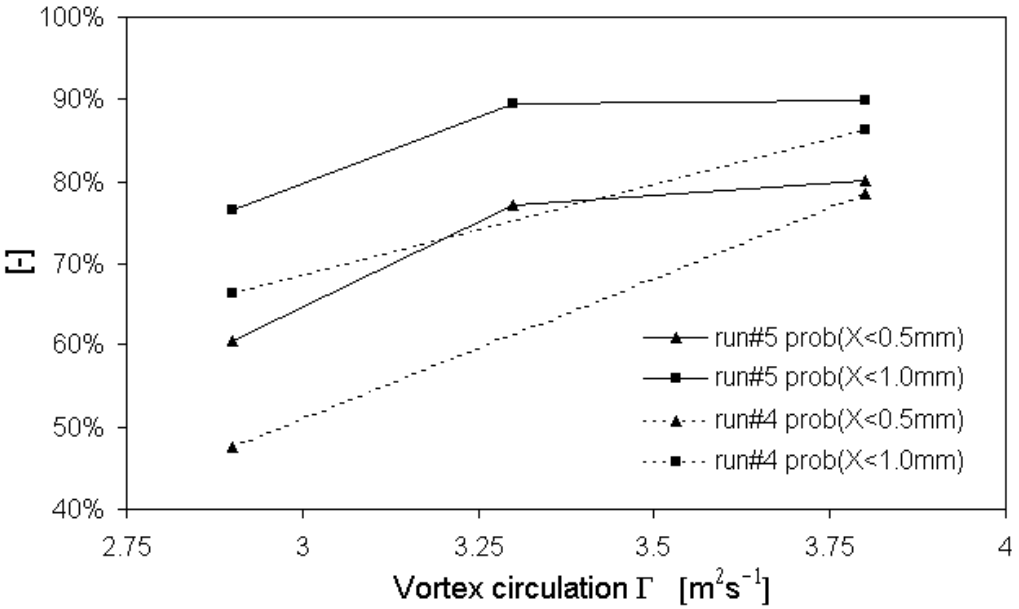

Figure 8.26: Influence of Γ on the collapse location through the estimators prob(X<1mm) and prob(X<0.5mm) (run# 4&5). As the vortex intensity increases, the collapses are statistically located closer to the wall.

Chapitre 9

Shock waves of cavitation vortex collapse

9.1 Measurement

9.1.1 Hydrodynamic conditions

The present study is realized for the hydrodynamic conditions that were already studied in the chapter 8 dealing with the luminescence of the cavitation vortex :
- N = 200 rpm, Q = 0.76 l/s and $\sigma = 0.9$;
- N = 200 rpm, Q = 0.64 l/s and $\sigma = 1.2$;
- N = 200 rpm, Q = 0.58 l/s and $\sigma = 1.6$.

Experiments take place in the 4-windows test section. The experimental protocol, which is already discussed in paragraph 8.1.1, is applied.

9.1.2 High-speed visualisations

High-speed visualisations can be achieved as follows. On the one hand, spark generators of the Cranz-Schardin camera (CS) are triggered when the dynamic pressure signal reaches a threshold value just before the collapse. On the other hand, due to a minimum internal delay of image sensors of the CS (200 μs), the video acquisition must first be cocked by the valve signal prior to the collapse. The collapse event has to occur during a time window of 17 ms, which corresponds to the integration period of the CCD modules of the CS (20 ms minus the blanking period). If the collapse occurs outside this time window, an additional delay for arming the video system can be programmed. The details of the acquisition set-up are schematically presented in figure 9.1. For each visualisation, the corresponding pressure signal as well as the light signal given by the photodiode are measured. In order to compare the signals and the

sequences, the reference time zero of the signals corresponds to the maximum pressure peak which corresponds to the collapse.

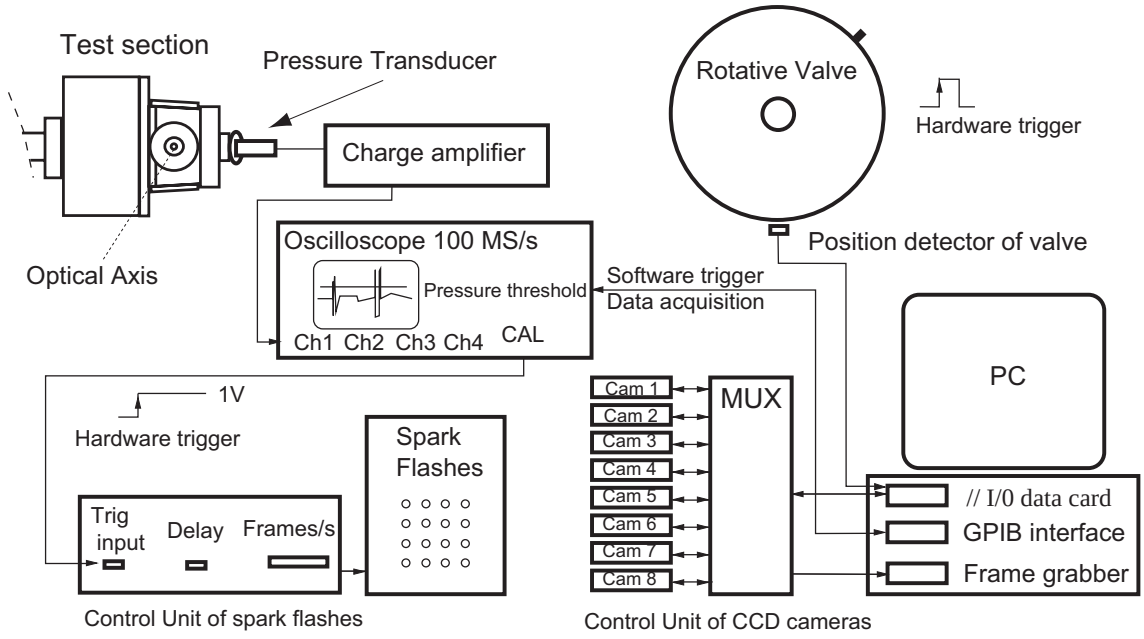

Figure 9.1: Schematic of the high-speed visualisations

9.2 Optical considerations

9.2.1 Shadowgraphy

The shadowgraphy technique is used to study the distributions of density gradients. This technique is based on the changes in illumination caused by a redistribution of light rays from one place to another. In other words, an incident beam is deviated due to the mean transverse index gradients, and the arrangement of the transmitted beam is modified by the anisotropy of these gradients. The relative illumination of the projected shadow is proportional to the second derivative of the transverse density gradient.

In the present study, the gradients are caused by variations of the water density due to the presence of wave pressure transients, vapour structures, and high tensile strength (Bruhat, 1992).

9.2.2 Refraction index in compressed water

The pressure gradient created by the shock wave allows the shape of the shock waves to be visualised by the shadowgraphy technique. The pressure can be related to the density by using the equation of state of water (Tait's equation) :

$$\frac{p+B}{p_o+B} = \left[\frac{\rho}{\rho_0}\right]^n \tag{9.1}$$

$$B = \rho a_0^2/n = 3021\, bar \tag{9.2}$$

where ρ is the maximum density, p the maximum pressure in the shock, $\rho_0 = 999.13$ $kg.m^{-3}$ the ambient density, a_0=1455 $m\ s^{-1}$ the wave velocity in water at T=15 $°C$ (Nordling & Österman, 1987; Handbook of Chem. and Phys., 1982), p_0= 1 bar the ambient pressure, n=7 as suggested by many authors (Batchelor, 1967).

The refraction index n_r can be related with the local density by using the Lorentz-Lorentz equation (Bruhat, 1992) :

$$\frac{n_r^2-1}{n_r^2+2} = (LL)\rho \tag{9.3}$$

where n_r is the index of refraction. The Lorentz-Lorentz constant for water is $(LL) = 0.2053\,10^{-3}\ m^3.kg^{-1}$. As graphically shown in figure 9.2, a large variation of refraction index can only be achieved by a large local overpressure in water. For example, a change of the refraction index $\Delta n_r = 0.09$ is obtained for a theoretical overpressure of 1 GPa, which is equivalent to the 25 % change of an air/water interface.

9.2.3 Shadow of shock waves

In order to explain the observed circular shock wave on the shadowgraph, one can plot the transmitted light paths of incident parallel rays through an ideal step function of the shock wave. The actual path of the beam can be obtained by applying Snell's law to the shock boundary. Ray tracing is shown in figure 9.3, where the amplitude of the step of the wave front is arbitrarily set to 1 GPa, with an external radius of 5 mm and a width of 0.5 mm. If the shock wave is crossed with a large angle of relative incidence α, its deviation $\Delta\alpha$ is small. When the incident beam becomes tangent to the shock interface, rays are highly refracted : little light is transmitted in the incident direction in this region. This creates the dark region on the shadowgraph.

However, the shape of the wave is certainly different from a step function. Therefore, rays are shifted into a region where the refraction index is no more constant. According

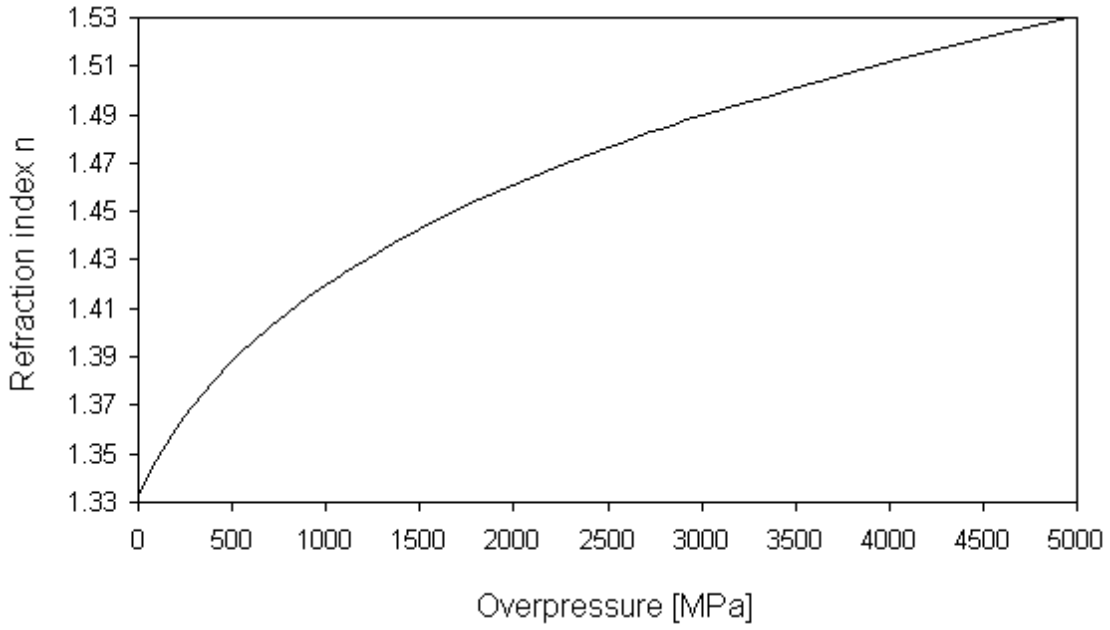

Figure 9.2: Refraction index of compressed water

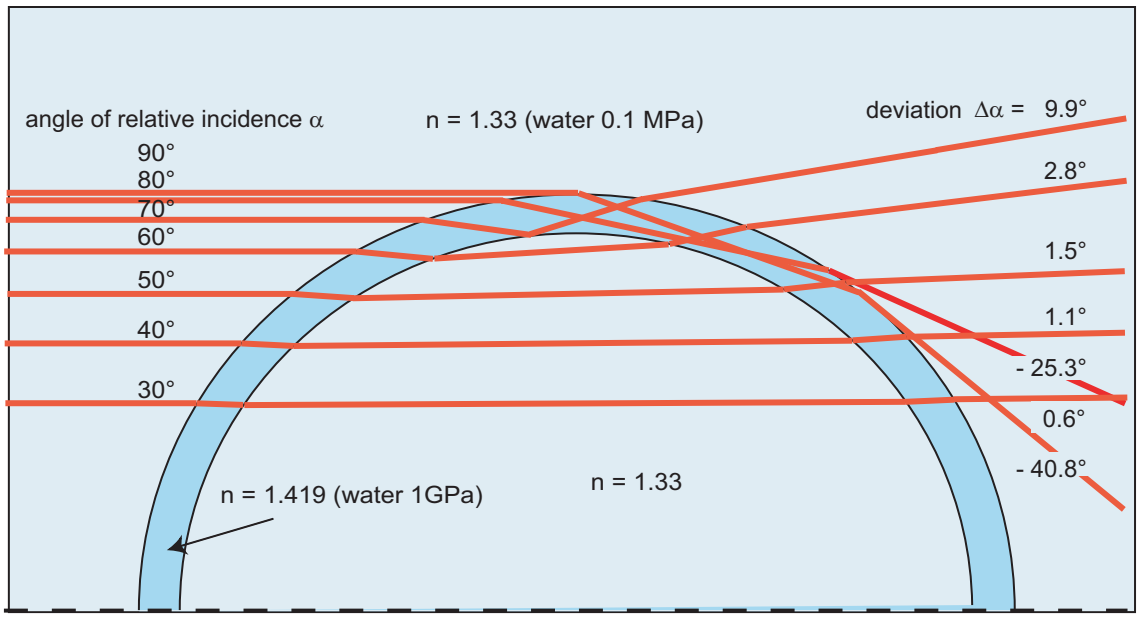

Figure 9.3: Light ray tracing through an ideal shock wave

to equation 9.4, they deviate in the direction of high values of refraction index.

$$\vec{\nabla}\, n_r = \frac{d(n\vec{t})}{ds} \tag{9.4}$$

where s is the curve abscissa and $\vec{t}$ is the tangent vector of the ray. However, as the function of the wave is unknown, the calculation of rays is not possible. Nevertheless, since deviation of light rays is proportional to the second derivative of the gradient, the deviation amplitude depends on both the wave "width" and amplitude. Moreover, there is a threshold for which the gradient index can not be detected by the visualisation system.

As a conclusion, the observed shadows of the shock waves depend on the wave characteristics as follows :

1. The thickness of the wave on the shadowgraph depends on both the width and the amplitude of the shock wave.
2. The darker the region on the shadowgraph, the greater the pressure in that region.
3. An actual shock wave has its maximum pressure gradient located on the side ahead of the shock. On the back side, a slightly decrease of the pressure amplitude takes place. Consequently, the outer envelope of the dark phase on the shadowgraph might be the best approximation of the shock-front radius.

9.3 Image processing

9.3.1 Vapour cavity contour

In order to trace the vapour interface growth and collapse, an efficient image processing procedure has been implemented. This allows not only the vapour cavity contour to be segregated from the background image, but also from the dark surrounding contrast and the complicated wave pattern. The following method has been achieved.

- Each image of a sequence is aligned and calibrated by placing a calibration target in the test section (see calibration procedure 1.5.2).
- Each intensity image of the sequence is scaled independently, prior to a specific image threshold operation which is applied to the test section zone. The threshold operation is realized in two steps :
    1. A usual threshold operation is applied in order to create a region of interest (ROI) corresponding to the vapour phase and the surrounding dark contrast created by high pressure gradients
    2. A gradient operator of Sobel type is applied to the image to isolate the contour in the previous ROI.

The interest of such a method is to provide an accurate gradient detection method, and to avoid the detection of the background noise in the whole image. This result could not be obtained by using an unique gradient operation on the whole image. On the one hand, a unique gradient would actually lead to numerous contours due to the noise in images, and on the other hand, a unique threshold operation is not suitable because of the difference of light exposure and gradient contrast.

- By performing morphological operation and blob analysis, the main geometric characteristics of the different vapour cores are calculated : centre, area and the equivalent radius.

As a summary, the steps for contour detection can be represented by the synoptic diagram in figure 9.4.

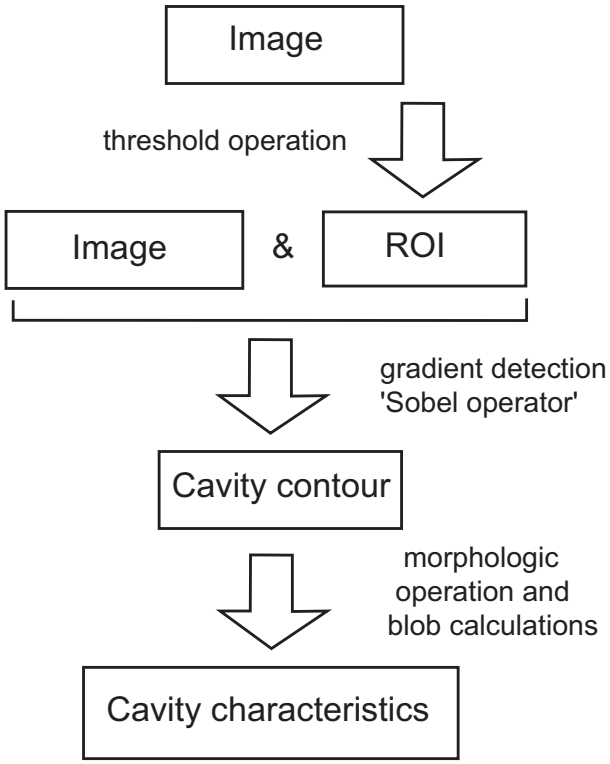

Figure 9.4: Vapour cavity contour detection

9.3.2 Wave pattern matching method

As successive shock waves can yield a very complicated wave pattern, a specific image processing method has been developed. In fact, refraction index gradients due to instantaneous pressure transients correspond to contrast functions in images. These can be modified by light exposure and intensity, and probably parallax effects. Consequently, the shock wave front is not well defined, and so far, threshold and gradient methods to detect wave displacement are not suitable.

In order to calculate the displacement of the wave transient, a suitable normalized intercorrelation method has been implemented. This method is able to follow a moving target, which is in our case a travelling wave pattern. In addition, one must point out that the normalized intercorrelation method is not sensitive to light exposure differences between frames. As an illustration of the wave pattern matching method, see figure 9.5.

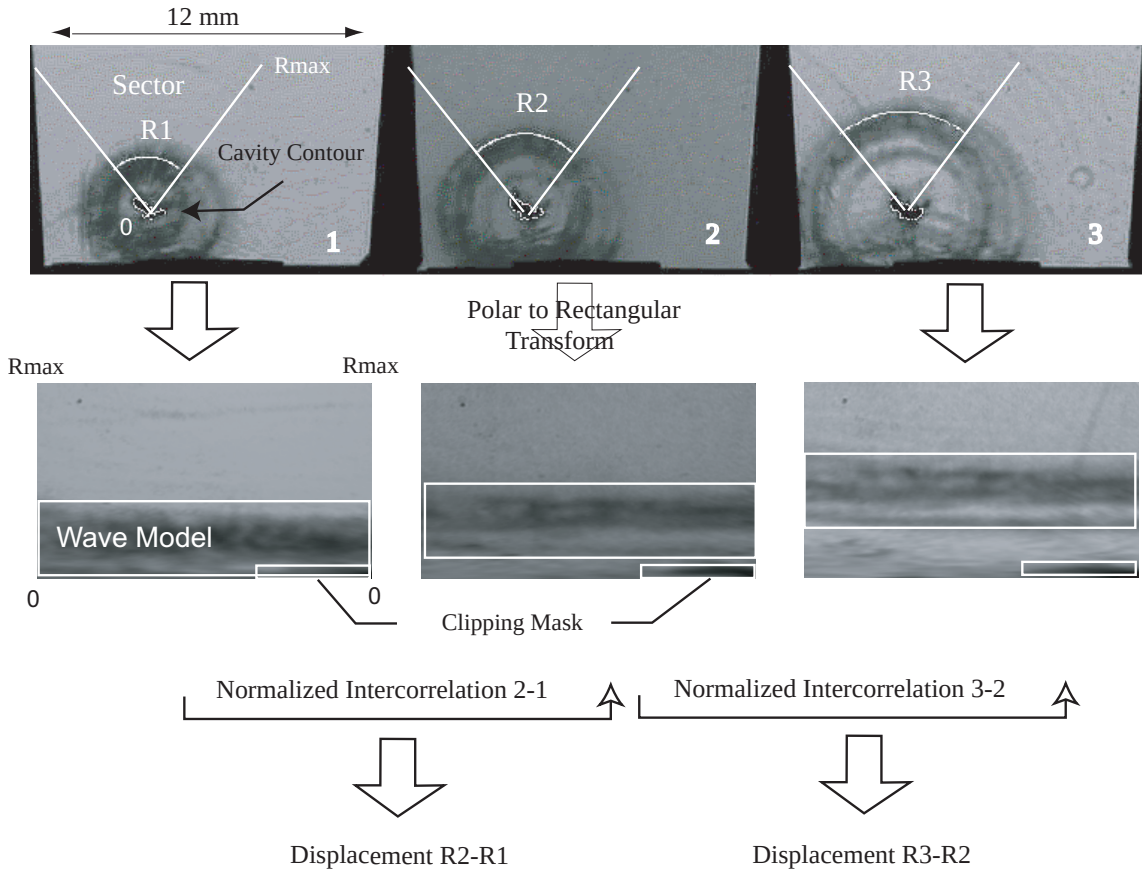

Figure 9.5: The Wave Pattern Matching Method. The change from polar to rectangular coordinates produces the flat shock front. The normalized intercorrelation method is then used to calculate the displacements of the front in the frames.

The steps leading to the determination of the wave pattern displacement are the following.

1. In order to transform "spherical waves" to "cartesian waves", a polar to rectangular transform is applied by taking the origin of the transformation as the calculated centre of the main vapour cavity, from which the wave is supposed to detach. An angular sector of interest in the test section is defined. As a result of the transformation, the shock front now appears to be straight and horizontal instead of being circular.
2. The normalized intercorrelation between consecutive warped images is achieved. The vertical displacement of the wave pattern is calculated by comparing the location of a unique model, taken from a rectangular region of interest of the wave pattern, with its actual location in next target image. It is problematic that the vapour cavity shadow is included in the wave pattern model. Indeed, this could introduce an offset in the displacement result, or even worse, the score of the intercorrelation would not be sufficient to calculate the displacement. Therefore, a clipping mask, which corresponds to the pixels of the vapour shadow, and which is obtained by a threshold operation, is defined : the pixels corresponding to the clipping mask are not taken into account in the intercorrelation calculation.
   As the final result, the vertical displacement of shock wave pattern is equivalent to the difference in radius in the real coordinates.
3. By giving the initial radius, which corresponds to the outer envelope of the shock wave, the next radius are calculated by considering the successive displacements.
4. The result can be validated by superposing the original sequences with the obtained radius.

9.4 Time history of the cavitation vortex

Repetitive visualisations obtained by setting a variable delay from the valve closure have shown that the cavitation vortex can be regenerated several times during a CVG cycle. However, questioning about the dynamics of the cavitation vortex would be beyond the scope of the present study, and thus the investigation time window is restricted to some milliseconds following the main cavity collapse, where most of the significant pressure transients are detected.

Low frame rate permits to visualise the cavitation vortex during the first 8 ms that follow the main collapse. An example of such visualisations can be seen on the sequences in figure 9.6. The first image corresponds to the emission of the shock wave at the main cavity collapse. This is followed by a regeneration of a vapour core, which collapses again. An important observation is that breaking process of the cavitation

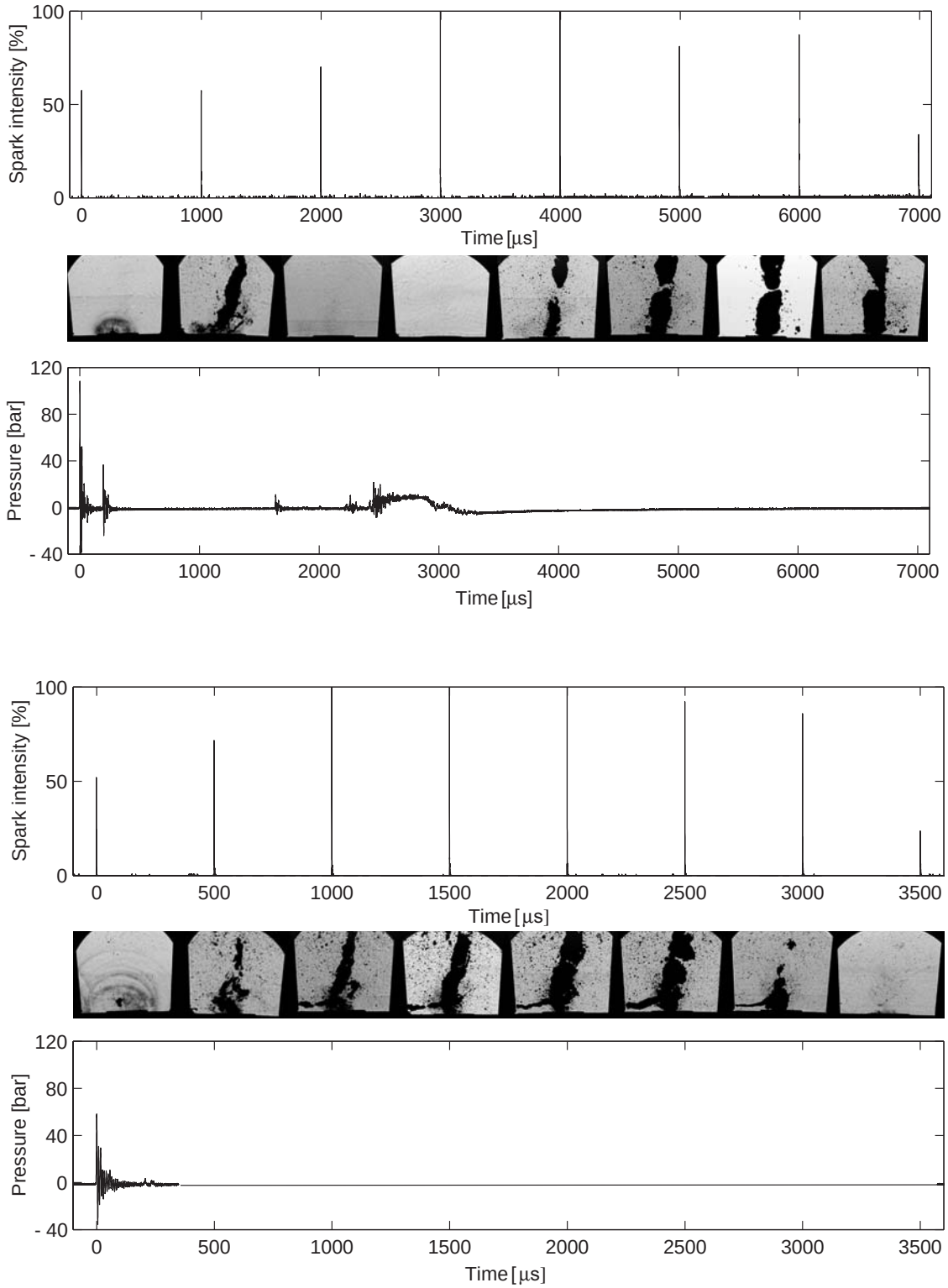

Figure 9.6: Vortex dynamics following the main cavity collapse
(first sequence) N=200 rpm, Q=0.66 l/s, σ=1.2
(second sequence) N=200 rpm, Q=0.76 l/s, σ=0.9

vortex during the collapse after being regenerated is similar to the one of the first collapse. This common characteristic can be found in the photos in figure 8.12, with a delay from the valve closure about 17–19 ms.

A relatively smooth pressure transient is usually observed after an elapsed time of 2–3 ms. It can be stated that no vapour is present during this period.

Investigations have been restricted to the 250 μs following the main collapse. It appears that the main collapse can be followed by a second rebound of the vapour cavity after an elapsed time of 15–20 μs (see figure 9.7). Then, another collapse usually occurs in the time window 200–220 μs. The emission of the first shock wave, which is due to the main collapse, as well as the emission of a second weak shock wave, is illustrated by visualisations in figure 9.8 (first sequence).

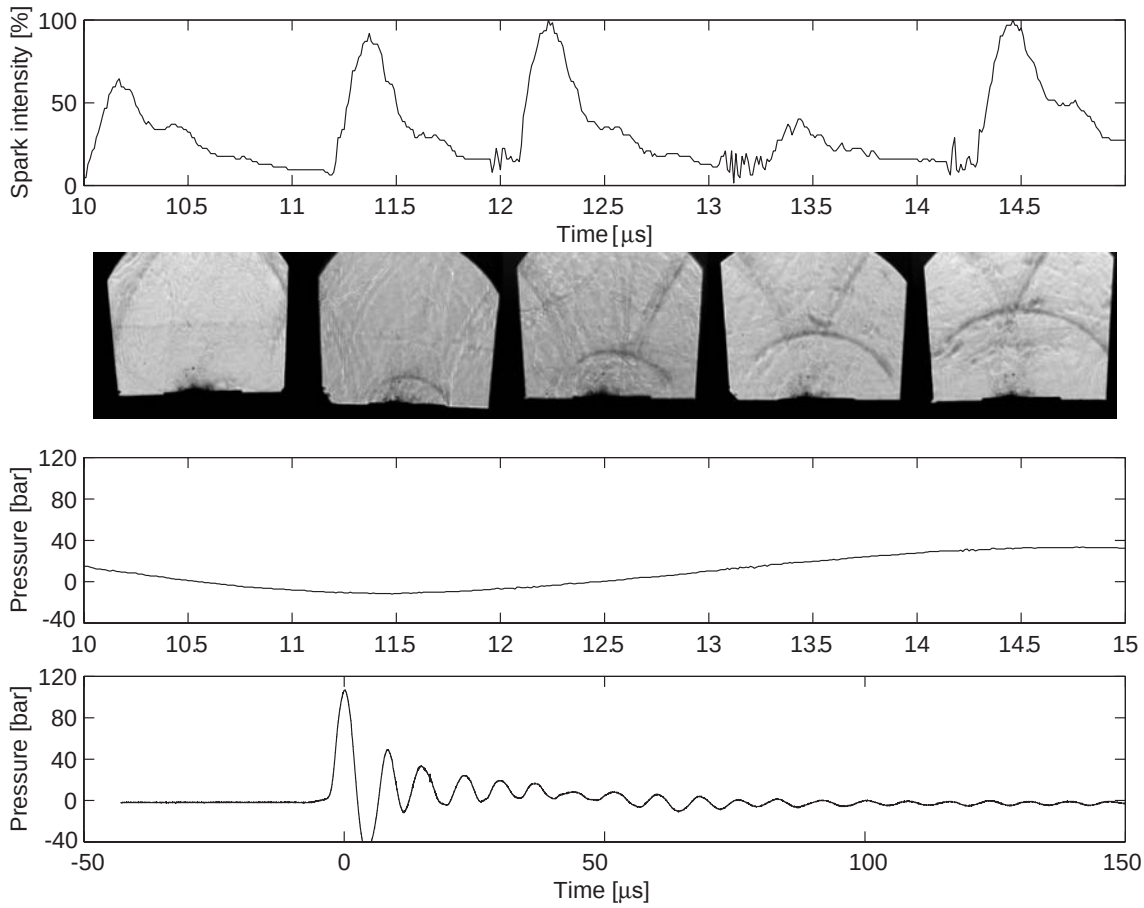

Figure 9.7: Second rebound of the main cavity with emission of a weak shock wave N=200 rpm, Q=0.76 l/s, σ=0.9

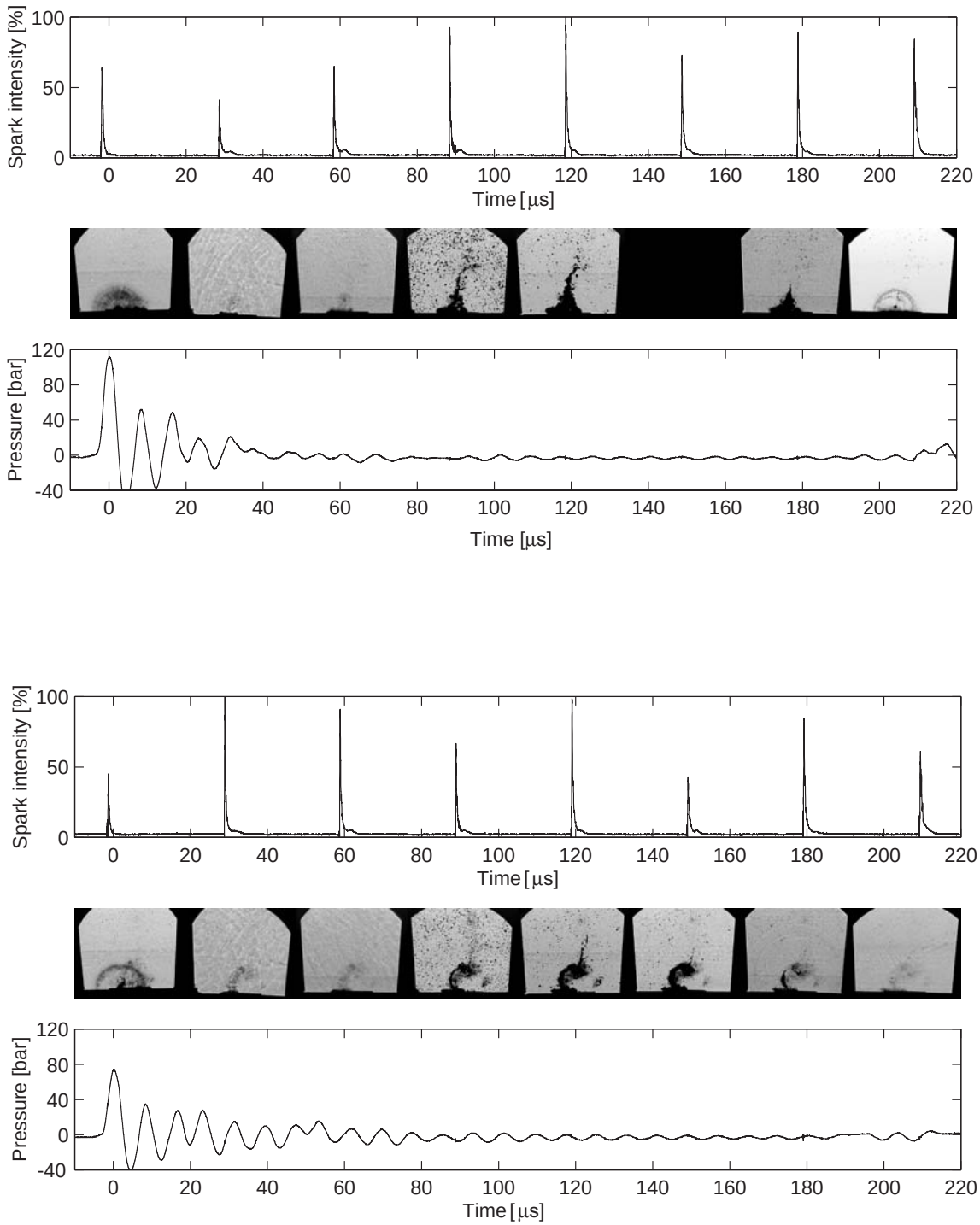

Figure 9.8: The 200 μs following the main cavity collapse
N=200 rpm, Q=0.76 l/s, σ=0.9

9.5 Phenomenological study

9.5.1 Shock waves emission

Strong shock waves emission is systematically associated with the main cavity collapse. Most of the collapses take place near the wall, as it was already pointed out by the luminescence results in figures 8.23–8.25. In order to visualise the vapour phase just before the emission of the shock wave, the pressure threshold is set to a minimum : approximately 0.4 MPa. As shown in figure 9.9, the maximum value of the pressure signal is delayed with respect to the production of the shock wave, and the pressure transducer is excited to its natural frequency of 130 kHz.

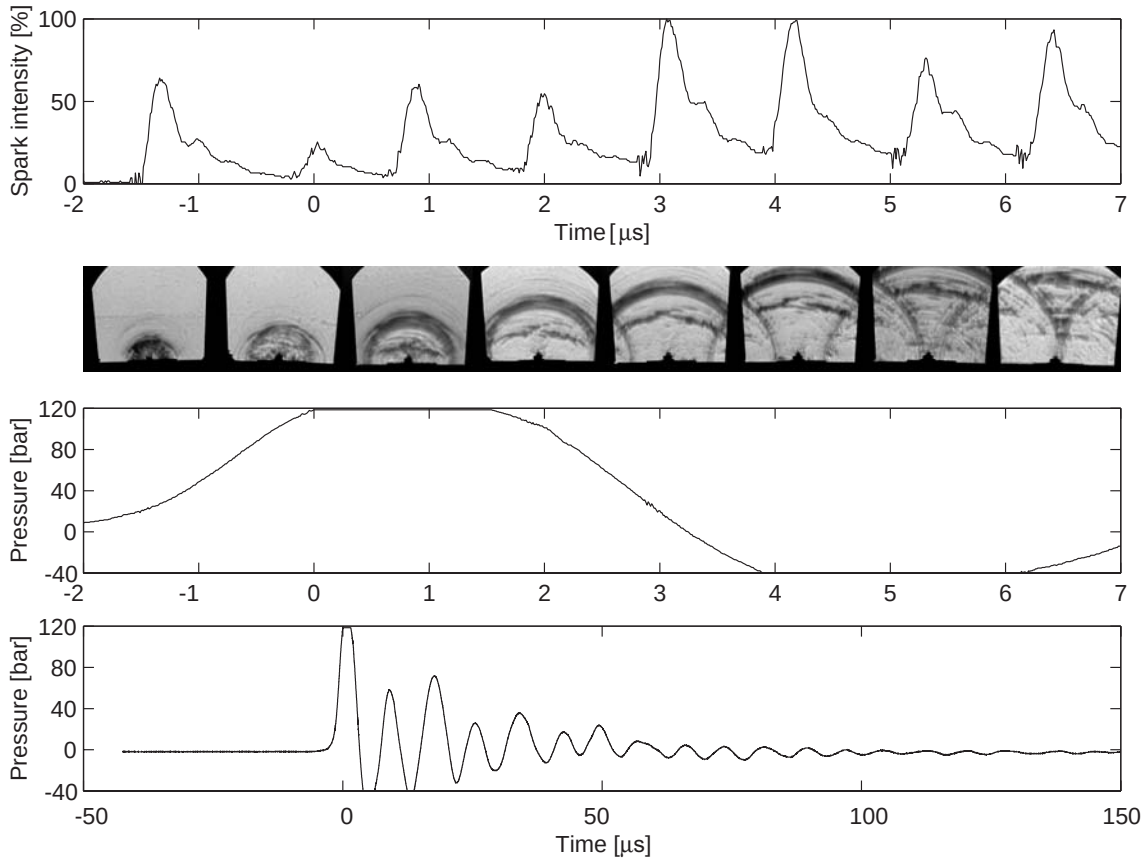

Figure 9.9: Strong shock wave emission at near wall cavity collapse, 10^6 fps
N=200 rpm, Q = 0.76 l/s, σ=0.9

On the basis of the analysis of sequences, the main characteristics of shock waves can be outlined.

- Firstly, shock waves have a straight pattern after the polar to rectangular transform, which obviously demonstrates their spherical nature despite that the shock waves are generated by the global collapse of a complex vapour structure (see example in figure 9.5). The "epicentre" of waves corresponds well to the calculated vapour phase centre. Additionally, the wave pattern is often anisotropic, which can be explained by two reasons :

  1. in some cases, by the wave interference with previously emitted shock waves
  2. more generally, by the anisotropy of the liquid media : the main cavity is usually surrounded by a cloudy grey contrast which can be explained by the presence of micro-bubbles.

- Secondly, before the shock front is clearly detached from the vapour cavity and propagates spherically, the vapour cavity is initially surrounded by a dark contrast, which can be explained by a high change in the refraction index due to the shock formation. However, this dark zone merges with the shadow of the vapour phase and grows at a relatively slow rate compared to the following outgoing shock wave.
  This observation is consistent with the numerical calculations of Hickling & Plesset (1964), which describe the flow in the vicinity of a collapsing bubble in water : the pressure near the bubble boundary during the last stage of the collapse is already increased, and then, as the liquid rebounds, it forms a compression wave which moves outwards and steepens into a shock. It is also shown that the shock steepens over a time interval $(t - \tau)$ where τ is the Rayleigh time of the collapse, so that $(\tau - t)10^4/\tau \simeq 16$ for an initial partial pressure within the cavity of 10^{-3} bar. Moreover, the corresponding perturbation distance is approximately $2\ 10^{-1} \times R_0$, for a bubble radius of $0.08 \times R_0$. On the basis of these theoretical assumptions, the obtained shadowgraphy pattern around the collapse time can be predicted. As an estimation, hypothetical initial conditions can be set : - the maximum size bubble radius to 6 mm (half size of the test section), - the partial pressure within the cavity to 10^{-3} bar, - and the driving pressure to 6 bar. The numerical application resulted in a time of shock formation over the first 350 ns, with a perturbation distance shorter than 1.8 mm from the bubble with a radius of 0.5 $\pm$0.2 mm. Furthermore, similar calculation with a higher initial pressure would lead to a longer time for the formation the shock.
  Consequently, as the exposure time is around 150–300 ns, the time duration of the shock formation is expected to be comparable with the exposure time of the light flashes. Moreover, the frame period of the visualisations is 500 ns. This is roughly equal to the time required for the shock to steepen.

- Thirdly, an incident wave propagates in water until it reflects on the sides of the

test section. In the case of near wall collapses, the incident wave is immediately followed by a reflected wave which propagates in the same direction and velocity than the incident shock wave (at approximately the sound speed).

- Fourthly, instead of an incident shock wave with an unique and definite wave front, the wave pattern is often composed of multiple shock waves which cannot be explained by the reflection of a unique wave with the wall (this would only lead to two shock fronts). However, if the cavitation vortex has a complex geometry with multiple contacts with the surface then multiple shock waves may be produced, see figure 9.10(a).
- Finally, it must be emphasized that the observed thick waves are not due to blur effects, but this must be related with the nature of the pressure transient itself, in terms of amplitude and wave characteristics. As an argument for this assumption, let us consider for example frame 2 of the sequence in figure 9.11(c). Although the thicknesses of the two waves are different, the propagation velocity for both waves is identical.

  In fact, the theoretical blur could be estimated from the thickness of the sharper wave. Previous experimental work has demonstrated that a shock pressure pulse travelling at a speed of 1500 $m\,s^{-1}$ and emitted by a cavitation bubble collapse, has a duration of about 140 ns (Ward & Emmony, 1990). Considering that the whole wave function width is visualised in the shadowgraphy image, and assuming a negligible blur, the expected physical thickness of the pressure transient would be 0.2 mm. Then, considering an exposure time of 300 ns, which is roughly the mean exposure time of the light pulses, the final apparent wave thickness should be 0.65 mm. The actual measured thickness of the sharpest wave, which is associated to a small vapour cavity, is 0.2 mm, which is less than half the expected value. Therefore, the effective exposure time, which is resulting from both the exposure time and the gain of the CCD image sensor, would be only 130 ns.

  In fact, considering the following frames of the sequence, it can be suggested that the apparent thick front wave actually corresponds to a superposition of two successive shock waves, which have the same epicentre, and which travel at the same velocity. Moreover, from a general point of view, a thick and dark shock wave might be the result of merging smaller shock waves and thus, since their pressures combine, the total pressure in some regions is greatly increased.

  This characteristic of the thick pressure transient is confirmed by all visualisations concerning large cavities. Unlike a large cavity, the collapse of a small cavity generates an unique shock wave, whose front is well defined and thus appears much thinner.

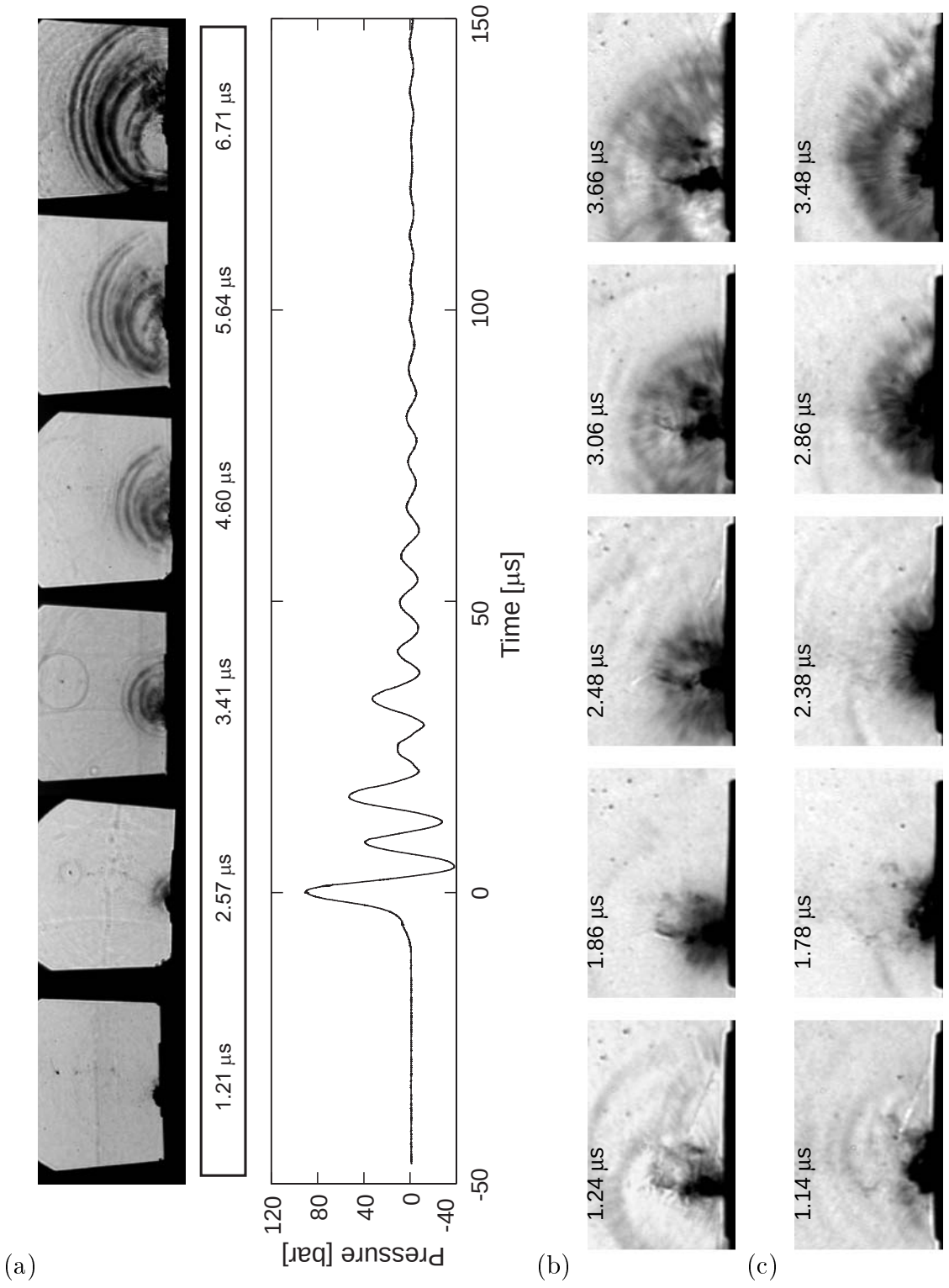

Figure 9.10: (a) Production of multiple shock waves at the final stage of the collapse and dynamic pressure. (a)(b)(c) Production of shock waves for collapses located near the wall, N=200 rpm, Q=0.66 l/s, σ=1.2, 10^6 fps

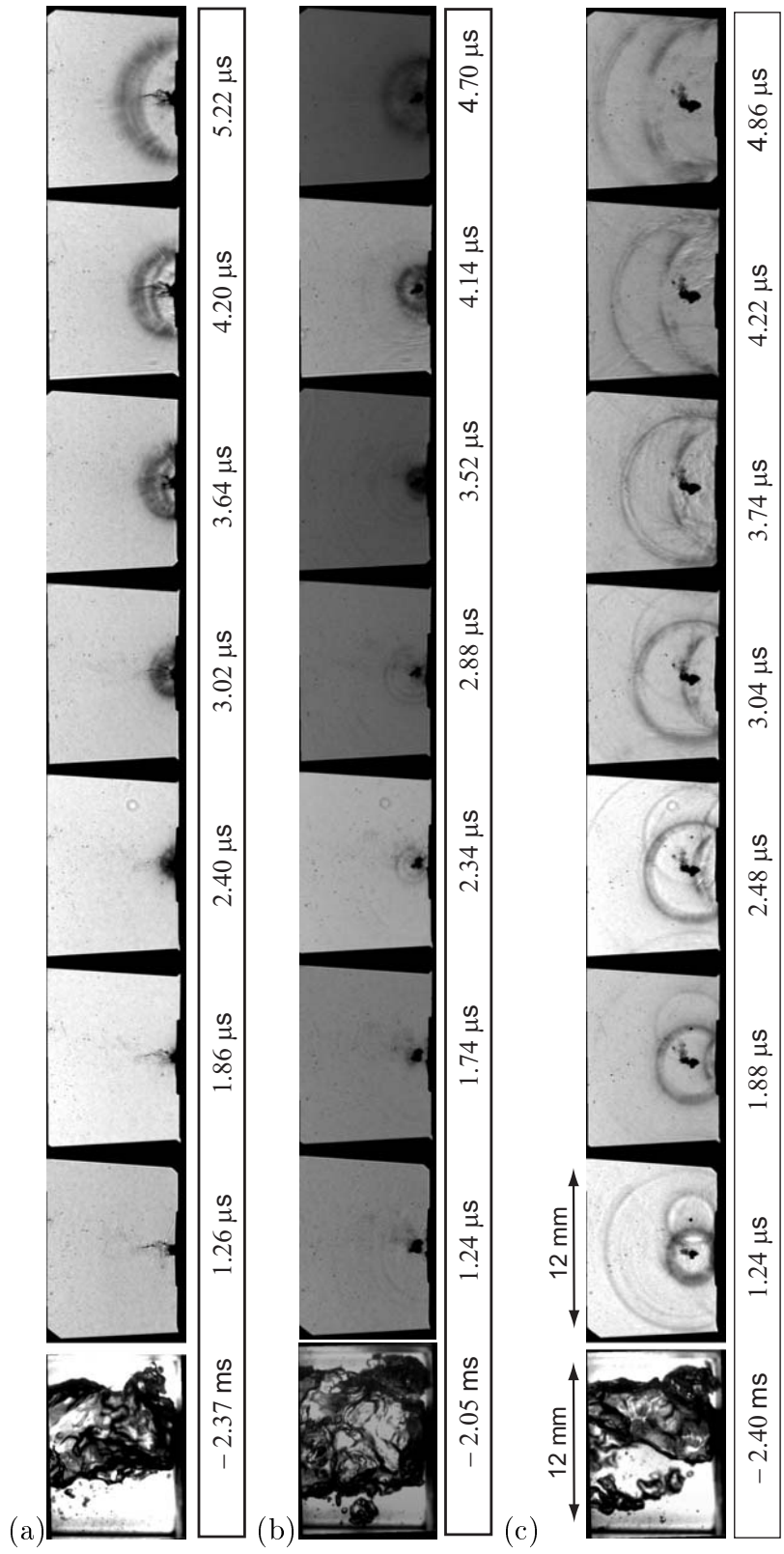

Figure 9.11: Near wall and far wall cavitation vortex collapse, 2 10^6 fps
(a)(b)(c) N=200 rpm, Q=0.76 l/s , σ=0.9

9.5.2 Vortex cavities characteristics

First of all, one has to distinguish the case of a near wall collapse, and the case of a far wall collapse, reminding that most of the collapses are near wall collapses. As an illustration, see the sequences in figure 9.11, where the first image is a photo of the cavitation vortex 2–2.5 ms prior to the emission of the shock wave. It is shown that the cavitation vortex leads to either a near wall collapse or a far wall collapse for the same hydrodynamic conditions.

- In the case of a near wall collapse, the vapour phase can be either cavities attached to the wall, or can have a more ellipsoidal shape, which is still in contact with the wall. As an illustration of these types of collapses, typical sequences are given in figure 9.10.
- As an intermediate situation between far wall collapse and near wall collapse, there are also cases where the main cavity is remaining at the same position and is attached to the wall via a short vapour bridge which breaks during the collapse, see 9.14(a)(b) and 9.18(b). In this case, the hypothesis of the presence of a micro-jet, which was first predicted by Kornfeld & Suronov (1944) for a collapsing bubble near a solid boundary, cannot be excluded. In addition, there are some situations where the main cavity is attached to the wall via a thin vapour filament (9.12(a), 9.13(a), 9.14(c), 9.17(c), 9.18(a)). This might be related to the presence of a thin and intense vortex tube ending at the wall. Other vortex filaments, which are not attached to the wall and depart from the main cavity, can be also observed, like in sequence 9.17(c). This shows how the micro turbulences of the flow can interact with the vapour phase : an existing vapour volume can extend rapidly along micro-hydrodynamic structures which eventually coalesce.
- Concerning isolated vapour cavities, they are never spherical, and the main cavity is usually associated with other surrounding smaller cavities. Moreover, the main cavity does not collapse in a regular way, so that the initial cavity can disintegrate and yields several isolated vapour structures which nearly collapse at the same time. Some examples of complex collapses and breaking processes are given in figures 9.14(a), 9.16(a)(b), 9.17(a). This behaviour is also consistent with the observed breaking process of the cavitation vortex when it begins to collapse. As supposed earlier in the case of near wall collapses, the observed main cavity around collapse time could correspond to the shadow of numerous vapour structures which coalesce during the rebound. Indeed, this could explain how a main cavity causes the production of a thick shock wave pattern.
  It is clear that the collapse and the associated shock wave is a very local phenomenon which is at first initiated by a part of a vapour structure, and then propagates within it (see 9.15(c)). This is another characteristic of the collapse of

isolated cavities. Moreover, although a cavity is submitted to the shock wave transient generated by another cavity, it generally does not collapse instantaneously (see 9.17(b)), which could show that a shock wave transient might not have a dominant influence on the collapse time of independent cavities.

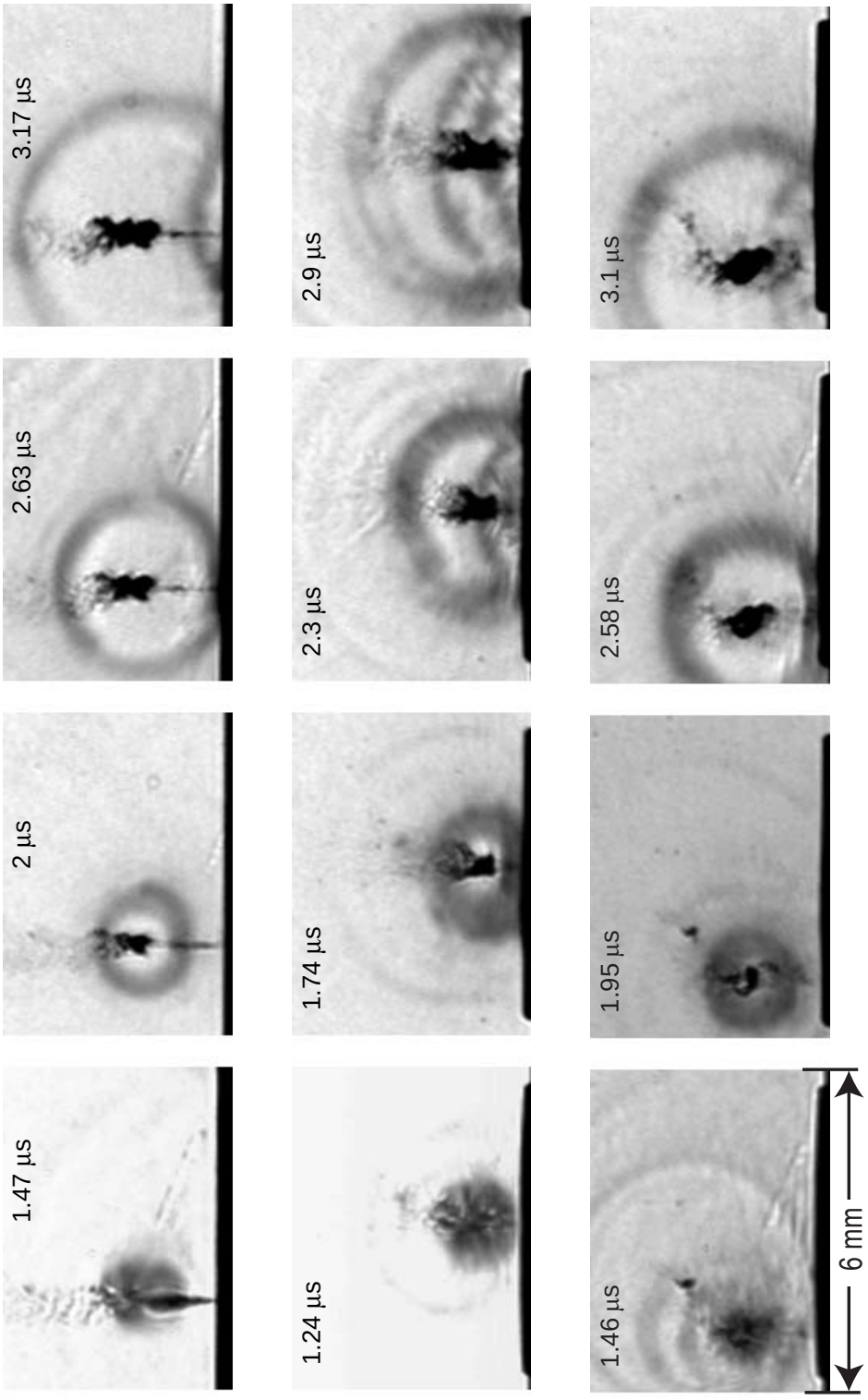

Figure 9.12: High-speed visualisations at 2.10^6 fps
(a) N=200 rpm, Q=0.58 l/s, σ=1.6
(b) (c) N=200 rpm, Q=0.66 l/s, σ=1.2

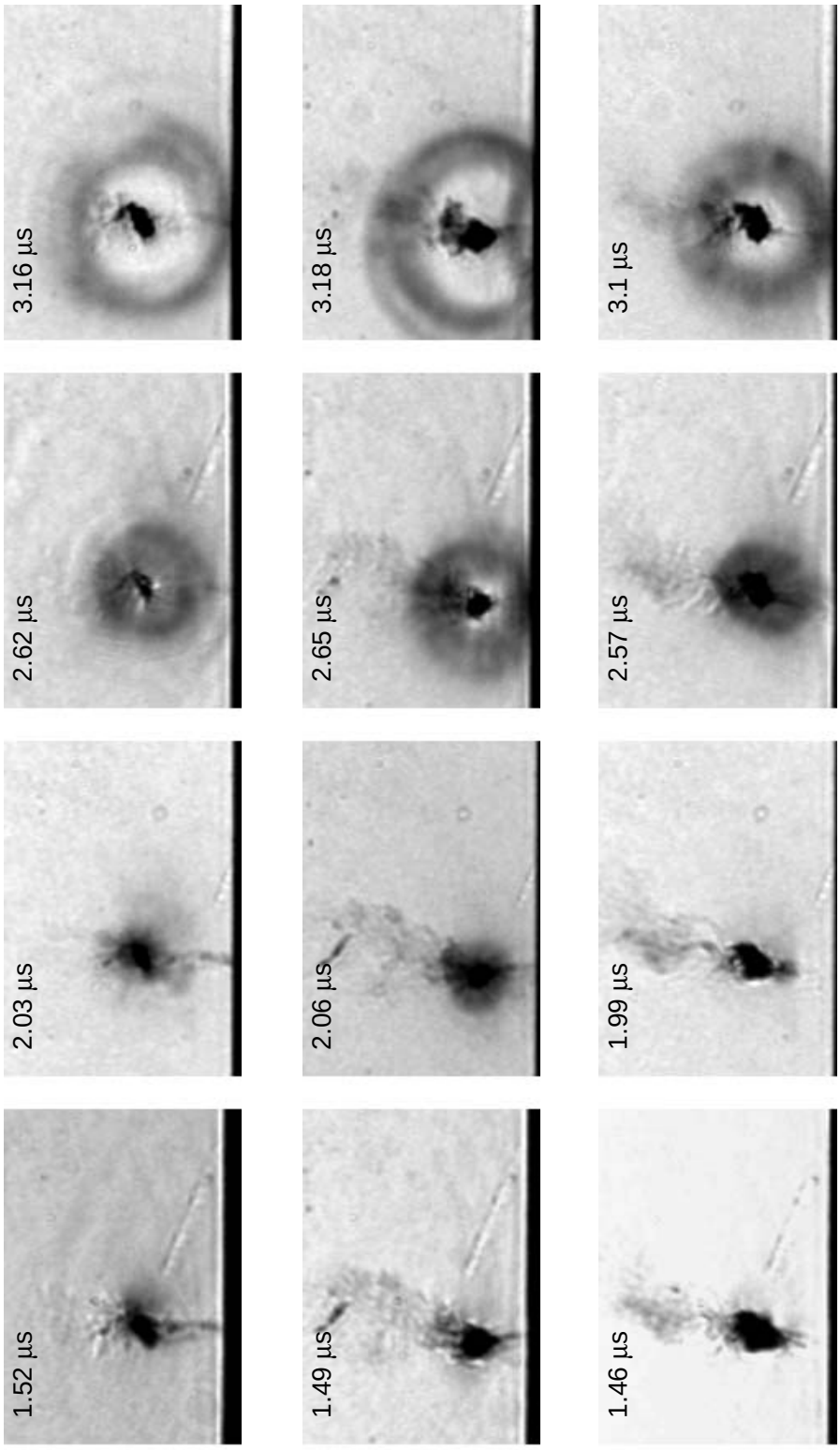

Figure 9.13: High-speed visualisations at 2.10^6 fps
(a) (b) (c) N=200 rpm, Q=0.58 l/s, σ=1.6

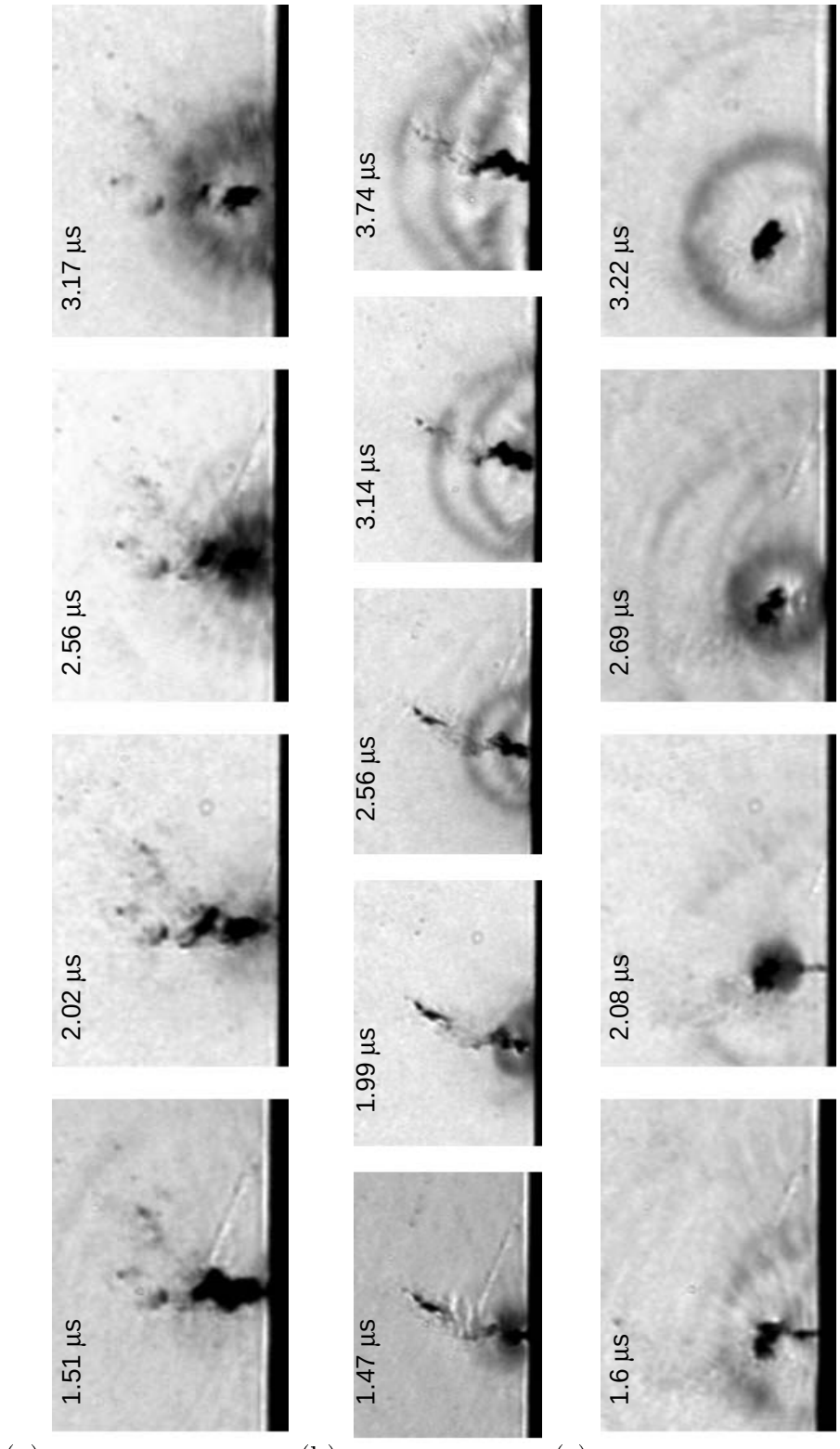

Figure 9.14: High-speed visualisations at 2.10^6 fps
(a) (b) (c) N=200 rpm, Q=0.58 l/s, σ=1.6

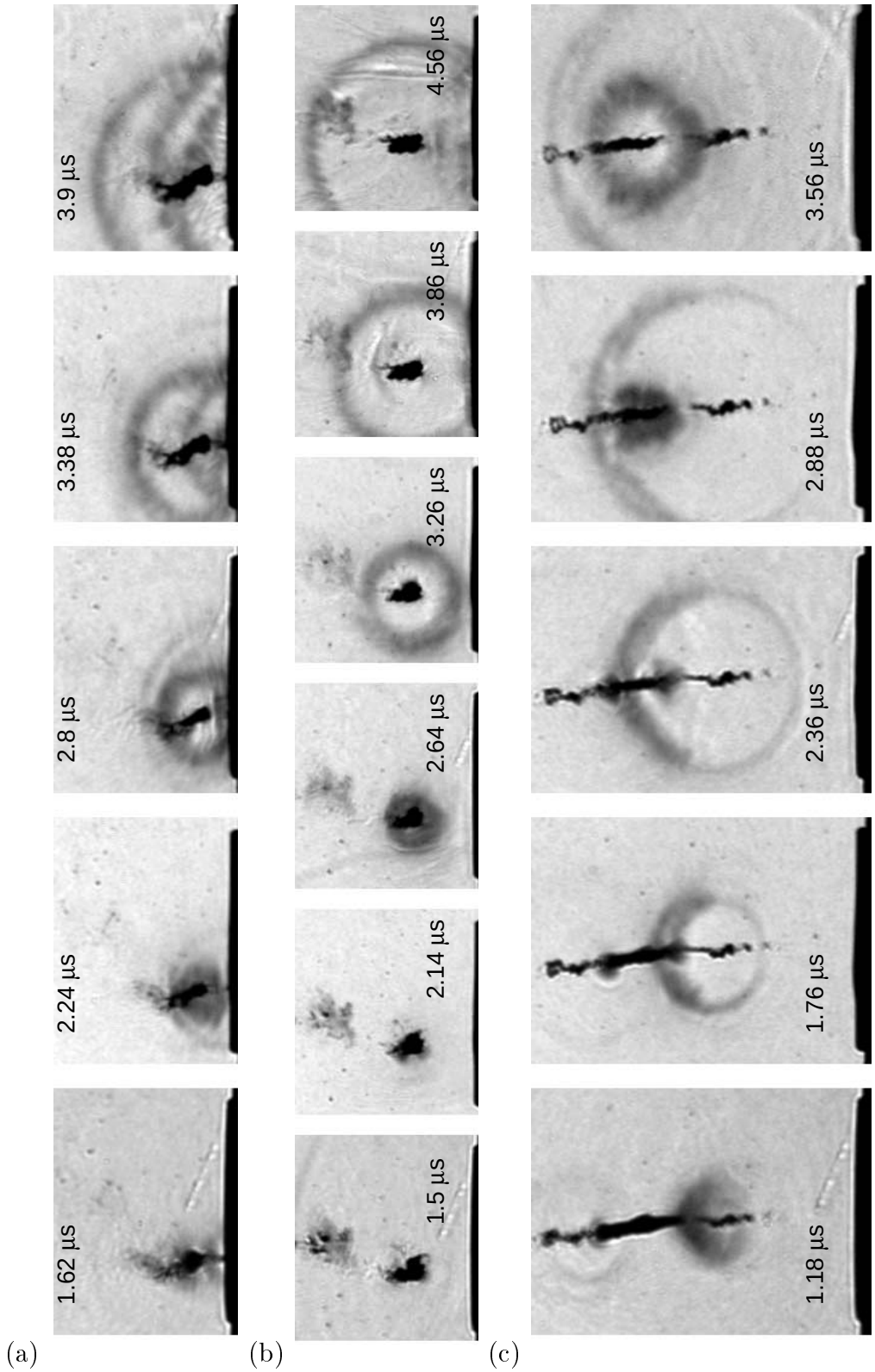

Figure 9.15: High-speed visualisations at 2.10^6 fps
(a) (b) (c) N=200 rpm, Q=0.66 l/s, σ=1.2

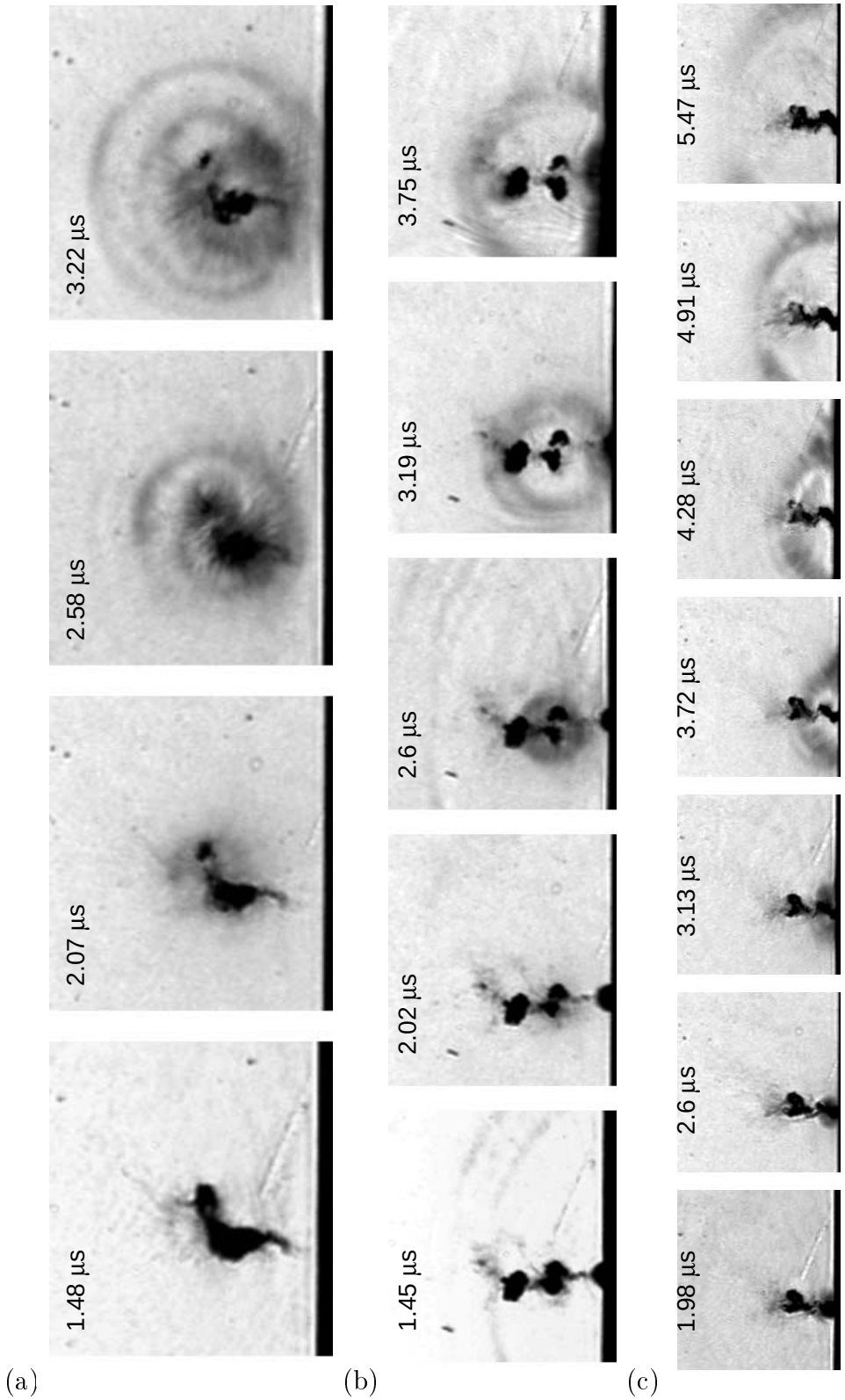

Figure 9.16: High-speed visualisations at 2.10^6 fps
(a) (b) (c) N=200 rpm, Q=0.58 l/s, σ=1.6

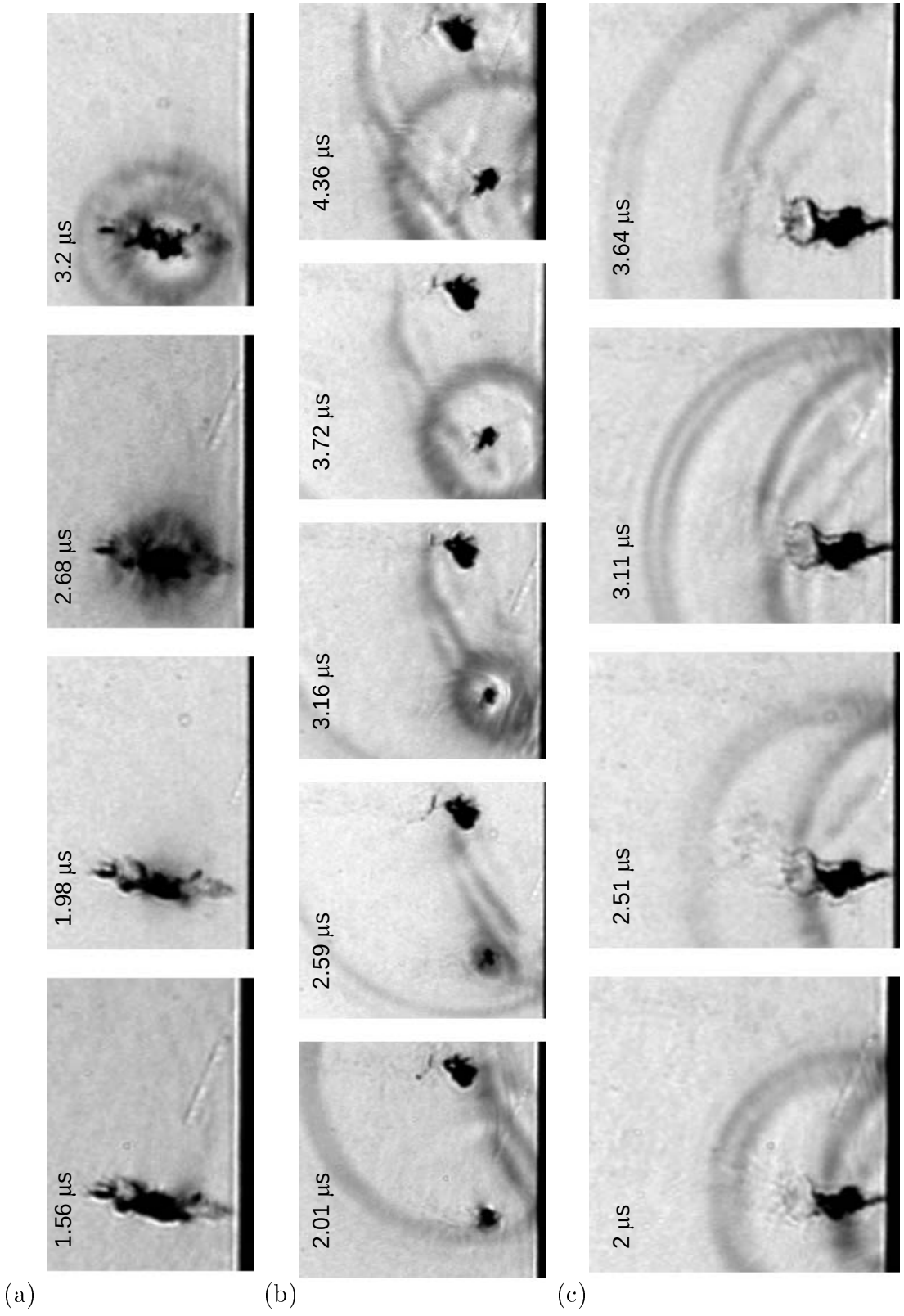

Figure 9.17: High-speed visualisations at 2.10^6 fps
(a) (b) (c) N=200 rpm, Q=0.58 l/s, σ=1.6

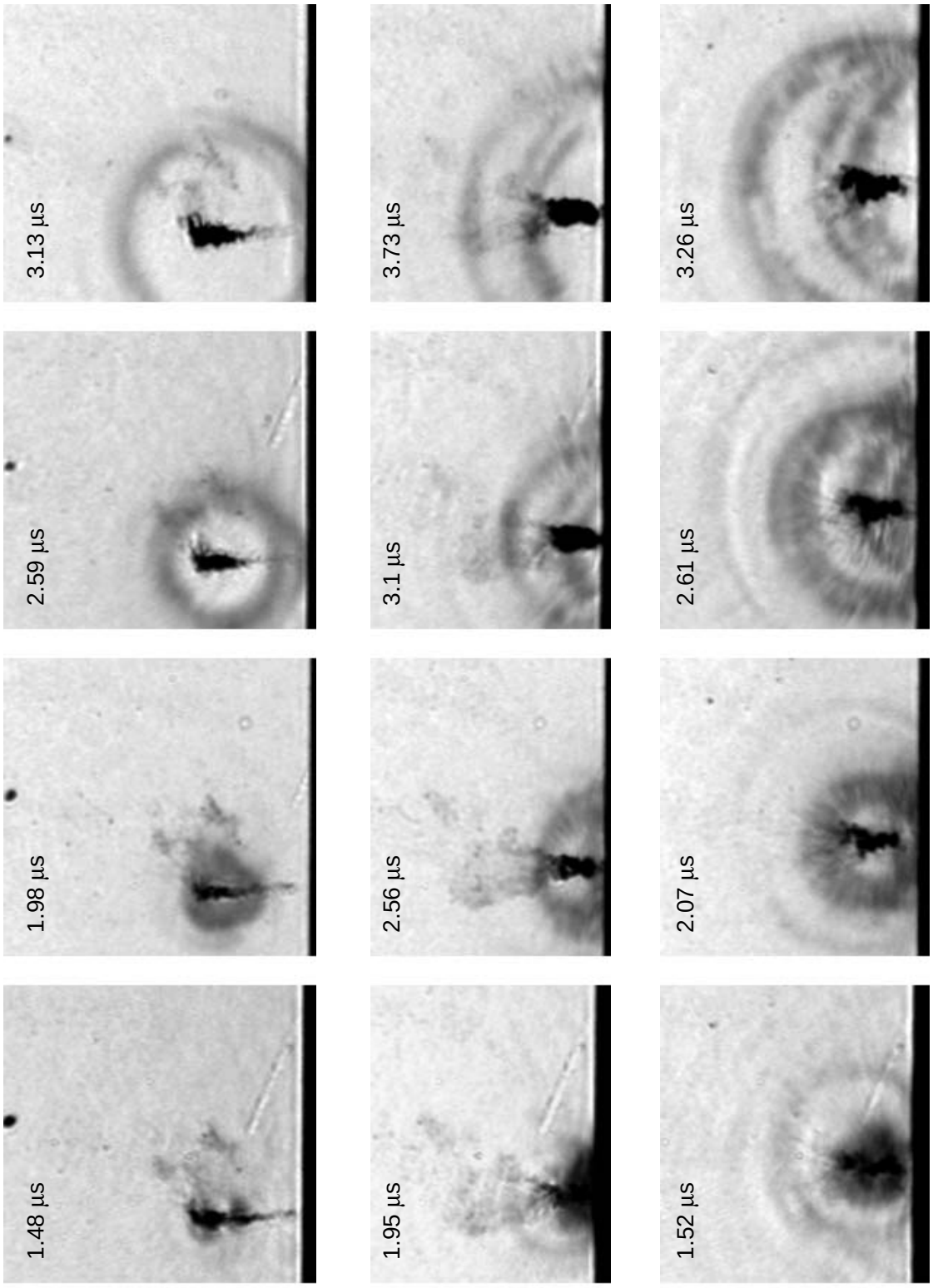

Figure 9.18: High-speed visualisations at 2.10^6 fps
(a) (b) (c) N=200 rpm, Q=0.58 l/s, σ=1.6

9.6 Collapse time and boundary velocity

9.6.1 Shock wave velocity

Propagation of shock waves is calculated by using the intercorrelation method that is presented in paragraph 9.3.2. The first wave radius corresponds to the outer envelope of the first wave pattern that can be clearly identified in the shadowgraph. The corresponding time is posterior to the time when the dark contrast merges with the vapour phase. Then, to estimate the velocity of incident shock waves that are propagating in the fluid, a linear regression curve is fitted on the calculated wave radius R_s data. Obtained velocities C_s for the different hydrodynamic conditions are listed in table 9.1. The measured velocities are nearly equal to the sound speed : between 1350 $m\,s^{-1}$ and 1400 $m\,s^{-1}$ in average.

Furthermore, since only sound velocities are measured, it shows that supersonic velocities must only concern the vicinity of vapour phase at collapse time. In fact, these occur when the dark light contrast around the vapour cavity is observed in shadowgraphs. This hypothesis would be in good agreement with recent experiments carried out by Holzfuss *et al.* (1998), where the early stage of the rebound of a sonoluminescent air bubble exited by acoustic waves is studied : the cavity is found to expand faster than the sound speed of the host liquid within a short distance of 100 μm. Afterwards, the wave slows down to the sound speed and continues as a normal acoustic transient.

9.6.2 Production of the shock

The time at which the shock departs can be estimated by considering a constant velocity of the shock wave. Then, the time at which the wave radius is zero gives the collapse time, noted t_c. However, assuming that the shock is supersonic at the early stage of the rebound, t_c might be underestimated. As an illustration of the obtained extrapolated collapse time, see figures 9.19 to 9.22.

9.6.3 Minimum volume of the cavitation vortex

Visualisations provide a way to investigate the mean vapour growth at the rebound of the cavitation vortex. However, because of both the lack of time and image resolutions, obviously it is impossible to determine exactly the time corresponding to the minimum volume, and thus to calculate the interface velocity at the early stage of the rebound. Nevertheless, there are some visualisations where the minimum volume could be situated in the first image, see the sequences in figures 9.12 (a)(b)(c). In these visualisations, the cavity grows rapidly between the first and the second frame, where the outgoing shock wave is clearly defined. In some other cases, like in figure 9.13 (a)(b),

the vapour volume is larger but still small ($<$0.4 mm) in the third frame where the vapour cavity is growing while the outgoing shock wave is just steepened.

On the other hand, there are many cases where the visualised minimum volume is larger, like in the figures 9.13(c), 9.14 (a)(c) and 9.15 (a)(b). However, as it was already suggested, the collapse is a very local phenomenon. Thus, only a part of the cavity collapse at a time, so that the global volume remains important.

9.6.4 Vortex boundary velocity

Boundary velocities $V_c = \delta R_c(t)/\delta t$ are calculated by considering pairs of consecutive frames in sequences. As an example, let us consider the visualisations in which the time of minimum volume is the most probable in the first frame, in figures 9.19 and 9.20 (see corresponding enlarged sequences in figure 9.12 (b)(a)). Maximum velocities are obtained at the rebound with a velocity of 310 $m\,s^{-1}$ and 167 $m\,s^{-1}$. Afterwards, the growth rate diminishes. As other examples in figures 9.21 and 9.22, the rebounding velocities respectively are 210 $m\,s^{-1}$ and 198 $m\,s^{-1}$.
Similar velocities have been calculated for 42 visualisations, giving mean values between 149 $m\,s^{-1}$ and 229 $m\,s^{-1}$ (see table 9.1). Nevertheless, as these velocities do not exactly concern the rebound, they are underestimated.

Boundary velocity at the rebound can be estimated by considering an extrapolated collapse time. This can be either done by taking t_c, which is deduced from a constant velocity of the shock wave, or by considering a constant acceleration of the bubble expansion, giving the collapse time t_c'. In fact, a constant acceleration extrapolation is a compromise between the velocity predicted by the theory of Gilmore (1952) (valid for $V_c/a_0 < 0.3$), and the velocity that would be obtained by taking into account the compressibility of the gas within the cavity. The Gilmore model leads to velocities which tend to infinity as $(R_0/R_c)^{0.5}$ (where R_0 is the size of initial radius of a bubble). However, since the collapse is decelerated because of the presence of gas within the bubble, velocities are overestimated at collapse time.

To compare the time of the minimum volume and the estimated collapse times t_c and t_c', let us simply consider the examples presented in figures 9.19 and 9.20, where the cavity volume are minimum in the first image, at time 1.24 μs and 1.47 μs. The extrapolated collapse times are respectively $t_c = 0.89\ \mu s$ and $t_c' = 0.88\ \mu s$ for 9.19, and $t_c = 1.51\ \mu s$ and $t_c' = 1.39\ \mu s$ for 9.20. Therefore, both the calculated collapse times are consistent, and lead to an uncertainty which is roughly equal to the exposure time of the visualisation (150-300 ns). Moreover, since the collapse time is calculated by considering a constant velocity of the shock wave, this confirms that supersonic velocity concerns the very vicinity of the vapour cavity at collapse time.

Furthermore, by taking the extrapolated collapse time t_c, the mean boundary veloc-

ity of the cavitation vortex is calculated by considering the time t_1 which corresponds to the first cavity radius R_1 posterior to t_c. This velocity is noted V_c' and is defined as :

$$V_c' = \frac{R_1}{t_1 - t_c} \text{ with } t_1 - t_c > 0 \tag{9.5}$$

Obtained results are given in table 9.1. As it was expected, cavitation vortex boundary velocities are greater than the instantaneous velocities V_c : between 343 $m\ s^{-1}$ and 490 $m\ s^{-1}$.

As has been shown earlier in paragraph 9.6.3, the collapse is a very local phenomenon. Thus the local velocities involved in a complicated vapour cavity collapse may be even much higher than the measured mean growth rate.

Q	σ	C_s	ΔC_s	V_c	ΔV_c	V_c'	ΔV_c'	Pop.
0.58 l/s	1.6	1345 m/s	43 m/s	149 m/s	35 m/s	343 m/s	113 m/s	22
0.66 l/s	1.2	1398 m/s	62 m/s	181 m/s	77 m/s	486 m/s	205 m/s	12
0.76 l/s	0.9	1407 m/s	39 m/s	229 m/s	99 m/s	490 m/s	265 m/s	8

Table 9.1: Shock wave velocity and maximum boundary velocity

9.6.5 Impact efficiency of the cavitation vortex generator

It is interesting to compare the number of cycles of CVG with the number of generated impacts. This has been realized in the context of the work of Maamouri (1989). In these tests, copper specimens were used, and hydrodynamic conditions were similar to those of the present study, with $Q = 0.76\ 10^{-3}\ m^3 \cdot s^{-1}$, $N = 200\ rpm$. It appears that the number of impacts is greater than the number of cycles of CVG : a factor 2.5 is measured with a short exposure time of 30 s, in which case overlapping of impacts is eliminated. In addition, grouped impacts are observed. Consequently, this confirm that each isolated cavitation vortex yields multiple impacts.

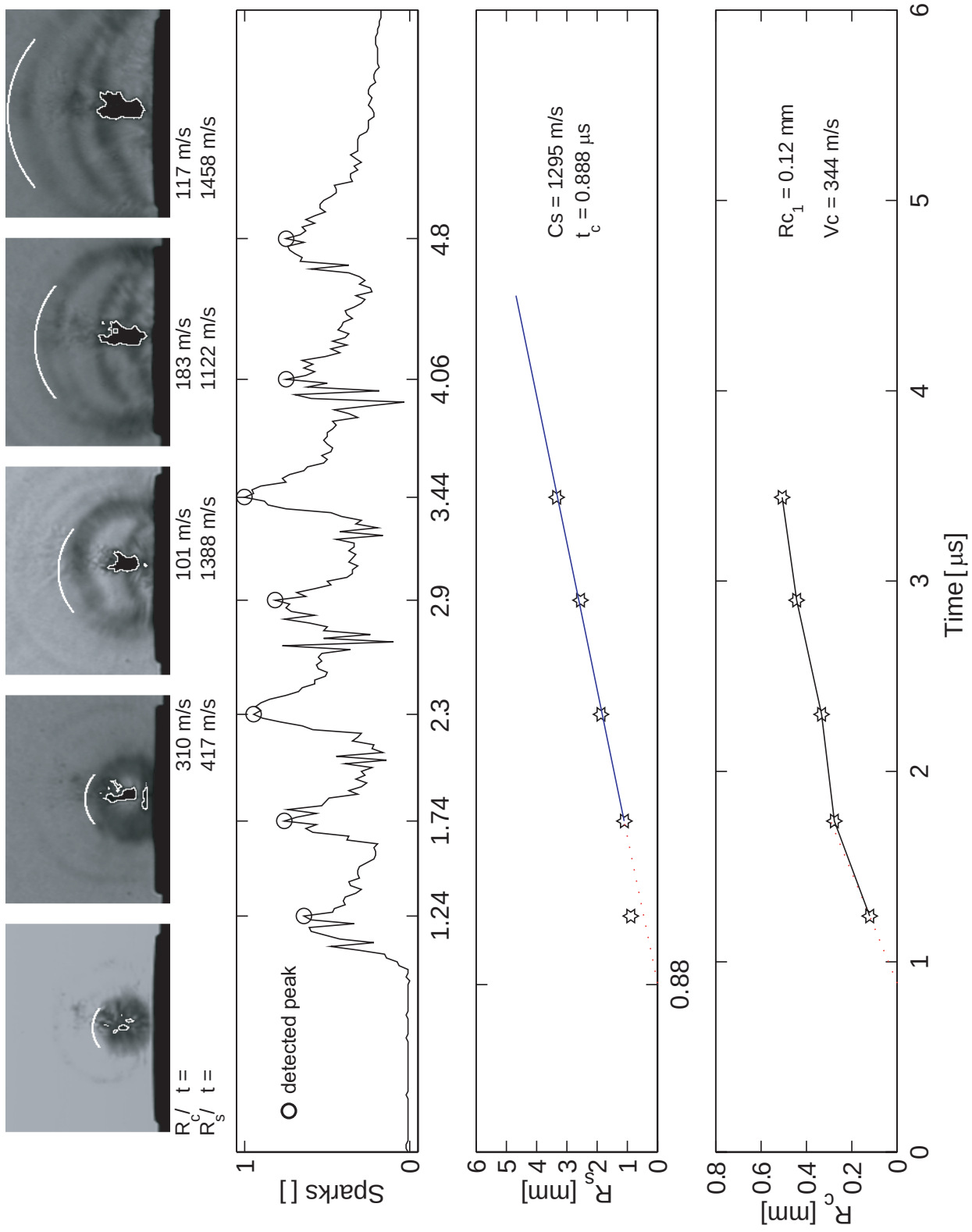

Figure 9.19: Collapse time determination and cavitation vortex characteristics N=200 rpm, Q=0.66 l/s, σ=1.2

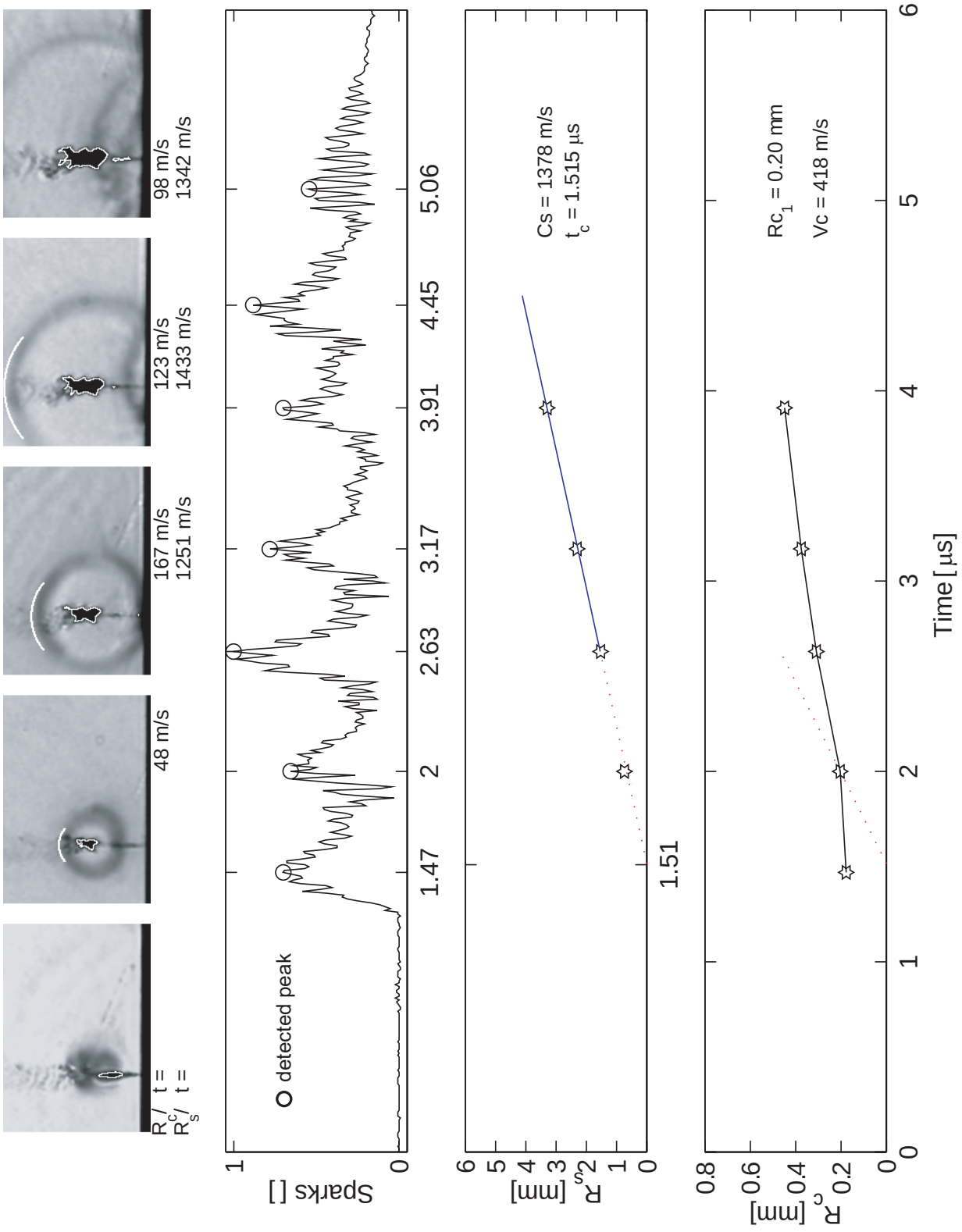

Figure 9.20: Collapse time determination and cavitation vortex characteristics N=200 rpm, Q=0.58 l/s, σ=1.6

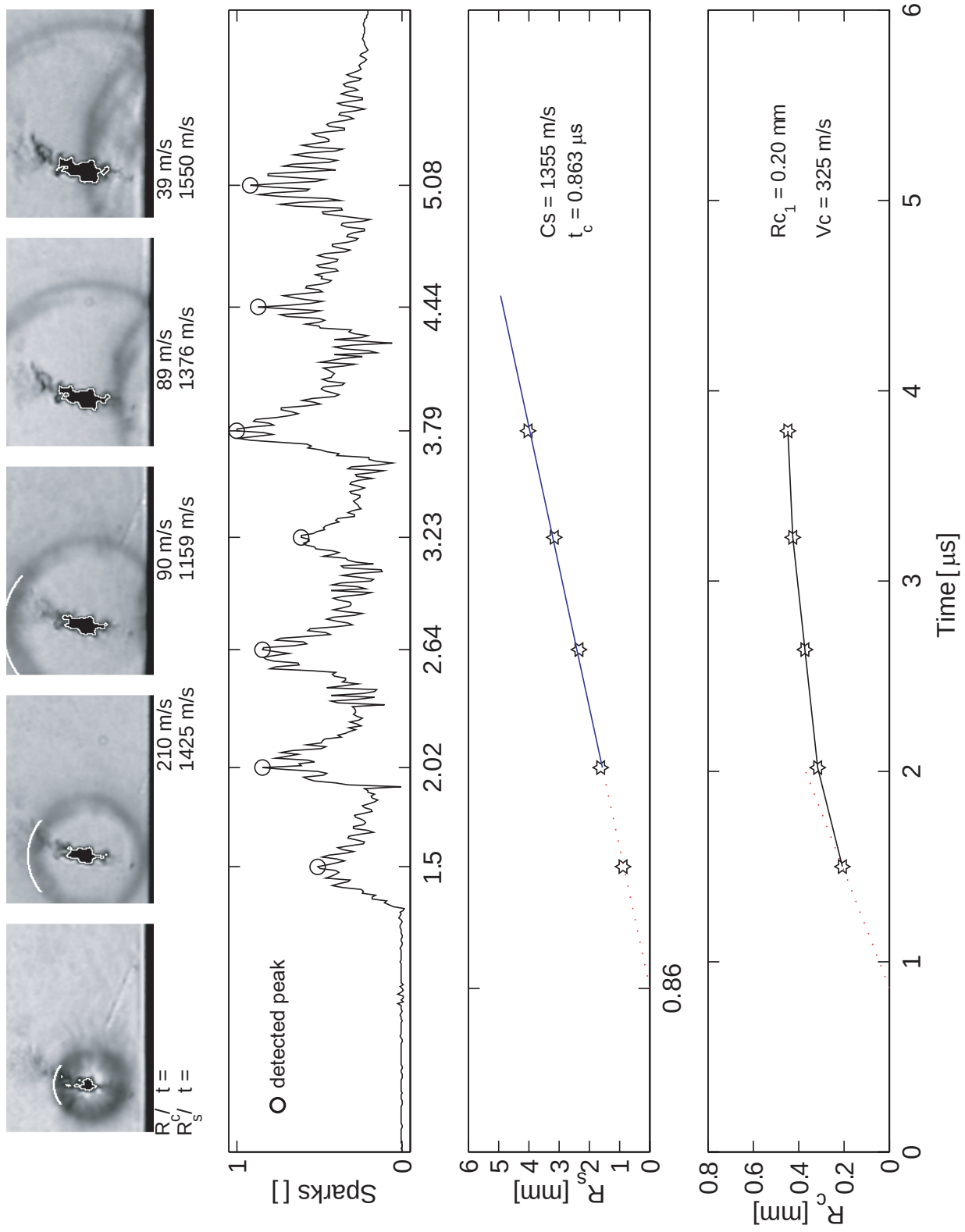

Figure 9.21: Collapse time determination and cavitation vortex characteristics
N=200 rpm, Q=0.58 l/s, σ=1.6

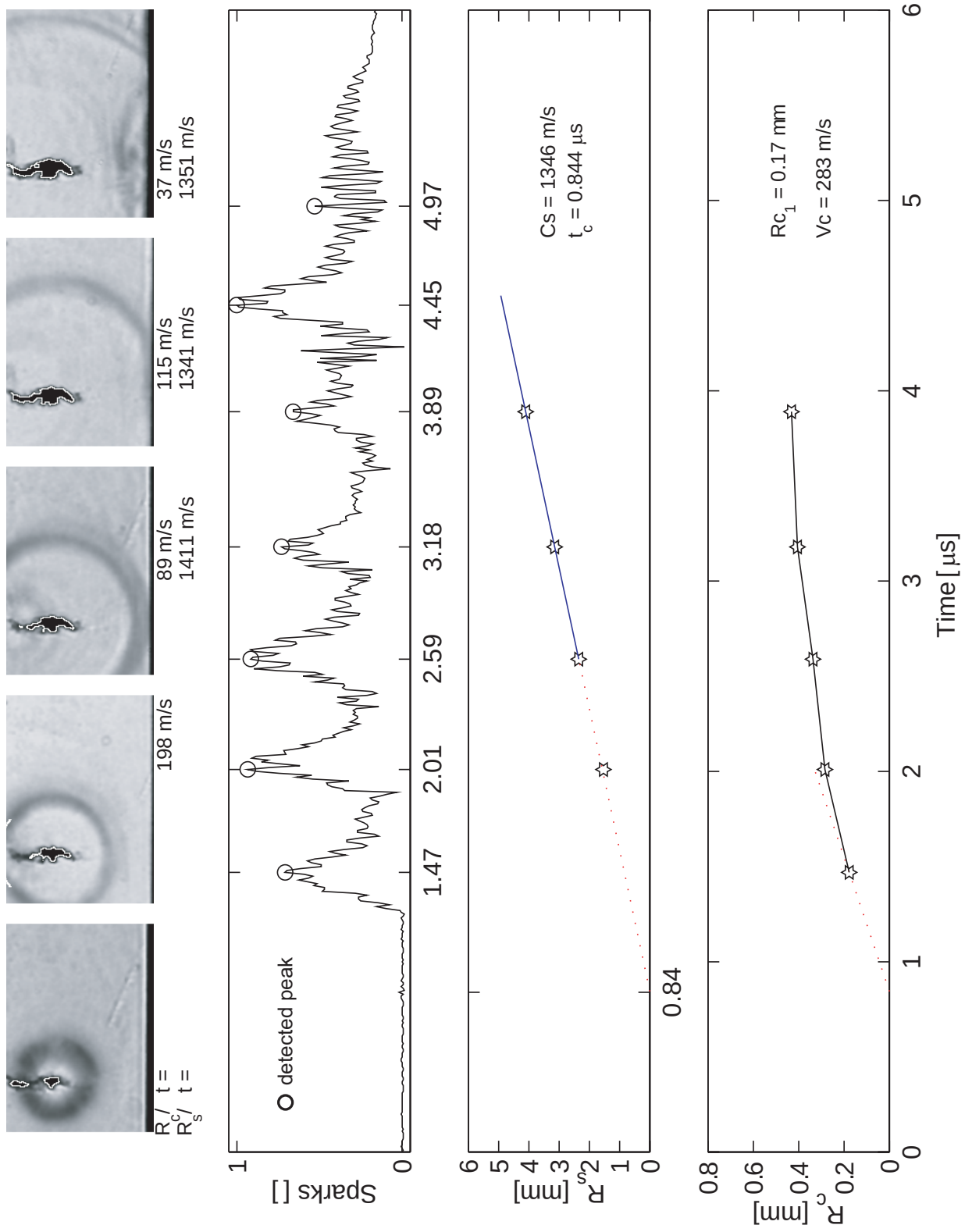

Figure 9.22: Collapse time determination and cavitation vortex characteristics N=200 rpm, Q=0.58 l/s, σ=1.6

Chapitre 10

Simultaneous captures of shock waves and luminescence

10.1 Measurement

10.1.1 Hydrodynamic conditions

These experiments are performed for a single hydrodynamic condition with the flow rate Q = 0.58 l/s in the 4-windows test section. This condition is the most suitable because it statistically generates more far wall collapses, in which cases the entire cavity and incident shock wave contours can be well segregated from the test section wall and from the complicated shadowgraphy pattern. Furthermore, both the exposure time of the intensified light camera and the frame period of high-speed visualisations are set to 500 ns, which provide us with an acceptable probability of capturing of the luminescence emission, which is small because of the collapse jitter of the cavitation vortex.

10.1.2 Image acquisition

The image acquisition is based on the high-speed visualisation system, on which the intensified light camera (IC *QUICK 05A* ®) is implemented and replaces one of the 8 CCD modules (Philipps FTM 800) of the Cranz-Schardin camera (CS).
The details of the acquisition are presented schematically in figure 10.1. The acquisition can be briefly described as follows : a video acquisition of 8 frames (1 from the IC and 7 from CS) is realized with the Genesis frame grabber, whose digitiser specifications are configured for the CCD modules. Indeed, the IC camera and modules works with the CCIR video standard (290 lines of 758 pixels/line), and therefore all video fields can be acquired in the same manner. This requires that both the separated

vertical and horizontal synchronization signals V_{synch} and H_{synch}, as well as the video signal, are supplied to the frame grabber. However, as the IC camera does not have a storage section and delivers a continuous video signal, the video field containing luminescence must be asynchronously grabbed. This asynchronous capture is triggered by the vertical synchronization signal V_{Synch} of the IC camera. Then, once the video field containing luminescence is acquired, video fields of the CCD modules are sequentially retrieved by the frame grabber.

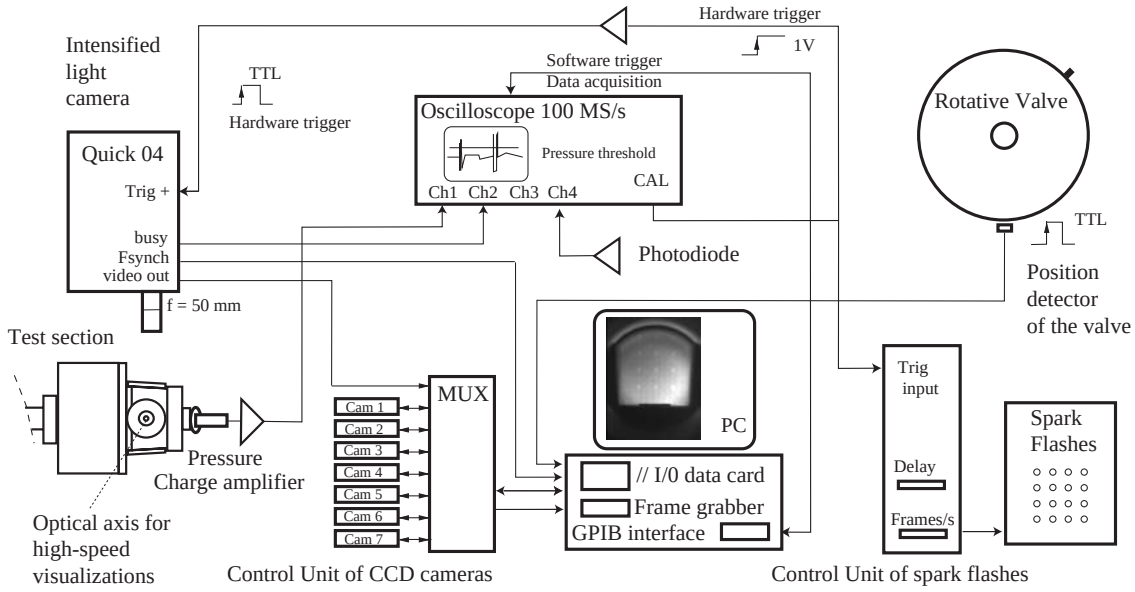

Figure 10.1: Schematic of the simultaneous visualisations

It has to be noted that the principal requirement to obtain simultaneous visualisations is to close the shutter of the IC just before the flashing of the CS. Both the sparks of the high-speed shadowgraphy and the shutter of the IC camera are triggered on a threshold of the dynamic pressure signal through the oscilloscope. The shutter of the IC is controlled with an accuracy of 50 ns.

10.2 Synchronous shock wave and luminescence emission

Assuming that luminescence is emitted when the vapour volume reaches its minimum volume (Barber & Putterman, 1992), the luminescence time occurrence would correspond to the collapse time. Furthermore, assuming that the production of the

shock is generated by the rebound of the vapour cavity, the appearance of the luminescence must correspond to the production of the shock.

In order to test whether these hypothesis are still consistent in the case of the cavitation vortex, simultaneous visualisations are performed. As a first example, the simultaneous visualisations presented in figure 10.2 are examined. The vapour cavity is captured both before and after the luminescence emission. Then, the extrapolated collapse time is 3.24 μs for a shock wave velocity of 1422 $m\ s^{-1}$, which lies within the integration period of the IC : 3.16–3.91 μs.
As a second example, let us consider the simultaneous visualisations in figure 10.3. Although luminescence is principally unique, this is a counterexample where the emission of a double luminescence source is clearly observed prior to the outgoing shock wave, whose measured velocity is 1417 $m\ s^{-1}$. The corresponding collapse time is 0.80 μs, which is still included in the exposure time windows of 0.7–1.2 μs.

Similar analysis of other simultaneous visualisations (D.1, D.2, D.3 and D.4) leads to the same results. The shock wave and the luminescence are emitted synchronously, with a time uncertainty of 500 ns. Moreover, the epicentre of the shock wave corresponds to the location of the luminescence source (Couty *et al.*, 2001).

10.3 Overpressure estimations

As it was demonstrated earlier, supersonic velocities might only concern the very vicinity of the vapour cavity at collapse time. Then, because of both lack of time and image resolution, the estimation of the collapse time and of the velocities has a large uncertainty. Nevertheless, on the basis of the visualisation results, the measured cavitation vortex boundary Mach number can be known in function of the equivalent radius of the vortex. Afterwards, assuming a bubble analogy, the Gilmore model could be applied to the characteristics of the cavitation vortex by considering some initial conditions : - the initial equivalent radius R_o, the driving pressure p_∞, and the sound speed in water $a_0 = 1500\ m\ s^{-1}$. Then, the bubble boundary velocity V_c and the radius R_c is governed by the relation :

$$\left[\frac{R_0}{R_c}\right]^3 = \left[1 - \frac{V_c}{3a_0}\right]^4 \left[1 + \frac{3\rho_\infty V_c^2}{2(p_\infty - p_o)}\right] \tag{10.1}$$

It can be noted that as R_c tends to zero, V_c varies as $R_c^{-\frac{1}{2}}$, in contrast to the incompressible theory in which V_c varies as $R_c^{-\frac{3}{2}}$. Thereafter, measured Mach numbers at the rebound of the cavitation vortex are compared with Gilmore's prediction in figures 10.5 ((a) corresponding to high-speed visualisations in figures 9.19 - 9.22) and (b) to simultaneous visualisations in figures 10.3 and 10.4).

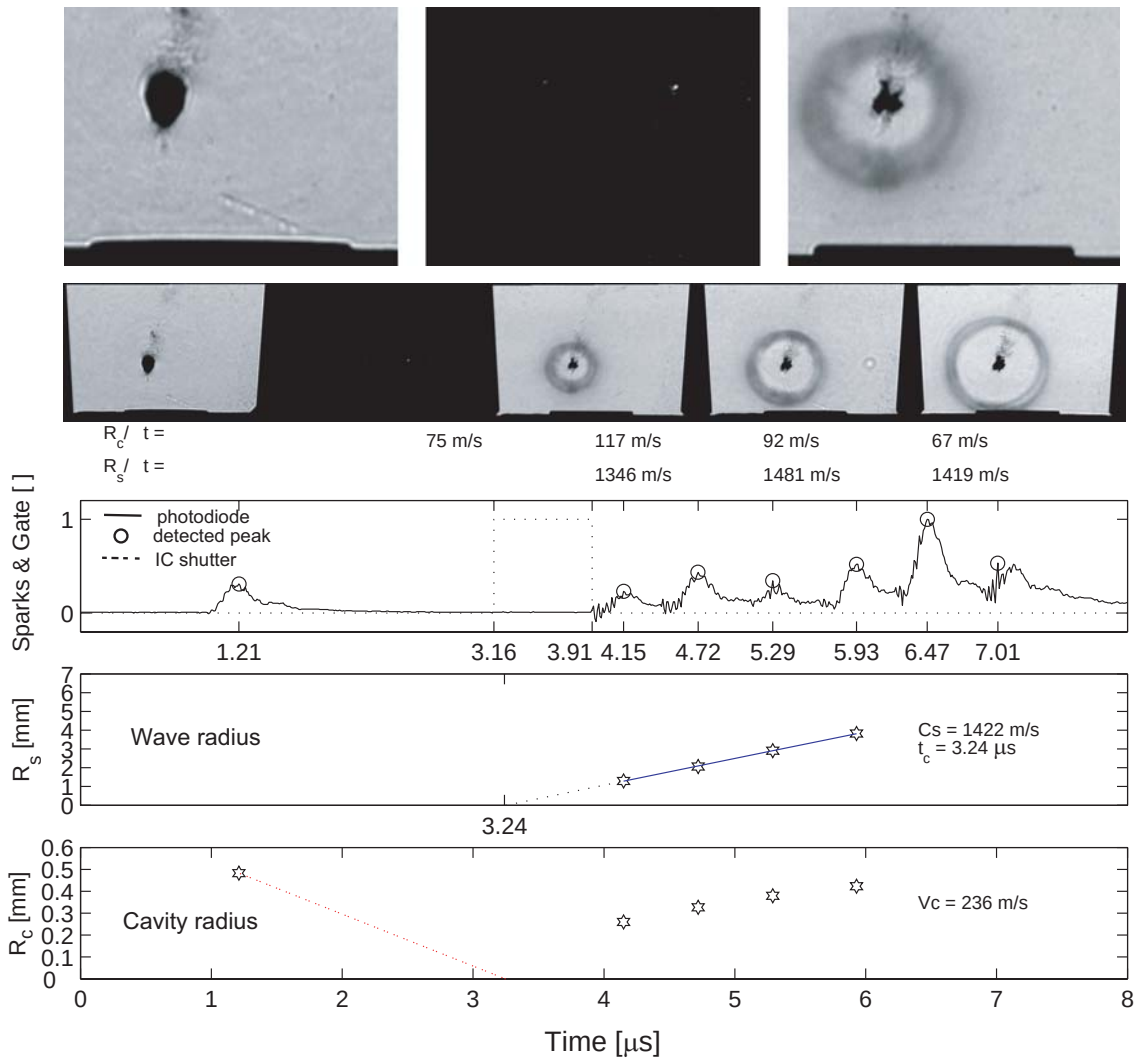

Figure 10.2: Simultaneous captures of luminescence and shock wave (2 10^6fps). Note the first image of the sequence where the vapour cavity is visible 3 μs prior to the luminescence spark. Q=0.66 l/s, σ=1.6, N=200 rpm

So far, since initial conditions are only estimated, and as the cavities are not spherical, velocities remarkably have the same order of magnitude as those predicted by the model.

Furthermore, by extrapolating the evolution of the radius by considering Gilmore's model, and assuming that the minimum size of the cavity is similar to the size of observed impacts in CVG, typically 10 μm, the corresponding minimum radius ratio would be $10e-6/6e-3 \simeq 1.6e-3$, leading to a Vortex Mach number > 1. Moreover, overpressure up to several GPa has been obtained, whose amplitude is inversely

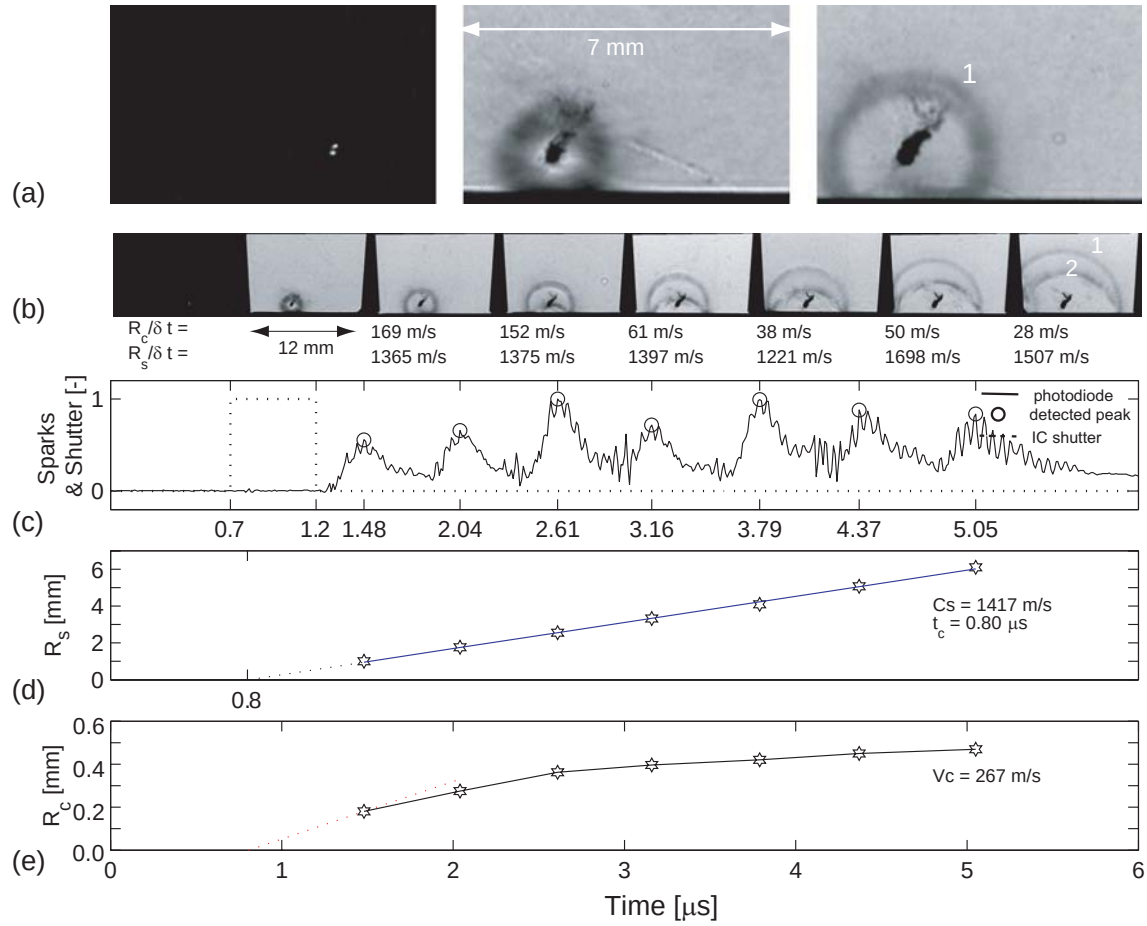

Figure 10.3: (a) Simultaneous captures of luminescence and shock wave (2 10^6fps). (b) Sequence showing the development of the shock wave. The white subscript 1 indicates the primary wave and subscript 2 indicates the wave reflected at the bottom surface. (c) Timing of spark pulses of the CS and shutter signal of the IC. (d) Shock velocity versus time. (e) Cavity growth versus time. Q=0.58 l/s, σ=1.6, N=200 rpm

proportional to the distance from the epicentre. However, it can be noted that the decelerating effect due to the presence of a non condensable gas in the bubble is not taken into account, so that the cavitation vortex Mach number might be overestimated.

However, Mach numbers greater than 0.25 (350 $m\,s^{-1}$) are therefore confirmed by both the extrapolated velocity V_c' (equation 9.5) and the theoretical boundary motion of an equivalent Gilmore bubble (equation 10.1). As an estimation of the overpressure, the water hammer approximation can be used :

$$\Delta P = \rho V_c C_s \tag{10.2}$$

Then, the equation proposed by Heymann (10.3) gives an approximation of the shock

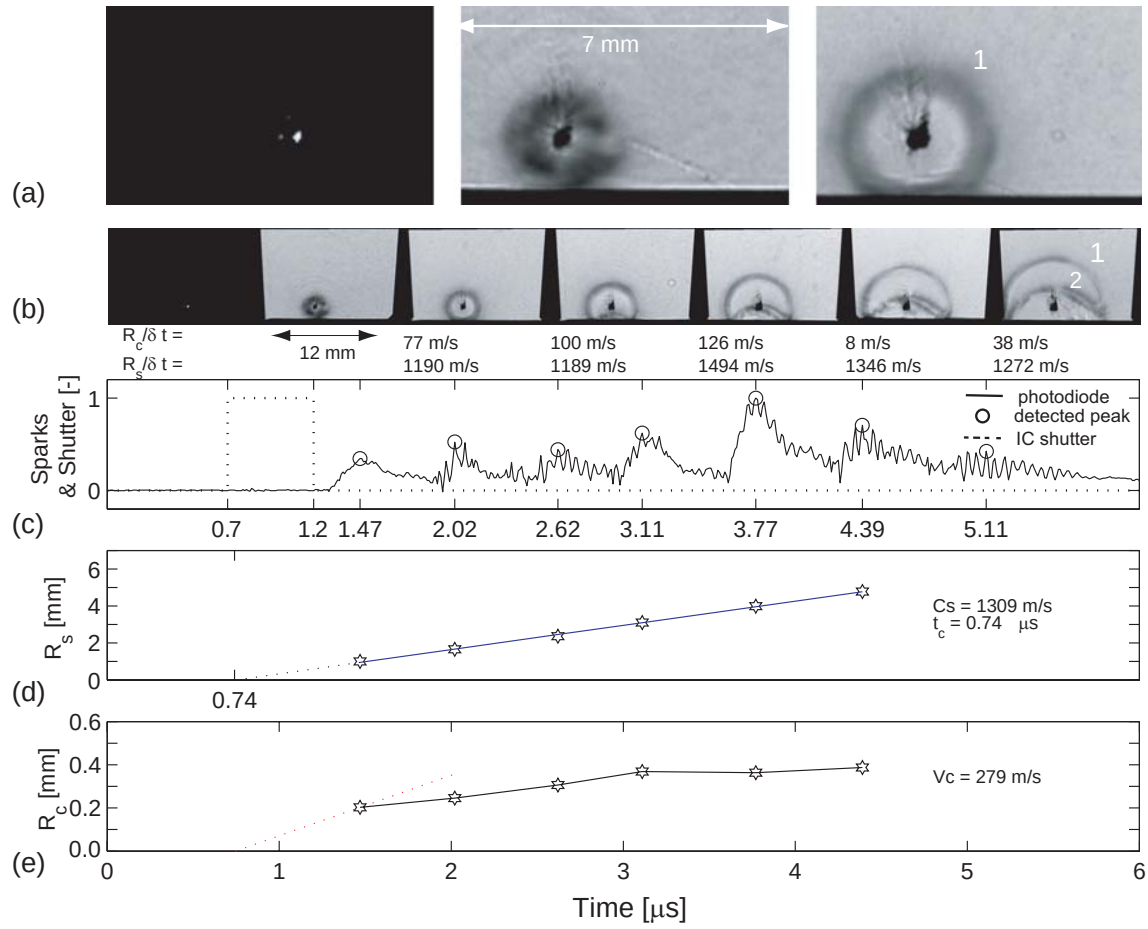

Figure 10.4: (a) Simultaneous captures of luminescence and shock wave (2 10^6fps). (b) Sequence showing the development of the shock wave. The white subscript 1 indicates the primary wave and subscript 2 indicates the wave reflected at the bottom surface. (c) Timing of spark pulses of the CS and shutter signal of the IC. (d) Shock velocity versus time. (e) Cavity growth versus time. Q=0.58 l/s, σ=1.6, N=200 rpm

velocity. Finally, both equations 10.2 and 10.3 can be used to estimate the overpressure, which according to Ridah (1987, 1988), gives very good results compared to the exact solution of Tait's equation.

$$C_s = a_0(1 + \frac{2V_c}{a_0}) \tag{10.3}$$

Thus, a lower limit of the overpressure is found to be equal to 770 MPa, which is sufficient to cause cavitation damage on material such as stainless steel :

$$\Delta P \geq \rho V_c C_s = \rho V_c \left[a_0(1 + \frac{2V_c}{a_0}) \right] = 770\ MPa \tag{10.4}$$

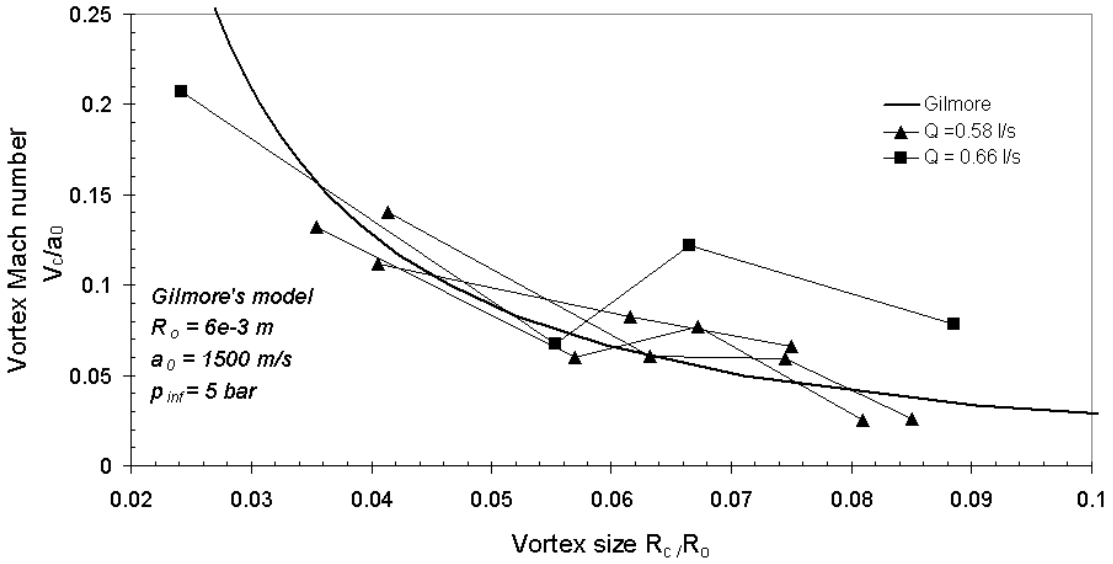

(a)

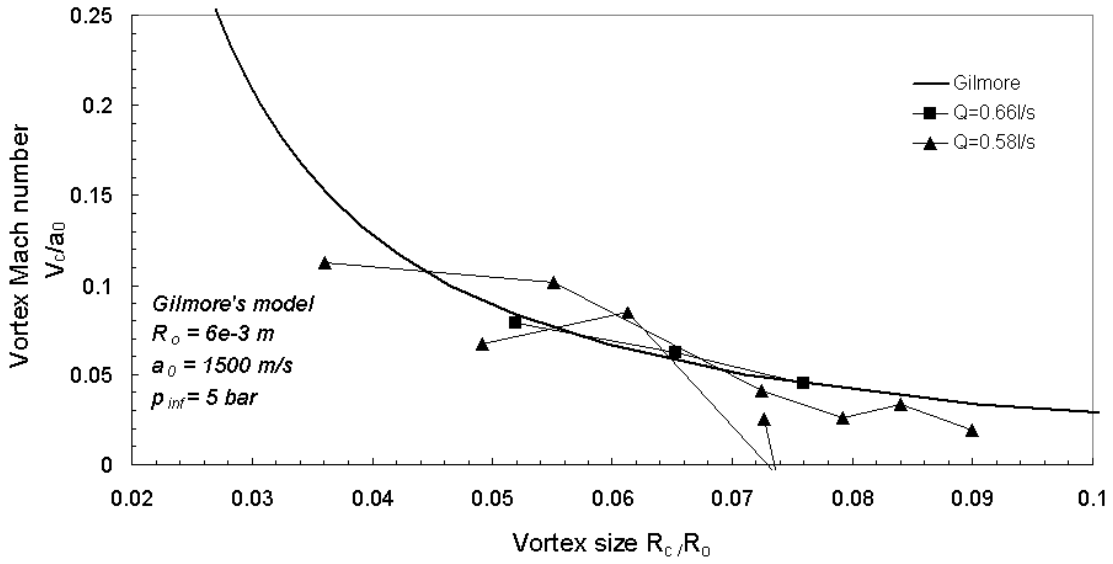

(b)

Figure 10.5: Vortex boundary Mach number. (a) From high-speed visualisations presented in figures 9.19–9.22. (b) From simultaneous visualisations presented in figures 10.3–10.4

Chapitre 11

Synthesis

11.1 Luminescence of cavitation vortex

The cavitation vortex collapse generate luminescence. Luminescence has been characterized in terms of location, occurrence in vortex dynamics and intensity. Moreover, the sensitivity to experimental parameters as well as the influence of flow parameters have been studied :

1. Most of luminescence is emitted at the first collapse time by the main cavity.
2. Emission occurs as short light bursts with a duration down to 10 ns and up to 100 ns.
3. Simultaneous visualisations have demonstrated that luminescence sources mingle with the shock waves epicentres. Moreover, luminescence and shock wave initiation occur within a time interval which is less than 500 ns. Furthermore, luminescence does not require the initial vapour cavity to be spherical. Although the source can be multiple, this is principally unique. Therefore, the luminescence phenomenon can be used to determine the collapse location.
4. Luminescence, in terms of detection success and intensity, is clearly increased with dissolved gas in water.
5. The vortex intensity is a driving parameter of the luminescence intensity. Moreover, the collapse location is strongly influenced by the intensity of the vortex : the last stage of the cavitation vortex collapse takes place closer to the wall when the vortex intensity increases. Furthermore, considering both the decrease of the wall distance and the increase of collapse strength with the increasing vortex intensity, one could suggest that there is an increase of cavitation aggressiveness when the vortex intensifies.

11.2 Cavitation vortex collapse

The main phenomenological observations and quantitative estimations can be summarized as follows :

1. The vapour cavity shape and structure are extremely variable. The collapse and the associated emission of shock waves are very local phenomena which can arise from different locations from the same main cavity. Indeed, vapour cavities can fission and principally emit multiple and successive shock waves from different epicentres. These shock waves can be either clearly segregated or combined, which can lead to a resulting strong shock wave.
2. Estimations of the mean boundary velocity result in maximum values greater than 350 $m\,s^{-1}$ at the rebound. As the collapse is not regular, local velocity at the boundary might be much higher. Measured mean boundary Mach numbers are in agreement with theoretical estimations of an equivalent "Gilmore" bubble.
3. As only sonic velocity of shock waves can be estimated, supersonic velocities must concern the very vicinity of the vapour structure at the collapse time.

CONCLUSIONS AND PERSPECTIVES

Conclusions

Cavitation aggressiveness on 2-D blades

Marking tests have been performed in the cavitation tunnel on 2D profiles with inserted specimens made of three different materials : aluminium, copper and stainless steel. The hydrodynamic parameters have been the flow velocity, the length of the leading edge cavitation cavity, and the presence of an additional pressure gradient, which has been simulated by a diverging duct. Then, 3-D profilometry analysis have been achieved, and pitting rates have been calculated : deformation volume rates, deformation energy rates and pitting rates. Finally, the collapse efficiency, which is defined as the ratio between a statistical energy distribution of cavity energy and the distribution of impact deformation energy, has been estimated. The results led to the following remarks :

1. In the case of the stable leading edge cavitation, impacts are principally concentrated at about the main cavity closure and are non overlapping impacts. For an unstable leading edge cavitation, impacts are more spread around the main cavity closure, and the presence of grouped impacts is usually observed.
2. Among the macroscopic flow parameters, the flow velocity is the main parameter on which pitting rates and deformation volume rates depends. Higher rates have been obtained in the case of the diverging test section (up to a factor 10). A scale effect can be noted by comparing rates obtained with the 2-D blades of different scales. Higher impact volumes are noted for the full scale 2-D blade than for the small scale one.
3. The collapse efficiency strongly depends on the flow velocity, the material and the flow angle of incidence. It is constant over the whole scale of energies for high flow velocities. Nevertheless, it is not constant for moderate flow velocities : it is lower for higher energies. As an explanation, it can be suggested that largest vapour structures, whose collapse times are higher, are transported more far away the cavity closure, and collapse at a larger distance to the wall than the smaller cavities. However, because of the lack of data for the large pits, this suggestion has to be considered with care.

Physical investigation of a cavitation vortex

Luminescence and collapse location

The observation of the luminescence of an isolated cavitation vortex collapse has been experimentally achieved for the first time. Moreover, simultaneous capture of luminescence and shock waves have been achieved. Luminescence has been detected with the help of a photomultiplier tube and an intensified light camera. Then, specific signal and image processing methods have been implemented in order to study the characteristics of the luminescence emission in terms of intensity and occurrence in the cavitation vortex dynamics. Furthermore, the sensitivity to experimental parameters, as well as the link with physical characteristics of the cavitation vortex and associated phenomena have been established :

1. Luminescence does not require the initial vapour cavity to be spherical. Although the source can be multiple, it is principally unique and corresponds to the centre of the main vapour cavity.
2. Most of luminescence is emitted at the first collapse time by the main cavity.
3. Emission occurs as short light bursts with a duration down to 10 ns and up to 100 ns.
4. Simultaneous visualizations have demonstrated that luminescence sources mingle with the shock waves epicentres. Moreover, luminescence and shock wave initiation occur within a time interval which is less than 500 ns.
5. Luminescence emission, in terms of detection success and intensity, is clearly increased with dissolved gas in water.
6. The vortex intensity is a driving parameter of the luminescence emission.

Then, the luminescence phenomenon has been used to determine the collapse location. As a remarkable result, the collapse location is strongly influenced by the intensity of the vortex : the last stage of the cavitation vortex collapse takes place closer to the wall when the vortex intensity increases.

Cavitation vortex collapse

The physical investigation of a cavitation vortex collapse with the help of shadowgraphy visualizations have been carried out. This study confirmed the complex hydrodynamic characteristics that can be involved in a cavitation vortex collapse. Furthermore, specific image processing methods have been developed in order to estimate the cavitation vortex boundary velocities and velocities of shock waves. Main phenomenological observations and quantitative estimations can be summarized as follows :

1. The cavitation vortex collapse leads to an irregular vapour cavity shape at the final stage. The collapse and the associated emission of shock waves are very local phenomena which can arise from different locations from the same main cavity. Indeed, vapour cavities can fission and principally emit multiple and successive shock waves from different epicentres. These shock waves can be either clearly segregated or combined, which can lead to a resulting strong shock wave.
2. Estimations of the mean boundary velocity result in maximum values greater than 350 $m\,s^{-1}$ at the rebound. As the collapse is not regular, local velocity at the boundary might be much higher. Measured mean boundary Mach numbers are in agreement with theoretical estimations of an equivalent "Gilmore" bubble.
3. As only sonic velocity of shock waves can be estimated, supersonic velocities must concern the very vicinity of the vapour structure at the collapse time.

Joint results : cavitation attack

The results of the cavitation vortex study (luminescence and collapse) suggest how the hydrodynamic parameters of the flow might be related with the cavitation aggressiveness. Cavitation attack principally depends on the following hydrodynamic parameters :

1. Assuming that luminescence intensity is related to the strength of the collapse, the increase of the intensity of the vortex leads to stronger collapses.
2. Independently of the types of vapour structures, each cavity can lead to multiple and successive micro-collapses, so that several impacts can be generated.
3. The last stage of the collapse of the cavitation vortices takes place closer to the wall, the more the circulation of the vortices in the flow increases.

Furthermore, it can be suggested that the flow velocity increases the intensity of the transient vortices which are generated by the leading edge cavitation. This leads the transient vortices collapse closer to the surface. Consequently, the cavitation aggressiveness of the leading edge cavitation increases.

Perspectives

Further investigations of a cavitation vortex

Cavitation impacts must be generated by hydrodynamic phenomena which take place in the very vicinity of the vortex cavity at collapse time. A cavitation vortex collapse presents complicated physical phenomena which requires more investigations. A proposal for further studies can be made :

1. Measurement of local boundary velocities and confirmation of the fission of vapour structures. High-speed visualisations with a spatial resolution down to 10 μm, and with an exposure time down to 10 ns are required.
2. Measurement of shock waves amplitudes and velocities in the very vicinity of the main cavity at collapse time. In fact, because of the combination of multiple shock waves which merge with the vapour cavity, a detailed study cannot be achieved with the shadowgraphy technique. More suitable visualisations techniques, such as color Schlieren photography or interferometric methods could be used. In addition, the collapse time can be determined by achieving simultaneous capture of luminescence and shock waves. Moreover, because of the collapse time jitter, the luminescence phenomenon must be used to synchronize the high-speed visualisations.
3. In future, the geometry of the CVG test section can be made 2-D by adding suitable transparent blocks. Thus, jets and effect of toral geometries might be visualised.
4. On the basis of the two preceding studies, estimation of a potential energy of a cavitation vortex might be made.

Aggressiveness of transient vortices

Although luminescence experiments need sophisticated experimental requirements, the luminescence phenomenon can be used to determine a map of collapse location of transient cavities in a more complicated flow, such as those generated downstream a leading edge cavitation. In addition, it would be interesting to study the interaction

of turbulent flow structures with the created vapour cores within these structures. Furthermore, toward an improvement of energetic models of cavitation aggressiveness prediction, potential energies of cavitation vortices, which are weighted by the collapse distance to the wall, could be considered in models.

Appendix A

Averaged pitting and deformation volume rates

Aluminium Echelle 1	X [%]	Nk	Sk [%]	τ_e [J/mm^2/s]	τ_v [µm^3/mm^2/s]	τ_n [/mm^2/s]	$\tau_e^{(1)}$ [J/mm^2/s]	$\tau_v^{(1)}$ [µm^3/mm^2/s]	$\tau_n^{(1)}$ [/mm^2/s]
a4152	10	10	0.03	1.78E-10	4.94E-02	1.11E-04	5.88E-11	1.29E-02	1.89E-05
a4152	20	4	0.05	2.69E-10	3.44E-02	4.44E-05	5.88E-11	1.29E-02	1.89E-05
a4152	30	4	0.02	1.30E-10	4.20E-02	4.44E-05	5.88E-11	1.29E-02	1.89E-05
a4152	40	2	0.01	7.52E-11	2.13E-02	2.22E-05	5.88E-11	1.29E-02	1.89E-05
a4154	30	10	0.04	1.97E-10	4.04E-02	1.66E-04	8.04E-11	1.25E-02	3.99E-05
a4154	40	10	0.06	3.92E-10	6.35E-02	1.66E-04	8.04E-11	1.25E-02	3.99E-05
a4154	50	5	0.04	2.48E-10	2.83E-02	8.32E-05	8.04E-11	1.25E-02	3.99E-05
a4154	60	2	0.01	2.22E-11	3.82E-03	3.33E-05	8.04E-11	1.25E-02	3.99E-05
a4202	10	9	0.02	1.78E-10	5.60E-02	1.50E-04	2.73E-09	4.62E-01	8.65E-04
a4202	20	493	3.44	2.61E-08	4.27E+00	8.20E-03	2.73E-09	4.62E-01	8.65E-04
a4202	30	18	0.07	7.10E-10	2.32E-01	2.99E-04	2.73E-09	4.62E-01	8.65E-04
a4202	40	3	0.03	4.61E-10	1.01E-01	4.99E-05	2.73E-09	4.62E-01	8.65E-04
a4204	30	7	0.03	6.42E-10	1.46E-01	3.10E-04	1.39E-08	3.33E+00	1.28E-03
a4204	40	269	2.73	1.37E-07	3.29E+01	1.19E-02	1.39E-08	3.33E+00	1.28E-03
a4204	50	10	0.08	1.64E-09	2.69E-01	4.44E-04	1.39E-08	3.33E+00	1.28E-03
a4204	60	5	0.02	3.39E-10	7.81E-02	2.22E-04	1.39E-08	3.33E+00	1.28E-03
a4252	20	274	2.42	1.02E-07	1.48E+01	2.43E-02	3.36E-08	4.45E+00	4.17E-03
a4252	30	243	3.97	2.51E-07	3.22E+01	2.16E-02	3.36E-08	4.45E+00	4.17E-03
a4252	40	14	0.1	3.50E-09	4.81E-01	1.24E-03	3.36E-08	4.45E+00	4.17E-03
a4252	50	10	0.12	6.24E-09	8.98E-01	8.87E-04	3.36E-08	4.45E+00	4.17E-03
a4302	10	10	0.04	5.80E-09	9.67E-01	4.44E-03	7.32E-08	1.12E+01	1.82E-02
a4302	20	395	3.1	7.06E-07	1.09E+02	1.75E-01	7.32E-08	1.12E+01	1.82E-02
a4302	30	7	0.08	2.14E-08	2.96E+00	3.10E-03	7.32E-08	1.12E+01	1.82E-02
a4302	40	0	0	0	0	0	7.32E-08	1.12E+01	1.82E-02
a4302	50	1	0	3.59E-10	9.98E-02	4.44E-04	7.32E-08	1.12E+01	1.82E-02
a4304	30	67	0.6	1.94E-07	2.83E+01	4.46E-02	1.45E-07	1.87E+01	2.26E-02
a4304	40	289	3.51	1.25E-06	1.59E+02	1.92E-01	1.45E-07	1.87E+01	2.26E-02
a4304	50	1	0.11	7.74E-08	8.64E+00	6.65E-04	1.45E-07	1.87E+01	2.26E-02
a6152	10	68	0.51	8.06E-08	1.22E+01	1.81E-02	9.52E-08	1.14E+01	6.95E-03
a6152	20	118	2.04	5.38E-07	6.59E+01	3.14E-02	9.52E-08	1.14E+01	6.95E-03
a6152	30	63	1.26	2.82E-07	2.86E+01	1.68E-02	9.52E-08	1.14E+01	6.95E-03
a6152	40	26	0.38	6.61E-08	9.39E+00	6.92E-03	9.52E-08	1.14E+01	6.95E-03
a6152	50	4	0.05	6.98E-09	9.95E-01	1.06E-03	9.52E-08	1.14E+01	6.95E-03
a6154	20	13	0.15	1.82E-08	2.64E+00	2.47E-03	6.45E-08	7.48E+00	2.63E-03
a6154	30	31	0.33	2.92E-08	3.73E+00	5.89E-03	6.45E-08	7.48E+00	2.63E-03
a6154	40	55	1.49	2.42E-07	2.33E+01	1.05E-02	6.45E-08	7.48E+00	2.63E-03
a6154	50	27	0.88	2.37E-07	3.85E+01	5.13E-03	6.45E-08	7.48E+00	2.63E-03
a6154	60	12	0.71	1.21E-07	6.79E+00	2.28E-03	6.45E-08	7.48E+00	2.63E-03
a6154	70	5	0.04	3.62E-09	5.94E-01	9.50E-04	6.45E-08	7.48E+00	2.63E-03

Cuivre Echelle1	X [%]	Nk	Sk [%]	τ_e [J/mm^2/s]	τ_v [µm^3/mm^2/s]	τ_n [/mm^2/s]	$\tau_e^{(1)}$ [J/mm^2/s]	$\tau_v^{(1)}$ [µm^3/mm^2/s]	$\tau_n^{(1)}$ [/mm^2/s]
c4202	10	36	0.15	4.63E-09	8.00E-02	2.00E-04	3.94E-09	4.59E-02	1.25E-04
c4202	20	79	0.45	1.29E-08	1.55E-01	4.38E-04	3.94E-09	4.59E-02	1.25E-04
c4202	30	104	0.66	1.64E-08	1.73E-01	5.77E-04	3.94E-09	4.59E-02	1.25E-04
c4202	40	5	0.01	4.39E-10	1.31E-02	2.77E-05	3.94E-09	4.59E-02	1.25E-04
c4202	50	6	0.09	5.19E-09	0.044	3.33E-05	3.94E-09	0.0459	0.000125
c4202	60	5	0.04	1.42E-09	1.90E-02	2.77E-05	3.94E-09	4.59E-02	1.25E-04
c4204	30	89	0.51	1.64E-08	1.91E-01	6.58E-04	8.93E-09	9.26E-02	2.04E-04
c4204	40	196	1.52	6.93E-08	7.19E-01	1.45E-03	8.93E-09	9.26E-02	2.04E-04
c4204	50	12	0.15	7.59E-09	0.063	8.87E-05	8.93E-09	0.0926	0.000204
c4204	60	2	0	1.30E-10	2.35E-03	1.48E-05	8.93E-09	9.26E-02	2.04E-04
c4252	20	1012	7.74	3.58E-07	3.85E+00	7.48E-03	5.69E-08	5.09E-01	6.64E-04
c4252	30	51	2.06	2.11E-07	1.31E+00	3.77E-04	5.69E-08	5.09E-01	6.64E-04
c4252	40	51	1.04	7.97E-08	0.669	0.000377	5.69E-08	0.509	0.000664
c4252	50	30	0.12	7.92E-09	2.00E-01	2.22E-04	5.69E-08	5.09E-01	6.64E-04
c4252	60	10	0.06	2.24E-09	2.65E-02	7.39E-05	5.69E-08	5.09E-01	6.64E-04
c4254	20	11	0.24	4.88E-08	3.64E-01	1.83E-04	6.35E-08	6.52E-01	1.18E-03
c4254	30	37	0.24	2.26E-08	0.319	0.000615	6.35E-08	0.652	0.00118
c4254	40	642	5.35	5.32E-07	5.50E+00	1.07E-02	6.35E-08	6.52E-01	1.18E-03
c4254	50	20	0.19	1.93E-08	1.93E-01	3.33E-04	6.35E-08	6.52E-01	1.18E-03
c4254	60	5	0.13	3.24E-08	3.15E-01	8.32E-05	6.35E-08	6.52E-01	1.18E-03
c4302	30	24	0.57	2.63E-07	1.87	0.00106	8.97E-08	0.502	0.000411
c4302	40	13	0.84	5.67E-07	2.39E+00	5.77E-04	8.97E-08	5.02E-01	4.11E-04
c4302	50	61	0.45	1.32E-07	1.22E+00	2.71E-03	8.97E-08	5.02E-01	4.11E-04
c4302	60	1	0	4.23E-10	1.44E-02	4.44E-05	8.97E-08	5.02E-01	4.11E-04
c4304	30	29	0.25	1.09E-07	1.16E+00	1.93E-03	3.56E-07	2.36E+00	2.30E-03
c4304	40	312	3.44	1.54E-06	1.44E+01	2.08E-02	3.56E-07	2.36E+00	2.30E-03
c4304	50	15	2.18	2.58E-06	1.11E+01	9.98E-04	3.56E-07	2.36E+00	2.30E-03
c4322	20	777	11.9	5.13E-06	5.12E+01	3.45E-02	5.30E-06	4.53E+01	6.16E-03
c4322	30	377	21.9	2.01E-05	186	0.0167	0.0000053	45.3	0.00616
c4322	40	275	17.9	1.45E-05	1.16E+02	1.22E-02	5.30E-06	4.53E+01	6.16E-03
c4322	50	120	14.2	1.41E-05	1.09E+02	5.32E-03	5.30E-06	4.53E+01	6.16E-03
c4322	60	46	1.27	6.20E-07	4.70E+00	2.04E-03	5.30E-06	4.53E+01	6.16E-03
c4324	20	19	0.15	5.16E-08	5.14E-01	1.26E-03	2.31E-06	1.98E+01	7.87E-03
c4324	30	155	2.23	1.23E-06	1.09E+01	1.03E-02	2.31E-06	1.98E+01	7.87E-03
c4324	40	874	16.6	1.49E-05	1.43E+02	5.82E-02	2.31E-06	1.98E+01	7.87E-03
c4324	50	116	5.69	5.24E-06	3.39E+01	7.72E-03	2.31E-06	1.98E+01	7.87E-03
c4324	60	31	2.19	2.24E-06	1.30E+01	2.06E-03	2.31E-06	1.98E+01	7.87E-03

Cuivre Echelle1	X [%]	Nk	Sk [%]	τ_e [J/mm^2/s]	τ_v [µm^3/mm^2/s]	τ_n [/mm^2/s]	$\tau_e^{(1)}$ [J/mm^2/s]	$\tau_v^{(1)}$ [µm^3/mm^2/s]	$\tau_n^{(1)}$ [/mm^2/s]
c6152	10	37	0.17	4.61E-08	8.50E-01	1.76E-03	2.52E-07	1.92E+00	1.56E-03
c6152	20	97	1.91	7.93E-07	6.18E+00	4.61E-03	2.52E-07	1.92E+00	1.56E-03
c6152	30	153	2.81	1.19E-06	8.94E+00	7.27E-03	2.52E-07	1.92E+00	1.56E-03
c6152	40	33	0.87	3.42E-07	2.48E+00	1.57E-03	2.52E-07	1.92E+00	1.56E-03
c6152	50	16	0.42	1.62E-07	0.969	0.00076	2.52E-07	1.92	0.00156
c6152	60	1	0	9.36E-10	3.63E-02	4.75E-05	2.52E-07	1.92E+00	1.56E-03
c6154	20	17	0.19	4.96E-08	4.64E-01	5.66E-04	5.04E-07	3.16E+00	1.68E-03
c6154	30	331	2.36	4.15E-07	4.62E+00	1.10E-02	5.04E-07	3.16E+00	1.68E-03
c6154	40	70	3.28	1.51E-06	10.1	0.00233	5.04E-07	3.16	0.00168
c6154	50	53	3.76	1.70E-06	8.40E+00	1.76E-03	5.04E-07	3.16E+00	1.68E-03
c6154	60	33	1.91	8.66E-07	5.25E+00	1.10E-03	5.04E-07	3.16E+00	1.68E-03
c6154	70	9	0.95	6.83E-07	3.88E+00	2.99E-04	5.04E-07	3.16E+00	1.68E-03
c6202	20	136	3.49	4.42E-06	27.9	0.0181	2.47E-06	12.7	0.00336
c6202	30	81	5.9	1.18E-05	6.15E+01	1.08E-02	2.47E-06	1.27E+01	3.36E-03
c6202	40	45	4.16	9.06E-06	4.06E+01	5.99E-03	2.47E-06	1.27E+01	3.36E-03
c6202	50	13	0.41	4.32E-07	2.58E+00	1.73E-03	2.47E-06	1.27E+01	3.36E-03
c6202	60	15	0.12	1.53E-07	1.59E+00	2.00E-03	2.47E-06	1.27E+01	3.36E-03
c6204	20	52	0.59	6.15E-07	5.19E+00	6.92E-03	5.96E-06	3.29E+01	8.08E-03
c6204	30	110	4.24	6.90E-06	3.78E+01	1.46E-02	5.96E-06	3.29E+01	8.08E-03
c6204	40	227	8.26	1.40E-05	9.49E+01	3.02E-02	5.96E-06	3.29E+01	8.08E-03
c6204	50	130	11.3	3.01E-05	1.54E+02	1.73E+00	5.96E-06	3.29E+01	8.08E-03
c6204	60	71	2.36	3.34E-06	19.7	0.00945	5.96E-06	32.9	0.00808
c6204	70	40	3.13	6.40E-06	2.49E+01	5.32E-03	5.96E-06	3.29E+01	8.08E-03
c6252	20	143	1.97	1.49E-05	1.32E+02	1.27E-01	8.03E-06	4.71E+01	1.90E-02
c6252	30	78	4.54	5.04E-05	279	0.0692	8.03E-06	47.1	0.019
c6252	40	18	1.24	1.29E-05	5.45E+01	1.60E-02	8.03E-06	4.71E+01	1.90E-02
c6252	50	10	0.48	5.80E-06	3.73E+01	8.87E-03	8.03E-06	4.71E+01	1.90E-02
c6252	60	1	0.02	8.96E-08	6.55E-01	8.87E-04	8.03E-06	4.71E+01	1.90E-02
c6254	10	42	0.17	5.97E-07	8.30E+00	2.79E-02	4.44E-05	2.83E+02	3.75E-02
c6254	20	33	0.59	2.96E-06	21.7	0.022	0.0000444	283	0.0375
c6254	30	95	4.4	3.72E-05	2.03E+02	6.32E-02	4.44E-05	2.83E+02	3.75E-02
c6254	40	234	10.8	1.08E-04	6.63E+02	1.56E-01	4.44E-05	2.83E+02	3.75E-02
c6254	50	89	13.4	1.99E-04	1.38E+03	5.92E-02	4.44E-05	2.83E+02	3.75E-02
c6254	60	47	4.78	5.08E-05	2.74E+02	3.13E-02	4.44E-05	2.83E+02	3.75E-02
c6254	70	46	4.89	6.07E-05	3.69E+02	3.06E-02	4.44E-05	2.83E+02	3.75E-02

Acier Inox Echelle 1	X [%]	Nk	Sk [%]	τ_e [J/mm^2/s]	τ_v [µm^3/mm^2/s]	τ_n [/mm^2/s]	$\tau_e^{(1)}$ [J/mm^2/s]	$\tau_v^{(1)}$ [µm^3/mm^2/s]	$\tau_n^{(1)}$ [/mm^2/s]
i4302	10	3	0.01	1.15E-09	4.12E-03	1.60E-05	9.98E-10	2.54E-03	4.53E-06
i4302	20	4	0.02	1.97E-09	6.15E-03	2.13E-05	9.98E-10	2.54E-03	4.53E-06
i4302	30	3	0.06	9.52E-09	2.16E-02	1.60E-05	9.98E-10	2.54E-03	4.53E-06
i4304	30	4	0.01	7.84E-10	0.00413	2.96E-05	8.07E-09	0.0211	5.14E-05
i4304	40	59	0.37	4.99E-08	1.49E-01	4.36E-04	8.07E-09	2.11E-02	5.14E-05
i4304	50	10	0.22	4.03E-08	7.89E-02	7.39E-05	8.07E-09	2.11E-02	5.14E-05
i4322	20	106	1.05	1.83E-07	5.94E-01	5.88E-04	7.36E-08	1.70E-01	1.62E-04
i4322	30	130	2.48	4.03E-07	0.82	0.000721	7.36E-08	0.17	0.000162
i4322	40	50	0.52	7.72E-08	2.09E-01	2.77E-04	7.36E-08	1.70E-01	1.62E-04
i4322	50	22	0.35	6.11E-08	1.59E-01	1.22E-04	7.36E-08	1.70E-01	1.62E-04
i4322	60	14	0.44	7.65E-08	8.82E-02	7.76E-05	7.36E-08	1.70E-01	1.62E-04
i4324	20	17	0.07	8.88E-09	0.0459	0.000113	5.16E-08	0.134	0.000174
i4324	30	21	0.15	1.80E-08	4.78E-02	1.40E-04	5.16E-08	1.34E-01	1.74E-04
i4324	40	149	1.55	2.33E-07	6.58E-01	9.91E-04	5.16E-08	1.34E-01	1.74E-04
i4324	50	59	1.07	2.08E-07	4.45E-01	3.93E-04	5.16E-08	1.34E-01	1.74E-04
i4324	60	27	0.32	6.56E-08	2.12E-01	1.80E-04	5.16E-08	1.34E-01	1.74E-04

Acier Inox Echelle1	X [%]	Nk	Sk [%]	τ_e [J/mm^2/s]	τ_v [µm^3/mm^2/s]	τ_n [/mm^2/s]	$\tau_e^{(1)}$ [J/mm^2/s]	$\tau_v^{(1)}$ [µm^3/mm^2/s]	$\tau_n^{(1)}$ [/mm^2/s]
i6152	10	2	0	4.68E-10	3.23E-03	1.11E-05	3.57E-10	1.35E-03	5.82E-06
i6152	20	1	0	3.29E-10	1.38E-03	5.54E-06	3.57E-10	1.35E-03	5.82E-06
i6152	30	5	0.02	1.56E-09	5.35E-03	2.77E-05	3.57E-10	1.35E-03	5.82E-06
i6152	40	4	0.02	1.78E-09	5.82E-03	2.22E-05	3.57E-10	1.35E-03	5.82E-06
i6154	30	1	0	2.77E-10	1.04E-03	4.93E-06	1.29E-09	3.40E-03	6.90E-06
i6154	40	4	0.01	9.72E-10	6.54E-03	1.97E-05	1.29E-09	3.40E-03	6.90E-06
i6154	50	7	0.1	1.15E-08	2.37E-02	3.45E-05	1.29E-09	3.40E-03	6.90E-06
i6154	60	3	0	4.10E-10	3.96E-03	1.48E-05	1.29E-09	3.40E-03	6.90E-06
i6202	10	1	0	3.85E-10	2.16E-03	1.66E-05	6.92E-09	2.38E-02	5.24E-05
i6202	20	16	0.09	2.79E-08	8.49E-02	2.66E-04	6.92E-09	2.38E-02	5.24E-05
i6202	30	8	0.07	2.66E-08	9.23E-02	1.33E-04	6.92E-09	2.38E-02	5.24E-05
i6202	40	9	0.05	1.93E-08	7.92E-02	1.50E-04	6.92E-09	2.38E-02	5.24E-05
i6204	30	4	0.01	2.71E-09	1.04E-02	4.44E-05	1.51E-07	2.68E-01	1.23E-04
i6204	40	34	0.38	8.60E-08	1.77E-01	3.77E-04	1.51E-07	2.68E-01	1.23E-04
i6204	50	36	1.81	1.07E-06	1.90E+00	3.99E-04	1.51E-07	2.68E-01	1.23E-04
i6204	60	25	0.64	2.13E-07	3.51E-01	2.77E-04	1.51E-07	2.68E-01	1.23E-04
i6204	70	17	0.54	1.85E-07	0.32	0.000189	1.51E-07	0.268	0.000123
i6252	20	9	0.1	1.83E-07	3.73E-01	7.49E-04	5.88E-08	1.41E-01	1.48E-04
i6252	30	7	0.09	1.52E-07	3.61E-01	5.82E-04	5.88E-08	1.41E-01	1.48E-04
i6252	40	1	0	4.54E-09	1.54E-02	8.32E-05	5.88E-08	1.41E-01	1.48E-04
i6252	50	4	0.1	3.92E-07	1	0.000333	5.88E-08	0.141	0.000148
i6254	40	27	0.52	7.19E-07	1.37E+00	1.50E-03	2.95E-07	4.95E-01	3.67E-04
i6254	50	29	0.86	1.63E-06	2.75E+00	1.61E-03	2.95E-07	4.95E-01	3.67E-04
i6254	60	14	0.42	7.64E-07	1.12	0.000776	2.95E-07	0.495	0.000367
i6254	70	4	0.03	2.74E-08	6.36E-02	2.22E-04	2.95E-07	4.95E-01	3.67E-04
i6302	20	9	0.08	5.78E-07	1.49E+00	3.59E-03	1.31E-07	3.54E-01	4.19E-04
i6302	30	5	0.08	1.17E-06	3.23E+00	2.00E-03	1.31E-07	3.54E-01	4.19E-04
i6304	30	18	0.32	2.36E-06	5.2	0.00479	5.43E-06	10.3	0.00353
i6304	40	53	1.6	1.68E-05	3.24E+01	1.41E-02	5.43E-06	1.03E+01	3.53E-03
i6304	50	35	1.77	2.44E-05	4.38E+01	9.31E-03	5.43E-06	1.03E+01	3.53E-03
i6304	60	16	0.67	6.22E-06	1.01E+01	4.26E-03	5.43E-06	1.03E+01	3.53E-03
i6304	70	20	0.51	6.63E-06	1.69E+01	5.32E-03	5.43E-06	1.03E+01	3.53E-03

Veine divergente	X [%]	Nk	Sk [%]	τ_e [J/mm^2/s]	τ_v [µm^3/mm^2/s]	τ_n [/mm^2/s]	$\tau_e^{(1)}$ [J/mm^2/s]	$\tau_v^{(1)}$ [µm^3/mm^2/s]	$\tau_n^{(1)}$ [/mm^2/s]
dc4202	20	985	6.38	1.66E-07	1.76E+00	5.46E-03	4.20E-08	4.53E-01	1.35E-03
dc4202	30	915	6.24	1.67E-07	1.75E+00	5.07E-03	4.20E-08	4.53E-01	1.35E-03
dc4202	40	1050	6.5	1.71E-07	1.95E+00	5.82E-03	4.20E-08	4.53E-01	1.35E-03
dc4204	30	2540	11.3	4.19E-07	5.87	0.0188	8.28E-08	1.15	0.00416
dc4204	40	2141	8.98	3.10E-07	4.23E+00	1.58E-02	8.28E-08	1.15E+00	4.16E-03
dc4204	50	2112	7.96	2.72E-07	3.85E+00	1.56E-02	8.28E-08	1.15E+00	4.16E-03
dc4302	30	1391	8.36	2.99E-06	3.48E+01	9.25E-02	9.00E-07	1.03E+01	3.02E-02
dc4302	40	1990	11.2	3.58E-06	41.8	0.132	0.0000009	10.3	0.0302
dc4302	50	2016	13.1	4.24E-06	4.64E+01	1.34E-01	9.00E-07	1.03E+01	3.02E-02
dc4304	40	492	10.5	2.09E-05	1.72E+02	6.55E-02	1.50E-05	1.16E+02	2.72E-02
dc4304	50	463	15	3.51E-05	2.88E+02	6.16E-02	1.50E-05	1.16E+02	2.72E-02
dc4304	60	497	16.1	4.66E-05	380	0.0661	0.000015	116	0.0272
dc4304	70	643	20.6	4.85E-05	3.38E+02	8.56E-02	1.50E-05	1.16E+02	2.72E-02
dc4304	80	92	2.59	5.50E-06	3.86E+01	1.22E-02	1.50E-05	1.16E+02	2.72E-02
dc4304b	40	1414	6.21	1.48E-05	1.86E+02	7.53E-01	1.03E-05	1.23E+02	4.10E-01
dc4304b	50	1761	8.42	2.13E-05	270	0.937	0.0000103	123	0.41
dc4304b	60	1542	7.19	1.74E-05	2.16E+02	8.21E-01	1.03E-05	1.23E+02	4.10E-01
dc4304b	70	2541	14.6	4.38E-05	4.92E+02	1.35E+00	1.03E-05	1.23E+02	4.10E-01
dc4304b	80	1060	4.96	1.19E-05	1.47E+02	5.64E-01	1.03E-05	1.23E+02	4.10E-01
dc6202	20	169	1.06	2.62E-06	25.9	0.09	4.61E-07	4.67	0.011
dc6202	30	42	0.26	6.83E-07	7.70E+00	2.24E-02	4.61E-07	4.67E+00	1.10E-02
dc6202	40	14	0.25	1.50E-06	1.39E+01	7.45E-03	4.61E-07	4.67E+00	1.10E-02
dc6202	50	31	0.18	6.23E-07	7.56E+00	1.65E-02	4.61E-07	4.67E+00	1.10E-02
dc6204	30	218	1.73	1.05E-05	8.24E+01	1.45E-01	1.79E-05	1.08E+02	4.23E-02
dc6204	40	149	2.03	1.59E-05	1.27E+02	9.91E-02	1.79E-05	1.08E+02	4.23E-02
dc6204	50	99	4.5	6.74E-05	4.35E+02	6.59E-02	1.79E-05	1.08E+02	4.23E-02
dc6204	60	43	1.28	1.32E-05	8.22E+01	2.86E-02	1.79E-05	1.08E+02	4.23E-02
dc6204	70	176	5.78	7.46E-05	3.71E+02	1.17E-01	1.79E-05	1.08E+02	4.23E-02
dc6204	80	7	0.05	1.45E-07	1.45	0.00466	0.0000179	108	0.0423
di6252	20	8	0.05	1.51E-07	7.02E-01	1.06E-03	1.44E-06	1.56E+00	5.72E-04
di6252	30	22	0.33	1.12E-06	2.29E+00	2.93E-03	1.44E-06	1.56E+00	5.72E-04
di6252	40	0	0	0	0	0	1.44E-06	1.56E+00	5.72E-04
di6252	50	5	0.21	8.56E-07	1.34E+00	6.65E-04	1.44E-06	1.56E+00	5.72E-04
di6252	60	12	1.98	1.64E-05	1.53E+01	1.60E-03	1.44E-06	1.56E+00	5.72E-04
di6254	30	24	0.43	8.13E-07	1.72E+00	1.77E-03	3.81E-06	6.46E+00	1.58E-03
di6254	40	36	1.53	5.35E-06	8.45E+00	2.66E-03	3.81E-06	6.46E+00	1.58E-03
di6254	50	89	4.9	1.92E-05	3.25E+01	6.58E-03	3.81E-06	6.46E+00	1.58E-03
di6254	60	52	2.89	1.06E-05	1.81E+01	3.84E-03	3.81E-06	6.46E+00	1.58E-03
di6254	70	16	0.69	1.87E-06	3.12E+00	1.18E-03	3.81E-06	6.46E+00	1.58E-03
di6254	80	4	0.17	5.92E-07	1.60E+00	2.96E-04	3.81E-06	6.46E+00	1.58E-03

Aluminium Echelle 0.6	X [%]	Nk	Sk [%]	τ_e [J/mm^2/s]	τ_v [µm^3/mm^2/s]	τ_n [/mm^2/s]	$\tau_e^{(1)}$ [J/mm^2/s]	$\tau_v^{(1)}$ [µm^3/mm^2/s]	$\tau_n^{(1)}$ [/mm^2/s]
pa4204	40	57	0.23	2.58E-09	6.26E-01	7.02E-03	3.08E-10	7.61E-02	8.97E-04
pa4204	50	40	0.14	1.52E-09	3.89E-01	4.93E-03	3.08E-10	7.61E-02	8.97E-04
pa4252	20	71	0.39	8.09E-09	1.49E+00	1.75E-02	7.95E-10	1.45E-01	1.79E-03
pa4252	30	26	0.13	2.51E-09	0.443	0.00641	7.95E-10	0.145	0.00179
pa4254	40	632	4.11	1.61E-07	3.06E+01	2.34E-01	1.78E-08	3.32E+00	2.81E-02
pa4254	50	380	2.27	7.65E-08	1.37E+01	1.40E-01	1.78E-08	3.32E+00	2.81E-02
pa4302	20	149	1	1.28E-07	24.1	0.184	1.19E-08	2.19	0.0183
pa4302	30	49	0.29	3.09E-08	5.04E+00	6.04E-02	1.19E-08	2.19E+00	1.83E-02
pa4304	40	483	6.93	2.28E-06	3.24E+02	8.93E-01	5.44E-07	7.12E+01	1.08E-01
pa4304	50	297	8.71	4.97E-06	6.26E+02	5.49E-01	5.44E-07	7.12E+01	1.08E-01
pa6152	20	150	1.23	1.12E-07	1.89E+01	1.01E-01	1.46E-08	2.29E+00	1.02E-02
pa6152	30	52	0.67	8.17E-08	1.17E+01	3.49E-02	1.46E-08	2.29E+00	1.02E-02
pa6154	40	96	1.45	1.26E-07	1.70E+01	5.07E-02	1.68E-08	2.32E+00	6.38E-03
pa6154	50	65	1.1	9.82E-08	14	0.0343	1.68E-08	2.32	0.00638
pa6202	20	249	5.24	2.23E-06	3.03E+02	4.60E-01	2.41E-07	3.46E+01	5.09E-02
pa6202	30	118	2.41	9.91E-07	1.58E+02	2.18E-01	2.41E-07	3.46E+01	5.09E-02
pa6204	40	55	0.37	2.65E-08	5.51	0.0343	9.07E-09	1.67	0.00599
pa6204	50	73	0.68	9.43E-08	1.68E+01	4.55E-02	9.07E-09	1.67E+00	5.99E-03
pa6252	20	438	9.94	1.00E-05	1.61E+03	1.62E+00	1.41E-06	1.97E+02	1.85E-01
pa6252	30	228	7.62	8.7E-06	1010	0.843	1.41E-06	197	0.185
pa6254	40	379	11.9	9.78E-06	1.27E+03	9.34E-01	2.09E-06	2.87E+02	2.20E-01
pa6254	50	446	10.8	9.25E-06	1.32E+03	1.10E+00	2.09E-06	2.87E+02	2.20E-01
pa6254	60	214	6.68	5.77E-06	8.01E+02	5.27E-01	2.09E-06	2.87E+02	2.20E-01
pabis6254	40	601	20.7	6.43E-06	1080	0.444	1.46E-06	238	0.0791
pabis6254	50	389	18.8	6.82E-06	1.14E+03	2.88E-01	1.46E-06	2.38E+02	7.91E-02
pabis6254	60	306	13.6	3.89E-06	5.80E+02	2.26E-01	1.46E-06	2.38E+02	7.91E-02

Appendix B

Characteristics of the impacts

Aluminium Full Scale	Time	X [%]	$R_{10\% min}$ [micron]	$R_{10\% moy}$ [micron]	$R_{10\% max}$ [micron]	H_{min} [micron]	H_{moy} [micron]	H_{max} [micron]	$V_{d min}$ [m^3]	$V_{d moy}$ [m^3]	$V_{d max}$ [m^3]	$E_{d min}$ [J]	$E_{d moy}$ [J]	$E_{d max}$ [J]	N	$e^{(0)}$ [J/mm²/s]	$e^{(1)}$ [J/mm²/s]	$v^{(0)}$ [m^3/mm²/s]	$v^{(1)}$ [m^3/mm²/s]	$n^{(0)}$ [/mm²/s]	$n^{(1)}$ [/mm²/s]
a4152	60 mn 0 s	10	9.52	15.97	26.04	0.4	1.39	2.28	112.25	445.06	1531.09	3.39E-07	1.60E-06	5.73E-06	20	7.24E-11	5.88E-11	1.63E-02	1.29E-02	2.46E-05	1.89E05
a4152	60 mn 0 s	20	17.26	27.75	57.67	0.31	1.337	2.38	208.85	776.16	1238.86	1.30E-06	6.06E-06	1.84E-05	20	7.24E-11	5.88E-11	1.63E-02	1.29E-02	2.46E-05	1.89E-05
a4152	60 mn 0 s	30	16.17	19.51	23.55	0.73	1.915	3.34	229.29	946.5	1814.71	1.10E-06	2.92E-06	4.49E-06	20	7.24E-11	5.88E-11	1.63E-02	1.29E-02	2.46E-05	1.89E-05
a4152	60 mn 0 s	40	16.93	22.64	28.36	0.56	2.29	4.02	540.98	962.54	13841	2.75E-06	3.39E-06	4.03E-06	20	7.24E-11	5.88E-11	1.63E-02	1.29E-02	2.46E-05	1.85E-05
a4154	40 mn 0 s	30	8.81	17.29	24.06	0.28	0.775	3.48	92.27	243.16	10198	2.73E-07	1.18E-06	2.13E-06	27	9.55E-11	8.04E-11	1.51E-02	1.25E-02	4.99E-05	3.99E05
a4154	40 mn 0 s	40	13.65	21.52	32.44	0.25	0.794	3.21	82.14	382.03	996.22	7.05E-07	2.36E-06	6.37E-06	27	9.55E-11	8.04E-11	1.51E-02	1.25E-02	4.99E-05	3.99E-05
a4154	40 mn 0 s	50	13.09	21.73	43.27	0.4	0.506	0.7	118.78	340.7	1057.49	6.33E-07	2.98E-06	1.08E-05	27	9.55E-11	8.04E-11	1.51E-02	1.25E-02	4.99E-05	3.99E05
a4154	40 mn 0 s	60	12.53	14.27	16.01	0.45	0.46	0.47	84.85	114.83	144.81	4.60E-07	6.67E-07	8.73E-07	27	9.55E-11	8.04E-11	1.51E-02	1.25E-02	4.99E-05	3.99E05
a4202	40 mn 0 s	10	10.18	14.5	18.67	0.39	1.366	3.18	119.49	373.85	1331.38	4.53E-07	1.19E-06	3.16E-06	523	3.05E-09	2.73E-09	5.17E-01	4.62E-01	9.67E-04	8.65E-04
a4202	40 mn 0 s	20	8.15	22.02	66.94	0.26	0.769	3.32	62.31	520.48	67827	2.07E-07	3.19E-06	5.18E-05	523	3.05E-09	2.73E-09	5.17E-01	4.62E-01	9.67E-04	8.65E-04
a4202	40 mn 0 s	30	10.64	17.07	30.6	0.61	1.744	3.9	150.99	773.32	3081.77	4.65E-07	2.37E-06	1.03E-05	523	3.05E-09	2.73E-09	5.17E-01	4.62E-01	9.67E-04	8.65E-04
a4202	40 mn 0 s	40	12.88	25.21	46.09	1.03	1.953	2.81	343.13	2019.63	5155.33	1.17E-06	9.23E-06	2.51E-05	523	3.05E-09	2.73E-09	5.17E-01	4.62E-01	9.67E-04	8.65E-04
a4204	15 mn 0 s	30	12.54	19.06	28.54	0.43	1.193	3.28	198.53	470.78	936.32	8.09E-07	2.07E-06	4.78E-06	291	1.55E-08	1.39E-08	3.71E+00	3.33E+00	1.43E-03	1.28E-03
a4204	15 mn 0 s	40	9.28	24.75	176.78	0.27	0.818	15.46	56.38	2758.09	5804576	3.43E-07	1.14E-05	1.96E-03	291	1.55E-08	1.39E-08	3.71E+00	3.33E+00	1.43E-03	1.28E-03
a4204	15 mn 0 s	50	11.62	23.83	39.5	0.49	1.029	3.38	225.29	605.59	16685	9.78E-07	3.71E-06	1.16E-05	291	1.55E-08	1.39E-08	3.71E+00	3.33E+00	1.43E-03	1.28E-03
a4204	15 mn 0 s	60	13.57	17	22.14	0.46	0.866	1.39	113.13	352.01	818.87	6.49E-07	1.53E-06	3.30E-06	291	1.55E-08	1.39E-08	3.71E+00	3.33E+00	1.43E-03	1.28E03
a4252	7 mn 30 s	20	8.15	24.42	65.21	0.25	0.734	3.69	61.96	608.36	5093.02	2.18E-07	4.21E-06	4.22E-05	541	4.03E-08	3.36E-08	5.38E+00	4.45E+00	5.33E-03	4.17E-03
a4252	7 mn 30 s	30	9.82	30.94	137.42	0.26	0.83	4.84	64.51	1495.43	35957.79	3.89E-07	1.16E-05	2.76E-04	541	4.03E-08	3.36E-08	5.38E+00	4.45E+00	5.33E-03	4.17E-03
a4252	7 mn 30 s	40	8.47	22.54	41.15	0.33	0.832	2.44	137.13	387.09	671.29	3.77E-07	2.82E-06	8.06E-06	541	4.03E-08	3.36E-08	5.38E+00	4.45E+00	5.33E-03	4.1

Copper Full scale	Time	X [%]	$R_{10\% min}$ [micron]	$R_{10\% moy}$ [micron]	$R_{10\% max}$ [micron]	H_{min} [micron]	H_{moy} [micron]	H_{max} [micron]	$V_{d\ min}$ [m^3]	$V_{d\ moy}$ [m^3]	$V_{d\ max}$ [m^3]	$E_{d\ min}$ [J]	$E_{d\ moy}$ [J]	$E_{d\ max}$ [J]	N	$e^{(0)}$ [J/mm^2/s]	$e^{(1)}$ [J/mm^2/s]	$v^{(0)}$ [m^3/mm^2/s]	$v^{(1)}$ [m^3/mm^2/s]	$n^{(0)}$ [/mm^2/s]	$n^{(1)}$ [/mm^2/s]
c4202	120 mn 0 s	10	8.35	16.51	41.9	0.34	1.31	4.07	92.67	400.96	2081.14	4.65E-06	2.32E-05	1.26E-04	235	4.55E-09	3.94E-09	5.37E-02	4.59E-02	1.45E-04	1.25E-04
c4202	120 mn 0 s	20	8.47	19.95	47.41	0.27	0.754	3.17	82.69	353.08	1608.2	3.30E-06	2.94E-05	1.80E-04	235	4.55E-09	3.94E-09	5.37E-02	4.59E-02	1.45E-04	1.25E-04
c4202	120 mn 0 s	30	8.64	21.87	39.92	0.28	0.542	3.03	105.04	299.99	1374.52	4.02E-06	2.84E-05	1.19E-04	235	4.55E-09	3.94E-09	5.37E-02	4.59E-02	1.45E-04	1.25E-04
c4202	120 mn 0 s	40	10.92	13.21	18.25	0.49	1.66	3.9	86.26	472.87	1560.26	5.69E-06	1.58E-05	4.48E-05	235	4.55E-09	3.94E-09	5.37E-02	4.59E-02	1.45E-04	1.25E-04
c4202	120 mn 0 s	50	11.01	25.02	80.67	0.75	1.562	2.45	172.56	1322.72	5863.57	8.90E-06	1.56E-04	8.58E-04	235	4.55E-09	3.94E-09	5.37E-02	4.59E-02	1.45E-04	1.25E-04
c4202	120 mn 0 s	60	11.68	22.08	36.5	0.4	1.004	1.76	97.07	684.21	2176.61	6.42E-06	5.12E-05	1.55E-04	235	4.55E-09	3.94E-09	5.37E-02	4.59E-02	1.45E-04	1.25E-04
c4204	90 mn 0 s	30	11.96	21.05	33.75	0.3	0.521	6.42	84.93	289.67	4441.11	6.50E-06	2.50E-05	1.14E-04	299	1.04E-08	8.93E-09	1.08E-01	9.26E-02	2.46E-04	2.04E-04
c4204	90 mn 0 s	40	8.15	22.46	96.36	0.27	0.751	3.58	76.04	496.05	10931.79	3.44E-06	4.78E-05	1.53E-03	299	1.04E-08	8.93E-09	1.08E-01	9.26E-02	2.46E-04	2.04E-04
c4204	90 mn 0 s	50	10.3	26.59	69.97	0.33	0.781	1.67	152.19	710.4	3588.25	6.55E-06	8.55E-05	5.43E-04	299	1.04E-08	8.93E-09	1.08E-01	9.26E-02	2.46E-04	2.04E-04
c4204	90 mn 0 s	60	12.12	12.95	13.77	0.64	0.77	0.9	113.04	158.98	204.92	6.72E-06	8.80E-06	1.09E-05	299	1.04E-08	8.93E-09	1.08E-01	9.26E-02	2.46E-04	2.04E-04
c4252	90 mn	20	8.15	22.61	107.46	0.27	0.695	3.35	61.51	514.97	24835.79	2.70E-06	4.78E-05	2.69E-03	1154	7.32E-08	5.69E-08	6.73E-01	5.09E-01	9.48E-04	6.64E-04
c4252	90 mn	30	13.61	43.3	217.69	0.27	0.617	1.94	60.05	3476.36	68320.81	5.93E-06	5.60E-04	1.31E-02	1154	7.32E-08	5.69E-08	6.73E-01	5.09E-01	9.48E-04	6.64E-04
c4252	90 mn	40	10.39	31.96	107.06	0.28	0.711	1.69	62.76	1773.25	13909.69	4.80E-06	2.11E-04	2.02E-03	1154	7.32E-08	5.69E-08	6.73E-01	5.09E-01	9.48E-04	6.64E-04
c4252	90 mn	50	10.16	17.29	33.32	0.46	1.897	5.93	119.03	900.54	4072.41	5.66E-06	3.57E-05	1.48E-04	1154	7.32E-08	5.69E-08	6.73E-01	5.09E-01	9.48E-04	6.64E-04
c4252	90 mn	60	11.77	21.12	31.91	0.35	0.663	0.96	151.39	358.19	991.04	7.38E-06	3.03E-05	8.61E-05	1154	7.32E-08	5.69E-08	6.73E-01	5.09E-01	9.48E-04	6.64E-04
c4254	40 mn	20	15.48	31.52	115.25	0.29	0.555	1.2	135.28	1990.64	18671.61	1.07E-05	2.66E-04	2.61E-03	715	7.28E-08	6.35E-08	7.43E-01	6.52E-01	1.32E-03	1.18E-03
c4254	40 mn	30	10.48	21.66	39.01	0.29	0.678	4.24	80.98	517.52	7750.97	5.43E-06	3.67E-05	3.16E-04	715	7.28E-08	6.35E-08	7.43E-01	6.52E-01	1.32E-03	1.18E-03
c4254	40 mn	40	8.15	23.89	89.14	0.28	0.639	3.57	56.04	514.72	14033.97	2.62E-06	4.98E-05	1.53E-03	715	7.28E-08	6.35E-08	7.43E-01	6.52E-01	1.32E-03	1.18E-03
c4254	40 mn	50	11.77	25.05	51.68	0.27	0.622	1.7	131.42	578.79	2552.89	6.89E-06	5.79E-05	2.39E-04	715	7.28E-08	6.35E-08	7.43E-01	6.52E-01	1.32E-03	1.18E-03
c4254	40 mn	60	16.54	36.18	93.3	0.29	0.614	1.73	95.33	3789.16	18093.22	1.00E-05	3.90E-04	1.85E-03	715	7.28E-08	6.35E-08	7.43E-01	6.52E-01	1.32E-03	1.18E-03
c4302	15 mn 0 s	30	13.26	33.16	111.29	0.3	0.77	1.7	115.12	1753.53	14149.47	8.89E-06	2.47E-04	1.91E-03	99	1.07E-07	8.97E-08	6.10E-01	5.02E-01	4.88E-04	4.11E-04
c4302	15 mn 0 s	40	12.76	43.96	236.5	0.28	0.818	2.18	132.47	4150.53	40992.48	1.15E-05	9.84E-04	1.17E-02	99	1.07E-07	8.97E-08	6.10E-01	5.02E-01	4.88E-04	4.11E-04
c4302	15 mn 0 s	50	8.26	22.02	96.19	0.28	0.507	5.8	73.43	450.34	12672.63	4.35E-06	4.89E-05	1.64E-03	99	1.07E-07	8.97E-08	6.10E-01	5.02E-01	4.88E-04	4.11E-04
c4302	15 mn 0 s	60	10.96	10.96	10.96	2.25	2.25	2.25	324.75	324.75	324.75	9.53E-06	9.53E-06	9.53E-06	99	1.07E-07	8.97E-08	6.10E-01	5.02E-01	4.88E-04	4.11E-04
c4304	10 mn 0 s	30	8.15	23.07	56.09	0.28	0.752	2.01	105.46	601.34	3893.86	3.50E-06	5.66E-05	4.00E-04	356	4.70E-07	3.56E-07	2.96E+00	2.36E+00	2.63E-03	2.30E-03
c4304	10 mn 0 s	40	8.24	26.08	86.09	0.25	0.732	5.51	58.72	692.49	11498.61	2.68E-06	7.41E-05	1.02E-03	356	4.70E-07	3.56E-07	2.96E+00	2.36E+00	2.63E-03	2.30E-03
c4304	10 mn 0 s	50	9.42	68.32	305.21	0.28	1.023	4.6	98.33	11169.95	69389.27	5.19E-06	2.59E-03	2.24E-02	356	4.70E-07	3.56E-07	2.96E+00	2.36E+00	2.63E-03	2.30E-03
c4322	15 mn	20	8.15	29.69	138.83	0.24	0.813	3.7	61.51	1485.26	85684.94	2.70E-06	1.49E-04	7.26E-03	1595	6.04E-06	5.30E-06	5.19E+01	4.53E+01	7.86E-03	6.16E-03
c4322	15 mn	30	9.54	52.14	294.68	0.27	1.248	6.81	109.19	11109.74	222510.6	4.82E-06	1.20E-03	3.18E-02	1595	6.04E-06	5.30E-06	5.19E+01	4.53E+01	7.86E-03	6.16E-03
c4322	15 mn	40	11.29	56.23	256.53	0.23	1.135	5.72	59.22	9528.73	188213.7	6.60E-06	1.19E-03	2.44E-02	1595	6.04E-06	5.30E-06	5.19E+01	4.53E+01	7.86E-03	6.16E-03
c4322	15 mn	50	8.15	73.69	265.67	0.25	1.233	5.48	56.72	20497.72	253489.5	2.60E-06	2.65E-03	2.83E-02	1595	6.04E-06	5.30E-06	5.19E+01	4.53E+01	7.86E-03	6.16E-03
c4322	15 mn	60	9.8	35.01	111.93	0.27	0.976	5.18	78.64	2302.65	18832.18	5.59E-06	3.04E-04	2.10E-03	1595	6.04E-06	5.30E-06	5.19E+01	4.53E+01	7.86E-03	6.16E-03
c4324	10 mn	20	13.95	23.35	41.88	0.28	0.648	1.51	123.93	406.53	1159.21	1.20E-05	4.08E-05	1.42E-04	1195	2.63E-06	2.31E-06	2.23E+01	1.98E+01	8.83E-03	7.87E-03
c4324	10 mn	30	8.18	28.87	120.78	0.28	0.718	2.38	108.15	1056.62	18051.65	4.45E-06	1.19E-04	2.76E-03	1195	2.63E-06	2.31E-06	2.23E+01	1.98E+01	8.83E-03	7.87E-03
c4324	10 mn	40	8.15	30.67	204.18	0.26	0.873	5.95	64.79	2454.96	270411	2.88E-06	0.000257	0.0213	1195	2.6E-06	2.3E-06	22.3	19.8	0.00883	0.00787
c4324	10 mn	50	8.36	46.5	212.03	0.26	0.847	4.01	82.69	4396.97	67437.83	3.52E-06	0.00068	0.0109	1195	2.6E-06	2.3E-06	22.3	19.8	0.00883	0.00787
c4324	10 mn	60	9.33	55.21	227.65	0.28	0.913	3.05	69.11	6308.75	60397.11	3.57E-06	0.00109	0.0133	1195	2.6E-06	2.3E-06	22.3	19.8	0.00883	0.00787

Copper Full scale	Time	X [%]	$R_{10\% min}$ [micron]	$R_{10\% moy}$ [micron]	$R_{10\% max}$ [micron]	H_{min} [micron]	H_{moy} [micron]	H_{max} [micron]	$V_{d min}$ [m^3]	$V_{d moy}$ [m^3]	$V_{d max}$ [m^3]	$E_{d min}$ [J]	$E_{d moy}$ [J]	$E_{d max}$ [J]	N	$e^{(0)}$ [J/mm²/s]	$e^{(1)}$ [J/mm²/s]	$v^{(0)}$ [m^3/mm²/s]	$v^{(1)}$ [m^3/mm²/s]	$n^{(0)}$ [/mm²/s]	$n^{(1)}$ [/mm²/s]
c6152	14 mn 0 s	10	8.68	17.82	35.71	0.3	1.474	4.43	109.45	483.61	1811.51	3.93E-06	2.62E-05	8.71E-05	337	2.81E-07	2.52E-07	2.16E+00	1.92E+00	1.78E-03	1.56E-03
c6152	14 mn 0 s	20	9.54	33.24	160.39	0.26	0.779	3.34	98.78	1339.63	24108.55	4.93E-06	1.72E-04	4.94E-03	337	2.81E-07	2.52E-07	2.16E+00	1.92E+00	1.78E-03	1.56E-03
c6152	14 mn 0 s	30	10.99	31.51	122.66	0.26	0.568	4.57	113.88	1229.6	16106.3	7.53E-06	1.63E-04	2.32E-03	337	2.81E-07	2.52E-07	2.16E+00	1.92E+00	1.78E-03	1.56E-03
c6152	14 mn 0 s	40	9.6	39.07	108.03	0.26	0.704	2.24	116.24	1580.58	10516.78	4.73E-06	2.18E-04	1.79E-03	337	2.81E-07	2.52E-07	2.16E+00	1.92E+00	1.78E-03	1.56E-03
c6152	14 mn 0 s	50	9.88	34.27	118.82	0.26	1.252	3.61	129.03	1273.95	7293.65	7.76E-06	2.14E-04	1.74E-03	337	2.81E-07	2.52E-07	2.16E+00	1.92E+00	1.78E-03	1.56E-03
c6152	14 mn 0 s	60	13.42	13.42	13.42	3.53	3.53	3.53	763.75	763.75	763.75	1.97E-05	1.97E-05	1.97E-05	337	2.81E-07	2.52E-07	2.16E+00	1.92E+00	1.78E-03	1.56E-03
c6154	20 mn 0 s	20	10.53	23.41	79.4	0.45	1.468	6.16	151.39	819.58	5529.24	7.13E-06	8.76E-05	8.14E-04	513	5.81E-07	5.04E-07	3.63E+00	3.16E+00	1.90E-03	1.68E-03
c6154	20 mn 0 s	30	8.15	22.83	76.52	0.24	0.664	2.45	75.59	419.6	3517.05	4.49E-06	3.77E-05	6.18E-04	513	5.81E-07	5.04E-07	3.63E+00	3.16E+00	1.90E-03	1.68E-03
c6154	20 mn 0 s	40	11.14	45.65	171.54	0.24	0.833	5.84	54.62	4338.11	43421.31	5.43E-06	6.47E-04	5.85E-03	513	5.81E-07	5.04E-07	3.63E+00	3.16E+00	1.90E-03	1.68E-03
c6154	20 mn 0 s	50	9.99	56.02	218.06	0.25	0.632	2.4	86.61	4765.04	49240.94	6.53E-06	9.67E-04	1.11E-02	513	5.81E-07	5.04E-07	3.63E+00	3.16E+00	1.90E-03	1.68E-03
c6154	20 mn 0 s	60	8.15	50.07	189.85	0.24	0.718	2.94	53.53	4778.29	64781.28	2.59E-06	7.89E-04	8.08E-03	513	5.81E-07	5.04E-07	3.63E+00	3.16E+00	1.90E-03	1.68E-03
c6154	20 mn 0 s	70	12.38	57.83	231.67	0.3	1.327	4.26	171.55	12958.06	92859.59	1.76E-05	2.28E-03	1.68E-02	513	5.81E-07	5.04E-07	3.63E+00	3.16E+00	1.90E-03	1.68E-03
c6202	5 mn 0 s	20	10.01	35.65	169.1	0.24	0.608	2.59	81.89	1539.88	26816.86	4.98E-06	2.44E-04	4.93E-03	290	2.87E-06	2.47E-06	1.49E+01	1.27E+01	4.29E-03	3.36E-03
c6202	5 mn 0 s	30	8.15	55.3	262.6	0.25	0.677	4.34	52.78	5710.3	102398.5	3.93E-06	1.09E-03	1.62E-02	290	2.87E-06	2.47E-06	1.49E+01	1.27E+01	4.29E-03	3.36E-03
c6202	5 mn 0 s	40	8.15	57.42	330.22	0.26	0.699	2.73	88.44	6788.55	107428.3	4.23E-06	1.51E-03	3.12E-02	290	2.87E-06	2.47E-06	1.49E+01	1.27E+01	4.29E-03	3.36E-03
c6202	5 mn 0 s	50	14.15	42.44	105.57	0.25	0.654	2.57	119.16	1493.46	5624.08	1.33E-05	2.49E-04	1.28E-03	290	2.87E-06	2.47E-06	1.49E+01	1.27E+01	4.29E-03	3.36E-03
c6202	5 mn 0 s	60	8.15	19.79	74.02	0.36	0.852	1.32	80.69	796.26	8689.29	3.08E-06	7.67E-05	9.07E-04	290	2.87E-06	2.47E-06	1.49E+01	1.27E+01	4.29E-03	3.36E-03
c6204	5 mn 0 s	20	8.15	25.71	88.43	0.25	0.561	1.78	82.14	749.4	8549.47	4.04E-06	8.89E-05	1.19E-03	630	6.82E-06	5.96E-06	3.74E+01	3.29E+01	9.31E-03	8.08E-03
c6204	5 mn 0 s	30	8.15	40.2	222.46	0.23	0.722	4.34	66.62	2582.5	65893.08	4.12E-06	4.71E-04	1.10E-02	630	6.82E-06	5.96E-06	3.74E+01	3.29E+01	9.31E-03	8.08E-03
c6204	5 mn 0 s	40	8.15	41.15	203.21	0.22	0.701	2.93	66.62	3140.85	60617.09	4.01E-06	4.63E-04	9.13E-03	630	6.82E-06	5.96E-06	3.74E+01	3.29E+01	9.31E-03	8.08E-03
c6204	5 mn 0 s	50	8.15	53.4	426.85	0.23	0.749	4.39	66.62	8889.79	210149.5	3.25E-06	1.74E-03	6.43E-02	630	6.82E-06	5.96E-06	3.74E+01	3.29E+01	9.31E-03	8.08E-03
c6204	5 mn 0 s	60	13.43	39.15	180.99	0.24	0.523	4.04	65.51	2080.76	27247.62	6.62E-06	3.53E-04	5.95E-03	630	6.82E-06	5.96E-06	3.74E+01	3.29E+01	9.31E-03	8.08E-03
c6204	5 mn 0 s	70	8.15	49.72	276.67	0.26	0.482	1.81	92.39	4677.44	76333.21	4.01E-06	1.20E-03	2.01E-02	630	6.82E-06	5.96E-06	3.74E+01	3.29E+01	9.31E-03	8.08E-03
c6252	0 mn 45 s	20	8.15	27.77	108.75	0.26	0.72	4.54	62.31	1044.32	11935.64	3.29E-06	1.17E-04	1.92E-03	250	9.34E-06	8.03E-06	5.60E+01	4.71E+01	2.46E-02	1.90E-02
c6252	0 mn 45 s	30	11.19	52.46	234.69	0.24	0.639	2.26	50.95	4033.3	57268.34	4.69E-06	7.29E-04	1.28E-02	250	9.34E-06	8.03E-06	5.60E+01	4.71E+01	2.46E-02	1.90E-02
c6252	0 mn 45 s	40	10.03	52.92	214.05	0.33	0.868	1.99	130.62	3410.64	29725.25	5.36E-06	8.05E-04	8.56E-03	250	9.34E-06	8.03E-06	5.60E+01	4.71E+01	2.46E-02	1.90E-02
c6252	0 mn 45 s	50	8.15	44.21	146.21	0.24	0.901	1.97	114.64	4210.09	20165.97	4.24E-06	6.54E-04	3.69E-03	250	9.34E-06	8.03E-06	5.60E+01	4.71E+01	2.46E-02	1.90E-02
c6252	0 mn 45 s	60	38.72	38.72	38.72	0.41	0.41	0.41	738.4	738.4	738.4	1.01E-04	1.01E-04	1.01E-04	250	9.34E-06	8.03E-06	5.60E+01	4.71E+01	2.46E-02	1.90E-02
c6254	1 mn 0 s	10	9.74	16.96	52.51	0.33	0.845	3.73	81.47	297	2351.96	5.60E-06	2.14E-05	2.83E-04	586	5.10E-05	4.44E-05	3.25E+02	2.83E+02	4.33E-02	3.75E-02
c6254	1 mn 0 s	20	9.36	31.71	96.7	0.3	0.751	3.65	76.69	986.31	6516.75	4.33E-06	1.35E-04	1.20E-03	586	5.10E-05	4.44E-05	3.25E+02	2.83E+02	4.33E-02	3.75E-02
c6254	1 mn 0 s	30	8.15	44.79	257.62	0.26	0.604	2.82	58.65	3204.23	49439.02	4.03E-06	5.89E-04	1.46E-02	586	5.10E-05	4.44E-05	3.25E+02	2.83E+02	4.33E-02	3.75E-02
c6254	1 mn 0 s	40	8.15	43.36	313.35	0.23	0.691	5.38	44.41	4260.91	160433.1	3.82E-06	6.94E-04	3.49E-02	586	5.10E-05	4.44E-05	3.25E+02	2.83E+02	4.33E-02	3.75E-02
c6254	1 mn 0 s	50	8.15	78.21	315.6	0.22	1.101	8.38	56.38	23345.96	403781.9	4.11E-06	3.36E-03	3.85E-02	586	5.10E-05	4.44E-05	3.25E+02	2.83E+02	4.33E-02	3.75E-02
c6254	1 mn 0 s	60	8.15	64.51	247.72	0.22	0.673	2.76	72.49	8748.24	123746	4.04E-06	1.62E-03	1.56E-02	586	5.10E-05	4.44E-05	3.25E+02	2.83E+02	4.33E-02	3.75E-02
c6254	1 mn 0 s	70	8.15	65.57	258.6	0.25	0.793	3.15	112.09	12063.89	253083.6	3.94E-06	1.98E-03	3.22E-02	586	5.10E-05	4.44E-05	3.25E+02	2.83E+02	4.33E-02	3.75E-02

Stainless steel Full scale	Time	X [%]	$R_{10\% min}$ [micron]	$R_{10\% moy}$ [micron]	$R_{10\% max}$ [micron]	H_{min} [micron]	H_{moy} [micron]	H_{max} [micron]	$V_{d min}$ [m^3]	$V_{d moy}$ [m^3]	$V_{d max}$ [m^3]	$E_{d min}$ [J]	$E_{d moy}$ [J]	$E_{d max}$ [J]	N	$e^{(0)}$ [J/mm^2/s]	$e^{(1)}$ [J/mm^2/s]	$v^{(0)}$ [m^3/mm^2/s]	$v^{(1)}$ [m^3/mm^2/s]	$n^{(0)}$ [/mm^2/s]	$n^{(1)}$ [/mm^2/s]
i4302	125 mn 1 s	10	14.29	18.16	25.76	0.43	0.723	1.05	172.56	257.71	342.91	3.76E-05	7.19E-05	1.34E-04	10	1.40E-09	9.98E-10	3.54E-03	2.54E-03	5.91E-06	4.53E-06
i4302	125 mn 1 s	20	8.15	19.54	27.12	0.45	0.9	2.13	166.84	288.74	433.06	1.45E-05	9.26E-05	1.62E-04	10	1.40E-09	9.98E-10	3.54E-03	2.54E-03	5.91E-06	4.53E-06
i4302	125 mn 1 s	30	15.17	31.96	64.54	0.63	1.223	1.56	409.44	1350.82	3152.88	6.01E-05	5.96E-04	1.66E-03	10	1.40E-09	9.98E-10	3.54E-03	2.54E-03	5.91E-06	4.53E-06
i4304	90 mn 0 s	30	9.1	12.17	15.29	0.36	0.928	1.55	101.16	139.73	187.74	1.54E-05	2.65E-05	4.14E-05	73	1.01E-08	8.07E-09	2.58E-02	2.11E-02	6.00E-05	5.14E-05
i4304	90 mn 0 s	40	9.07	20.55	49.91	0.33	0.657	1.79	80.29	341.57	2843.7	1.37E-05	1.14E-04	1.03E-03	73	1.01E-08	8.07E-09	2.58E-02	2.11E-02	6.00E-05	5.14E-05
i4304	90 mn 0 s	50	13.55	36.59	74.81	0.27	0.629	1.38	134.62	1066.77	2991.51	3.03E-05	5.45E-04	1.90E-03	73	1.01E-08	8.07E-09	2.58E-02	2.11E-02	6.00E-05	5.14E-05
i4322	120 mn	20	9.06	24.36	92.42	0.22	0.703	3.13	74.3	1010.45	27969.31	1.38E-05	3.12E-04	7.83E-03	322	8.90E-08	7.36E-08	2.08E-01	1.70E-01	1.98E-04	1.62E-04
i4322	120 mn	30	8.49	33.18	128.71	0.21	0.635	4.64	51.82	1137.67	14529.9	1.09E-05	5.59E-04	1.03E-02	322	8.90E-08	7.36E-08	2.08E-01	1.70E-01	1.98E-04	1.62E-04
i4322	120 mn	40	9.92	24.95	87.74	0.26	0.769	2.9	93.84	752.63	11376	1.91E-05	2.79E-04	4.89E-03	322	8.90E-08	7.36E-08	2.08E-01	1.70E-01	1.98E-04	1.62E-04
i4322	120 mn	50	10.27	29.58	79.92	0.22	0.82	3.67	82.14	1302.51	11358.42	1.65E-05	5.01E-04	4.19E-03	322	8.90E-08	7.36E-08	2.08E-01	1.70E-01	1.98E-04	1.62E-04
i4322	120 mn	60	11.53	36	139.53	0.24	0.658	1.85	102.42	1136.51	7953.33	2.56E-05	9.85E-04	9.00E-03	322	8.90E-08	7.36E-08	2.08E-01	1.70E-01	1.98E-04	1.62E-04
i4324	100 mn	20	8.8	17.29	31.3	0.22	1.161	3.45	64.44	406.05	1403.28	1.47E-05	7.85E-05	2.25E-04	273	5.94E-08	5.16E-08	1.57E-01	1.34E-01	2.02E-04	1.74E-04
i4324	100 mn	30	9.03	21.61	46.7	0.28	0.64	1.76	88.68	342.31	1257.69	1.69E-05	1.29E-04	6.42E-04	273	5.94E-08	5.16E-08	1.57E-01	1.34E-01	2.02E-04	1.74E-04
i4324	100 mn	40	8.15	26.17	74.91	0.24	0.798	5.14	66.31	663.49	4180.22	9.51E-06	2.35E-04	2.41E-03	273	5.94E-08	5.16E-08	1.57E-01	1.34E-01	2.02E-04	1.74E-04
i4324	100 mn	50	8.15	31.7	96.57	0.22	0.778	6.39	56.72	1134.71	9963.09	8.87E-06	5.31E-04	4.43E-03	273	5.94E-08	5.16E-08	1.57E-01	1.34E-01	2.02E-04	1.74E-04
i4324	100 mn	60	10.74	26.28	72.41	0.25	0.9	3.68	110.65	1182.02	14741	2.16E-05	3.65E-04	3.99E-03	273	5.94E-08	5.16E-08	1.57E-01	1.34E-01	2.02E-04	1.74E-04

Stainless steel Full scale	Time	X [%]	$R_{10\%\ min}$ [micron]	$R_{10\%\ moy}$ [micron]	$R_{10\%\ max}$ [micron]	H_{min} [micron]	H_{moy} [micron]	H_{max} [micron]	$V_{d\ min}$ [m^3]	$V_{d\ moy}$ [m^3]	$V_{d\ max}$ [m^3]	$E_{d\ min}$ [J]	$E_{d\ moy}$ [J]	$E_{d\ max}$ [J]	N	$e_n^{(0)}$ [J/mm^2/s]	$e_n^{(1)}$ [J/mm^2/s]	$v_n^{(0)}$ [m^3/mm^2/s]	$v_n^{(1)}$ [m^3/mm^2/s]	$n_n^{(0)}$ [/mm^2/s]	$n_n^{(1)}$ [/mm^2/s]
i6152	120 mn 0 s	10	11.74	13.27	14.8	1.02	1.295	1.57	168.97	291	413.03	2.65E-05	4.22E-05	5.79E-05	12	4.59E-10	3.57E-10	1.75E-03	1.35E-03	7.39E-06	5.82E-06
i6152	120 mn 0 s	20	17.2	17.2	17.2	0.7	0.7	0.7	248.86	248.86	248.86	5.93E-05	5.93E-05	5.93E-05	12	4.59E-10	3.57E-10	1.75E-03	1.35E-03	7.39E-06	5.82E-06
i6152	120 mn 0 s	30	8.2	16.84	22.81	0.35	0.654	1.23	99.46	193.03	306.31	1.15E-05	5.62E-05	1.04E-04	12	4.59E-10	3.57E-10	1.75E-03	1.35E-03	7.39E-06	5.82E-06
i6152	120 mn 0 s	40	14.6	19.76	28.09	0.31	0.598	0.96	162.75	262.48	424.22	3.80E-05	8.03E-05	1.44E-04	12	4.59E-10	3.57E-10	1.75E-03	1.35E-03	7.39E-06	5.82E-06
i6154	135 mn 0 s	30	17.4	17.4	17.4	0.58	0.58	0.58	210.88	210.88	210.88	5.61E-05	5.61E-05	5.61E-05	15	1.46E-09	1.29E-09	3.91E-03	3.40E-03	8.21E-06	6.90E-06
i6154	135 mn 0 s	40	10.51	14.18	16.34	0.76	1.492	2.31	243.66	331.54	395.46	2.88E-05	4.93E-05	6.10E-05	15	1.46E-09	1.29E-09	3.91E-03	3.40E-03	8.21E-06	6.90E-06
i6154	135 mn 0 s	50	9.8	26.08	75.28	0.32	1.306	4.47	181.75	686.47	2178.55	2.13E-05	3.32E-04	1.81E-03	15	1.46E-09	1.29E-09	3.91E-03	3.40E-03	8.21E-06	6.90E-06
i6154	135 mn 0 s	60	8.97	10.64	12.5	0.83	1.947	2.69	108.65	268.16	435.8	1.79E-05	2.77E-05	4.48E-05	15	1.46E-09	1.29E-09	3.91E-03	3.40E-03	8.21E-06	6.90E-06
i6202	40 mn 0 s	10	11.62	11.62	11.62	0.8	0.8	0.8	129.82	129.82	129.82	2.31E-05	2.31E-05	2.31E-05	34	8.24E-09	6.92E-09	2.87E-02	2.38E-02	6.28E-05	5.24E-05
i6202	40 mn 0 s	20	10	19.92	36.88	0.35	0.722	1.93	103.39	319.13	931.28	2.11E-05	1.05E-04	3.79E+00	34	8.24E-09	6.92E-09	2.87E-02	2.38E-02	6.28E-05	5.24E-05
i6202	40 mn 0 s	30	14.81	25.24	39.21	0.31	0.781	1.37	153.37	693.38	1726.03	3.74E-05	2.00E-04	4.54E-04	34	8.24E-09	6.92E-09	2.87E-02	2.38E-02	6.28E-05	5.24E-05
i6202	40 mn 0 s	40	14.01	20.34	33.85	0.4	0.778	1.96	177.12	528.98	2660.75	3.83E-05	1.29E-04	5.20E-04	34	8.24E-09	6.92E-09	2.87E-02	2.38E-02	6.28E-05	5.24E-05
i6204	60 mn 0 s	30	9.73	15.91	26.73	0.46	0.878	1.25	142.2	233.46	394.98	1.79E-05	6.10E-05	1.52E-04	116	1.73E-07	1.51E-07	3.06E-01	2.68E-01	1.43E-04	1.23E-04
i6204	60 mn 0 s	40	9.79	26.19	68.39	0.27	0.551	1.48	97.07	468.39	2191.48	1.87E-05	2.28E-04	1.55E-03	116	1.73E-07	1.51E-07	3.06E-01	2.68E-01	1.43E-04	1.23E-04
i6204	60 mn 0 s	50	14.77	48.83	190.77	0.25	0.727	2.29	125.99	4762.27	62086.97	3.61E-05	2.68E-03	3.79E-02	116	1.73E-07	1.51E-07	3.06E-01	2.68E-01	1.43E-04	1.23E-04
i6204	60 mn 0 s	60	14.3	36.9	117.94	0.26	0.614	2.39	129.03	1265.24	7853.98	4.06E-05	7.69E-04	6.77E-03	116	1.73E-07	1.51E-07	3.06E-01	2.68E-01	1.43E-04	1.23E-04
i6204	60 mn 0 s	70	14.39	43.18	112.69	0.27	0.605	1.19	84.57	1695.74	9307.61	2.72E-05	9.81E-04	6.77E-03	116	1.73E-07	1.51E-07	3.06E-01	2.68E-01	1.43E-04	1.23E-04
i6252	8 mn 0 s	20	11.17	24.74	66.71	0.37	0.61	0.85	115.04	498.25	2245.86	2.15E-05	2.45E-04	1.50E-03	21	8.13E-08	5.88E-08	1.95E-01	1.41E-01	1.94E-04	1.48E-04
i6252	8 mn 0 s	30	15.25	28.9	54.4	0.4	0.606	1	170.56	620.53	1493.31	4.10E-05	2.61E-04	8.93E-04	21	8.13E-08	5.88E-08	1.95E-01	1.41E-01	1.94E-04	1.48E-04
i6252	8 mn 0 s	40	17.72	17.72	17.72	0.49	0.49	0.49	184.84	184.84	184.84	5.46E-05	5.46E-05	5.46E-05	21	8.13E-08	5.88E-08	1.95E-01	1.41E-01	1.94E-04	1.48E-04
i6252	8 mn 0 s	50	11.96	36.59	82.96	0.63	0.868	1.29	115.04	3009.48	10667.78	2.30E-05	1.18E-03	4.33E-03	21	8.13E-08	5.88E-08	1.95E-01	1.41E-01	1.94E-04	1.48E-04
i6254	12 mn 0 s	40	8.93	34.12	82.01	0.26	0.604	2.17	95.33	918.19	3635.94	1.84E-05	4.80E-04	2.63E-03	74	3.49E-07	2.95E-07	5.89E-01	4.95E-01	4.56E-04	3.67E-04
i6254	12 mn 0 s	50	10.97	39.4	124.61	0.26	0.588	1.25	128.7	1710.5	11379.92	2.16E-05	1.01E-03	8.76E-03	74	3.49E-07	2.95E-07	5.89E-01	4.95E-01	4.56E-04	3.67E-04
i6254	12 mn 0 s	60	15.75	39.13	126.41	0.31	0.526	0.92	185.04	1438.43	9791.37	4.97E-05	9.84E-04	8.38E-03	74	3.49E-07	2.95E-07	5.89E-01	4.95E-01	4.56E-04	3.67E-04
i6254	12 mn 0 s	70	21.32	25.48	29.96	0.26	0.355	0.48	147.4	286.74	442.05	6.70E-05	1.23E-04	1.93E-04	74	3.49E-07	2.95E-07	5.89E-01	4.95E-01	4.56E-04	3.67E-04
i6302	1 mn 40 s	20	13.23	24.8	39.81	0.37	0.587	0.85	159.78	414.17	818.93	3.15E-05	1.61E-04	4.07E-04	14	1.94E-07	1.31E-07	5.24E-01	3.54E-01	6.21E-04	4.19E-04
i6302	1 mn 40 s	30	12.48	30.64	66.31	0.5	0.882	1.19	170.17	1618.33	6286.93	2.94E-05	5.86E-04	2.36E-03	14	1.94E-07	1.31E-07	5.24E-01	3.54E-01	6.21E-04	4.19E-04
i6304	2 mn 30 s	30	9.99	33.66	68.03	0.32	0.594	0.93	111.45	1085.15	4255.34	1.68E-05	4.92E-04	1.93E-03	142	6.28E-06	5.43E-06	1.20E+01	1.03E+01	4.20E-03	3.53E-03
i6304	2 mn 30 s	40	9.62	39.32	152.87	0.27	0.659	1.87	86.71	2297.73	28003.22	1.46E-05	1.19E-03	1.57E-02	142	6.28E-06	5.43E-06	1.20E+01	1.03E+01	4.20E-03	3.53E-03
i6304	2 mn 30 s	50	16.36	49.98	184.45	0.28	0.741	2.32	113.39	4701.99	51110.02	4.27E-05	2.62E-03	3.03E-02	142	6.28E-06	5.43E-06	1.20E+01	1.03E+01	4.20E-03	3.53E-03
i6304	2 mn 30 s	60	10.63	46.32	128.02	0.35	0.827	1.97	128.22	2363.75	7843.61	2.40E-05	1.46E-03	7.68E-03	142	6.28E-06	5.43E-06	1.20E+01	1.03E+01	4.20E-03	3.53E-03
i6304	2 mn 30 s	70	13.49	34.65	115.94	0.33	1.007	3.42	176.51	3173.57	21941.87	4.40E-05	1.25E-03	9.48E-03	142	6.28E-06	5.43E-06	1.20E+01	1.03E+01	4.20E-03	3.53E-03

Copper Div. test section Full scale	Time	X [%]	$R_{10\%\ min}$ [micron]	$R_{10\%\ moy}$ [micron]	$R_{10\%\ max}$ [micron]	H_{min} [micron]	H_{moy} [micron]	H_{max} [micron]	$V_{d\ min}$ [m^3]	$V_{d\ moy}$ [m^3]	$V_{d\ max}$ [m^3]	$E_{d\ min}$ [J]	$E_{d\ moy}$ [J]	$E_{d\ max}$ [J]	N	$e^{(0)}$ [J/mm²/s]	$e^{(1)}$ [J/mm²/s]	$v^{(0)}$ [m^3/mm²/s]	$v^{(1)}$ [m^3/mm²/s]	$n^{(0)}$ [/mm²/s]	$n^{(1)}$ [/mm²/s]
dc4202	120 mn 0 s	20	8.15	22.02	48.47	0.23	0.546	2.86	64.71	322.82	1721.62	2.88E-06	3.03E-05	2.15E-04	2950	5.60E-08	4.20E-08	6.07E-01	4.53E-01	1.82E-03	1.35E-03
dc4202	120 mn 0 s	30	8.15	22.42	47.5	0.25	0.549	3.04	63.11	344.43	1896.19	2.74E-06	3.29E-05	2.00E-04	2950	5.60E-08	4.20E-08	6.07E-01	4.53E-01	1.82E-03	1.35E-03
dc4202	120 mn 0 s	40	8.15	21.45	41.31	0.25	0.608	5.15	65.91	335.11	3516.77	3.12E-06	2.94E-05	1.51E-04	2950	5.60E-08	4.20E-08	6.07E-01	4.53E-01	1.82E-03	1.35E-03
dc4204	90 mn 0 s	30	8.15	17.98	55.32	0.26	0.807	3.19	52.73	312.87	5957.04	2.51E-06	2.23E-05	4.81E-04	6793	1.11E-07	8.28E-08	1.55E+00	1.15E+00	5.58E-03	4.16E-03
dc4204	90 mn 0 s	40	8.15	17.61	42.25	0.24	0.751	2.93	54.32	267.42	2740.64	2.54E-06	1.96E-05	1.51E-04	6793	1.11E-07	8.28E-08	1.55E+00	1.15E+00	5.58E-03	4.16E-03
dc4204	90 mn 0 s	50	8.15	16.71	50.54	0.26	0.768	3.49	58.65	246.76	2669.94	2.67E-06	1.74E-05	2.84E-04	6793	1.11E-07	8.28E-08	1.55E+00	1.15E+00	5.58E-03	4.16E-03
dc4302	10 mn 0 s	30	8.15	20.73	89.62	0.26	0.661	3.48	65.51	375.76	20169.54	2.84E-06	3.23E-05	1.83E-03	5397	1.20E-06	9.00E-07	1.37E+01	1.03E+01	3.99E-02	3.02E-02
dc4302	10 mn 0 s	40	8.15	20.28	53.52	0.24	0.639	3.15	58.58	316.07	4286.53	3.09E-06	2.70E-05	2.95E-04	5397	1.20E-06	9.00E-07	1.37E+01	1.03E+01	3.99E-02	3.02E-02
dc4302	10 mn 0 s	50	8.15	21.84	69.64	0.21	0.598	4.1	43.99	345.98	3670.57	2.83E-06	3.16E-05	5.45E-04	5397	1.20E-06	9.00E-07	1.37E+01	1.03E+01	3.99E-02	3.02E-02
dc4304	5 mn 0 s	40	8.15	30.53	235.6	0.26	0.731	3.94	61.61	2634.58	240752.1	3.01E-06	3.19E-04	2.72E-02	2187	1.74E-05	1.50E-05	1.35E+02	1.16E+02	3.23E-02	2.72E-02
dc4304	5 mn 0 s	50	8.15	36.28	276.06	0.26	0.841	8.51	76.42	4675.69	186577.8	3.87E-06	5.69E-04	2.53E-02	2187	1.74E-05	1.50E-05	1.35E+02	1.16E+02	3.23E-02	2.72E-02
dc4304	5 mn 0 s	60	8.15	34.54	399.9	0.24	0.752	8.44	61.45	5745.21	486097	3.73E-06	7.04E-04	8.69E-02	2187	1.74E-05	1.50E-05	1.35E+02	1.16E+02	3.23E-02	2.72E-02
dc4304	5 mn 0 s	70	8.15	34.03	352.5	0.25	0.687	6.98	81.52	3950.79	213600.2	3.71E-06	5.67E-04	4.41E-02	2187	1.74E-05	1.50E-05	1.35E+02	1.16E+02	3.23E-02	2.72E-02
dc4304	5 mn 0 s	80	8.15	32.42	204.57	0.25	0.623	4.44	87.35	3149.7	59742.35	4.10E-06	4.50E-04	9.92E-03	2187	1.74E-05	1.50E-05	1.35E+02	1.16E+02	3.23E-02	2.72E-02
dc4304b	1 mn 15 s	40	8.15	18.09	45.49	0.24	0.634	2.53	54.32	246.75	3154.08	2.57E-06	1.96E-05	2.58E-04	8318	1.21E-05	1.03E-05	1.46E+02	1.23E+02	4.92E-01	4.10E-01
dc4304b	1 mn 15 s	50	8.15	18.78	64.18	0.26	0.678	2.93	55.12	288.28	7342.32	2.56E-06	2.27E-05	5.50E-04	8318	1.21E-05	1.03E-05	1.46E+02	1.23E+02	4.92E-01	4.10E-01
dc4304b	1 mn 15 s	60	8.15	18.6	43.35	0.27	0.644	2.92	57.12	263.04	1917.37	2.67E-06	2.13E-05	1.87E-04	8318	1.21E-05	1.03E-05	1.46E+02	1.23E+02	4.92E-01	4.10E-01
dc4304b	1 mn 15 s	70	8.15	19.96	175	0.24	0.69	2.81	53.13	363.49	38635.05	2.59E-06	3.24E-05	7.10E-03	8318	1.21E-05	1.03E-05	1.46E+02	1.23E+02	4.92E-01	4.10E-01
dc4304b	1 mn 15 s	80	8.15	18.67	44.39	0.25	0.637	2.88	67.11	260.06	2083.54	3.02E-06	2.11E-05	2.06E-04	8318	1.21E-05	1.03E-05	1.46E+02	1.23E+02	4.92E-01	4.10E-01
dc6202	1 mn 15 s	20	8.61	21.38	51.62	0.24	0.486	4.16	58.72	287.99	2976.72	2.87E-06	2.91E-05	3.09E-04	256	6.02E-07	4.61E-07	6.11E+00	4.67E+00	1.51E-02	1.10E-02
dc6202	1 mn 15 s	30	11.34	21.01	41.2	0.27	0.621	2.88	107.85	344.37	1451.21	6.66E-06	3.05E-05	1.42E-04	256	6.02E-07	4.61E-07	6.11E+00	4.67E+00	1.51E-02	1.10E-02
dc6202	1 mn 15 s	40	13.65	30.24	84.36	0.34	0.569	1.42	114.21	1860.38	12141.35	8.12E-06	2.01E-04	1.31E-03	256	6.02E-07	4.61E-07	6.11E+00	4.67E+00	1.51E-02	1.10E-02
dc6202	1 mn 15 s	50	10.12	19	60.38	0.3	0.655	2.06	69.47	458.35	5212.47	4.51E-06	3.78E-05	5.16E-04	256	6.02E-07	4.61E-07	6.11E+00	4.67E+00	1.51E-02	1.10E-02
dc6204	1 mn 0 s	30	8.15	21.35	181.45	0.26	0.563	2.78	93.47	567.96	45094.24	3.81E-06	7.23E-05	8.09E-03	692	2.02E-05	1.79E-05	1.22E+02	1.08E+02	5.12E-02	4.23E-02
dc6204	1 mn 0 s	40	8.15	24.61	149.31	0.27	0.647	2.52	65.51	1282.82	42587.29	3.96E-06	1.61E-04	5.81E-03	692	2.02E-05	1.79E-05	1.22E+02	1.08E+02	5.12E-02	4.23E-02
dc6204	1 mn 0 s	50	8.15	36.08	339.96	0.27	0.821	4.84	62.99	6610.78	186070.5	4.04E-06	1.02E-03	4.25E-02	692	2.02E-05	1.79E-05	1.22E+02	1.08E+02	5.12E-02	4.23E-02
dc6204	1 mn 0 s	60	8.15	33.23	223.65	0.23	0.738	5.36	37.01	2873.96	72113.71	3.65E-06	4.61E-04	1.40E-02	692	2.02E-05	1.79E-05	1.22E+02	1.08E+02	5.12E-02	4.23E-02
dc6204	1 mn 0 s	70	8.15	31.27	351.5	0.24	0.519	2.39	75.82	3167.22	173674	4.00E-06	6.37E-04	4.33E-02	692	2.02E-05	1.79E-05	1.22E+02	1.08E+02	5.12E-02	4.23E-02
dc6204	1 mn 0 s	80	18.09	23.31	28.23	0.41	0.461	0.58	165.14	311.21	448.59	1.50E-05	3.12E-05	4.71E-05	692	2.02E-05	1.79E-05	1.22E+02	1.08E+02	5.12E-02	4.23E-02

Stainless steel Div. test section Full scale	Time	X [%]	$R_{10\% min}$ [micron]	$R_{10\% moy}$ [micron]	$R_{10\% max}$ [micron]	H_{min} [micron]	H_{moy} [micron]	H_{max} [micron]	$V_{d min}$ [m^3]	$V_{d moy}$ [m^3]	$V_{d max}$ [m^3]	$E_{d min}$ [J]	$E_{d moy}$ [J]	$E_{d max}$ [J]	N	$e^{(0)}$ [J/mm²/s]	$e^{(1)}$ [J/mm²/s]	$v^{(0)}$ [m^3/mm²/s]	$v^{(1)}$ [m^3/mm²/s]	$n^{(0)}$ [/mm²/s]	$n^{(1)}$ [/mm²/s]
di6252	5 mn 0 s	20	10.1	19.33	33.79	0.56	0.974	2.41	127.42	659.01	3299.07	1.82E-05	1.42E-04	5.76E-04	48	2.06E-06	1.44E-06	2.18E+00	1.56E+00	7.10E-04	5.72E-04
di6252	5 mn 0 s	30	11.23	28.71	86.56	0.26	0.73	1.97	87.97	781.83	4641.99	2.19E-05	3.82E-04	2.73E-03	48	2.06E-06	1.44E-06	2.18E+00	1.56E+00	7.10E-04	5.72E-04
di6252	5 mn 0 s	40	0	0	0	0	0	0	0	0	0	0.00E+00	0.00E+00	0.00E+00	48	2.06E-06	1.44E-06	2.18E+00	1.56E+00	7.10E-04	5.72E-04
di6252	5 mn 0 s	50	23.17	51.67	93.8	0.34	0.478	0.58	354.83	2018.48	6130.78	1.14E-04	1.29E-03	4.15E-03	48	2.06E-06	1.44E-06	2.18E+00	1.56E+00	7.10E-04	5.72E-04
di6252	5 mn 0 s	60	8.15	71.26	281.33	0.3	0.931	1.82	87.48	9558.15	50058.84	1.17E-05	1.03E-02	6.17E-02	48	2.06E-06	1.44E-06	2.18E+00	1.56E+00	7.10E-04	5.72E-04
di6254	9 mn 0 s	30	15.75	33.4	74.95	0.31	0.621	1.31	141.72	966.98	3352.72	4.20E-05	4.58E-04	2.17E-03	221	4.28E-06	3.81E-06	7.27E+00	6.46E+00	1.82E-03	1.58E-03
di6254	9 mn 0 s	40	8.15	43.22	210.06	0.29	0.76	2.29	81.9	3175.44	33400.61	1.32E-05	2.01E-03	3.37E-02	221	4.28E-06	3.81E-06	7.27E+00	6.46E+00	1.82E-03	1.58E-03
di6254	9 mn 0 s	50	8.15	50.35	265.03	0.24	0.828	3.25	86.71	4937.85	94514.27	1.26E-05	2.93E-03	7.89E-02	221	4.28E-06	3.81E-06	7.27E+00	6.46E+00	1.82E-03	1.58E-03
di6254	9 mn 0 s	60	8.93	50.91	195.23	0.26	0.757	2.72	85.8	4698	50592.32	1.44E-05	2.77E-03	3.16E-02	221	4.28E-06	3.81E-06	7.27E+00	6.46E+00	1.82E-03	1.58E-03
di6254	9 mn 0 s	70	16.45	49.08	129.96	0.29	0.674	1.52	100.79	2638.89	14204.42	3.68E-05	1.58E-03	1.04E-02	221	4.28E-06	3.81E-06	7.27E+00	6.46E+00	1.82E-03	1.58E-03
di6254	9 mn 0 s	80	28.12	53.57	92.06	0.77	1.21	2	731.39	5423.35	12727.71	2.17E-04	2.00E-03	5.57E-03	221	4.28E-06	3.81E-06	7.27E+00	6.46E+00	1.82E-03	1.58E-03

Aluminium Small scale	Time	X [%]	$R_{10\%\ min}$ [micron]	$R_{10\%\ moy}$ [micron]	$R_{10\%\ max}$ [micron]	H_{min} [micron]	H_{moy} [micron]	H_{max} [micron]	$V_{d\ min}$ [m^3]	$V_{d\ moy}$ [m^3]	$V_{d\ max}$ [m^3]	$E_{d\ min}$ [J]	$E_{d\ moy}$ [J]	$E_{d\ max}$ [J]	N	$e^{(0)}$ [J/mm^2/s]	$e^{(1)}$ [J/mm^2/s]	$v^{(0)}$ [m^3/mm^2/s]	$v^{(1)}$ [m^3/mm^2/s]	$n^{(0)}$ [/mm^2/s]	$n^{(1)}$ [/mm^2/s]
pa4204	40 mn	40	5.58	10.3	20.34	0.25	0.763	3.16	39.34	89.08	346.68	8.85E-08	3.68E-07	1.48E-06	97	4.56E-10	3.08E-10	1.13E-01	7.61E-02	1.33E-03	8.97E-04
pa4204	40 mn	50	4.9	9.5	17.2	0.31	0.805	1.93	30.11	78.86	255.91	6.67E-08	3.09E-07	1.28E-06	97	4.56E-10	3.08E-10	1.13E-01	7.61E-02	1.33E-03	8.97E-04
pa4252	7 mn 30 s	20	5.63	12.21	21.46	0.25	0.512	1.66	36.32	85.37	224.06	1.05E-07	4.62E-07	1.49E-06	97	1.18E-09	7.95E-10	2.15E-01	1.45E-01	2.66E-03	1.79E-03
pa4252	7 mn 30 s	30	8.03	11.78	17.44	0.25	0.417	0.62	25.07	69.11	124.66	1.57E-07	3.91E-07	8.78E-07	97	1.18E-09	7.95E-10	2.15E-01	1.45E-01	2.66E-03	1.79E-03
pa4254	5 mn	40	4.9	12.87	42.82	0.23	0.606	10.28	18.69	131.09	2290.61	6.77E-08	6.90E-07	1.12E-05	1012	2.64E-08	1.78E-08	4.92E+00	3.32E+00	4.16E-02	2.81E-02
pa4254	5 mn	50	5.32	12.65	31.43	0.23	0.468	2.41	24.68	97.34	2824.75	7.04E-08	5.45E-07	1.03E-05	1012	2.64E-08	1.78E-08	4.92E+00	3.32E+00	4.16E-02	2.81E-02
pa4302	1 mn 30s	20	5.96	13.18	31.26	0.27	0.577	3.73	28.81	131.44	1861.51	1.09E-07	6.96E-07	7.01E-06	198	1.76E-08	1.19E-08	3.24E+00	2.19E+00	2.71E-02	1.83E-02
pa4302	1 mn 30 s	30	7.05	12.72	25.75	0.27	0.414	0.77	35.26	83.45	422.36	1.22E-07	5.12E-07	3.08E-06	198	1.76E-08	1.19E-08	3.24E+00	2.19E+00	2.71E-02	1.83E-02
pa4304	1 mn	40	4.9	17.17	105.6	0.22	0.639	4.13	20.34	362.46	9377.91	5.65E-08	2.55E-06	1.25E-04	780	8.05E-07	5.44E-07	1.06E+02	7.12E+01	1.60E-01	1.08E-01
pa4304	1 mn	50	5.73	21.48	127.29	0.24	0.718	5.05	29.23	1140.68	43136.26	8.57E-08	9.05E-06	3.13E-04	780	8.05E-07	5.44E-07	1.06E+02	7.12E+01	1.60E-01	1.08E-01
pa6152	2 mn 45 s	20	5.58	13.71	57.02	0.25	0.554	3.03	33.86	187.15	4920.99	9.80E-08	1.11E-06	3.45E-05	202	2.16E-08	1.46E-08	3.39E+00	2.29E+00	1.51E-02	1.02E-02
pa6152	2 mn 45 s	30	6.68	15.54	59.97	0.27	0.644	3.35	37.87	334.13	4428.46	1.61E-07	2.34E-06	3.52E-05	202	2.16E-08	1.46E-08	3.39E+00	2.29E+00	1.51E-02	1.02E-02
pa6154	3 mn 30 s	40	6.6	17.73	62.21	0.25	0.543	2.2	22.05	334.45	4557.44	1.22E-07	2.49E-06	3.83E-05	161	2.49E-08	1.68E-08	3.44E+00	2.32E+00	9.45E-03	6.38E-03
pa6154	3 mn 30 s	50	9.1	18.96	59.27	0.23	0.554	2.6	26.7	408.29	3228.78	1.75E-07	2.86E-06	2.67E-05	161	2.49E-08	1.68E-08	3.44E+00	2.32E+00	9.45E-03	6.38E-03
pa6202	1 mn	20	5.86	19.52	95.13	0.26	0.7	3.65	28.56	658.84	15210.12	8.97E-08	4.84E-06	1.22E-04	367	3.58E-07	2.41E-07	5.12E+01	3.46E+01	7.54E-02	5.09E-02
pa6202	1 mn	30	4.9	19.88	70.3	0.25	0.713	3.82	33.08	722.98	9405.94	8.18E-08	4.54E-06	6.36E-05	367	3.58E-07	2.41E-07	5.12E+01	3.46E+01	7.54E-02	5.09E-02
pa6204	3 mn 0 s	40	5.75	12.73	32.29	0.28	0.832	3.82	32.96	160.53	696.39	9.28E-08	7.74E-07	4.94E-06	128	1.34E-08	9.07E-09	2.48E+00	1.67E+00	8.87E-03	5.99E-03
pa6204	3 mn 0 s	50	4.9	12.85	73.18	0.24	0.96	5.06	29.97	369.13	11001.74	6.32E-08	2.07E-06	7.49E-05	128	1.34E-08	9.07E-09	2.48E+00	1.67E+00	8.87E-03	5.99E-03
pa6252	0 mn 30 s	20	5.69	20.58	121.49	0.25	0.753	4.45	30.06	993.43	67035.45	9.37E-08	6.20E-06	3.92E-04	666	2.08E-06	1.41E-06	2.91E+02	1.97E+02	2.74E-01	1.85E-01
pa6252	0 mn 30 s	30	4.9	22.43	161.47	0.23	0.67	5.79	26.7	1199.83	40407.04	8.11E-08	1.03E-05	4.86E-04	666	2.08E-06	1.41E-06	2.91E+02	1.97E+02	2.74E-01	1.85E-01
pa6254	0 mn 45 s	40	5.93	22.26	176.03	0.25	0.767	4.76	28.93	1364.38	63924.2	9.59E-08	1.05E-05	6.52E-04	1039	2.76E-06	2.09E-06	3.77E+02	2.87E+02	2.84E-01	2.20E-01
pa6254	0 mn 45 s	50	5.24	19.39	170.96	0.23	0.766	8.19	22.48	1196.88	75999.29	6.16E-08	8.42E-06	6.64E-04	1039	2.76E-06	2.09E-06	3.77E+02	2.87E+02	2.84E-01	2.20E-01
pa6254	0 mn 45 s	60	4.9	20.86	117.75	0.25	0.851	5.2	29.6	1518.05	45987.11	8.71E-08	1.09E-05	2.83E-04	1039	2.76E-06	2.09E-06	3.77E+02	2.87E+02	2.84E-01	2.20E-01
pabis6254	2 mn 30 s	40	4.9	23.19	209.98	0.26	1.11	16.13	31.93	2426.75	163165.7	7.71E-08	1.45E-05	1.42E-03	1296	1.90E-06	1.46E-06	3.11E+02	2.38E+02	1.06E-01	7.91E-02
pabis6254	2 mn 30 s	50	5.41	26.93	206.3	0.24	1.07	12	29.25	3964.21	330604.3	8.13E-08	2.37E-05	1.38E-03	1296	1.90E-06	1.46E-06	3.11E+02	2.38E+02	1.06E-01	7.91E-02
pabis6254	2 mn 30 s	60	4.9	26.15	159.88	0.24	0.863	7.07	29.55	2562.31	160743.8	8.32E-08	1.72E-05	7.20E-04	1296	1.90E-06	1.46E-06	3.11E+02	2.38E+02	1.06E-01	7.91E-02

Appendix C

High-speed visualisations

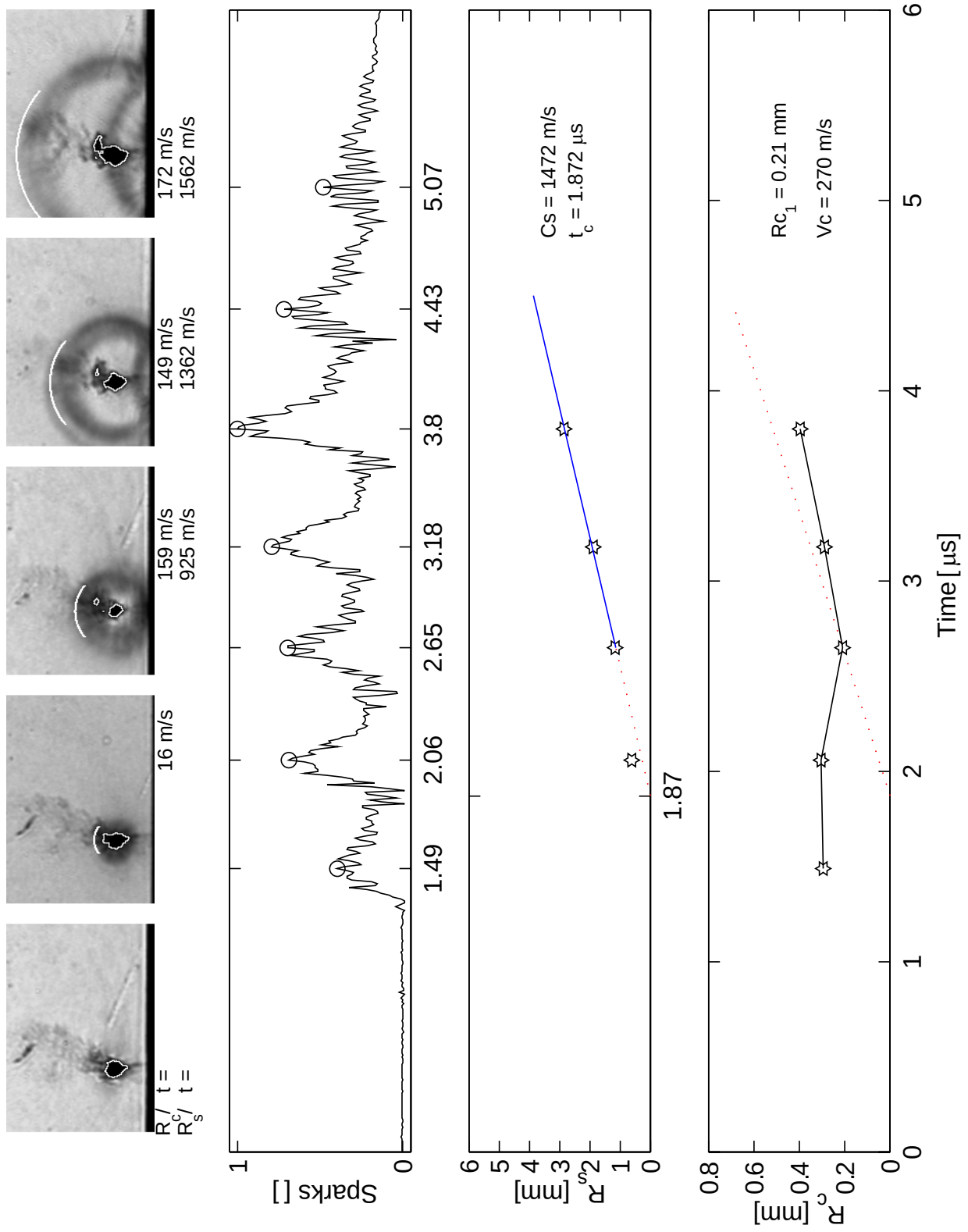

Figure C.1: Collapse time determination and cavitation vortex characteristics
N=200 rpm, Q=0.58 l/s, σ=1.6

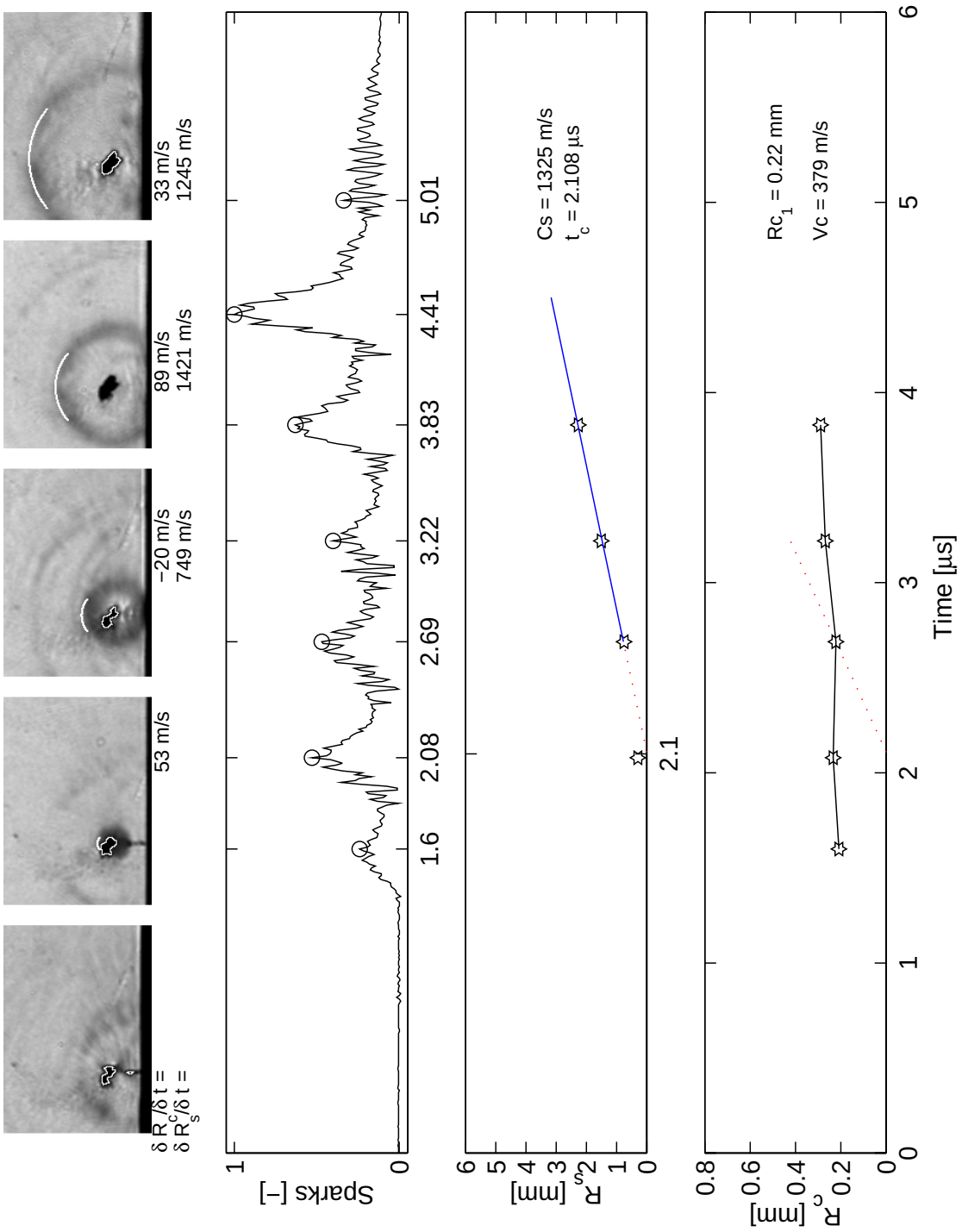

Figure C.2: Collapse time determination and cavitation vortex characteristics N=200 rpm, Q=0.58 l/s, σ=1.6

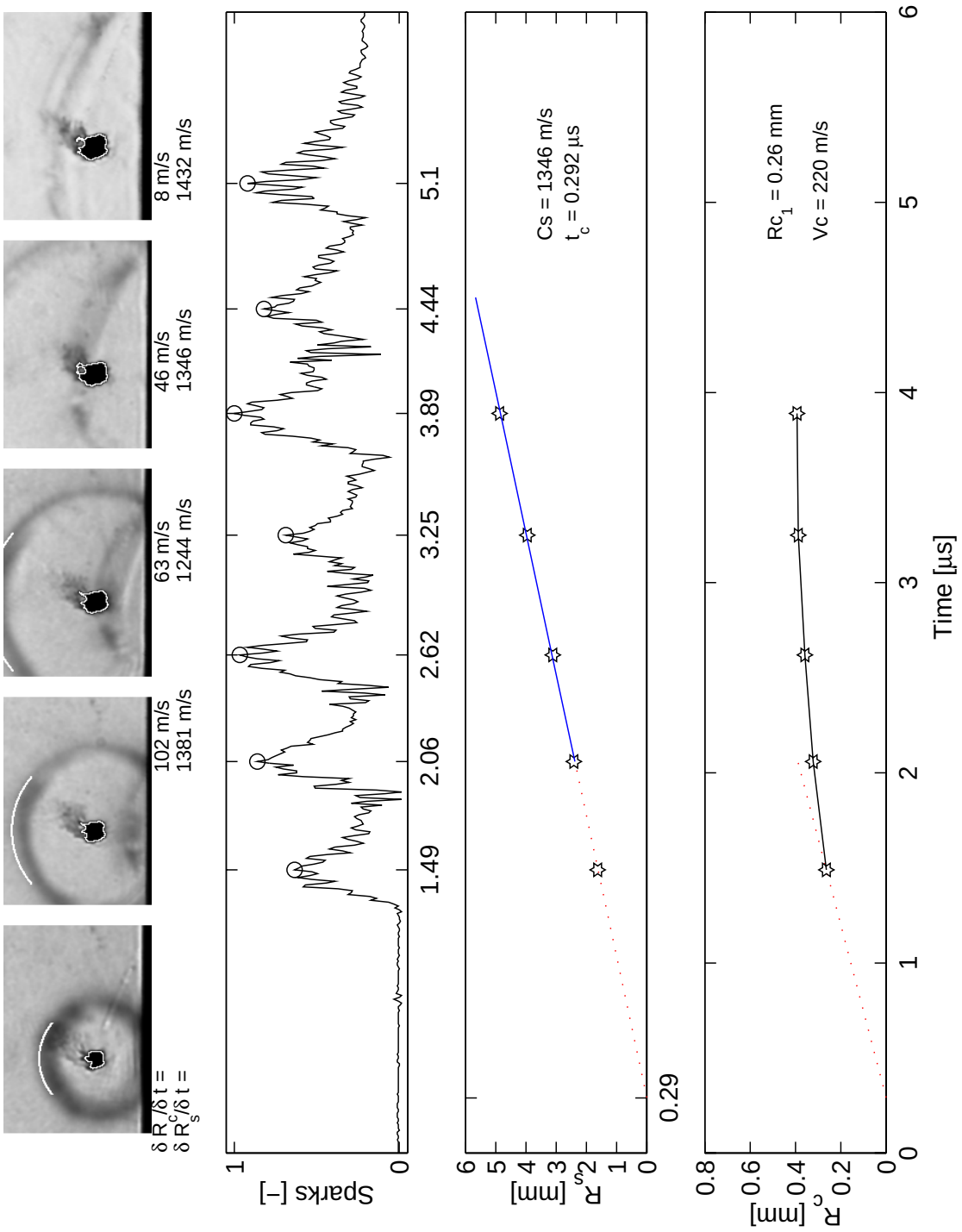

Figure C.3: Collapse time determination and cavitation vortex characteristics N=200 rpm, Q=0.58 l/s, σ=1.6

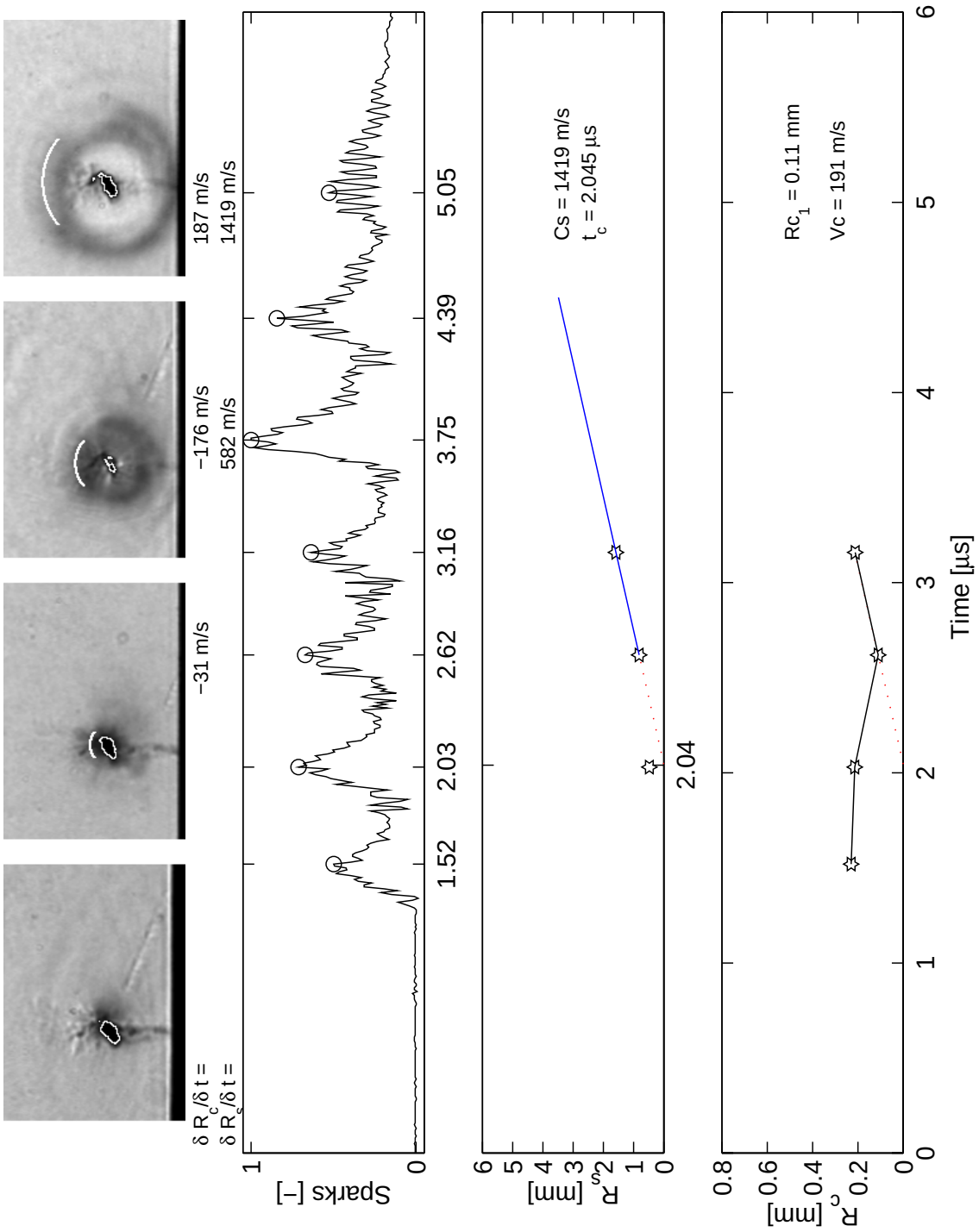

Figure C.4: Collapse time determination and cavitation vortex characteristics N=200 rpm, Q=0.58 l/s, σ=1.6

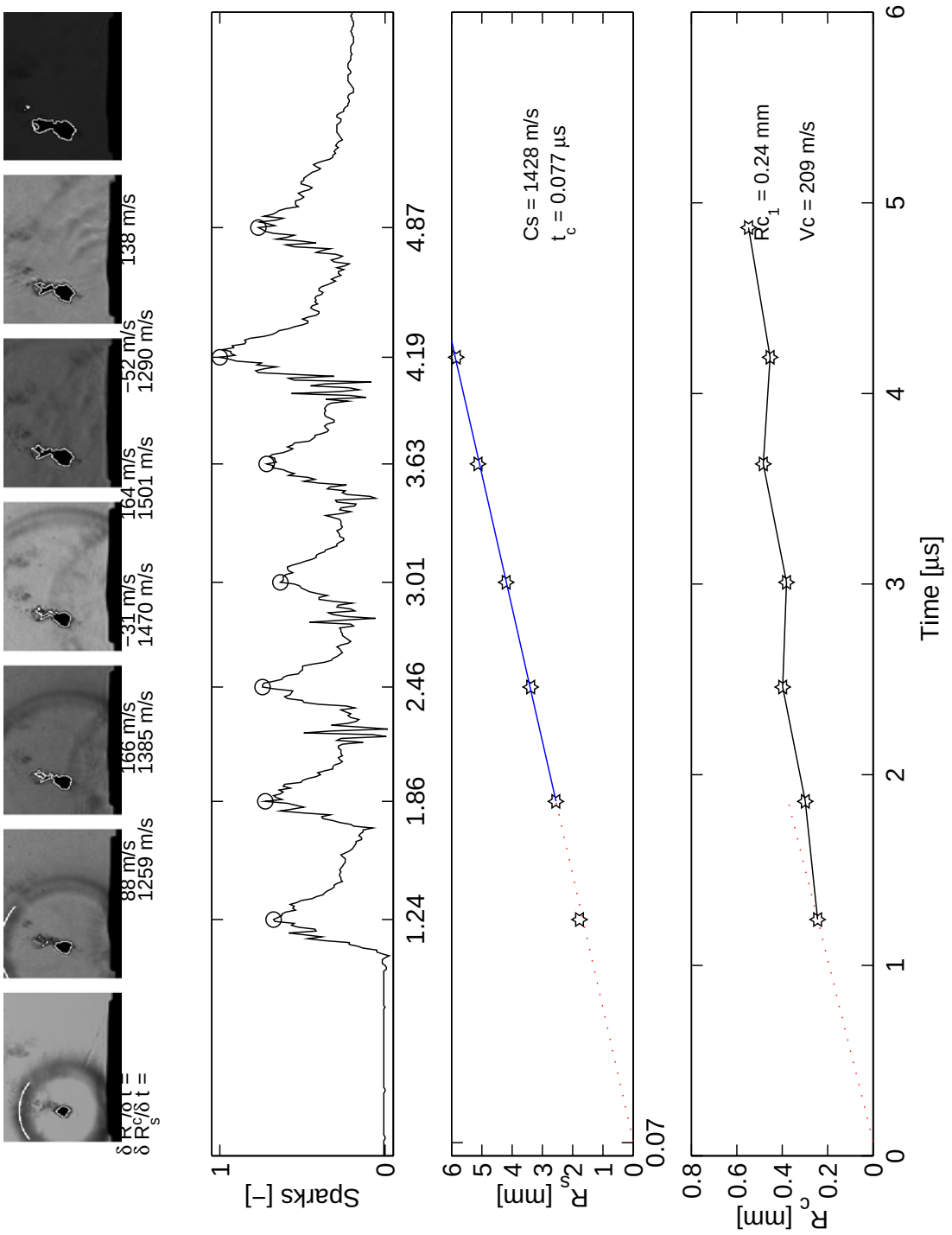

Figure C.5: Collapse time determination and cavitation vortex characteristics N=200 rpm, Q=0.58 l/s, σ=1.6

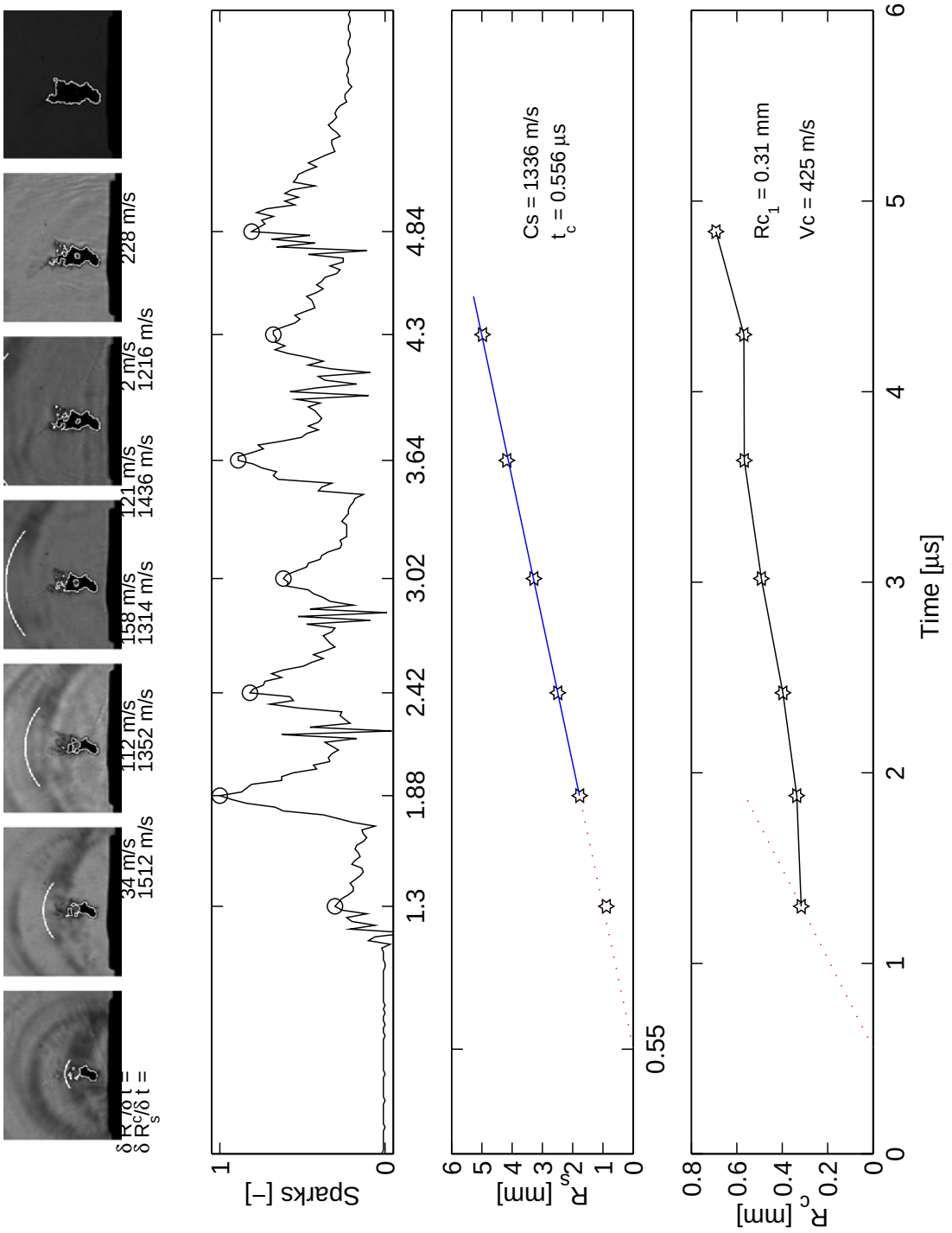

Figure C.6: Collapse time determination and cavitation vortex characteristics N=200 rpm, Q=0.58 l/s, σ=1.6

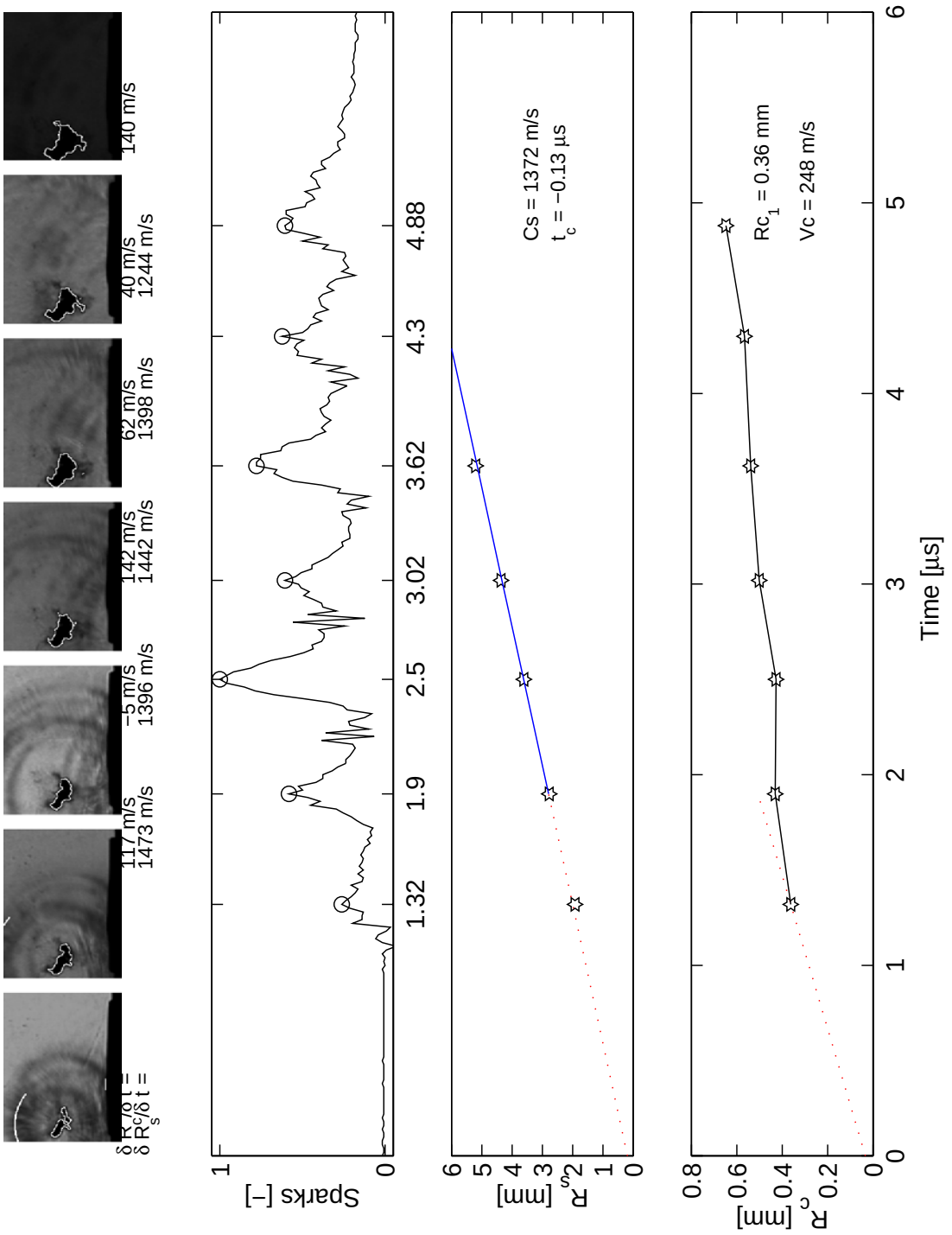

Figure C.7: Collapse time determination and cavitation vortex characteristics N=200 rpm, Q=0.58 l/s, σ=1.6

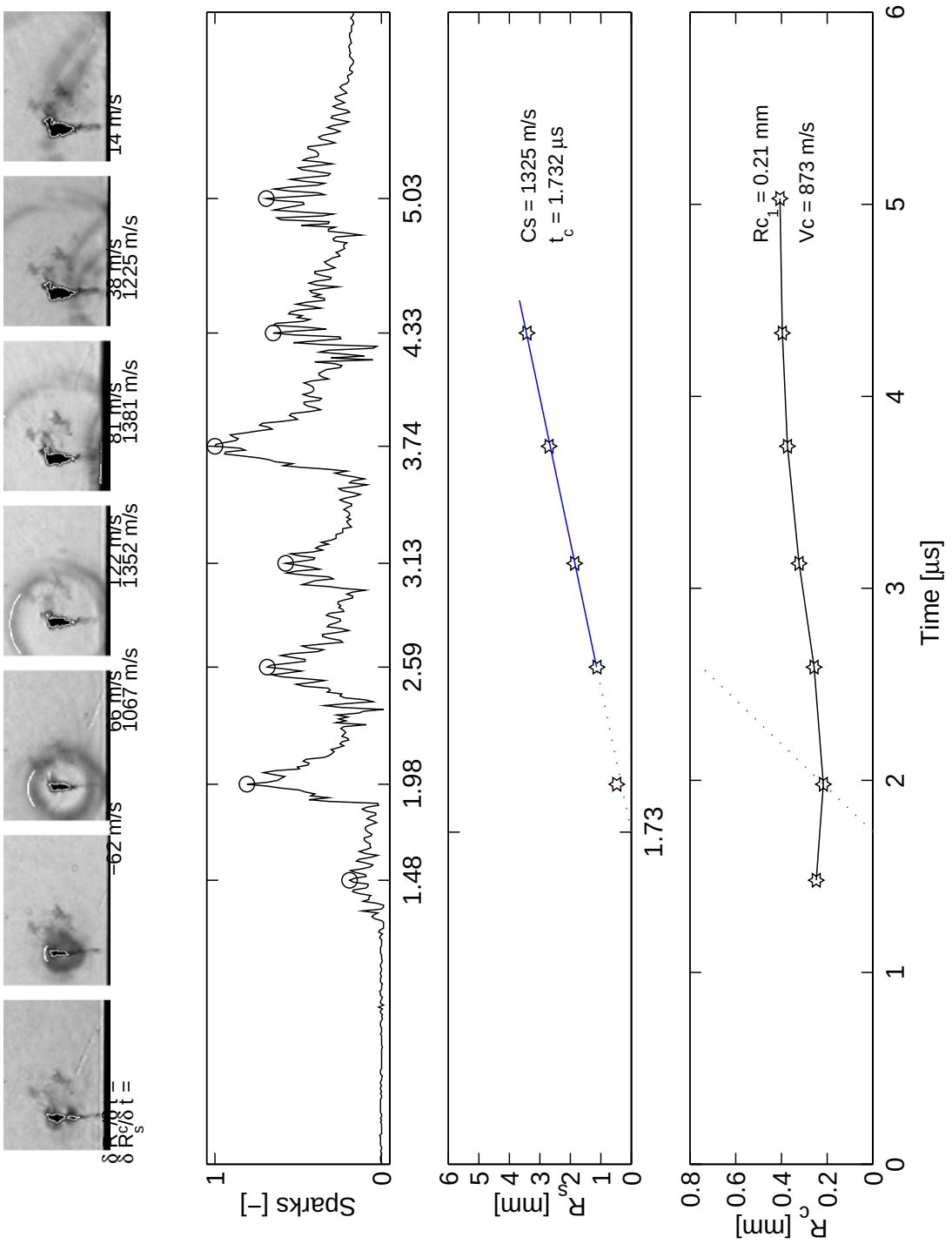

Figure C.8: Collapse time determination and cavitation vortex characteristics N=200 rpm, Q=0.58 l/s, σ=1.6

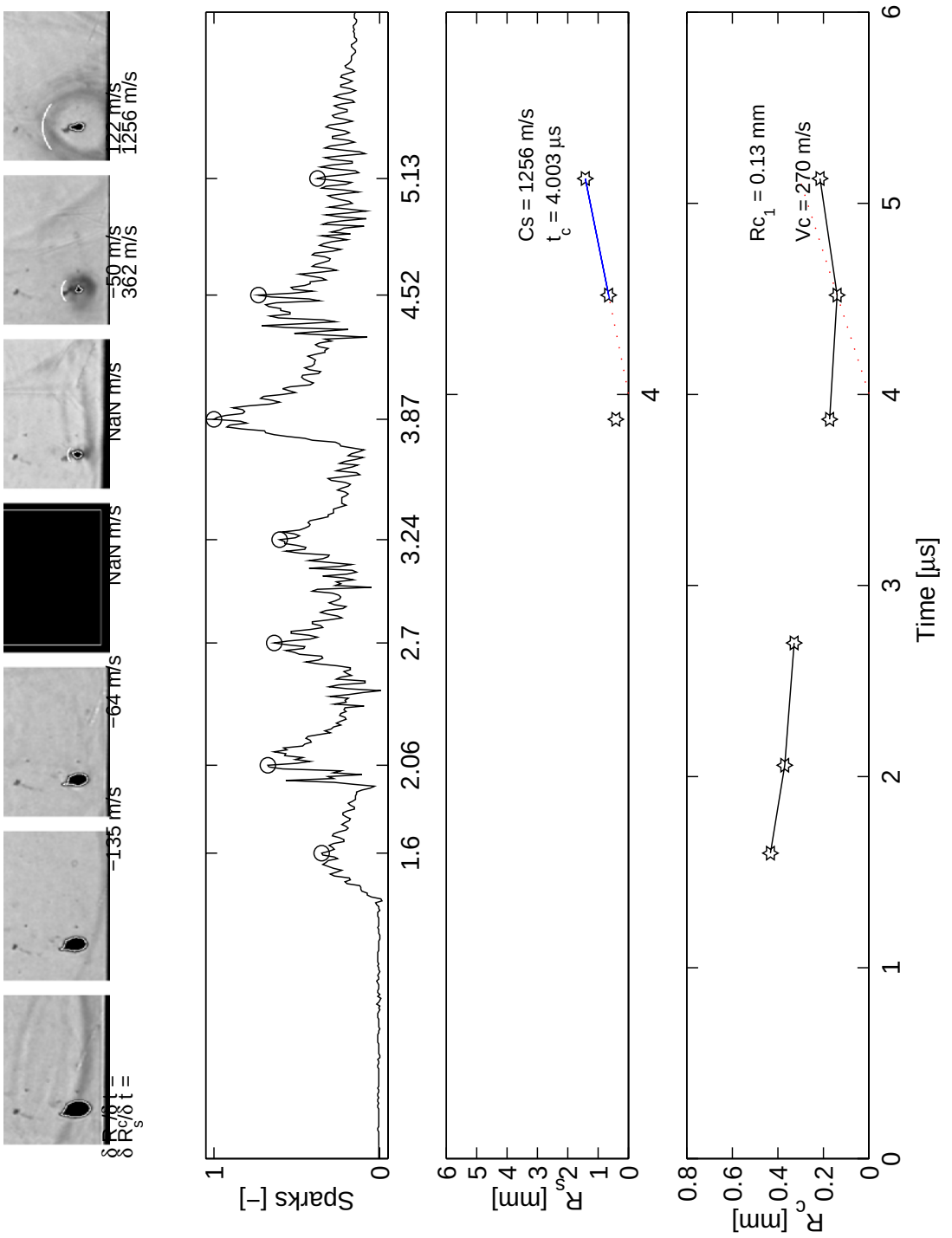

Figure C.9: Collapse time determination and cavitation vortex characteristics N=200 rpm, Q=0.58 l/s, σ=1.6

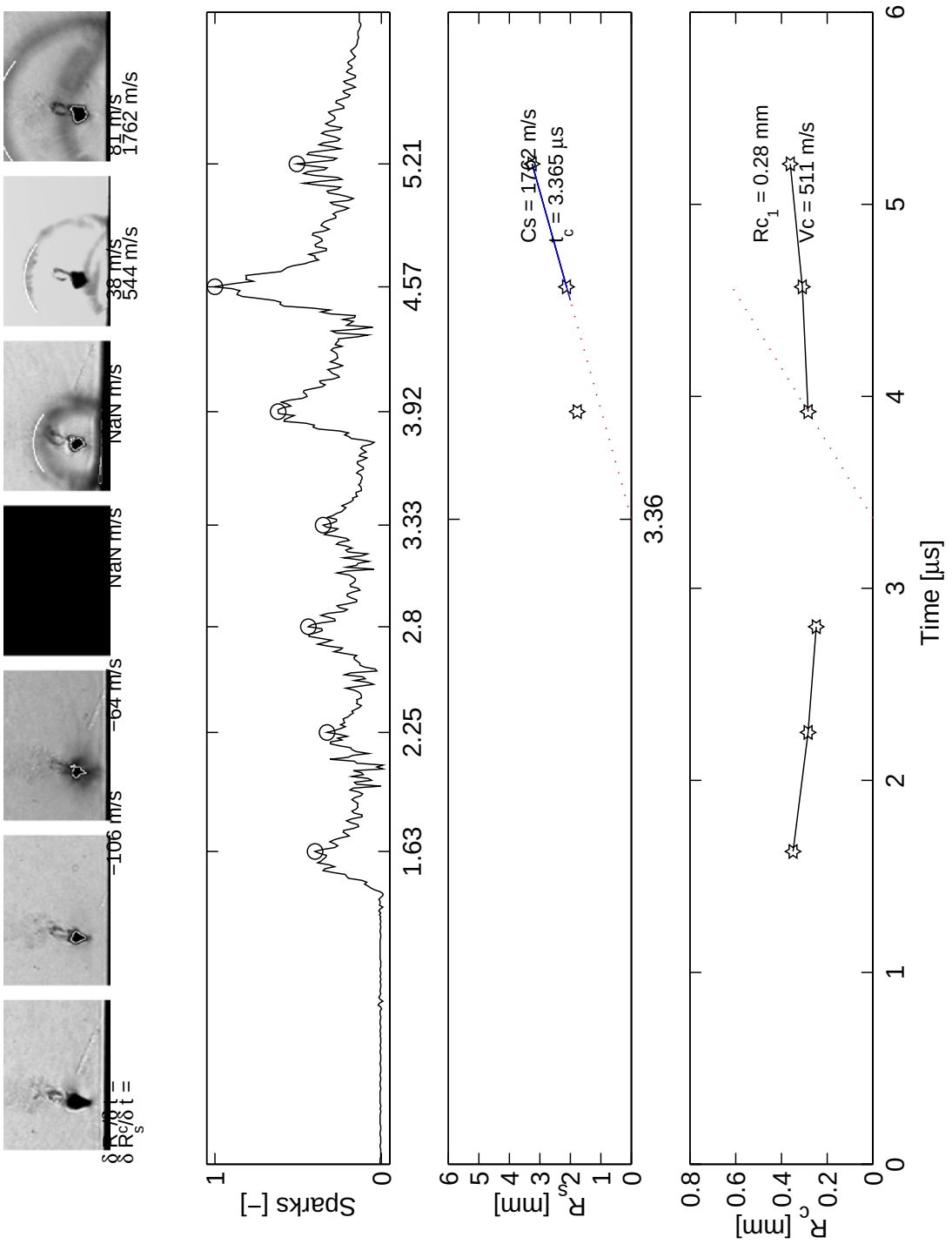

Figure C.10: Collapse time determination and cavitation vortex characteristics N=200 rpm, Q=0.58 l/s, σ=1.6

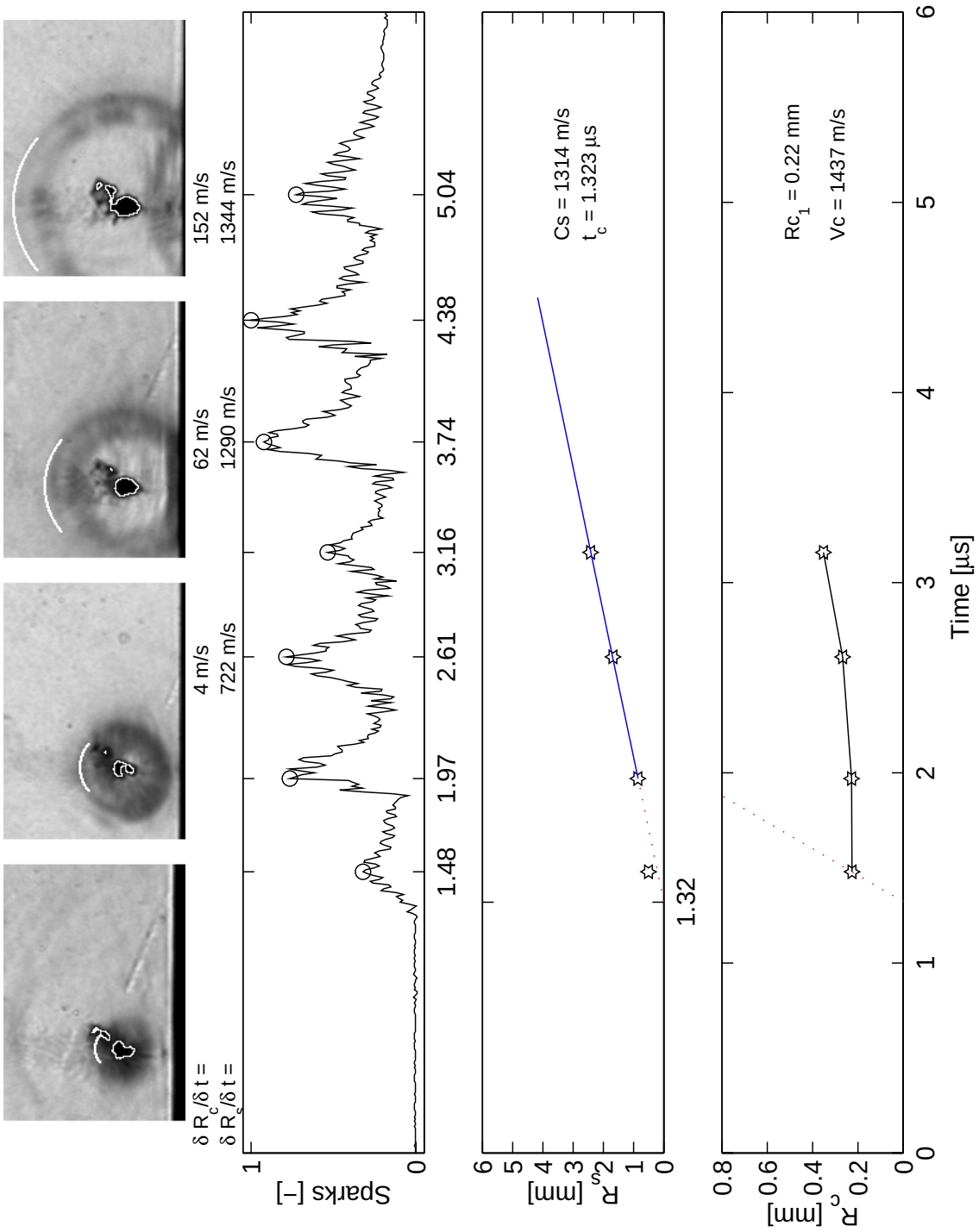

Figure C.11: Collapse time determination and cavitation vortex characteristics N=200 rpm, Q=0.58 l/s, σ=1.6

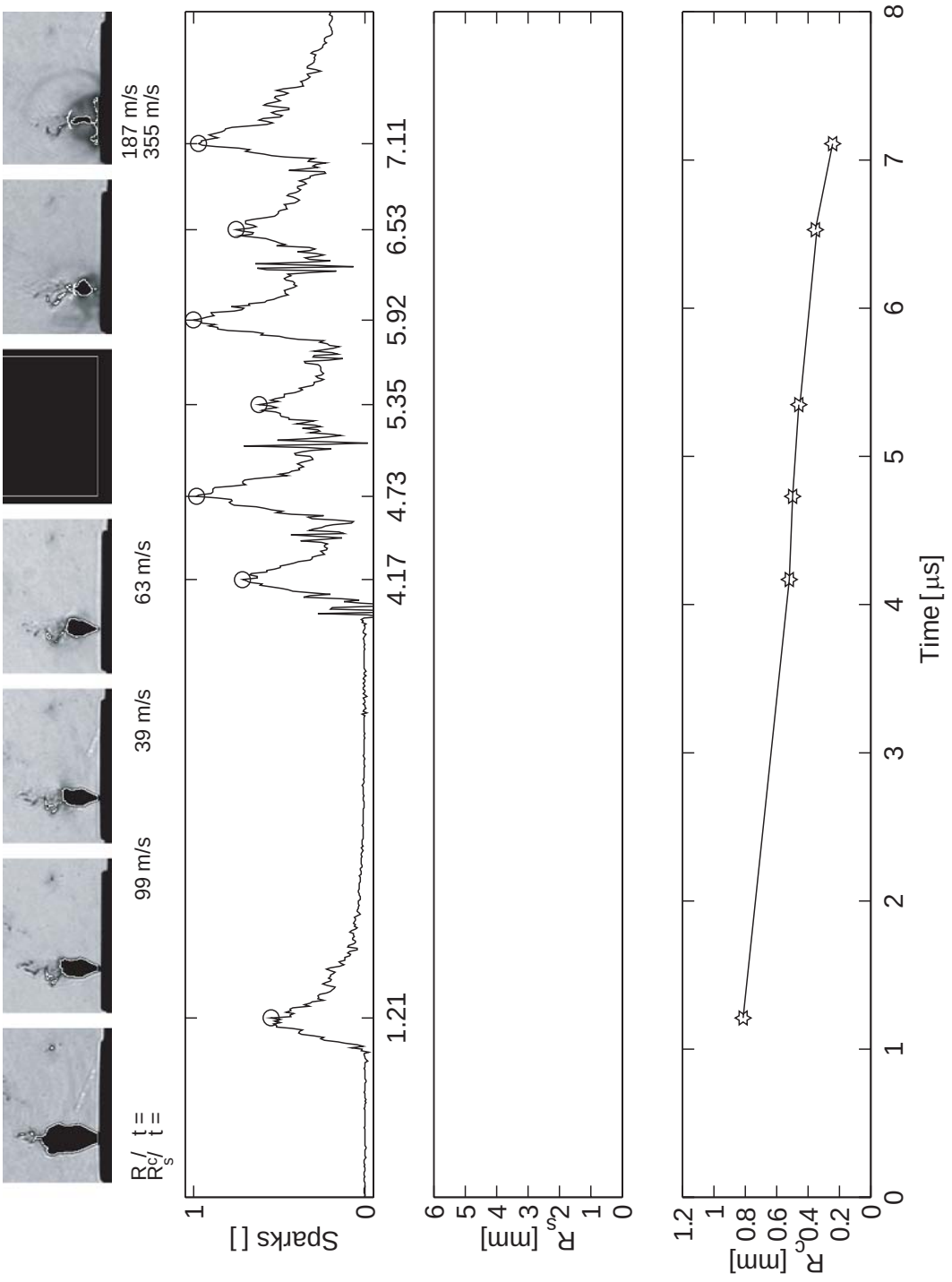

Figure C.12: Collapse time determination and cavitation vortex characteristics
N=200 rpm, Q=0.66 l/s, σ=1.2

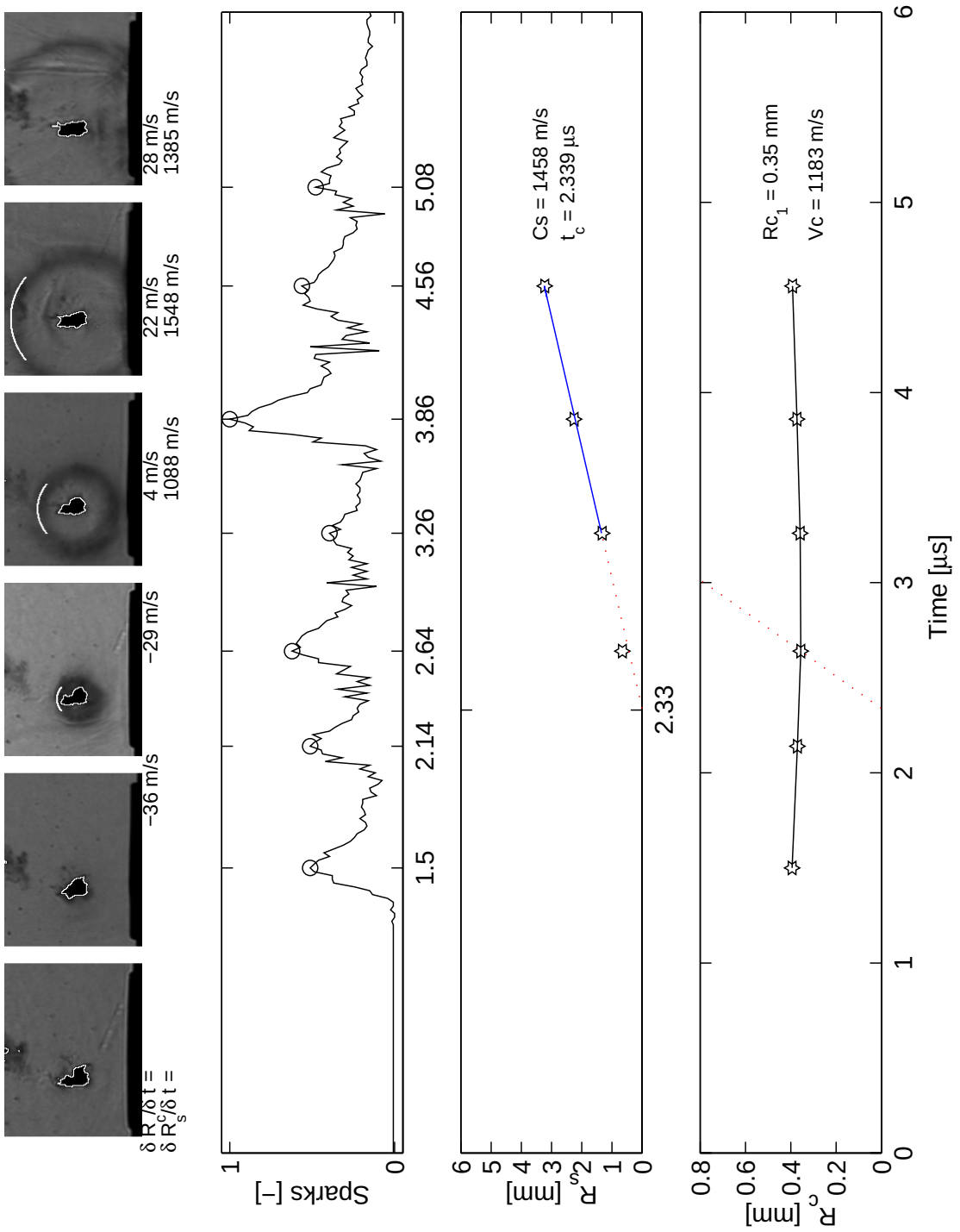

Figure C.13: Collapse time determination and cavitation vortex characteristics N=200 rpm, Q=0.66 l/s, σ=1.2

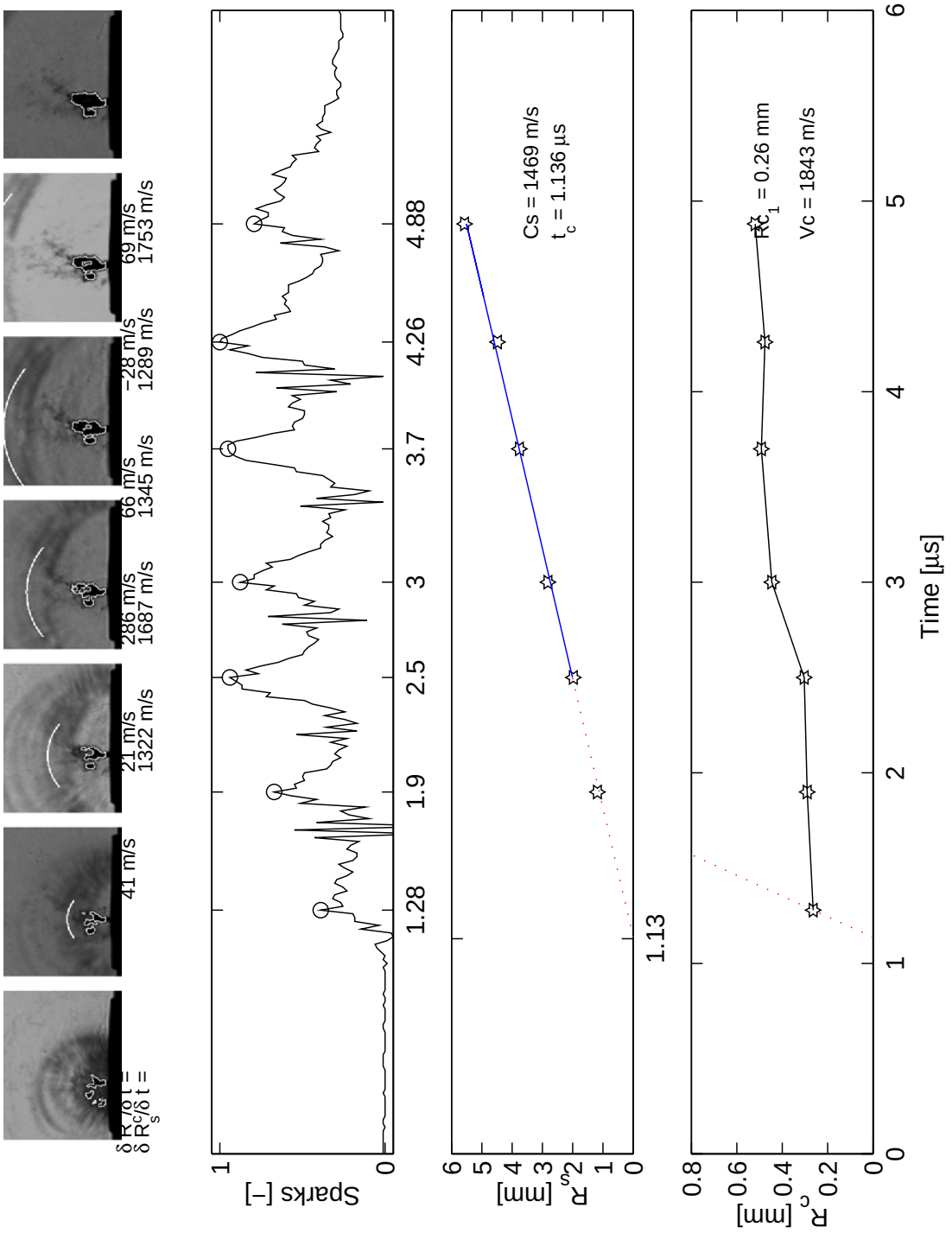

Figure C.14: Collapse time determination and cavitation vortex characteristics N=200 rpm, Q=0.66 l/s, σ=1.2

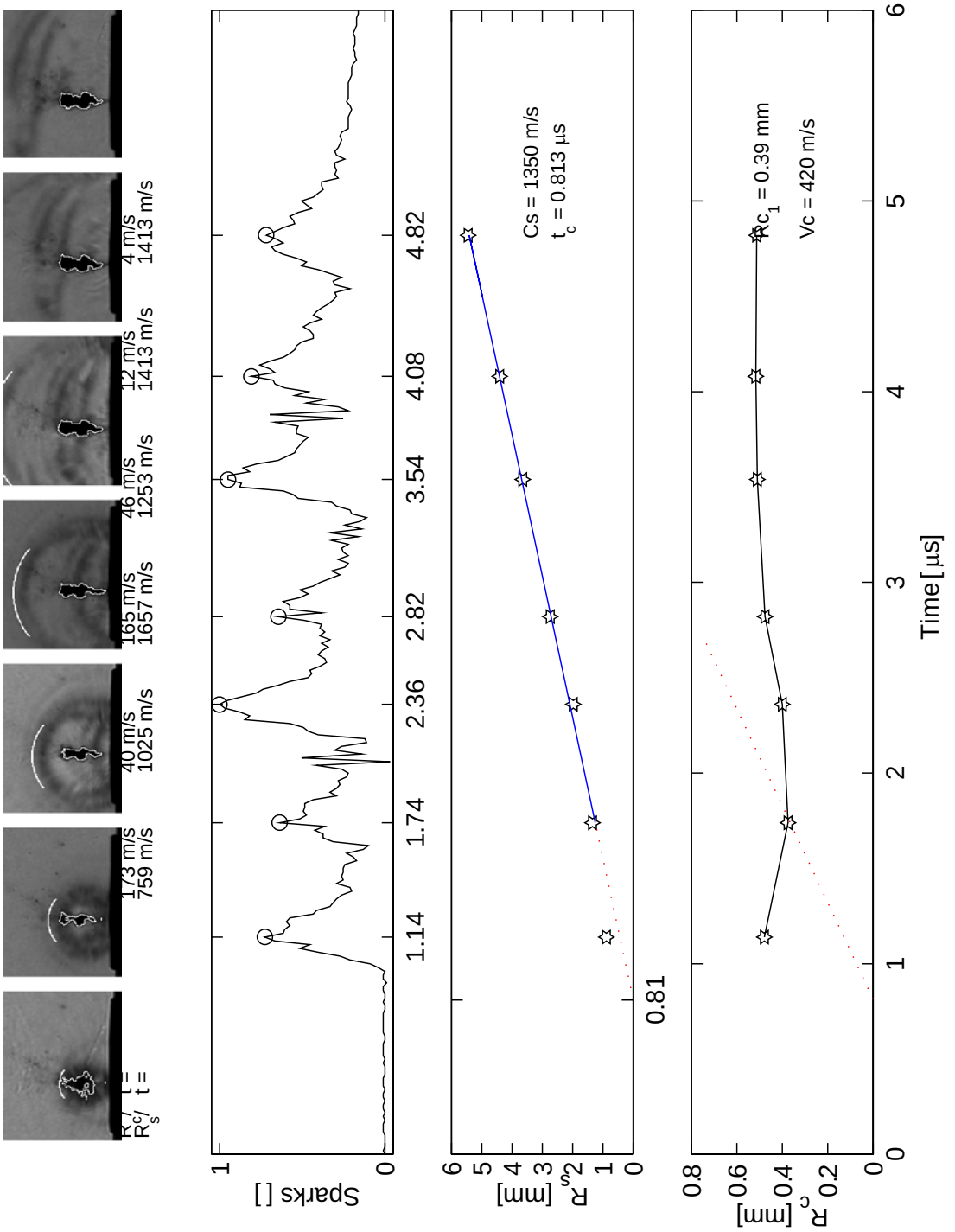

Figure C.15: Collapse time determination and cavitation vortex characteristics N=200 rpm, Q=0.66 l/s, σ=1.2

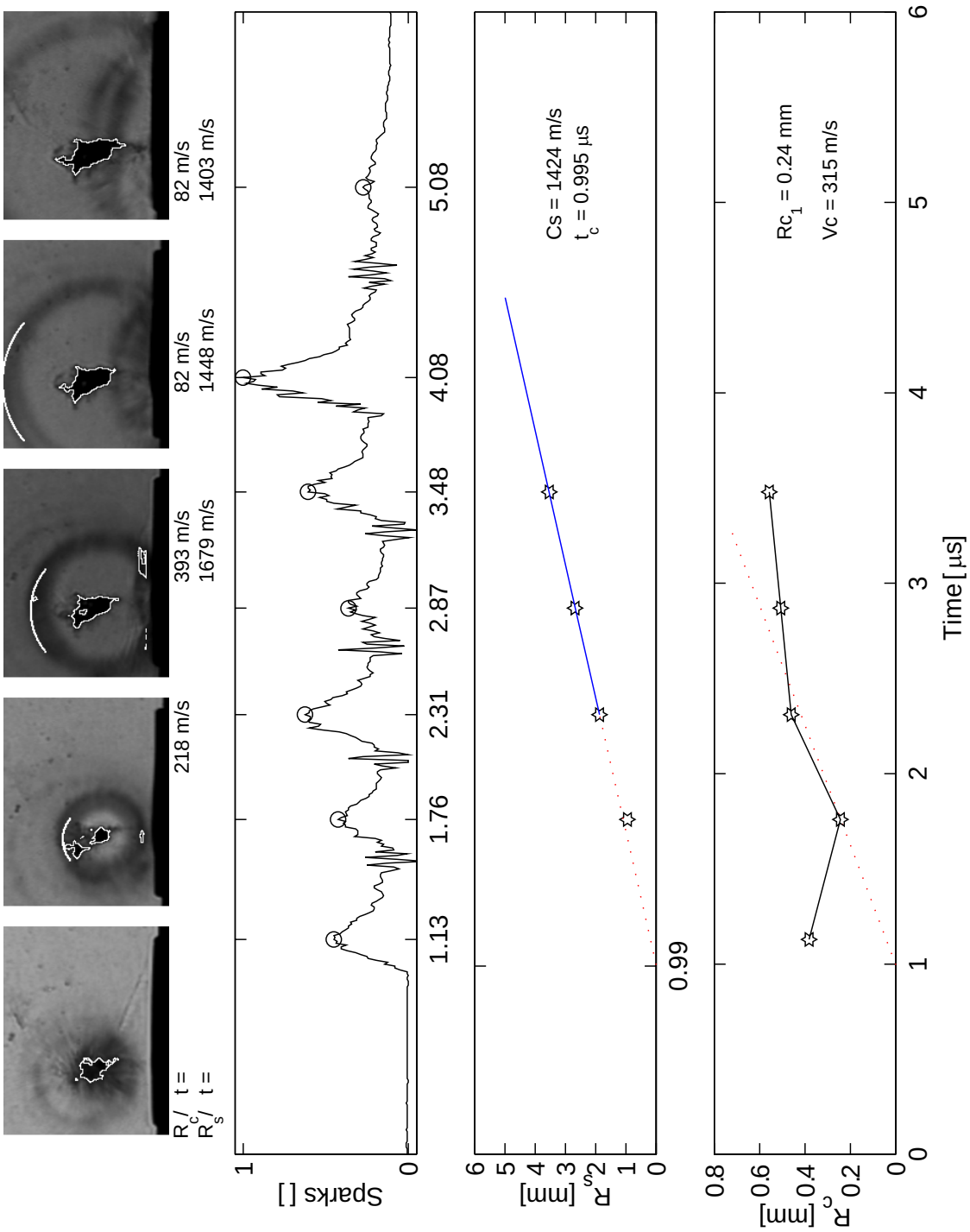

Figure C.16: Collapse time determination and cavitation vortex characteristics N=200 rpm, Q=0.76 l/s, σ=0.9

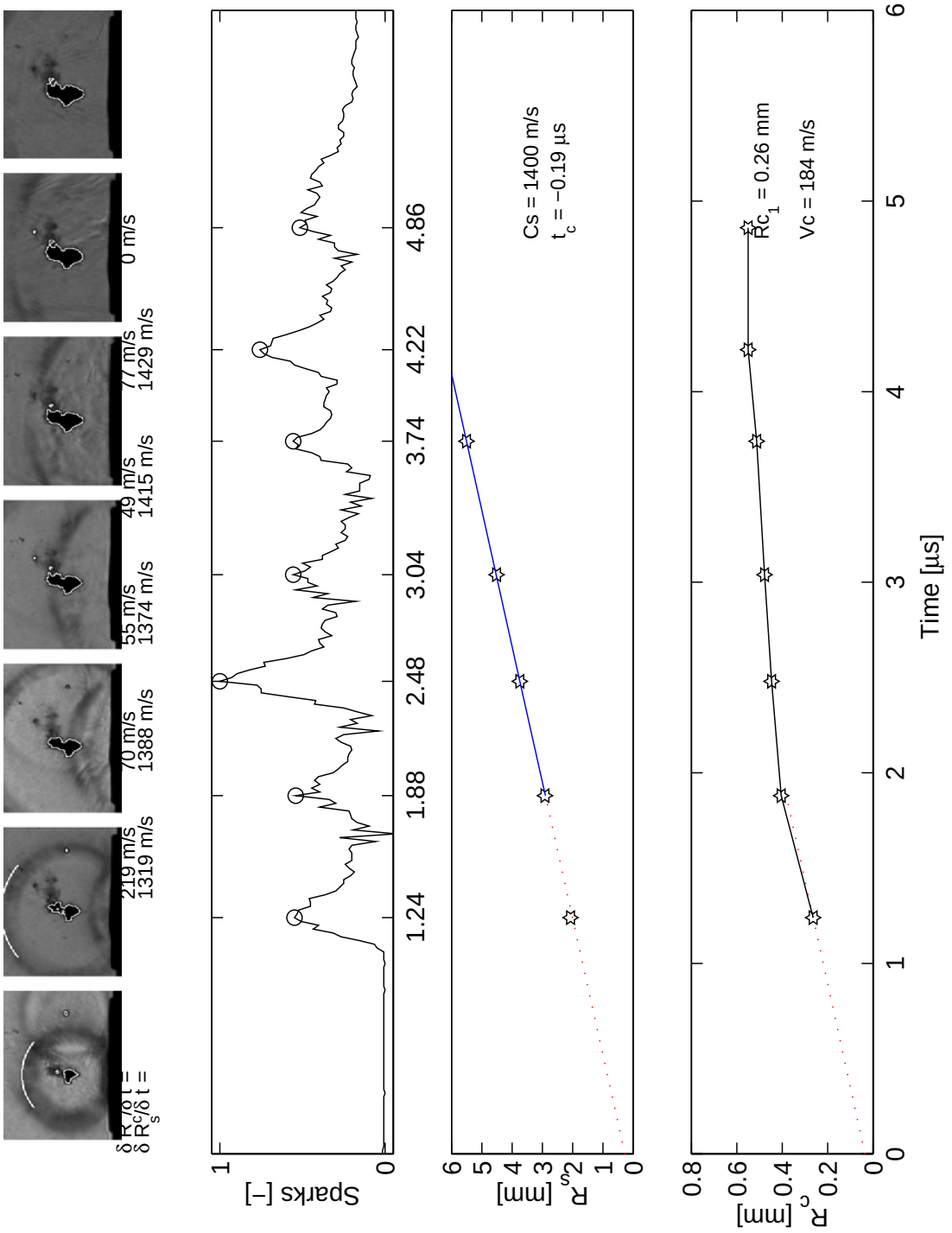

Figure C.17: Collapse time determination and cavitation vortex characteristics N=200 rpm, Q=0.76 l/s, σ=0.9

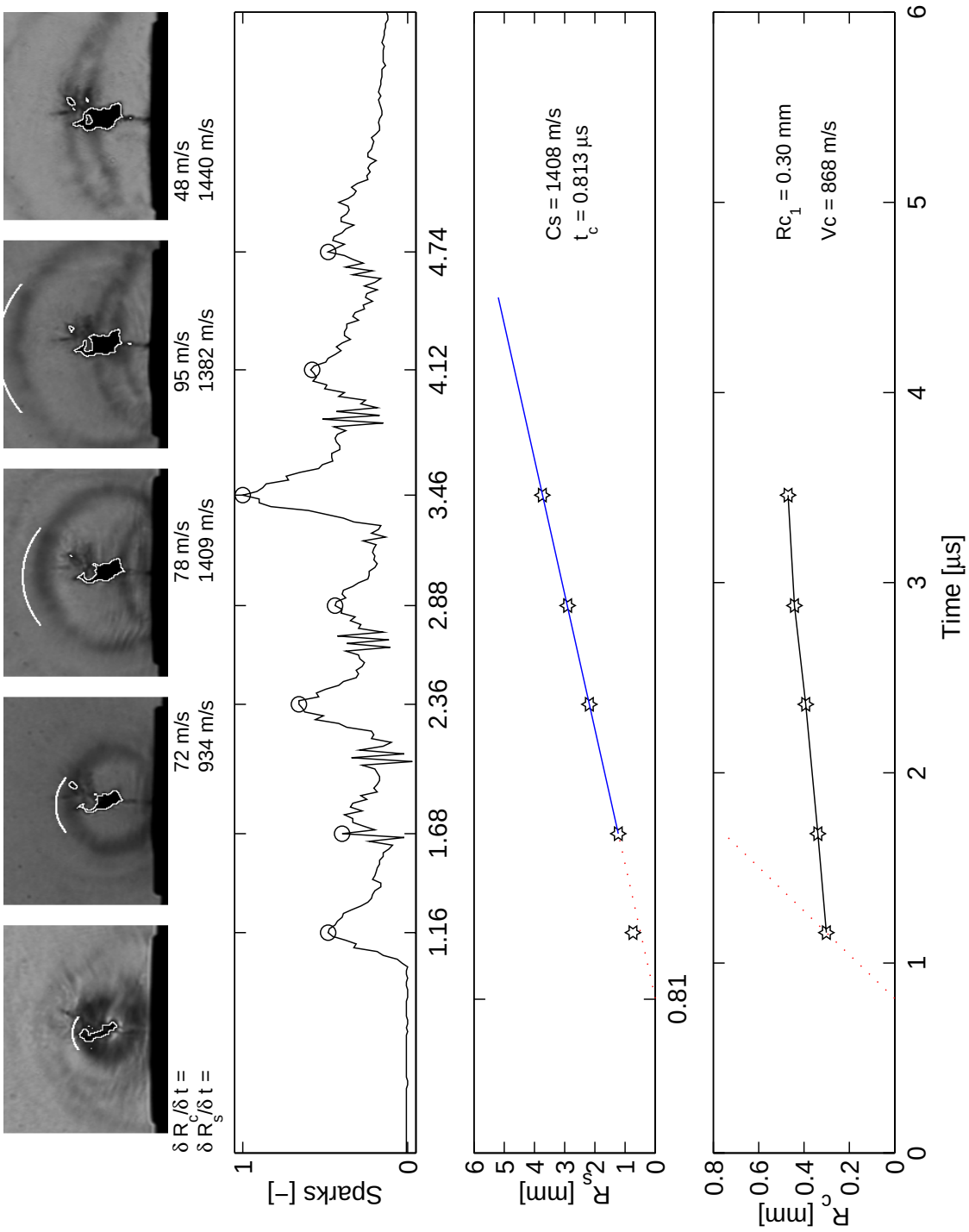

Figure C.18: Collapse time determination and cavitation vortex characteristics N=200 rpm, Q=0.76 l/s, σ=0.9

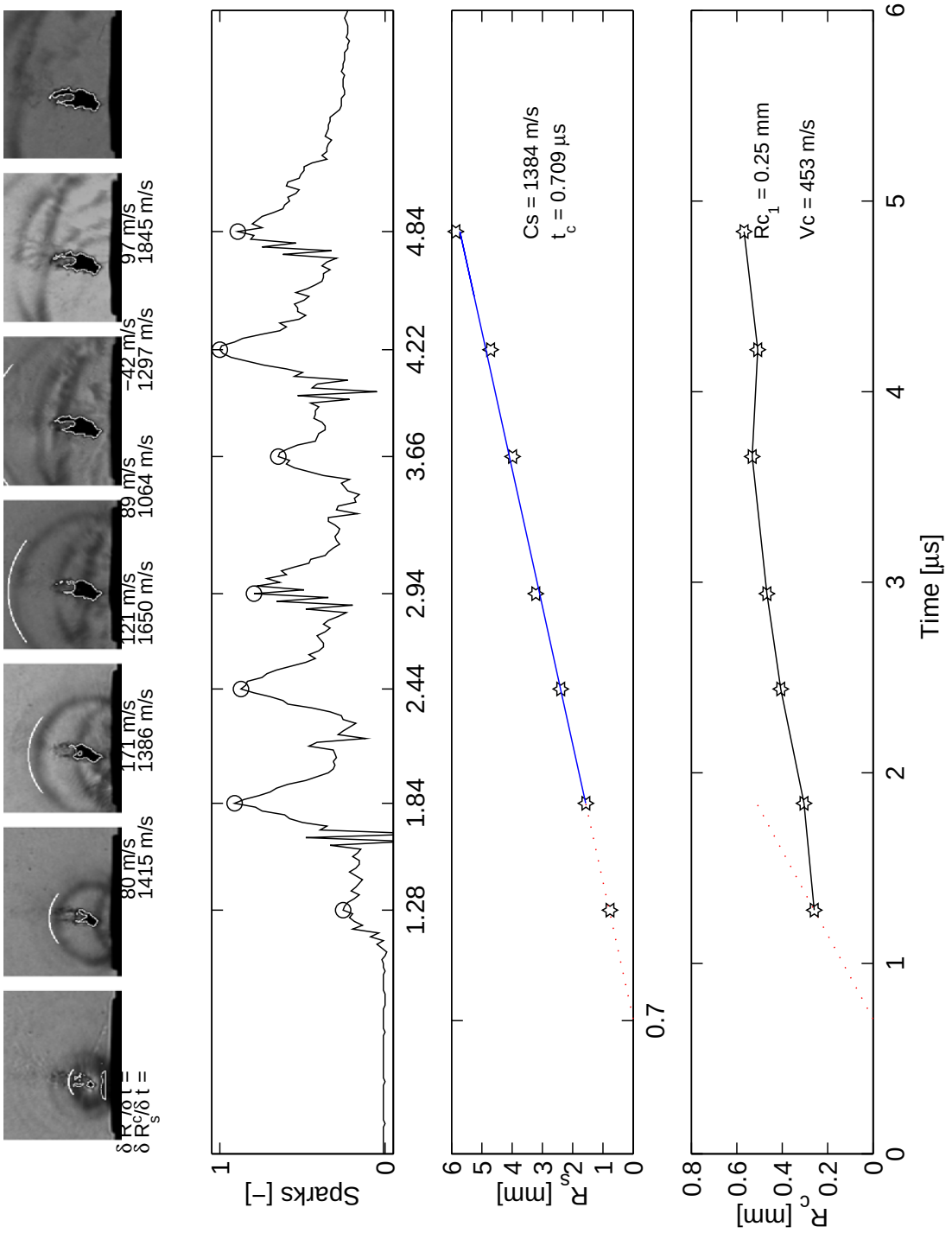

Figure C.19: Collapse time determination and cavitation vortex characteristics N=200 rpm, Q=0.76 l/s, σ=0.9

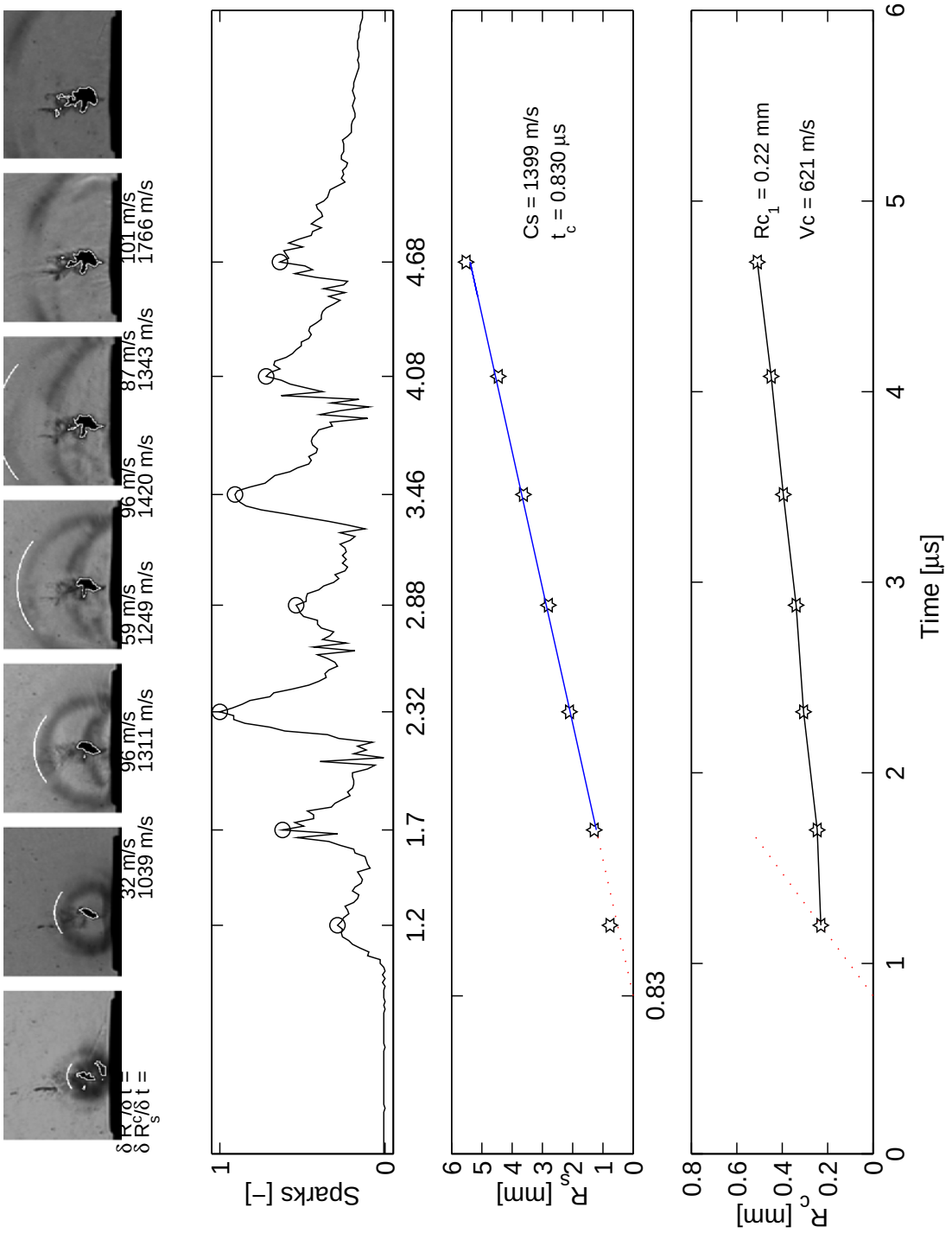

Figure C.20: Collapse time determination and cavitation vortex characteristics N=200 rpm, Q=0.76 l/s, σ=0.9

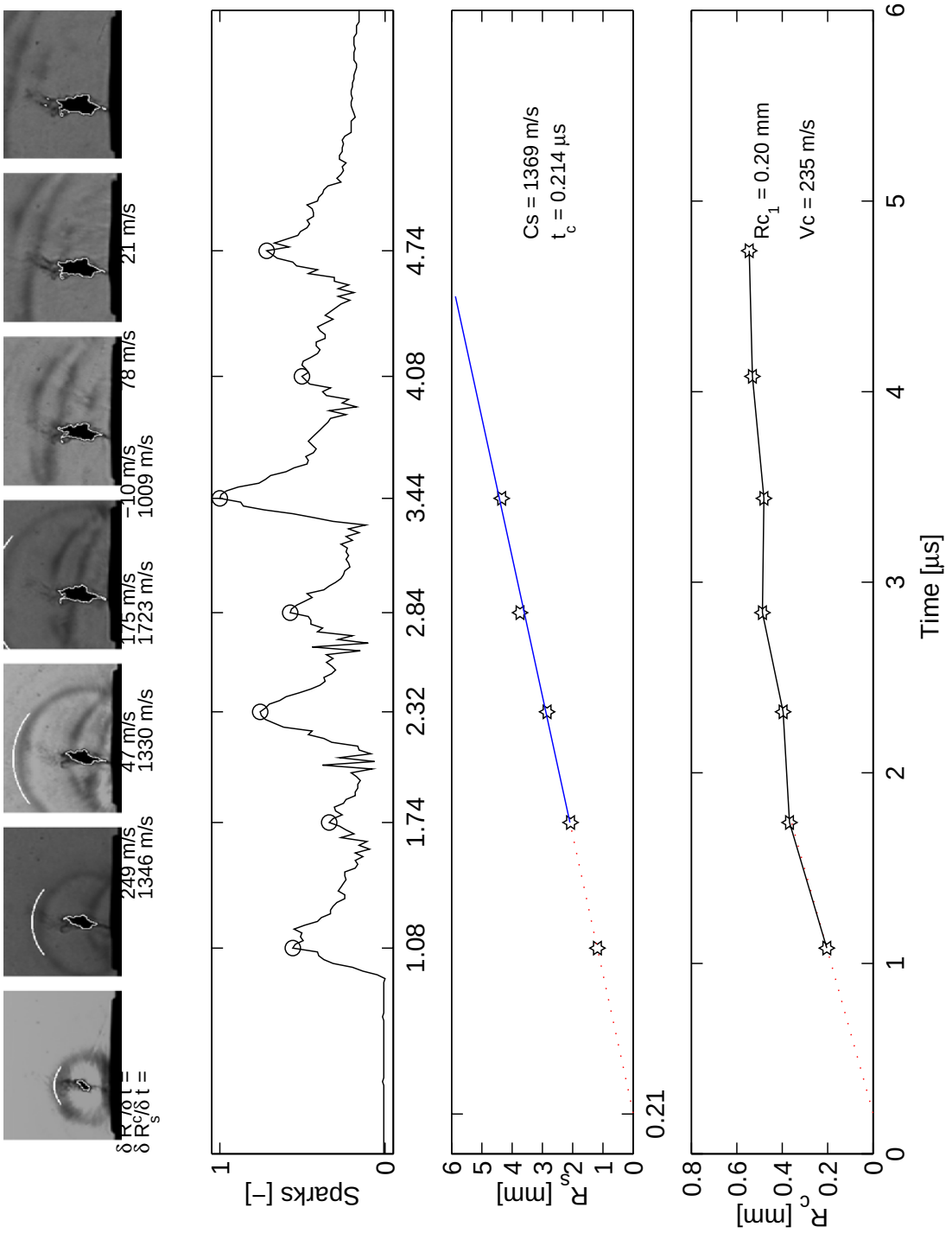

Figure C.21: Collapse time determination and cavitation vortex characteristics N=200 rpm, Q=0.76 l/s, σ=0.9

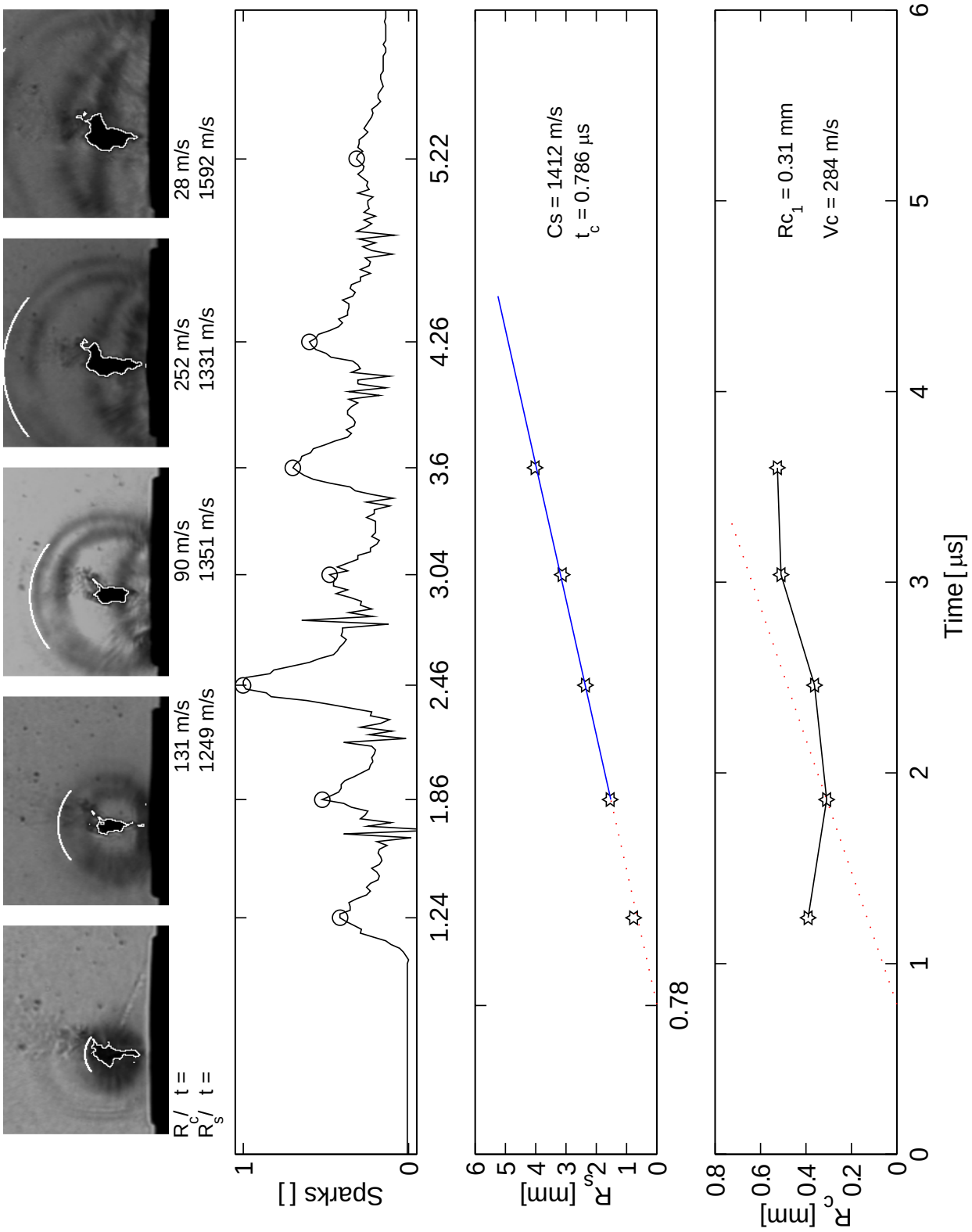

Figure C.22: Collapse time determination and cavitation vortex characteristics N=200 rpm, Q=0.76 l/s, σ=0.9

Appendix D

Simultaneous visualisations

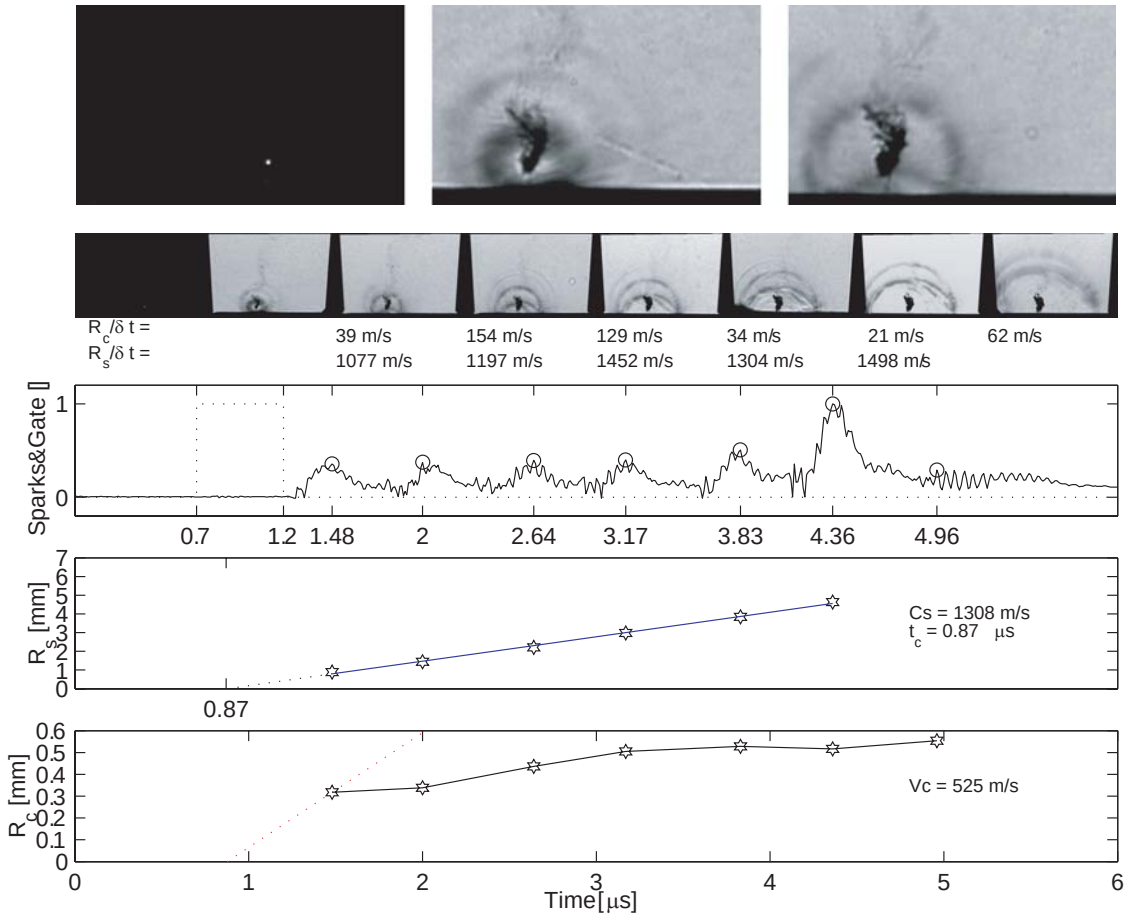

Figure D.1: Simultaneous captures of luminescence and shock wave
$2\ 10^6\ fps$, N=200 rpm, Q=0.58 l/s, σ=1.6

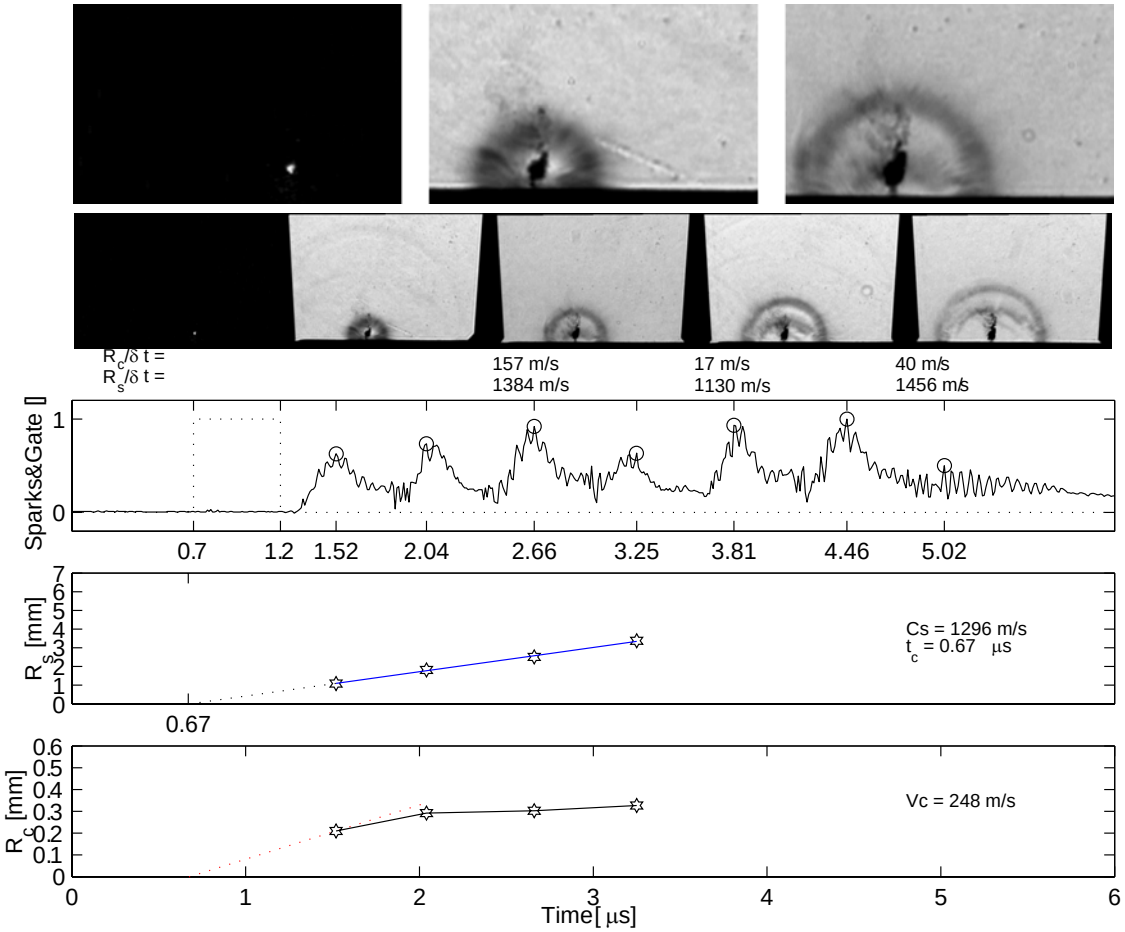

Figure D.2: Simultaneous captures of luminescence and shock wave
2 10^6 fps, N=200 rpm, Q=0.58 l/s, σ=1.6

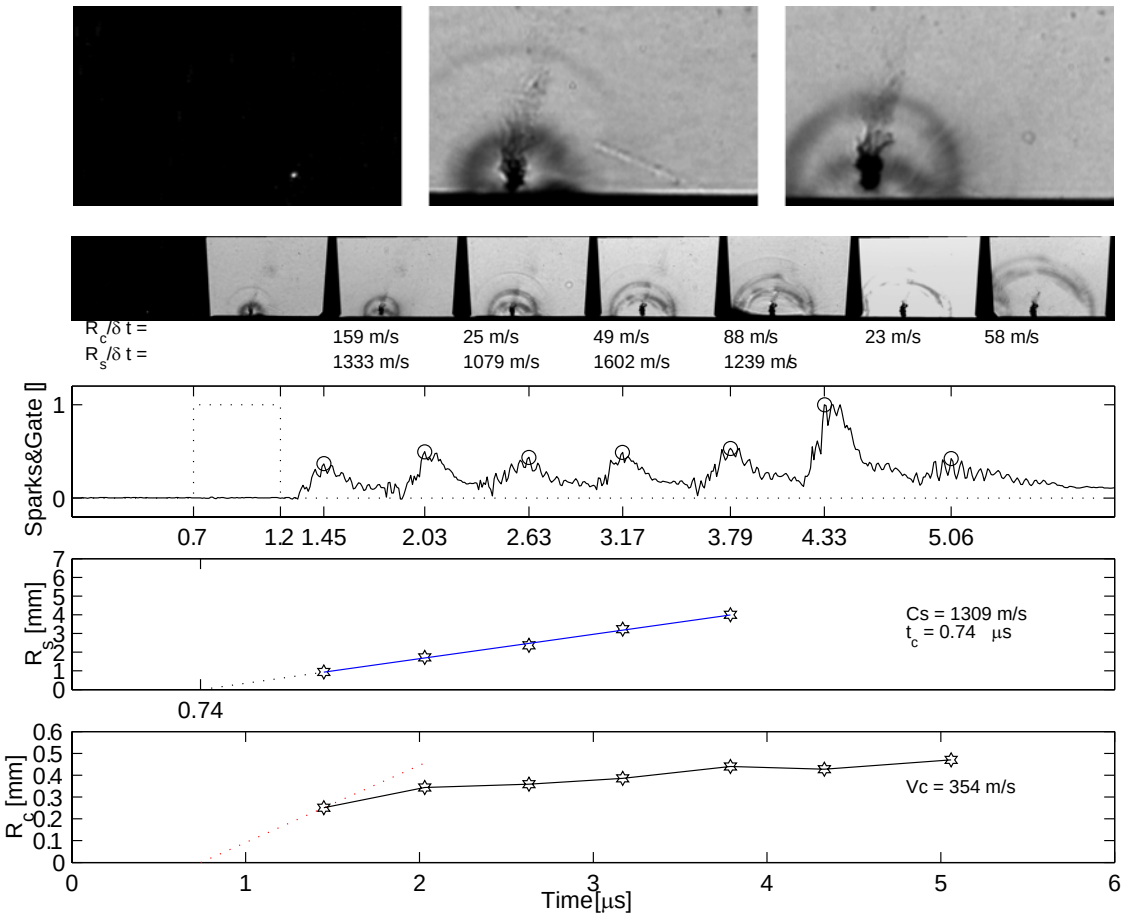

Figure D.3: Simultaneous captures of luminescence and shock wave
2 10^6 fps, N=200 rpm, Q=0.58 l/s, σ=1.6

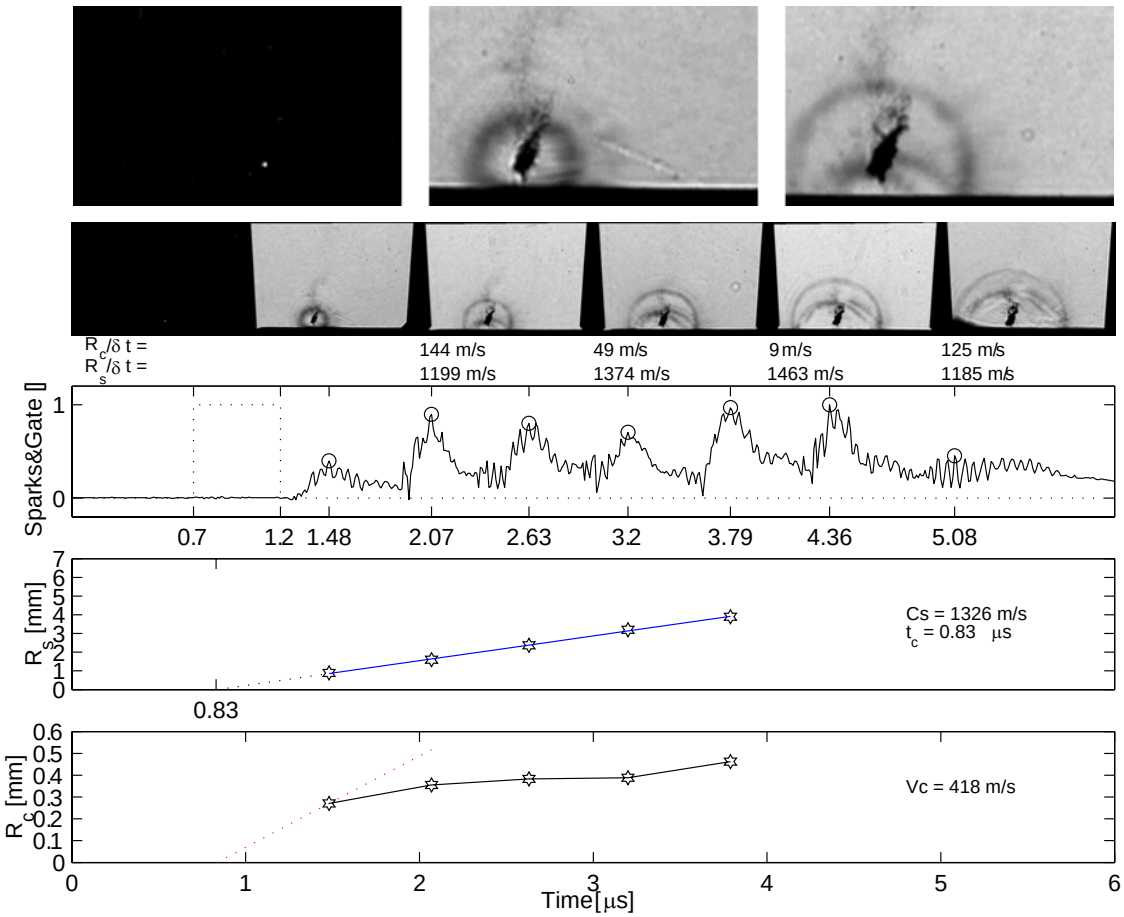

Figure D.4: Simultaneous captures of luminescence and shock wave
2 10^6 fps, N=200 rpm, Q=0.58 l/s, σ=1.6

Bibliography

Avellan, F., Dupont, Ph., Farhat, M. 1991 "Cavitation Erosion Power". *Cavitation 91 Symp., 1st ASME-JSME Fluids Eng. Conf*, Portland (USA).

Avellan, F., Dupont, Ph. 1988 "Cavitation Erosion of Hydraulic Machines : Generation and Dynamics of Erosive Cavities". *14th I.A.H.R Symp. on Progress within and large specific energy units*, Trondheim (Norway).

Avellan, F., Dupont, Ph., Ryhming, I. L. 1988 "Generation Mechanism and Dynamics of Cavitation Vortices Downstream of a Fixed Leading Edge Cavity". *17th O.N.R. Symp. on naval hydrodynamics*, The Hague (The Nederlands).

Avellan, F., Farhat, M. 1989 "Shock Pressure Generated by Cavitation Vortex Collapse". *presented at Third Inter. Symp. on Cavitation and Erosion in Fluid System*, 119–125, San Francisco (USA).

Avellan, F., Henry, P., Ryhming, I. L. 1988 "A New High Speed Cavitation Tunnel for Cavitation Studies in Hydraulic Machinery". *Proc. of Int. Symp. on Cavitation Research Facilities and techniques*, FED 57, 49–60, Boston (USA). ASME Winter Annual Meeting.

Avellan, F., Karimi, A. 1986 "Comparison of Erosion Mechanisms in Different Types of Cavitation". *Wear*, 113, 305–322.

Barber, B. P. & Putterman ,S. J. 1991 "Observation of Synchronous Picosecond Sonoluminescence". *Nature*, London, 352:318-320.

Barber, B. P. & Putterman ,S. J. 1992 "Light Scattering Measurements of a Repetitive Supersonic Implosion of Sonoluminescing Bubble". *Phys. rev. Lett.*, 69, 3839.

Barber, P., Wu, C. C., Löfstedt, R., Roberts, P. H., Putterman, S. J. 1994 "Sensitivity of Sonoluminescence to Experimental Parameters". *Phys. rev. Lett.*, 78, 9.

Bark, G., Berlekom, W. B. 1978 "Experimental Investigations of Cavitation Dynamics and Cavitation Noise". *Proc. of 12th ONR Symp. on Naval Hydrodynamic*, 470–493, Washington, DC (USA).

Batchelor, G. K. 1967 "An Introduction to Fluid Dynamics". Cambridge University Press.

BOURNE, N. K. & FIELD, J. E. 1992 "Shock-induced Collapse of Single Cavities in Liquids". *J. Fluid. Mech.*, vol. 244, 225–240.

BRENNEN, C. E. 1995 "Cavitation and Bubble Dynamics". *Oxford Engineering science series 44.*

BRUHAT, G. 1992 "Optique". Cours de physique générale, edition Masson.

BRUJAN, E. A., NAHEN, K., SCHMIDT, P. & VOGEL, A.01 2001 "Dynamics of laser-induced cavitation bubbles near elastic boundaries: influence of the elastic modulus". J. Fluid Mech., vol. 433, part 3, 283–314.

BRUNTON J. H. 1967 "Erosion by liquid shock". In *Int. Conf. Rain Erosion* (ed. A. A. Fyall & R. B. King), 821–823, RAE, UK.

CHAUDHRI, M. M. & FIELD, J. E. 1974 "The role of rapidly compressed gas pockets in the initiation of condensed explosives". In *Proc. R.Soc.Lond.*, **A340**, 113–128.

COLEY, G. D. & FIELD, J. E. 1973 "The role of cavities in the initiation and growth of explosion in liquids". In *Proc. R.Soc.Lond.*, **A335**, 67–86.

CHINCHOLLE, L. H. 1988 "Study of the Instantaneous Erosion of Cavitation versus Flow, Pressure and Temperature". *J. of Hydraulic Research*, vol. 26, 67–82.

COLE, R. H. 1948 "Underwater Explosions". *Princeton University Press*, Princeton, New Jersey.

COUTY, PH., DUPONT, PH., AVELLAN, F. 1998 "Développement d'une caméra Cranz-Schardin pour la visualisation du collapse d'un vortex cavitant". *XVIIième Colloque national de la commission d'imagerie rapide et photonique*, Strasbourg (France), ANRT.

COUTY, PH., FARHAT, M., AVELLAN, F. 1999 "Visualisation du collapse de cavites et sonoluminescence". *FLUVISU99*, Toulouse (France).

COUTY, PH. 2000 "Prédiction de l'érosion de cavitation sur un profil 2D" *Internal Report LMH-EPFL*, No. LMH-2000-002.

COUTY, PH., FARHAT, M., AVELLAN, F. 2001 "Physical Investigation of a Cavitation Vortex Collapse". *CAV'2001*, Int. Symp. on Cavitation, Pasadena (USA).

DEAR, J. P. & FIELD, J. E. 1988 "A Study of the Collapse of Arrays of Cavities". *J. Fluid. Mech.*, vol. 190, 409–425.

DEAR, J. P., FIELD, J. E. & WALTON, A. J. 1988 "Gas Compression and Jet Formation in Cavities Collapsed by a Shock Wave". *Nature*, Vol. 332, No. 6164, 505–508.

DUPONT, PH. 1993 *"Etude de la dynamique d'une poche de cavitation partielle en vue de la prédiction de l'érosion dans les turbomachines hydrauliques"*. Thèse de doctorat **931**, Ecole Polytechnique Fédérale de Lausanne, Institut de Machines Hydrauliques et de Mécanique des Fluides (IMHEF-LMH).

EVANS, A. K. 1996 "Instability of converging shock waves and sonoluminescence". *Physical rev. E.*, Vol. 54, No. 5.

FARHAT, M. 1994 *"Contribution à l'étude de l'érosion de cavitation : mécanismes hydrodynamiques et prédiction"*. Thèse de doctorat **1273**, École Polytechnique Fédérale de Lausanne, Institut de Machines Hydrauliques et de Mécanique des Fluides (IMHEF-LMH).

FARHAT, M., AVELLAN, F., PEREIRA, F. 1992 "Pressions instationnaires générées par une poche de cavitation partielle". Dans *Proc. des Deuxièmes Journées Cavitation SHF*, édité par "La Houille Blanche", tome 7, 579–585, Paris. Société Hydrotechnique de France.

FARHAT, M., PEREIRA, F., AVELLAN, F. 1991 "Cavitation Erosion Power as a Scaling Factor for Erosion of Hydraulic Machines". *Cavitation 91 Symp.*, 1st ASME-JSME Fluids Eng. Conf, Portland (USA).

FIELD, J. E. 1994 "Experimental studies of bubble collapse". *in J.R. Blake* et al. *(eds*, "Bubble dynamics and interface phenomena", Kluwer Academic Publ., The Netherlands, 17–311.

FIELD, J. E., BOURNE, N. K., PALMER, S. J. P., WALLEY, S. M. 1992 "Hot-spot Ignition Mechanisms for Explosives and Propellants". *Phil. Trans. R. Soc. Lond. A.*, **339**, 269–283.

FORTES-PATELLA, R. 1994 "Analyse de l'érosion de cavitation par simulations numériques d'impacts". *Thèse de Doctorat*, Institut National Polytechnique de Grenoble, CREMHyG, Grenoble (France).

FORTES-PATELLA, R., REBOUD, J. L. 1998 "A new Approach to Evaluate the Cavitation Erosion Power". *J. Fluids Engeneering*, Vol. 120, 335–344.

FUJIKAWA, S., AKAMATSU, T. 1980 "Effects of the Non-equilibrium Condensation of Vapour on the Pressure Wave Produced by the Collapse of a Bubble in a Liquid". J. Fluid Mech., vol. 97, part 3, 481–512.

GILMORE, F. R. 1952 "The Collapse and Growth of a Spherical Bubble in a Viscous Compressible Fluid". Cal. Inst. of Tech. Hydrodynamic Lab., Rep. No. 26-4.

HAMMITT, F. G. 1963 "Observations on Cavitation Damage in a Flowing System". *Trans. ASME, J. of Basic Engineering*, 347–367.

HANDBOOK OF CHEMISTERY AND PHYSICS 1982 62nd edition, CRC Press.

HERRING, C. 1941 "Theory of the Pulsations of the Gas Produced by an Underwater Explosion". Rept. No. 236, Office of Scientific Research and Developpment.

HICKLING, R., PLESSET, M. 1964 "Collapse and Rebound of Spherical Bubble in Water". *Phys. of Fluid* 7, 1.

HILGENFELDT, S., BRENNER, M. P., GROSSMANN, S., LOHSE, D. 1998 "Analysis of Rayleigh-Plesset Dynamics for Sonoluminescing bubbles". *J. Fluid Mech.*, vol. 365, 171–204.

HOLZFUSS, J., RUGGEBERG, M., BILLO A. 1998 "Shock Wave Emissions of a Sonoluminescing Bubble". *Phys. rev. Lett.* **81**, 23.

KATO, H., MAEDA, T., MAGAINO, A. 1978 "Mechanism and Scaling of Cavitation Erosion". *Proc. of the XVII ONR Symposium*, 452–469, Washington, D.C. (USA). ONR.

KIRKWOOD, J. G., BETHE, H. A. 1942 "The Pressure Wave Produced by an Underwater Explosion". Rept. No. 558, Office of Scientific Research and Developpment.

KORNFELD, M., SURONOV, L. 1944 "On the Destructive Action of Cavitation". *J. Appl. Phys.*, **15**, 495–506.

KNAPP, R., DAILY, J. W., HAMMITT, F. G. 1970 "Cavitation". *N.-Y. McGraw-Hill.* 578 pages.

LENTZ, W. J., ATCHLEY, A. A., GAITAN, D. F. 1995 "Mie Scattering from a Sonoluminescing Bubble in Water". *Applied Optics*, Vol. 34, num 15, 2648–2654.

LOHSE, D., HILGENFELDT, S. 1997 "Inert Gas Accumulation in Sonoluminescing Bubbles". *J. Chem. Physics*, Vol. 107, 6786–6797.

MAAMOURI, M. 1989 "Contribution à l'étude de l'érosion par cavitation dans l'eau". Thèse de doctorat, École Polytechnique Fédérale de Lausanne, No. 821.

NAUDÉ, C. F., ELLIS, A. T. 1961 "On the Mechanism of Cavitation Damage by Nonhemispherical Cavities in Contact with a Solid Boundary". *Trans. ASSME D, J. Basic Eng.*, **83**, 648–656.

NORDLING, C., OSTERMAN, J. 1987 "Physics Handbook". Studentlitteratur.

PEREIRA, F. 1997 *"Prédiction de l'érosion de cavitation: approche énergétique"*. Thèse de doctorat **1592**, École Polytechnique Fédérale de Lausanne, Institut de Machines Hydrauliques et de Mécanique des Fluides (IMHEF-LMH).

PEREIRA, F., AVELLAN, F., DUPONT, PH. 1998 "Prediction of Cavitation Erosion : An Energy Approach". *J. Fluids Engineering*, Vol. 120, 719–727.

PEREIRA, F., AVELLAN, F., DOREY, J. M. 1995 "Cavitation Erosion : Statistical Analysis of Transient Cavities". *Int. Symp. on Cavitation*, Cav'95, Deauville.

PEREIRA, F., FARHAT, M., AVELLAN, F. 1994 "Dynamic Calibration of Transient Sensors by Spark Generated Cavity J. R. Blake *et al.* (eds), *Bubble and Interface Phenomena*, 227–240.

PLESSET, M. 1949 "The Dynamics of Cavitation Bubbles". *J. Appl. Mech*, **16**, 277.

PUTTERMAN, S. J., WENINGER, K. R. 2000 "SONOLUMINESCENCE : How Bubbles Turn Sound into Light". *Annu. Rev. Fluid. Mech.*, vol. 32, 445–476.

RAYLEIGH L. 1917 "On the Pressure Developped in a Liquid during the Collapse of a Spherical Void". *Philosophical Magazine and Journal of Science*, **34**(6), 94–98.

REBOUD, J. L., FORTES-PATELLA, R., ARCHER, A, 1999 "Analysis of Damaged Surfaces : Part I : Cavitation Mark Measurements by 3D Laser Profilometry". *Proc. 3rd ASME/JSME Joint Fluids Eng. Conf.*, San Francisco (USA).

RIDAH, S. 1987 "Liquid jet Impact - Shock Waves in Water - Analytical Solutions". *Internal report, Dep. of Mech., Lab. for Hydraulic Machines.*

RIDAH, S. 1988 "Shock Waves in Water". *J. Appl. Phys.*, **64** (1), 152–158.

SAFFMAN, P. G. 1992 "Vortex Dynamics". *Cambridge monographs on Mechanics and Applied Mathematics.*

SELIM, S. M. A. 1985 "A Theoritical Study on Cavitation Erosion rate". *Cavitation in Hydraulic Structures and Turbomachinary*, Albuquerque, New Mexico (USA). ASCE/ASME Mechanics Conference.

SIMONEAU, R., AVELLAN, F., KUHN DE CHIZELLE, Y. 1989 "On Line Measurement of Cavitation Erosion Rate on a 2D NACA Profile". *Proc. of International Symposium on Cavitation Noise and Erosion in Fluid Systems*, tome FED 88, 95–102, San Francisco (USA), ASME Winter Annual Meeting.

THIRUVENGADAM, A. 1971 "Scaling Laws for Cavitation Erosion". *Proc. of IUTAM Symp. on flow of water at high speeds*, 405–425, Lenningrad.

SHIMA., A., TAKAYAMA, K., TOMITA, Y. & OHSAWA, N. 1983 "Mechanism of Impact Pressure Generation from Spark-Generated Bubble Collapse near a Wall". *AAAA*, **21**, 55–59.

TOMITA, Y. & SHIMA., A., TAKAHASHI, K. 1983 "The Collapse of a gas bubble attached to a solid wall by a shock wave". *J. Fluid Engng.*, **105**, 341–349.

TOMITA, Y., SHIMA., A. & OHNO, T. 1984 "Collapse of multiple gas bubbles by a shock wave and induced impulsive pressure". *J. Appl. Phys.*, **56**, 125.v

TOMITA, Y., SHIMA., A. 1986 "Mechanisms of Impulsive Pressure Generation and Damage Pit Formation by Bubble Collapse". *J. Fluid Mech.*, **169**, 535–564.

VOGEL, A., LAUTERBORN, W., TIMM, R. 1989 "Optical and Acoustic Investigations of the Dynamics of Laser-produced Bubbles Near a Solid Boundary". *J. Fluid. Mech.*, **206**, 299–338.

WALTON, A. J. & REYNOLDS, G. T. 1984 "Sonoluminescence". *Adv in Phys.*, Vol. 33, 595–660.

WANG, Y. C., BRENNEN, C. 1996 "Shock waves in Cloud Cavitation". submitted to *J. Fluid. Mech.*.

WARD, B., EMMONY, D. C. 1990 "The Energies and Pressures of Acoustic Transients Associated with Optical Cavitation in Water". *Journal of Modern Optics*, Vol. 37, No 4, 803–811.

Wu & Roberts 1994 "Shock-Wave Propagation in a Sonoluminescing Gas Bubble". *Phys. of Fluids*, Vol. 6, No. 9.

Fin.
... mais encore du pain sur la planche.
Merci à Stéphanie et Soline pour leurs encouragements et leur patience.